INVESTIGATING VOLCANIC ERUPTIONS AT THE SEAMOUNT TAFU: CHEMICAL AND GEOGRAPHIC VARIATION WITHIN THE NELSC

A THESIS SUBMITTED TO THE GRADUATE DIVISION OF THE UNIVERSITY OF HAWAIʻI AT MĀNOA IN PARTIAL FULFILLMENT OF THE REQUIREMENTS FOR THE DEGREE OF

MASTER OF SCIENCE
IN
GEOLOGY AND GEOPHYSICS

JULY 2020

by

Malia Christine Zinn

Thesis Committee
Ken Rubin, Chairperson
Scott Rowland
Tom Shea

1. Acknowledgements

I would like to primarily thank my advisor and committee chair, Dr. Ken Rubin, for his guidance through the process of completing this body of work. I appreciate his patience in explaining concepts that were foreign to me, and his support throughout my first significant dive into a completed research project. Finishing a thesis during quarantine in a global pandemic was a challenge I never expected to take on, but our weekly Zoom calls were a source of encouragement and guidance that kept me going.

I am grateful for the knowledge, support, and reassurance of my committee members, Dr. Tom Shea and Dr. Scott Rowland. Their assistance in completing this body of work was invaluable, and so very much appreciated. My classes with both Tom and Scott helped remove some of the fear and imposter syndrome around conducting my research; their guidance made it easier for me to ask questions, expand my knowledge, and learn without fear. I would like to thank Scott for his words of wisdom when writing a thesis felt unapproachable and for his check-ins to make sure I was not just progressing but progressing while keeping my health and happiness a priority as well. Thank you to Tom for the kind comments and encouragement regarding my writing, which was not always easy to complete or feel confident about.

I am indebted to my family for their endless support throughout this work. None of us knew what I was getting myself into, but they have been next to me every step of the way with every curveball and misstep. I am so lucky to have a family that loves me unconditionally. Thanks for loving on Mischka while I have been gone and sending updates on his daily musings (hiding in paper, sleeping on the couch, walking in the backyard, etc.).

To Kevin, I would like to give my unending appreciation for your daily support and encouragement. I cannot begin to express my gratitude for helping pick me up with every stumble and pushing me to finish when I needed it. Your sacrifices to help me complete this work have not gone unnoticed. Thank you for walking this path with me and being there for the length of this journey.

I am sincerely grateful to Sarah for helping provide me with the tools I needed to complete this degree. This process has challenged me in so many of my weaknesses, and in many ways I never expected. I am appreciative for your guidance in overcoming these obstacles and in learning to be patient with my progress and myself.

I would like to thank my fellow graduate students for their friendship and for the endless questions they have helped me answer in the process of navigating my master's degree.

I would like to thank the Native Hawaiian people of Oʻahu for allowing me to stay on native land as I have studied and pursued this degree in Mānoa. The Hawaiian Islands are irreplaceable, and I have learned so much outside of the scope of this study from living here. Geology directly studies the physical world, which cannot be separated from the culture of those who loved this land first. I look forward to continuing my education through this ʻāina in the future.

Lastly, I would like to thank the Schmidt Ocean Institute and the National Science Foundation. Thank you to the scientists and crew of the FK171110 cruise, whose work at sea made this study possible. This research was funded through the National Science Foundation, grant number OCE-1538121.

2. Abstract

Most eruptions on Earth are likely submarine (Rubin et al., 2012); however, relatively little is known about deep-sea eruptions due to the difficulty in detecting and observing them. The Northeast Lau Spreading Center (NELSC) in the Northeast Lau Basin is an excellent location to study these deep-sea processes, as it is one of the most volcanically active submarine provinces on Earth. This thesis presents reports on three known eruptions that occurred at the NELSC seamount Tafu between 2006 and 2017 and compares them to a 2008 eruption that occurred at Tafu's next-ridge neighbor, Puipui (Baker et al., 2011). The new Tafu eruption deposits were identified by bathymetric changes of up to 100m between repeated multibeam sonar surveys conducted over the past two decades.

The Schmidt Ocean Institute cruise FK171110 set out in 2017 to investigate the Northeast Lau Basin using both autonomous underwater vehicle (AUV) and ship-based bathymetric mapping. During this cruise, the remotely operated vehicle SuBastian conducted several dives, including two at the NELSC: one on Tafu's north flank, and one on Tafu's south flank. Photos and videos were taken throughout the dive, and rock and sediment samples were collected.

This study investigates the geochemistry, petrology, and morphology of samples collected, and how this relates to the locations in which they were emplaced. Pairing observations made from photo/video evidence from the dives with both electron microprobe analysis and Raman microscopy allows for reconstruction of magma formation history and eruption conditions.

3. Table of Contents

1. ACKNOWLEDGEMENTS.....2
2. ABSTRACT.....4
3. Table of Contents.....5
4. List of Figures.....7
5. List of Tables.....8

6. INTRODUCTION AND BACKGROUND.....9
6.1. Introduction.....9
6.2. Submarine Volcanism.....10
6.3. Geologic Setting.....11
6.4 Types of Submarine Lavas.....16
6.5 Timeline of NELSC Cruise Events.....20

7. METHODS.....25
7.1. Field methods.....25
7.2. Video observations.....35
7.3. Analytical methods.....35
7.3.1. Electron microprobe analysis (EPMA).....35
7.3.2. Raman spectroscopy.....40

8. RESULTS.....42
8.1. Field Results.....42
8.1.1. Video observations.....42
8.1.2. Grouping samples by eruption using geochemistry and video evidence.....48
8.2. Analytical Results.....52
8.2.1. Electron microprobe analysis of major elements in glass.....52
8.2.2. Visual observations of glasses using backscattered electron imaging.....57
8.2.3. Raman Spectroscopy.....59
8.2.3.1. VolatileCalc 2.0.....66

9. DISCUSSION.....68
9.1. MELTS modeling.....68
9.2. Water content as determined by Raman spectroscopy.....77
9.2.1. Change in water content with depth.....78
9.2.1.1. VolatileCalc 2.0.....79
9.2.2. Change in water content with MgO.....83
9.2.3. Change in water content with K_2O.....84
9.2.4. Change in water content with morphology.....85
9.3. Magma history: parent melts, mixing, and fractional crystallization.....86
9.4. Puipui.....97
9.5. Summary.....99

10. APPENDICES.....104
10.1. Appendix A: Photographs of rock and sediment samples.....104
10.2. Appendix B: Photographs of locations of sample collection.....125
10.3. Appendix C: Photomicrographs of glass chips.....144
10.4. Appendix D: Additional major element chemistry figures.....153
10.5. Appendix E: Water content figures using >7.6% variation rejection criteria, and no rejection criteria.....154
10.6. Appendix F: Additional MELTS models.....159

11. REFERENCES.....164

4. List of Figures

Figure 6.1. Bathymetric map of the Tonga intra-oceanic subduction zone.....13
Figure 6.2. Cartoon cross section of the NE Lau Basin.....14
Figure 6.3. Bathymetric map of the NE Lau Basin.....15
Figure 6.4. Influence of variables on submarine lava morphology.....17
Figure 6.5. Wax models, photographs, and sketches of submarine lava morphology.....18
Figure 6.6. Submarine lava morphology related to cooling rate, slope, and flow rate.....19
Figure 6.7. Photographs of plobate lavas, pillow tubes, and talus.....20
Figure 6.8. Dive tracks of J2-425 and J2-426 on AUV bathymetry data of Puipui.....23
Figure 6.9. Location of Dredge 1 and Dredge 2 from KM 1024.....24

Figure 7.1. Multibeam depth difference map of North and South Tafu.....27
Figure 7.2. Map of the completed FK171110-S98 dive track.....32
Figure 7.3. Map of the completed FK171110-S99 dive track.....33

Figure 8.1. Bathymetric map of South Tafu with morphologies and dive track.....44
Figure 8.2. Bathymetric map of North Tafu with morphologies and dive track.....47
Figure 8.3. Total Alkali Silica diagram of S98 and S99 rock and sediment samples.....52
Figure 8.4. Major element composition plots of S98 and S99 samples.....56
Figure 8.5. Backscattered electron image of rock S99-R06, glass chip 03.....58
Figure 8.6. Backscattered electron image of rock S99-R12, glass chip 03.....58
Figure 8.7. Wt.% H_2O vs. wt.% MgO.....63
Figure 8.8. Wt.% H_2O vs. wt.% K_2O.....63
Figure 8.9. Wt.% H_2O vs. water depth.....64
Figure 8.10. Comparison of wt.% H_2O with morphology type.....65
Figure 8.11. VolatileCalc 2.0 model.....67

Figure 9.1. Wt.% MgO vs. oxides of best fit MELTS models.....75
Figure 9.2. Wt.% H_2O vs. water depth with highlighted talus and sediments.....78
Figure 9.3. VolatileCalc 2.0 model with highlighted talus and sediments.....79
Figure 9.4. Wt.% H_2O vs. wt.% MgO.....84
Figure 9.5. Wt.% H_2O vs. wt.% K_2O.....85
Figure 9.6. Comparison of wt.% H_2O with morphology type.....86
Figure 9.7. Wt.% MgO vs. oxides of MELTS models, Tafu samples, and Puipui samples.....87
Figure 9.8. Crystal zoning in NT 2 samples.....94
Figure 9.9. Crystal zoning in South Tafu samples.....95

5. List of Tables

Table 7.1. Samples collected on dive FK171110-S98.....29
Table 7.2. Samples collected on dive FK171110-S99.....30
Table 7.3. EPMA element acquisition settings.....38
Table 7.4. Average measured and published values of standards A99 and VG2.....39

Table 8.1. Summary of definitions of eruptive groups.....51
Table 8.2. Microprobe glass analyses of major element compositions for FK171110-S98 and -S99 samples.....53
Table 8.3. Wt.% of H_2O in glass samples determined by Raman spectroscopy.....60

Table 9.1. Conditions used for best fit MELTS models.....69
Table 9.2. Compositions of parent melts used for best fit MELTS models.....70
Table 9.3. Major element compositions of all non-FK171110 Tafu samples.....96
Table 9.4. Summary of features of each eruptive group.....103

6. Introduction and Background

6.1 Introduction

Submarine volcanism is a main driver for ocean crust formation, heat transfer, and volatile transfer, and therefore is vital to understanding Earth's processes. However, due to the difficulty in detection and observation, deep-sea eruptions remain poorly understood compared to their subaerial cousins (Rubin et al., 2012). One place where deep sea eruptions are being consistently studied and monitored is the Lau Basin in the southwest Pacific Ocean. Despite its prominent location within the Lau Basin and proximity to comparatively well-studied submarine volcanoes, no in-depth investigations of Tafu, the subject of this study, have been completed. However, observations made at Tafu in December of 2017 on Schmidt Ocean Institute cruise FK171110 indicate that it is much more volcanically active than initially assumed. By exploring the geochemistry and petrology of recently erupted lava samples coupled with the geography and geomorphology of the volcano itself, we aim to reconstruct magma formation history and eruption conditions at Tafu. We seek to determine the number of eruptions that have occurred since observations there began, determine if the eruptions are chemically and/or temporally related, and compare these results to samples from Puipui, Tafu's neighbor, to determine if the eruptions are related. In doing this, we hope to better understand the processes driving Tafu's eruptions and make room for future investigations of different seamounts that could behave similarly to Tafu.

6.2 Submarine Volcanism

Submarine volcanoes are responsible for creating new oceanic crust; because oceanic lithosphere comprises almost two-thirds of the Earth's crust, this makes them an integral geologic process on Earth (Rubin et al., 2012). Despite their importance, at this time submarine volcanoes cannot be monitored, observed, explored, or studied with the depth and ease that subaerial volcanoes are. Of the 537 historically active volcanic eruptions that have been detected within the last 500 years, 497 have been subaerial, 23 have been shallow submarine, and 17 have been deep submarine (Rubin et al., 2012). This is not to say that subaerial eruptions are more numerous than submarine eruptions, only more easily observed. Submarine eruptions in the deep ocean along mid-ocean ridges, near subduction zones, and on mid-plate seamounts have comprised the greatest number and volume of volcanic eruptions on Earth (Rubin et al., 2012).

Many conventional volcano monitoring techniques and technologies cannot be used to observe eruptions in the deep ocean. Instead, land-based seismic networks, long-range hydroacoustic networks, hydrophone arrays, and serendipitous observations must be used to detect eruptions (Baker et al., 2012). For example, the eruptive products studied in this investigation were serendipitously discovered by repeated multibeam bathymetric surveys that bracketed the emplacement of the lava flows and sediments. Tools used to investigate initial detections of eruptions can include a conductivity, temperature, and depth sensor (CTD), remotely operated vehicles (ROV), human-occupied vehicles (HOV), autonomous underwater vehicles (AUV), in situ instruments if available, camera tows, and dredging among many others. Rock and sediment specimens used in this study were collected using the ROV SuBastian.

Responses to submarine eruptions once they have been detected can also pose unique challenges. The quickest seagoing response to a detected eruption was mobilized within about a week, and only 12 of 35 historical detection and response efforts occurred within 30 days of the detected eruption (Baker et al., 2012). Additionally, all but three of these efforts were in response to eruptions on the Juan de Fuca Ridge, easily within reach of US ports in the Pacific Northwest (Baker et al., 2012). Organizing and dispatching a response effort is no small task, and even a delay of one week risks losing observations of syn- and post- eruption processes (Baker et al., 2012). The difficulty in both detection of, and rapid response to, submarine eruptions make studying seafloor processes slow, difficult and expensive.

6.3 Geologic Setting

The fastest subduction and back-arc spreading rates in the world can be found at the Tonga Intra-Oceanic Subduction Zone (TIOSZ, Figure 6.1) (Zellmer and Taylor, 2001; Embley and Rubin, 2018; Baker et al., 2019); Zellmer and Taylor (2001) modeled spreading rates of 50-100 mm/year from the Mangatolu Triple Junction (MTJ) to the Fonualei Rift and Spreading Center (FRSC), both of which are spreading centers within the Lau Basin. Bird (2003) extrapolated these rates to estimate a spreading rate of up to 128 mm/year at the Northeast Lau Spreading Center (NELSC), one of many spreading centers in the Lau Basin and the focus of this study (Baker et al., 2019) (Figure 6.2). Additionally, of all intra-oceanic subduction zones, the NE Lau Basin has the highest upper mantle temperatures (Wiens et al., 2006), one of the coldest slab thermal parameters, and one of the highest slab water fluxes on Earth (van Keken et al., 2011; Embley and Rubin, 2018).

The submarine volcano Tafu is an isolated volcanic ridge located on the NELSC, about 250 km southwest of the Samoan island of Savai'i in the territorial waters of the Kingdom of Tonga. The NELSC is one of many spreading centers that sit within the larger Northern Lau Basin. On the eastern margin of this basin, the cold, water-saturated, and dense Pacific Plate is subducting beneath the Indo-Australian Plate, which is made of several smaller microplates. For the sake of simplicity and the purposes of this study, these microplates will be grouped together as the Indo-Australian Plate. As the Pacific Plate subducts, it releases volatiles that lower the liquidus temperature and allow surrounding rock to melt, rise, and erupt within the Tofua Volcanic Arc (Hannington, 2016) (Figure 6.2). The subducting Pacific plate tugs the edge of the Indo-Australian Plate downward and creates tension along the back-arc region (Figure 6.2). In the Northern Lau Basin, this tension is accommodated by several back-arc spreading centers (Figure 6.1), one of which is the NELSC. Back-arc spreading centers are caused when tension on the crust in the back-arc causes the crust to thin, which reduces pressure in the mantle wedge; this causes decompression melting (Hannington, 2016; Smith and Price, 2006; Hawkins, 1995), which leads to eruptions in the back-arc spreading centers.

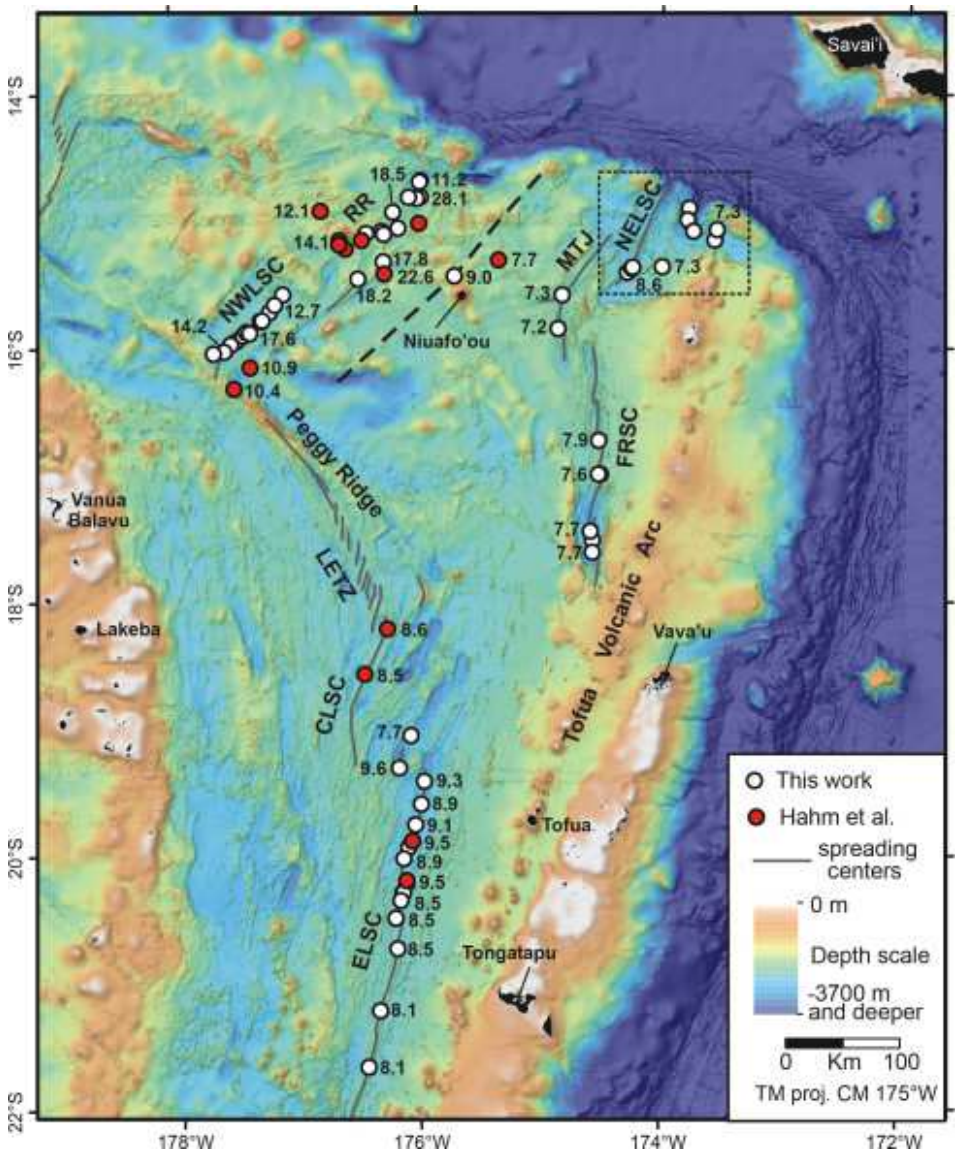

Figure 6.1. Bathymetric map of the Tonga Intra-Oceanic Subduction Zone (TIOSZ) from Lupton et al., 2015. Several spreading centers within the Lau Basin are shown, including the NELSC. Circles indicate samples studied in Lupton et al., 2015; these samples will not be applied to this study of Tafu and the NELSC. Abbreviations are as follows: Northwest Lau Spreading Center (NWLSC), Rochambeau Rifts (RR), Mangatolu Triple Junction (MTJ), Northeast Lau Spreading Center (NELSC), Fonualei Rift and Spreading Center (FRSC), Lau Extensional Transform Zone (LETZ), Central Lau Spreading Center (CLSC), and Eastern Lau Spreading Center (ELSC). The dashed box indicates an area further studied in Lupton et al., 2015, and does not apply to this study of Tafu. Solid lines indicate spreading centers and plate boundaries. Bold dashed lines indicate "the extent of influence of OIB or hotspot component into the northern Lau Basin, based on helium isotope ratios" (Lupton et al., 2015). Again, this subject will not be covered in this study.

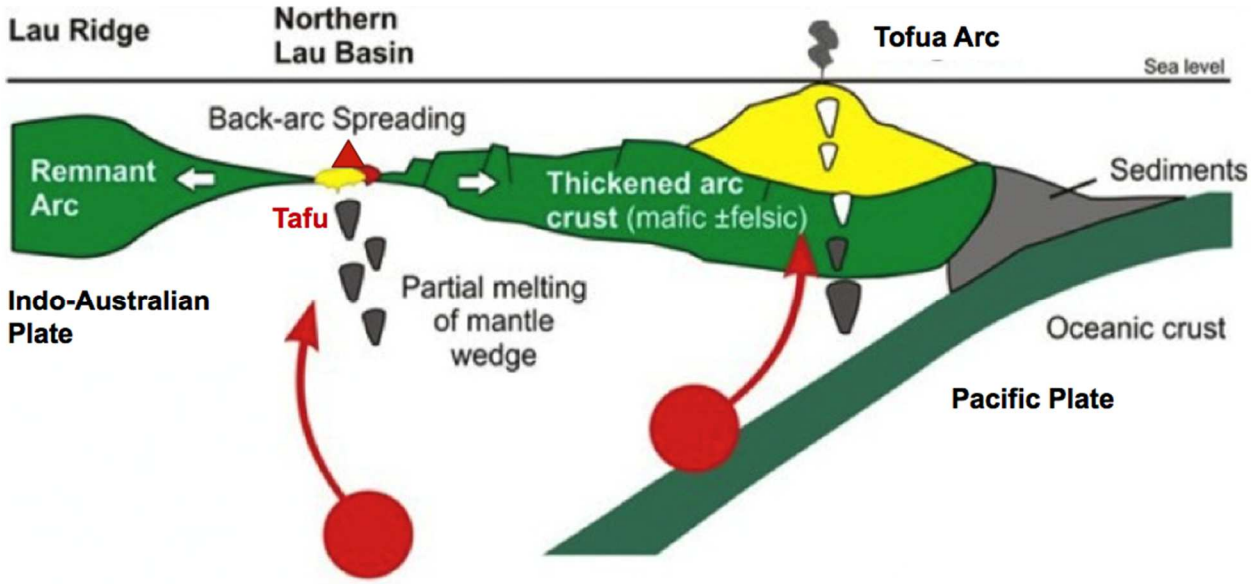

Figure 6.2. modified from Hannington, 2016. Cartoon cross section of the Northern Lau Basin and subducting Pacific Plate.

In the Lau Basin of the TIOSZ, this process has been occurring for approximately the last 4 Ma (Zellmer and Taylor 2001, Taylor and Martinez 2003, Embley and Rubin 2018). As mentioned previously, one of these spreading centers is the NELSC, where Tafu, the subject of this investigation, is located (Figure 6.3). The Puipui eruption site is south of Tafu and will also be briefly explored in this study. Water samples taken by "tow-yo" (a saw-tooth survey path through the water column) in November 2008 serendipitously found volcanic glass shards and extremely high hydrogen concentrations over Puipui. This event plume indicated an eruption had likely occurred at Puipui (Merle et. al, 2008; Baker et al., 2011; Rubin 2012).

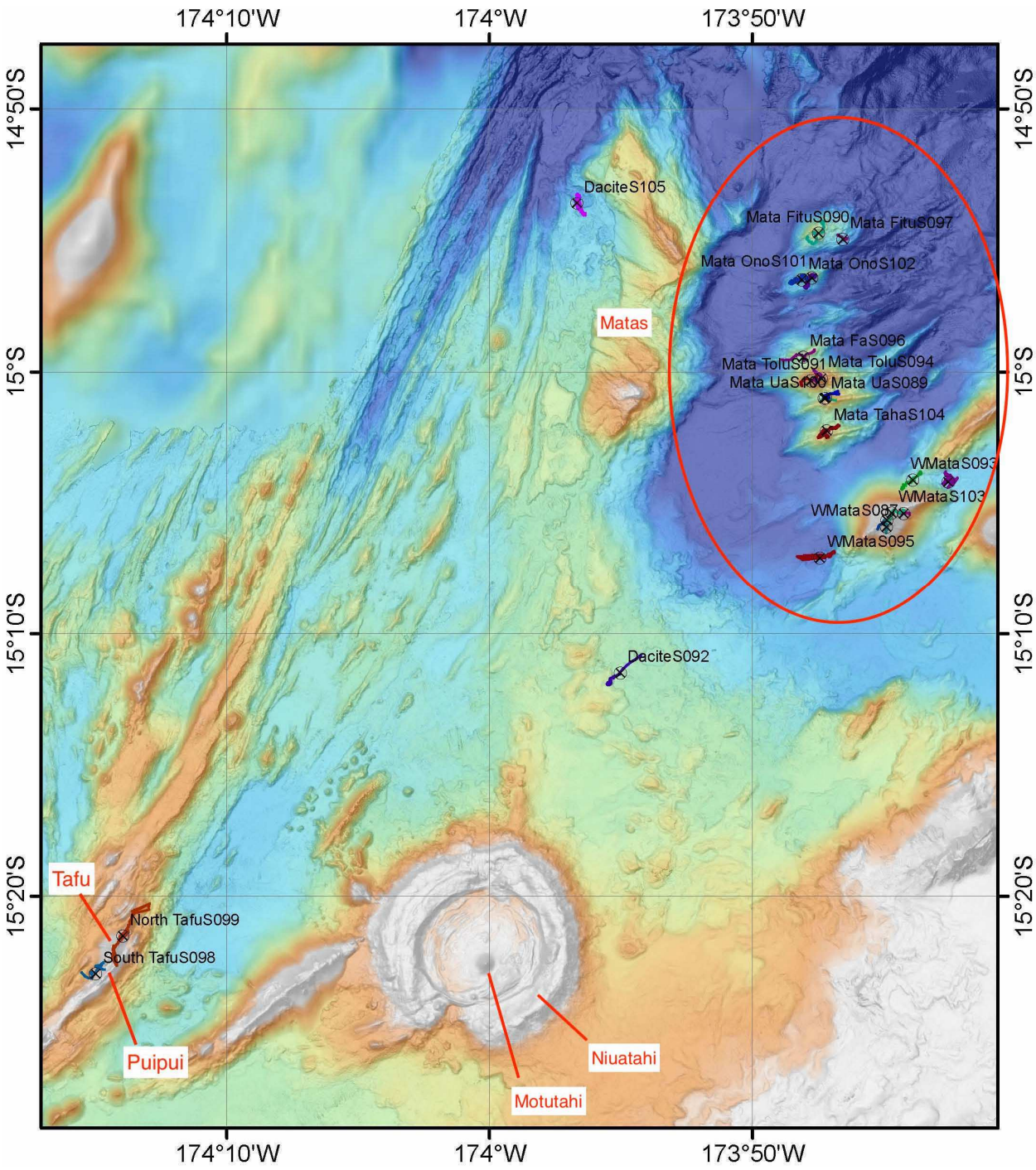

Figure 6.3. Bathymetric map of the Northeast Lau Basin showing the locations of several SuBastian dives from cruise FK171110, whose samples are the subject of this investigation. Tafu is in the southwest section of the figure with Puipui located south of Tafu. Niuatahi, Motutahi, and the Mata volcanoes are labeled for locational context; however, they will not be covered in this study. Bathymetric map is courtesy of Susan Merle.

6.4. Types of Submarine Lavas

Many different morphologies can be found in submarine eruptive products; these morphologies often depend on variables like effusion rate, slope, and viscosity, among others (Figure 6.4) (Bonatti and Harrison, 1988; Glancy, 2011). Gregg and Fink, 1995 used wax models in a laboratory setting to model how different morphologies can be produced by adjusting effusion rate, slope, and cooling rate. Figure 6.5 shows the different morphologies derived from this modeling. In this study on Tafu, the morphology labels "pillows," "lobate," and "jumbled sheet" will be used. Generally, submarine flows are classified as pillowed, lobate, or sheet flows, with pillows being formed from the lowest effusion rates, lobate flows from medium effusion rates, and sheet flows from the highest effusion rates (Figure 6.6)(Ballard et al., 1979; Luyendyk and Macdonald, 1985; Fox et al., 1987; Gregg and Fink, 1995). Sheet flows are further subdivided into lineated sheets, ropy sheets, and jumbled sheets in Gregg and Fink, 1995; however, only jumbled sheets were seen during the dives to Tafu that are the focus of this study. For this reason, the only sheet flow term used in this study will be "jumbled sheet."

	Pillow Basalts	Lobate Flows	Sheet Flows	
High	←———	Viscosity	←———	Low
High	←———	Crystal Content	←———	Low
High	←———	Composition (SiO_2 content)	←———	Low
Low	———→	Temperature at Eruption	———→	High
Narrow	———→	Conduit Width	———→	Wide
Long	———→	Conduit Length	———→	Short
Low	———→	**Effusion Rate**	———→	High
Low	———→	**Slope**	———→	High
Rough	———→	Surface Roughness	———→	Smooth
Low	———→	**Spreading Rate**	———→	High

Figure 6.4 from Glancy, 2011, adapted from Bonatti and Harrison, 1988. Influence of different variables on submarine lava morphology.

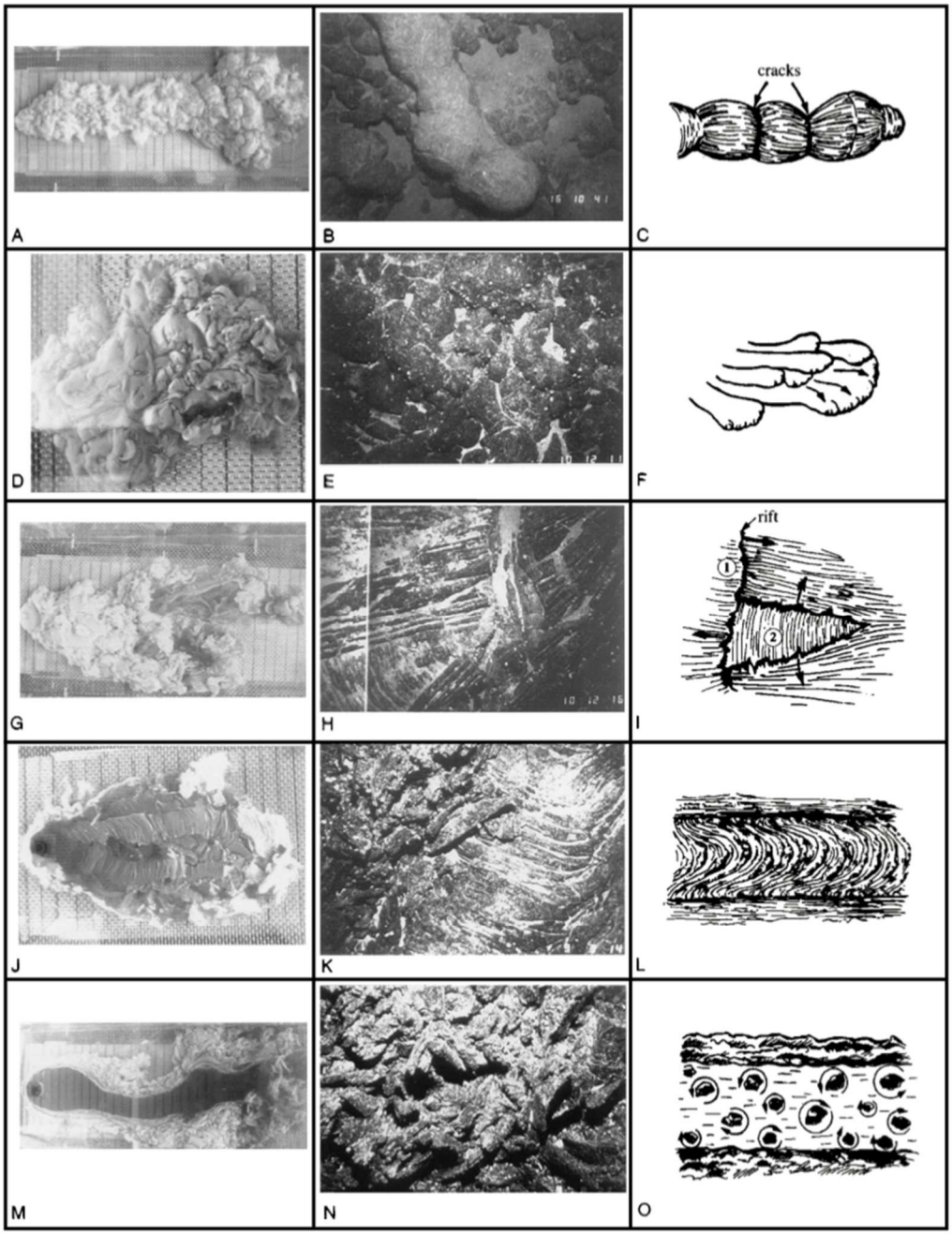

Figure 6.5 from Gregg and Fink, 1995. Left column shows wax models of submarine lava morphologies; lines on the tank floor are 2 cm spacing, and main flow direction is from left to right. Middle column shows photographs of submarine lavas, courtesy of Robert Embley at NOAA; field of view is about 5 m across. Right column shows sketches of morphologic formation, with flow direction left to right. From top to bottom, the rows show the following morphology types and models of morphology types: pillows, lobate flows, lineated sheet flows, ropey sheet flows, and jumbled sheet flows.

Laboratory morphology	Submarine morphology	Ψ 0° min	Cooling rate	Slope	Flow rate
pillows	pillows		↑	↓	↓
	lobate sheets				
rifts	lineated sheets	3			
folds	ropy sheets	10			
levees	jumbled sheets	30			

Figure 6.6 from Gregg and Fink, 1995. Submarine flow morphologies correlated with laboratory morphologies (not used in this study), cooling rate, slope, flow rate, and Ψ. Ψ is a dimensionless unit that represents the ratio of time required for solidification of flow surface to time required for head advection within the flow. Ψ can be ignored for the purposes of this study.

In addition to these labels from Gregg and Fink, 1995, the labels "plobate," "pillow tube," and "talus" will be used (Figure 6.7). "Plobate" refers to a morphology on the continuum between pillow and lobate flows. "Pillow tube" refers to an elongated pillow morphology, usually caused by lava flowing down a steep slope. "Chimney" refers to a rock taken from a hydrothermal chimney. "Talus" and "rubble" both refer to broken rock fragments caused by breakage off a main flow.

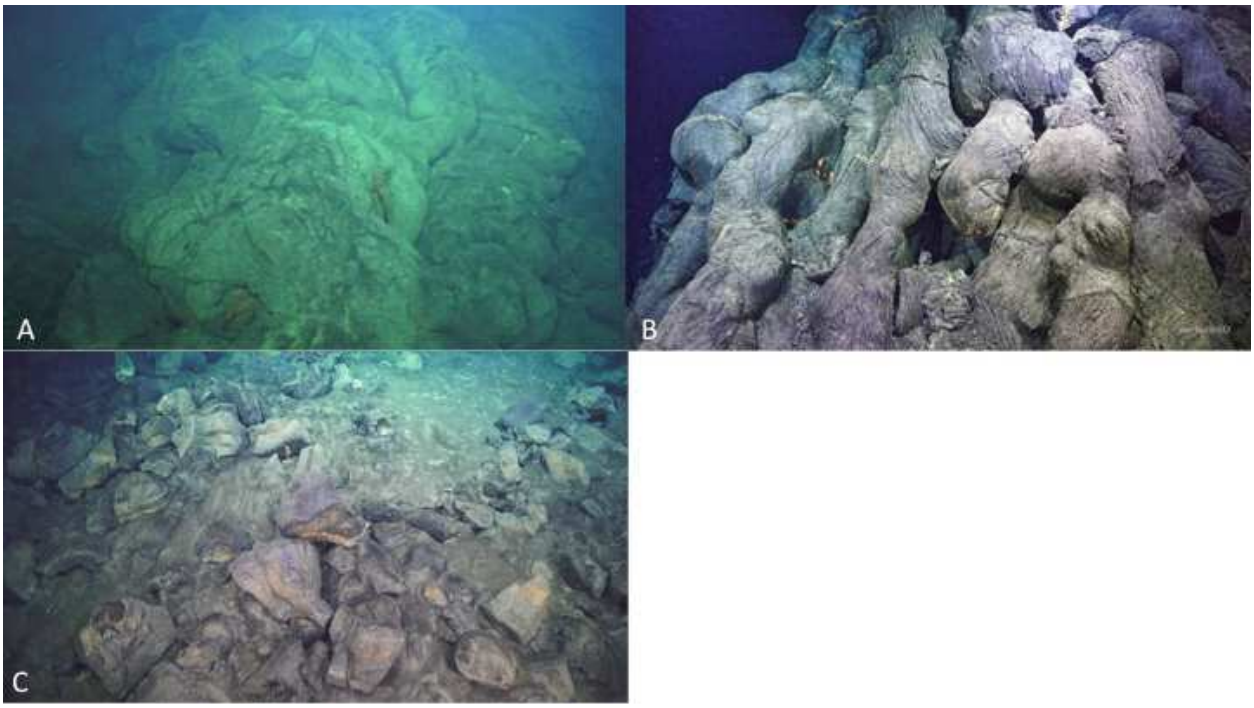

Figure 6.7. Photographs of plobate morphology (A), pillow tubes (B), and talus (C).

6.5. Timeline of NELSC Cruise Events

From 2006 to present, 8 cruises to the NELSC have been completed: a 2006 KORDI (Korean Ocean Research and Development Institute) cruise, cruise TN227 in November 2008, TN234 in May 2009, KM1008 in May 2010, KM 1024 in December 2010, KM1129a in November 2011, RR 1211 in September 2012, and FK171110 in November 2017, whose products have been the main focus of this study. Because cruise KM1129a was completed under Nautilus Minerals, there is no publicly available cruise report and therefore will not be discussed in depth in this study.

In 2006, a KORDI cruise visited the NELSC and gathered an EM120 multibeam data set (Merle et al., 2008). The data from this survey serves as the 2006 bound in time for the North Tafu 2006-2008 depth difference seen on North Tafu and visited on dive S99 (Merle et al., 2008).

TN227 completed a cruise to the NELSC in November of 2008. The following information is sourced from the TN227 published cruise report (Merle et al., 2008). The EM300 multibeam data set collected on this cruise showed a change in depth since the last bathymetry mapping done in 2006 by KORDI. These two multibeam data sets serve as the temporal bounds of the 2006-2008 North Tafu depth difference. During this cruise, strong evidence of an ongoing eruption was found near 15.39°S. 15.39°S near the summit of Puipui, 1 km south of Tafu. Connections between Tafu and Puipui will be explored in section 9.5. Vertical casts and tow-yos collected evidence of this eruption, and it included approximately 1000m-high rising plumes, high H_2 concentrations, and abundant glass shards in the plume. By the end of the cruise, eruptive activity had ceased.

A rapid response cruise, TN 234, was completed in May 2009 in response to the eruption observed in November 2008. No plume remained over Puipui by this time. Two dives, J415 and J416, were completed on Puipui using the ROV Jason. Figure 6.8 shows the dive track and samples collected on both dives. Young fresh black lava was found along the Puipui ridge, confirming the suspected eruption observed in November 2008; between these two dives, 13 rock samples and 5 sediment samples were collected. All observations made here are from the TN 234 cruise report (Merle et al., 2009).

The KM 1008 cruise in May 2010 completed three CTD tows, two CTD vertical casts, and one camera tow across the NELSC. CTD tows showed that at this time, there was a very weak plume over Tafu and a low intensity plume over the southern end of the 2008 Puipui eruption. A camera tow over Tafu showed evidence of fresh, young lava; some rocks were collected from the camera tow (see Table 9.2 for sample names). As stated in the KM 1008 cruise report (Merle et al., 2010a), evidence suggests that Tafu had active hydrothermal

venting during the 2008 TN227 cruise but was masked by the strong plume over Puipui (Kim et al., 2009). Multibeam bathymetry mapping of the NELSC was completed during this cruise.

A return to the NELSC in December 2010 on cruise KM1024 completed two dredges across the area on North Tafu where the 2006-2008 depth difference was seen. These dredges yielded 6 rocks that will be discussed in section 8.2.1. Figure 6.9 shows the location of these dredges on North Tafu. Multibeam bathymetry data were collected during this cruise, but no difference was found between the May 2010 and December 2010 surveys. All information from the KM1024 cruise was gathered from its cruise report (Merle et al., 2010b).

The September 2012 RR1211 cruise did not complete any extensive work at Tafu, Puipui, or the NELSC. During this cruise, EM122 multibeam data was collected over the NELSC (Merle et al., 2012); however, resolution of these data was too poor to complete any reliable depth differencing.

Details of the December 2017 FK171110 cruise are described in the methods section, as the products of this cruise are the main subject of this study. EM302 multibeam bathymetry data were collected over the NELSC; depth differencing between this data and the December 2010 KM1024 multibeam data revealed the depth differences seen on North and South Tafu (Bobbitt et al., 2017).

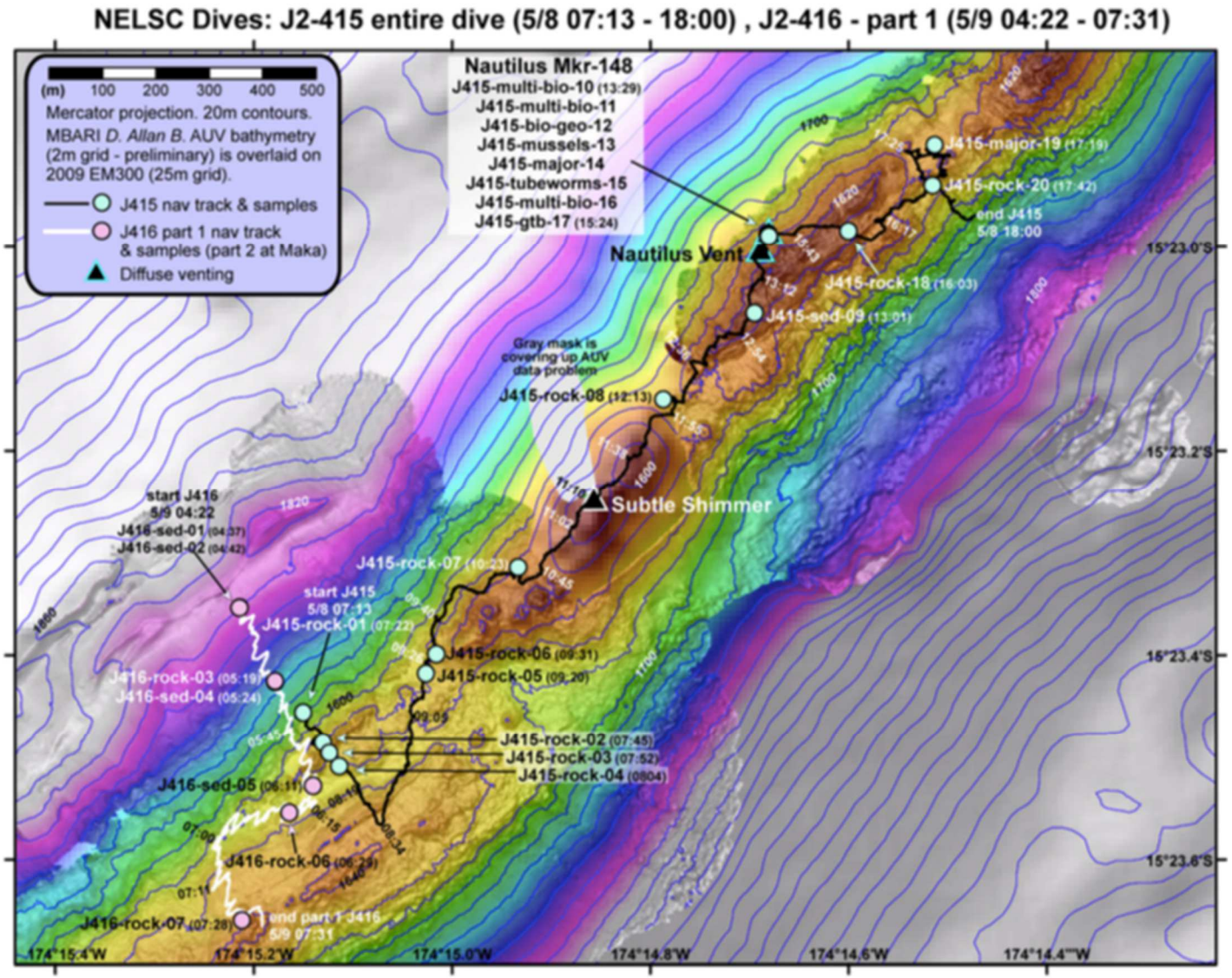

Figure 6.8. From Merle et al., 2009. Dive tracks of dives J2-415 and J2-416 overlain on AUV bathymetry data of Puipui. Samples collected are labeled along with vents visited.

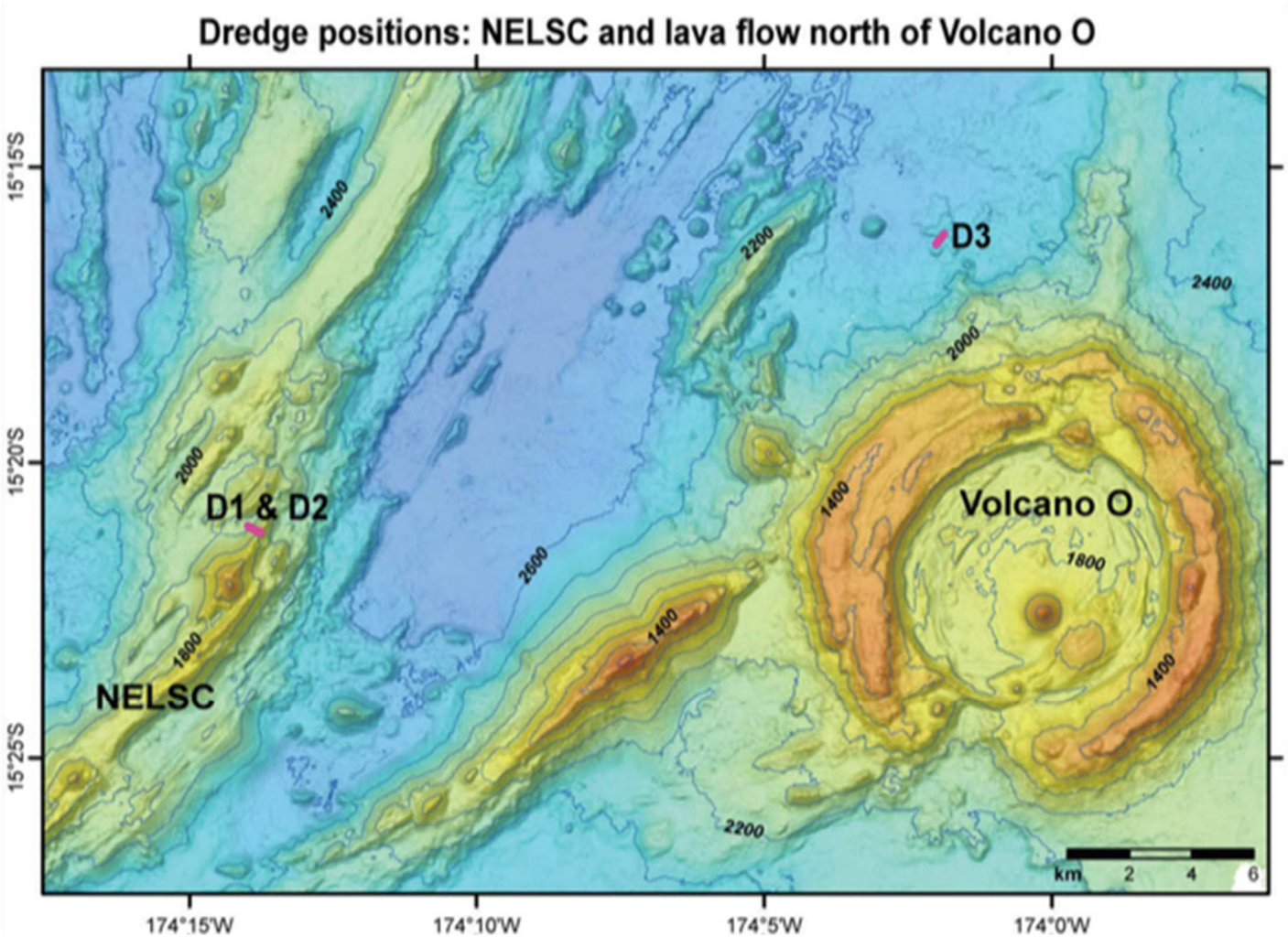

Figure 6.9. From Merle et al., 2010b. Location of Dredge 1 and Dredge 2 completed during KM 1024 in pink lines on North Tafu overlaid on EM300 and EM122 bathymetry. Niuatahi (Figure 6.3) is labeled here as "Volcano O." These are two names for the same structure.

7. Methods

7.1 Field Methods

The field observations in this study were made during Schmidt Ocean Institute research cruise FK171110 aboard the Research Vessel Falkor in 2017. This research cruise consisted of collecting bathymetry, sampling water column for volcanic emissions, and completing 21 dives with the Remotely Operated Vehicle (ROV) SuBastian on many different volcanoes in the Northeast Lau basin. The ROV dives were used for sampling of volcanic products (as well as hydrothermal fluids and biota not directly relevant to this study), and to collect visual observations.

The samples in this study were collected during two dives, FK171110-S98 and FK171110-S99. Dive S98 focused on making observations and collected samples from the southern flank of Tafu, whereas dive S99 made observations and collected samples from the northern flank of Tafu. Dive S98 was made on December 9, 2017, and dive S99 was made on December 10, 2017.

Extensive bathymetric surveying of the northeast Lau basin area was conducted with the R/V Falkor EM302 multibeam system at the time of this cruise. The bathymetry of the Northeast Lau Spreading Center had been mapped previously (Merle, 2008; Merle et al., 2009; Merle et al., 2010a; Merle et al., 2010b; Merle et al., 2012). By remapping, depth differences could be computed, revealing changes between the FK171110 survey and previous surveys. Three locations where the seafloor became shallower, interpreted to likely be recent eruptions, were discovered at Tafu by this method: two eruption sites on North Tafu, and one on South Tafu. The bathymetric change on South Tafu and one of the two on North Tafu occurred between the bathymetric survey completed in May 2010

(Merle et al., 2010a) and the 2017 bathymetric survey completed on FK171110 (Figure 7.1) (Bobbitt et al., 2017). The second location of bathymetric change on North Tafu was noticed in a data analysis by Susan Merle and Bill Chadwick (NOAA PMEL, personal communication), between a KORDI EM120 multibeam survey completed in 2006 and a multibeam survey conducted during expedition TN227 in November 2008 (Merle et. al, 2008).

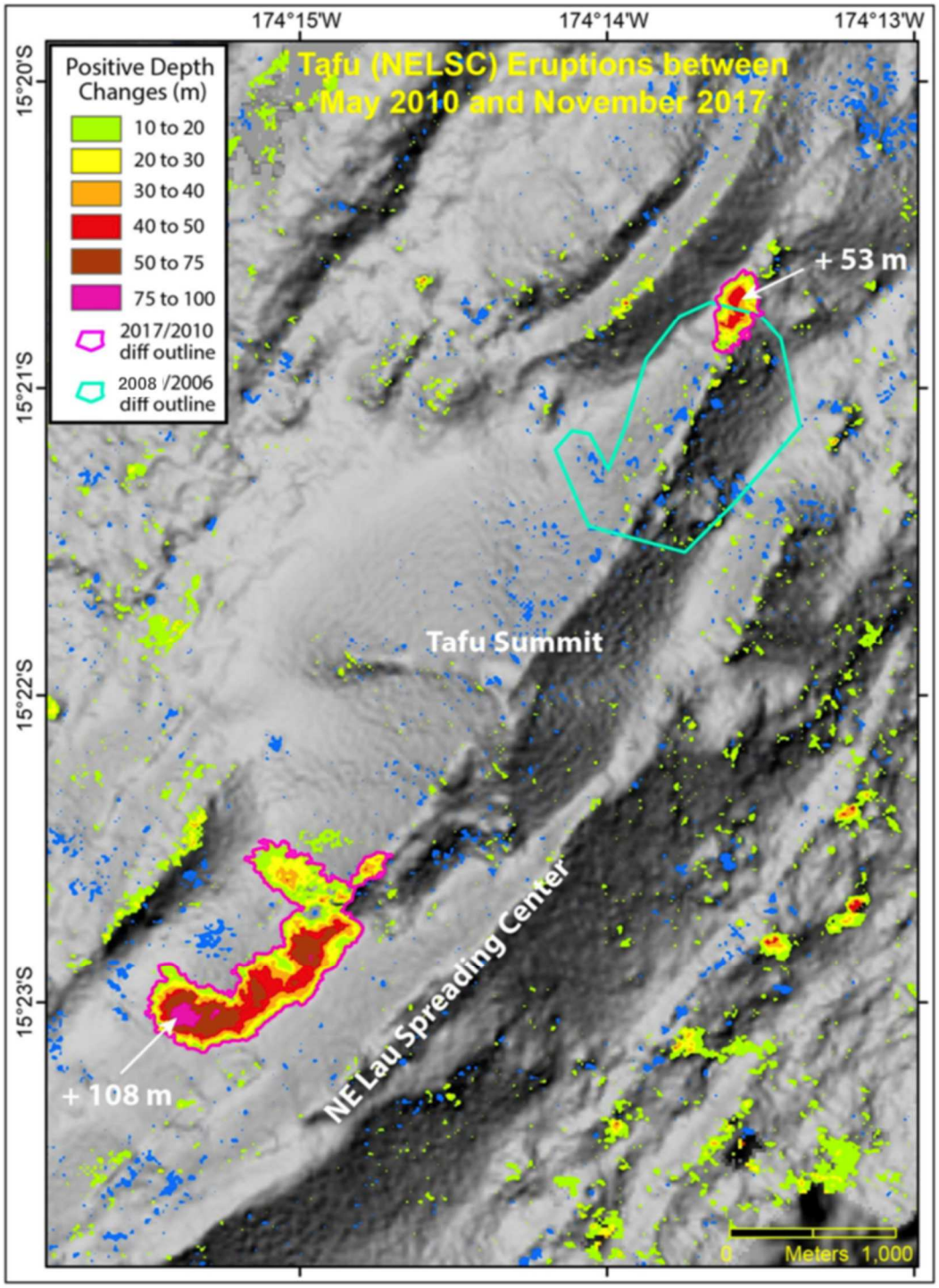

Figure 7.1. Multibeam depth difference map of North and South Tafu, which were investigated on dives FK171110-S98 and -S99. This map uses bathymetric surveys conducted in 2006, 2008, 2010, and 2017 as constraints for differences. The teal outline indicates depth differences occurring between 2006 and 2008, while the pink outlines indicate depth differences occurring between 2010 and 2017. White numbers (+108m, +53m) indicate maximum bathymetric changes.

14 rock samples and 5 sediment samples were collected at South Tafu on dive S98 (Table 7.1), and 17 rock samples and 3 sediment samples were collected at North Tafu on dive S99 (Table 7.2). The depths of these samples were determined by the ROV pressure sensor. Latitude and longitude were automatically determined relative to the R/V Falkor (which has continuous global positioning system navigation) using ultrashort baseline (USBL) and Doppler sonar fixes, taken every second, between ROV SuBastian and Falkor.

Sample	IGSN	Latitude	Longitude	Depth	Location	Dive	Morphology
S98-S01	KHR00028Y	-15.38171	-174.25877	2116.7	South Tafu	S98	sediment
S98-S02	KHR00028Z	-15.38223	-174.25812	2112.5	South Tafu	S98	sediment
S98-R03	KHR000290	-15.38315	-174.25729	2049.8	South Tafu	S98	talus
S98-R04	KHR000291	-15.38368	-174.25690	2002.9	South Tafu	S98	pillow
S98-R05	KHR000292	-15.38381	-174.25675	1961.9	South Tafu	S98	pillow tube
S98-S06	KHR000293	-15.38438	-174.25576	1934.7	South Tafu	S98	sediment
S98-R07	KHR000294	-15.38435	-174.25573	1934.0	South Tafu	S98	plobate
S98-R08	KHR000295	-15.38502	-174.25451	1908.3	South Tafu	S98	plobate
S98-R09	KHR000296	-15.38480	-174.25211	1904.2	South Tafu	S98	plobate
S98-R11	KHR000297	-15.38147	-174.25321	1938.0	South Tafu	S98	pillow tube
S98-R12	KHR000298	-15.38096	-174.24978	1808.1	South Tafu	S98	plobate
S98-S13	KHR000299	-15.37950	-174.24906	1807.6	South Tafu	S98	sediment
S98-R14	KHR00029A	-15.37797	-174.24876	1878.6	South Tafu	S98	pillow tube
S98-R15	KHR00029B	-15.37723	-174.24779	1761.3	South Tafu	S98	pillow
S98-S16	KHR00029C	-15.37748	-174.24731	1749.2	South Tafu	S98	sediment
S98-R17	KHR00029D	-15.37741	-174.24716	1740.3	South Tafu	S98	jumbled flow
S98-R18	KHR00029E	-15.37739	-174.24751	1740.2	South Tafu	S98	chimney
S98-R21	KHR00029F	-15.37588	-174.24597	1673.4	South Tafu	S98	pillow tube
S98-R22	KHR00029G	-15.37529	-174.24498	1658.9	South Tafu	S98	jumbled flow

Table 7.1. Table of samples from dive FK171110-S98 on December 9, 2017. The sample name refers to: number of dive – number of sample collected. IGSN (International Geologic Sample Number) is the unique number assigned to a sample to compile and codify all relevant sample meta data, for indexing and to prevent confusion in identifying samples across scientific literature. Depth is given in meters below sea level. All S98 samples were collected from the South flank of Tafu. Morphology gives the type of rock feature or sediment with definitions as follows: "Talus," broken, eroded pieces of a flow that are not in place, "pillow," pillow lavas, a morphology of submarine lava flows where lava inflates into a bulbous, pillow-like structure, "plobate," a morphology on the spectrum between a pillow lava and a lobate flow, "pillow tube," a tube-shaped pillow lava, often caused by an increase in slope, "chimney," a sample taken from a hydrothermal chimney, and "jumbled flow," a high-effusion rate type of sheet flow where the crust becomes broken and hackly.

Sample	IGSN	Latitude	Longitude	Depth	Location	Dive	Morphology
S99-R01	KHR00029H	-15.34295	-174.22479	1954.7	North Tafu	S99	plobate
S99-R02	KHR00029I	-15.34352	-174.22538	1953.4	North Tafu	S99	jumbled flow
S99-R03	KHR00029J	-15.34467	-174.22586	1998.9	North Tafu	S99	plobate
S99-R04	KHR00029K	-15.34476	-174.22639	1973.8	North Tafu	S99	jumbled flow
S99-R05	KHR00029L	-15.34482	-174.22664	1970.2	North Tafu	S99	pillow
S99-R06	KHR00029M	-15.34635	-174.22672	1965.4	North Tafu	S99	plobate
S99-R07	KHR00029N	-15.34760	-174.22730	1932.2	North Tafu	S99	jumbled flow
S99-R08	KHR00029O	-15.34791	-174.22751	1912.5	North Tafu	S99	pillow
S99-S09	KHR00029P	-15.34885	-174.22782	1892.7	North Tafu	S99	sediment
S99-R10	KHR00029Q	-15.34949	-174.22814	1849.4	North Tafu	S99	plobate
S99-R12	KHR00029S	-15.35162	-174.22940	1808.7	North Tafu	S99	pillow
S99-R13	KHR00029T	-15.35504	-174.23091	1763.4	North Tafu	S99	pillow tube
S99-R14	KHR00029U	-15.35669	-174.23176	1701.2	North Tafu	S99	pillow tube
S99-S15	KHR00029V	-15.35744	-174.23245	1674.2	North Tafu	S99	sediment
S99-R18	KHR00029W	-15.35888	-174.23308	1684.1	North Tafu	S99	plobate
S99-R20	KHR00029X	-15.36047	-174.23365	1620.5	North Tafu	S99	pillow
S99-R21	KHR00029Y	-15.36366	-174.23652	1490.5	North Tafu	S99	pillow
S99-S25	KHR00029Z	-15.36678	-174.23896	1378.7	North Tafu	S99	sediment
S99-R26	KHR000300	-15.36678	-174.23896	1378.4	North Tafu	S99	pillow

Table 7.2. Table of samples from dive FK171110-S98 on December 9, 2017. The sample name refers to: number of dive – number of sample collected. IGSN (International Geologic Sample Number) is the unique number assigned to a sample to compile and codify all relevant sample meta data, for indexing and to prevent confusion in identifying samples across scientific literature. Depth is given in meters below sea level. All S98 samples were collected from the South flank of Tafu. Morphology gives the type of rock feature or sediment with definitions as follows: "Talus," broken, eroded pieces of a flow that are not in place, "pillow," pillow lavas, a morphology of submarine lava flows where lava inflates into a bulbous, pillow-like structure, "plobate," a morphology on the spectrum between a pillow lava and a lobate flow, "pillow tube," a tube-shaped pillow lava, often caused by an increase in slope, and "jumbled," a high-effusion rate type of sheet flow where the crust becomes broken and hackly

Waypoints were chosen before each dive based on preselected points of interest determined from the multibeam bathymetry surveys, including the locations of the greatest depth changes, new flow contacts, pillow mounds, and traverses along the north and south ridges. Actual traverses did not follow the predetermined waypoints exactly, for the following reasons: the flow contact was reached before the waypoint, features outside of the preset path were investigated, insufficient time remaining in the dive to finish the planned track, and loss of navigation made it difficult to determine precise location. Completed dive tracks are shown in Figures 7.2 and 7.3. The S098 logs and S099 logs in these figures indicate points in space where the ROV was determined to be located using the method described previously. Those points in space whose depths did not match the known depth of the ROV (using pressure sensors) were rejected. For this reason, the trackline does not go through the rejected logs.

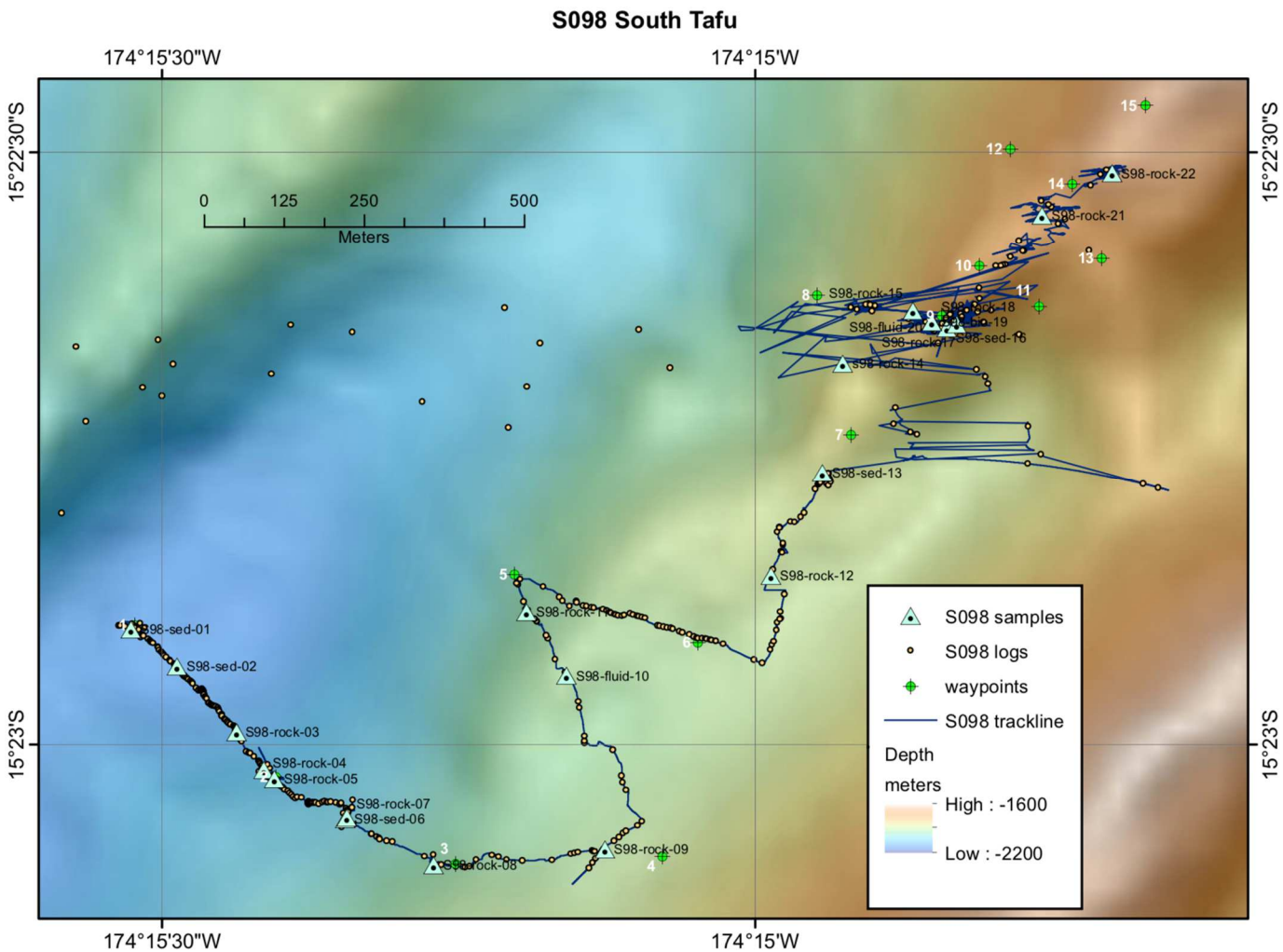

Figure 7.2. Map of completed dive track from dive FK171110-S98 including bathymetry data from the 2017 multibeam survey, courtesy of Susan Merle. Navigation of the ROV SuBastian malfunctioned at the end of the dive after collection of sample S98-sed-13; the trackline after this point does not accurately represent the actual track of the ROV. S098 logs represent points where the ROV was determined to be located. Logs that do not lie along the trackline were rejected because their depths did not match the known depth of the ROV at that point in time.

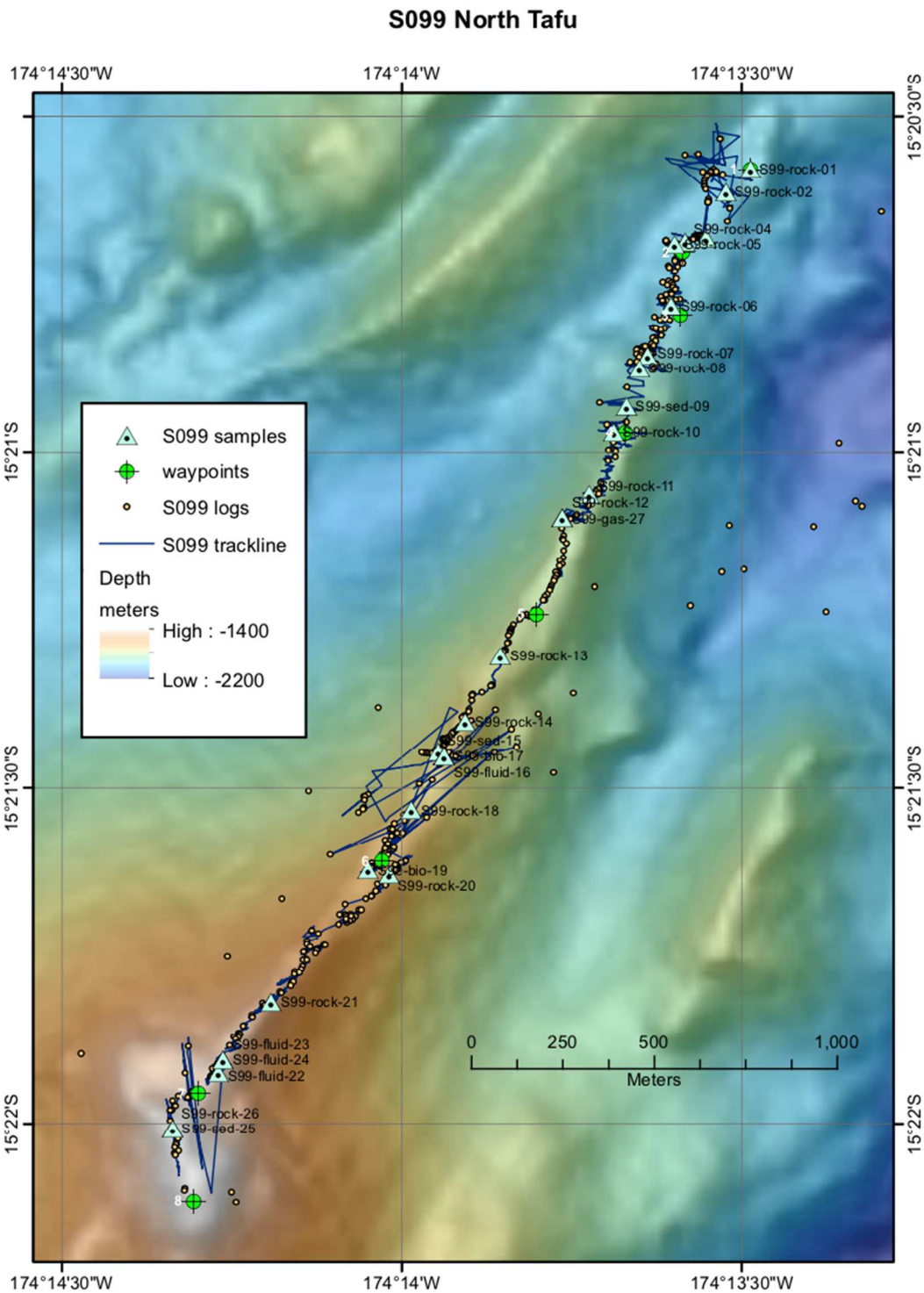

Figure 7.3. Map of completed dive track from dive FK171110-S99 including bathymetry data from the 2017 multibeam survey, courtesy of Susan Merle. Navigation of the ROV SuBastian malfunctioned during three sections of the dive (at the beginning of the dive, near 15°21'30"S, and just north of 15°22'S); the trackline in these sections do not accurately represent the actual track of the ROV. S099 logs represent points where the ROV was determined to be located. Logs that do not lie along the trackline were rejected because their depths did not match the known depth of the ROV at that point in time.

After the samples were brought to the surface, rock samples were rinsed in freshwater. After that, we measured their dimensions, described their physical characteristics, and photographed them (in section 11.1). Additionally, a small portion of the glassy crust on each sample was removed for later use. Sediment samples were rinsed in fresh water, photographed (in section 11.1), and left to dry in foil pans. Val Finlayson aided by Terry Newman completed these tasks during the FK171110 cruise.

7.2 Video observations

Combined, about 20 hours of video footage from both dives S98 and S99 were reviewed to gain an understanding of where each sample came from, how the sample's in situ placement related to its formation, and overall geomorphology of Tafu volcano. I used my own viewing of the video recordings as well as narration by Dr. Ken Rubin and Dr. Bill Chadwick to make notes about times and locations of events and features, such as sample collection, changes in bathymetry, sediment placement, and suspected locations of different eruptions. Screen grabs of the location of each sample's collection as well as screen grabs of each sample being collected are available in the section 11.2.

7.3. Analytical Methods

7.3.1 Electron Microprobe Analysis (EPMA)

The goal of using EPMA to analyze samples collected was to investigate the composition of the melt of the rock and sediment samples collected. In order to accomplish this, grain mounts of each rock and sediment sample were made.

If present, a small section of the shelly, glassy exterior of each lava sample was scraped off and separated from the sample on board the ship. From this glass, five glass chips with approximate diameters of 1-2mm were chosen from each rock sample to be made into grain mounts. Additionally, 10 glassy chips were chosen from each sediment sample, again with diameters of approximately 1-2mm. In both cases (lava and sediment glass chips), the chips were encased in epoxy within a mold and left to cure overnight. Once removed from the mold, the surfaces of the grain mounts were polished. To prevent charging on the

surface of the grain mounts, the Ted Pella 208HR High Resolution Sputter Coater was used to create a 150-200 angstrom thick carbon coating on the grain mounts.

For each rock sample, three of the five chips were chosen for analysis by a JEOL JXA-8500F hyperprobe at the University of Hawai`i at Mānoa. The hyperprobe is equipped with five spectrometers in order to analyze five elements simultaneously. Measurements were made using Probe for EPMA software. In order to measure only melt composition, measurements were made within the glass of each chip. This meant avoiding all crystals, from large crystals to microlites. Three of the five rock sample chips were chosen based on which chips had the fewest crystals and most available glass to measure. For each sediment sample, all ten of the ten chosen chips were measured. This was done to resolve any compositional variability in sediment samples. For every chip, spots within the glassiest parts of the chips were measured with a 10 μm beam diameter. Images were taken of each glass chip (section 11.3).

For EPMA measurements, the conditions defined in Table 7.3 were used to acquire X-ray intensities for the majority of measurements. For all measurements, an acceleration voltage of 15 keV, a 10μm beam diameter, and 10nA beam current were used. Calibration utilized the A99 Makaopuhi Lake Glass NMNH 113498-1 (Si, Fe, Mg, Al, Ca), Verma Garnet (Mn), Amelia Albite (Na), OR-1 Orthoclase (K), Troilite Meteorite (S), Apatite (P), Scapolite (Cl), and Sphene glass (Ti) standards. During calibration, X-ray peak intensities were measured for each element as well as X-ray background noise intensities on either side of peaks. Background noise intensities were linearly interpolated and subtracted from peak intensities using Probe for EPMA.

VG2 Juan de Fuca glass (catalog number NMNH 111240-52 in the Smithsonian Microbeam Standards Datasheets) and initially A99 Makaopuhi Lake Glass (catalog number NMNH 113498-1 in the Smithsonian Microbeam Standards Datasheets) were repeatedly analyzed as unknowns and used as glass standards for comparison throughout measurements. However, because A99 Makaopuhi Lake Glass was used as a standard in the calibration procedure, it could not be reliably measured as a standard as unknown. Using a standard for both calibration and as an unknown is circular logic and would be useless in providing information about the instrument's accuracy. Instead, it was mostly measured periodically to help monitor if there was any drift in measurements. A99 and VG2 were both used as standards as unknowns until November 24, 2019; three points on each standard were measured as unknowns after every nine unknown points. After November 24, VG2 continued to be analyzed as an unknown, while A99 was measured once at the beginning of that day's run, once in the middle, and once at the end to monitor drift.

To evaluate the microprobe data, I first averaged values collected from the three measurement points on each chip to get average major element compositions for each chip. These were used to determine average major element composition for each rock sample. Points with totals below 95.00 wt.% were discarded and not included in these averages. Points whose compositions caused that chip's mean to be outside of 0.5 standard deviations were discarded. I chose the discarded points by finding the point that was most different compositionally from the average of the chip's points.

Element	Line	Acquisition Order	Spectrometer	Crystal	Detector	On-peak count times (s)	Off-peak count times per background measurement (s)
Si	k-alpha	first	3	TAP	Gasflow	50	25
Ti	k-alpha	first	4	LiF	Xe-sealed	20	10
Al	k-alpha	second	1	TAP	Gasflow	50	25
Fe	k-alpha	second	4	LiF	Xe-sealed	50	25
Mn	k-alpha	third	4	LiF	Xe-sealed	50	25
Mg	k-alpha	second	3	TAP	Gasflow	60	30
Ca	k-alpha	first	2	PETH	Xe-sealed	50	25
Na	k-alpha	first	1	TAP	Gasflow	60	30
K	k-alpha	first	5	PETH	Gasflow	20	10
S	k-alpha	second	5	PETH	Gasflow	50	25
P	k-alpha	second	2	PETH	Xe-sealed	60	30
Cl	k-alpha	third	5	PETH	Gasflow	50	25

Table 7.3. EPMA element acquisition settings from 10/15/19 onward

Standards	**Elements**											
A99 Makaopuhi Lake Glass NMNH 113498-1	SiO_2	TiO_2	Al_2O_3	FeO	MnO	MgO	CaO	Na_2O	K_2O	SO_3	P_2O_5	Cl
Average Measured Standard as Unknown	50.80	4.01	12.53	13.29	0.19	5.10	9.29	2.73	0.84	0.03	0.43	0.02
3σ	1.775	0.706	0.409	0.576	0.085	0.146	0.121	0.254	0.069	0.053	0.054	0.025
Published Values	50.94	4.06	12.49	13.3	0.15	5.08	9.30	2.66	0.82	below detection	0.38	0.0002

VG2 Juan De Fuca Glass NMNH 111240-52	SiO_2	TiO_2	Al_2O_3	FeO	MnO	MgO	CaO	Na_2O	K_2O	SO_3	P_2O_5	Cl
Average Measured Standard as Unknown	50.46	1.87	14.01	11.59	0.20	7.00	11.21	2.70	0.19	0.35	0.20	0.03
3σ	1.627	0.478	0.507	0.555	0.088	0.158	0.156	0.200	0.036	0.069	0.045	0.027
Published Values	50.81	1.85	14.06	11.84	0.22	6.95	11.12	2.62	0.19	0.34*	0.20	0.033*

Table 7.4. Average measured values of standards A99 and VG2 shown with published values (Jarosewich et al., 1980). * indicates values gathered from GeoReM database.

7.3.2 Raman Spectroscopy

The objective of using Raman spectroscopy was to gain measurements of weight percent of water within the glass of the samples. The same grain mount samples used for EPMA measurements were used for Raman Spectroscopy measurements; however, the carbon coatings had to first be removed by re-polishing the surface of the grain mounts. Three points per glass chip were measured, avoiding all crystals. These three points were not necessarily the same points measured by electron microprobe. WiTec Control 1.4 software was used to operate the WiTec Confocal Raman Microscope (model Alpha R300) and 532 nm green laser. Three 20-second acquisitions were made on each spot measured and averaged to generate one spectrum per spot. A grating of 600 grooves/mm and a spectral center of 2300 cm^{-1} were used. This process generated three spectra for each glass chip (nine total spectra per rock sample, and 30 total spectra per sediment sample).

Weight percent of H_2O was derived from these spectra using SpeCTRa spot (Shea et al., 2014). Using SpeCTRa (Spectral Correction Tools for Raman) spot (Shea et al., 2014), baseline and long corrections were performed on each raw spectrum (e.g. Le Losq et al., 2012). No smoothing or corrections for parasitic epoxy signals were needed. The ratio of the area under the H_2O band and the aluminosilicate framework (ASF) bands provide information about the amount of water in each sample; however, to quantify this ratio, it must be compared to a standard with a known H_2O wt.%. For these standards, samples PC6 and PC18 (unrelated to the Tafu samples) were used. PC6 and PC18 had water contents of 0.8 wt.% and 1.88 wt.%, respectively, and their water content was previously measured through FTIR spectroscopy (Shea et al., 2014). SpeCTRa spot provided a ratio of area of H_2O to ASF bands. To derive weight percent water from this ratio, standards were

measured as unknowns, and the resultant H_2O/ASF ratio of the standards was plotted against the standards' known wt.% H_2O. A linear trend was derived from these data, and the resulting equation (y= 1.9461x-0.0505, where x is the H_2O/ASF ratio and y is weight percent of water) was used to derive weight percent water from the measured H_2O/ASF ratio of the rock and sediment samples.

In order to reduce noise in these data, two rejection procedures were conducted. First, an average water content was determined for each grain. Next, the percent variation for each grain was determined by the following formula:

$$percent\ variation = \frac{standard\ deviatio}{average} \times 100$$

If the percent variation was higher than 7.6%, then a point measured on that grain needed to be rejected. The point whose composition was most different from the average was rejected. In the case that all points were similarly different from the average, no point could reasonably be rejected. This procedure was repeated a second time, but with the criteria that all grains with a percent variation higher than 5.5% undergo rejection of a point.

8. Results

8.1. Field Results

8.1.1 Video Observations

Dive FK171110-S98 began with the ROV SuBastian located at 15°22.89787' S, 174°15.53185' W (point A in Figure 8.1; all points within this paragraph will refer to Figure 8.1) in a basin just west of the southern ridge of Tafu; this starting point outside of the lava flow was chosen so that the precise location of the western edge the 2010-2017 depth difference could be found. The basin floor consisted of black, glassy, rippled volcanic sand with a coating of orange iron floc on top (Figures 11.3a and 11.3b in section 11.2); a sediment sample, S98-S01, was collected from this location. From here, SuBastian headed southeast towards the flows of Tafu. While approaching the edge of the flows, SuBastian encountered rubbly pillow lava fragments. Eventually, in-place shelly pillow lavas were observed, indicating the margin of the flow (point B). The dive continued to traverse across the flow with the goal of reaching the flow's eastern margin, predicted to be near waypoint 4. During this traverse, the flow surface had plobate morphology (a working morphology term for a flow unit with characteristics of both a bulbous pillow and a lobate flow), with some well-defined pillow lavas and lobate flow lobes near waypoint 4. At point C the ROV reached the eastern edge of the lava flow. From here, the ROV SuBastian traveled on a NNW heading towards the western edge of the flow predicted to be near waypoint 5. Along this traverse from point C to point E, there were several pillow mounds with tube pillows on their steep sides and plobate morphology lavas on the tops of the mounds. Sediment coated these rocks. The ROV continued past the edge of the lava flow (point D), travelled through some rubble and talus, then turned around at point E. The ROV continued on an ESE

heading over more pillow mounds to the eastern edge of the flow once more, this time near waypoint 6 (point F). After this last traverse, the ROV followed the ridge crest towards the summit of Tafu over more pillow mounds. After collecting sample S98-S13, navigation became unreliable. During this period of poor navigation, a short deviation to the west was made to investigate a collapse pit seen on the multibeam bathymetric difference map. This cannot be labeled precisely on Figure 8.1 due to the navigation difficulties. After collection of sample S98-R17, the ROV SuBastian exited the area with the 2010-2017 depth difference. After crossing waypoint 10, navigation began to improve. Near the summit of Tafu (point G), the ROV encountered near-vent facies included spatter, jumbled sheet flows, and collapsed lava structures. A discontinuous fissure (point H) was found with tube pillows and jumbled morphologies along either of its sides and broken rubble within the fissure. The fissure pinched out and SuBastian continued upslope, following drained and tubular pillows. The dive finished after collecting sample S98-R22 near the summit of Tafu.

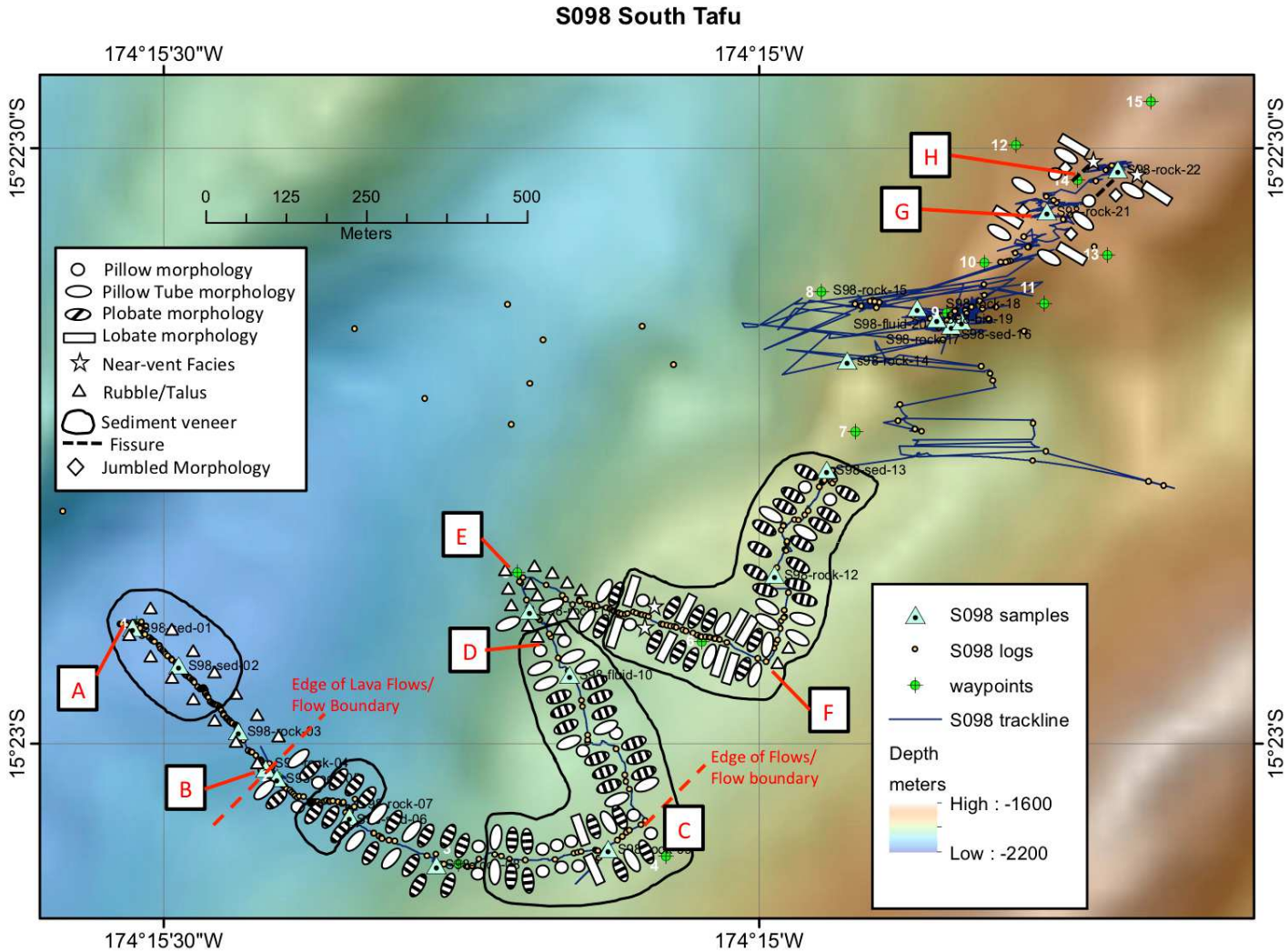

Figure 8.1. Bathymetric map and dive trackline are from Bobbitt et al., 2017. Morphology map of South Tafu along the dive track of ROV SuBastian on dive S98. A indicates the beginning of the dive. B and C indicate the western and eastern margins of the main flow, respectively. D marks another eastern edge of the main flow. E indicates where the ROV turned to begin a third traverse across Tafu's main flows. F is where the ROV navigated directly up Tafu's southern ridge. G is where near-vent facies were seen, and H is the location of a discontinuous fissure.

Dive FK171110-S99 began on the northernmost (deepest) section of Tafu's north ridge, at approximately 15° 20.577'S, 174°15.252'W and 1950m depth. The ROV began the dive outside of the 2010-2017 depth difference. Here, the surrounding topography was made of pillow lavas, some drained, and had a light dusting of volcanic sediment and hosted communities of hydroids, stalk corals, and anemones. During this segment of the dive, navigation systems failed, making logged locations of the ROV inaccurate. About 250m from the starting point of the dive near waypoint 2 and near the northern bathymetric difference boundary of the 2010-2017 flow (point A in Figure 8.2; all lettered points in this paragraph will refer to locations in Figure 8.2), lavas looked fresher and no longer hosted the variety and volume of benthic fauna the previously observed lavas did. These lavas consisted of pillow mounds with steep sides covered in pillow tubes and broken pillow faces; mound tops were plateaued and featured both pillow and plobate lavas. About halfway between waypoints 3 and 4 and near the southern boundary of the 2010-2017 depth difference (point B), SuBastian exited this flow into the area of the 2006-2008 depth difference; this flow was populated by more non-vent benthic fauna and occasional dusting of sediment. SuBastian continued southwest, following the northern ridge of Tafu. In many places this ridge was narrow due to pillows having collapsed on either side of the ridge. Just south of waypoint 4 at 15° 20.985'S, 174° 13.688'W (point C) a fissure with near-vent facies was observed. Further along near waypoint 5 (15° 21.242'S, 174° 13.828'W, point D), near-vent volcanic facies including spatter and jumbled sheet flows were seen. SuBastian took a quick pit stop at 15° 21.450'S, 174° 13.958' W to observe a site on a cliff edge of the northern ridge where several squat lobsters, scale worms, and shrimp were seen crawling amongst a white to pale yellow microbial mat in an area of weak diffuse flow hydrothermal

venting. This site was given the name “Cliff Contender” by those on the FK171110 cruise and is at point E in Figure 8.2. Shortly after visiting the Cliff Contender site, SuBastian began traveling through a lava terrain with much larger, more developed benthic non-vent faunas such as hydroids, stalked corals, anemones, glass sponges, sea stars, and crinoids. This change in fauna at point F coincided with the southern boundary of the 2006-2008 multibeam bathymetry depth difference. Here, the lava morphology alternated between tube pillows and jumbled sheet flow lavas with the tube pillows lying on top of the jumbled sheet flow. One pillow flow in this area of alternating morphologies appeared to be younger and had only small crinoids growing instead of longer crinoids, more developed sponges, corals, and other benthic fauna; rock sample S99-R21 was collected in this pillow flow. At 15° 21.918’ S, 174° 14.274’ W (point G in Figure 8.2), lavas and sediments began to have a significant orange iron staining on their surfaces. The staining and iron floc became thicker and more orange as the ROV continued towards the summit. The summit site had orange, yellow, and brown staining and shimmering hydrothermal flow. There were very little fauna present, mostly in the form of small corals, but there were small chimneys and shimmering water, as well as black volcanic sediment.

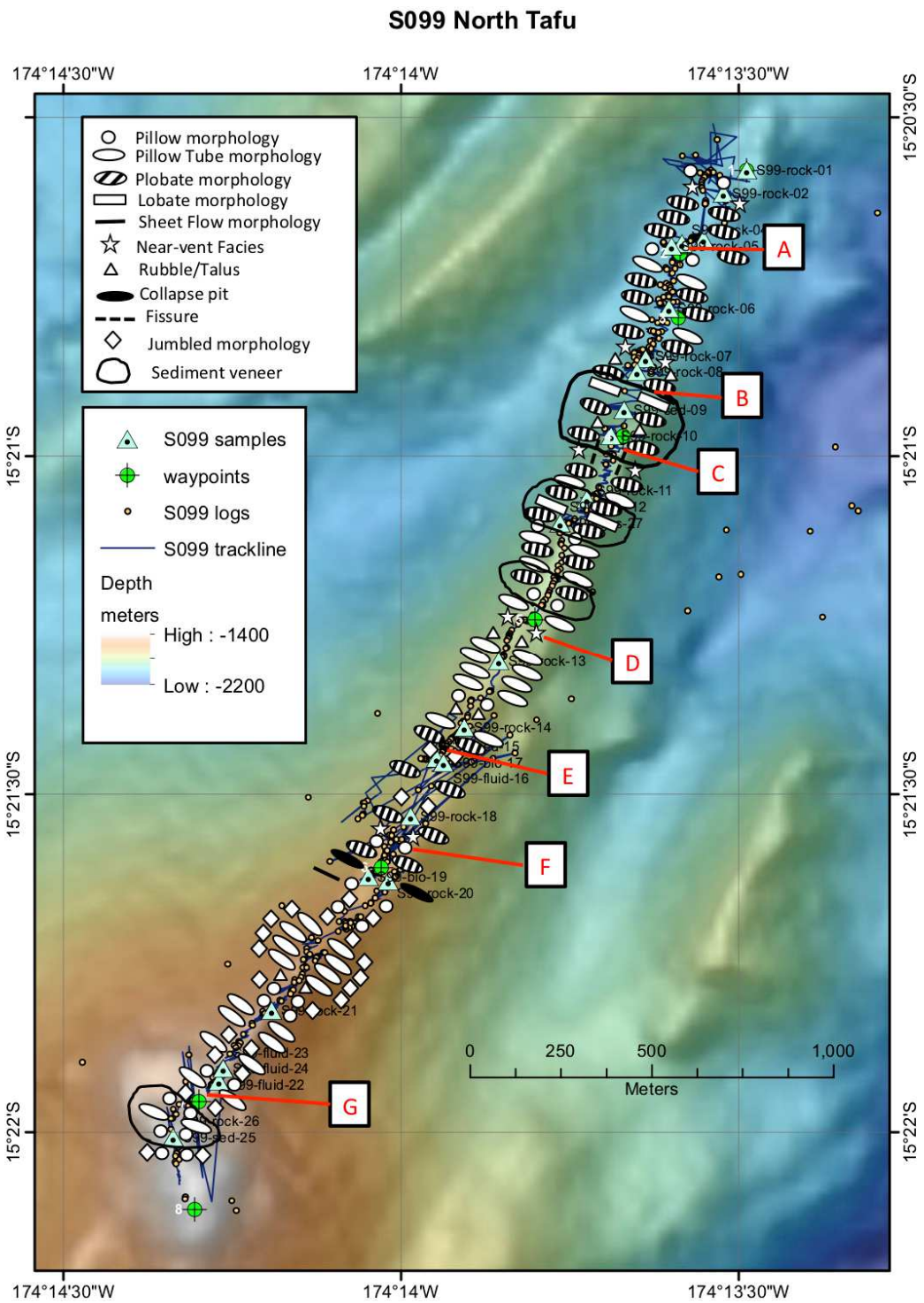

Figure 8.2. Bathymetric map and trackline are from Bobbitt et al., 2017. Morphology map of North Tafu along the dive track of ROV SuBastian on dive S99. Points A and B indicate the northern and southern bathymetric difference boundaries, respectively, of the 2010-2017 eruption. Point C labels the location of a fissure. Point D locates near-vent facies and spatter. E labels the Cliff Contender hydrothermal site. F indicates a change in fauna near the southern boundary of the 2006-2008 depth difference. Point G is where the orange iron floc seen near the summit was first observed.

8.1.2. Grouping samples by eruption using geochemistry and video evidence

As discussed previously in section 8.1.1., visual observations of the dive sites were used in tandem with multibeam depth difference data to determine which eruption unit the ROV SuBastian was over when it collected each sample. By combining these observations with geochemical analyses (introduced in section 8.2.1), rock and sediment samples could be grouped into suspected eruption groups (Table 8.1).

At the beginning of dive S98 on South Tafu, the ROV SuBastian travelled through a basin just outside of a pillow ridge making up the main edifice of Tafu's southern ridge. Samples S98-S01, -S02, -R03, and -R04 were all collected either in this basin (S01 and S02), or in an area of talus leading up to the cliff of pillows making up the main ridge (R03 and R04). These samples are grouped together as being outside of any of Tafu's lava flows, and their group is referred to as "ST Outside Boundary."

Once ascending the cliff of broken pillow faces, the ROV SuBastian was within the 2010-2017 depth difference and lavas looked fresh and young. All rock and sediment samples collected from S98-R05 to S98-R17 were within this depth difference, looked fresh, dark, and young, and had similar geochemical compositions. These samples are grouped together as "ST 1."

Sample S98-R18 was collected from a chimney-like structure (Figure 11.3q in section 11.2) near the boundary of the 2010-2017 depth difference. We consider this chimney-like structure to be part of the older eruption area due to its highly altered surface. After collecting sample S98-R18, the ROV entered lavas along a narrow ridge that were covered in staining and appeared to be older. These older lavas are placed in the eruptive group "ST 0." However, it is worth noting that all samples collected on South

Tafu's main ridge (i.e., not including the "ST Outside Boundary" group) have similar major element compositions, and no one group of samples stands out as being significantly different from rest of the South Tafu ridge samples.

In stark contrast to South Tafu, samples collected on North Tafu are heterogeneous in major element composition. As stated in section 8.1.1, Dive S99 on North Tafu began on pillow lavas covered in a light dusting of volcanic sediment and hosting a community of hydroids, stalk corals, and anemones; these characteristics indicated that the ROV SuBastian was outside of the 2010-2017 flow boundary. This is supported by the fact that these flows are not included in any of the depth differences on North Tafu and must therefore be older than the 2006-2008 eruption. All samples (S99-R01, R02, and R03) collected within this lava flow were grouped as "NT 0."

About 250 m from the starting point of the dive and near waypoint 2, lavas looked fresher and hosted fewer benthic fauna than the previous flows; this area coincided with the 2010-2017 depth difference. For these reasons, samples collected here (S99-R04 through S99-R08) were grouped together as "NT 2." Additionally, these rocks' major element compositions are similar to each other (for example, only 0.15 wt.% range in MgO), and had average MgO wt.% compositions of about 1.5 wt.% less than those samples grouped as S99 older eruptions.

The ROV exited the 2010-2017 depth difference area directly into the 2006-2008 depth difference area. Here, there were more non-vent fauna and more sediment covering the lavas. From the 2010-2017 depth difference boundary to at least the location of S99-S15, all samples collected were grouped as "NT 1." However, after this, it became difficult to determine where the 2006-2008 eruptive products ended and older eruptive products

began. Sample S99-R18 was tentatively defined as 2006-2008, although it may be older; however, after completing major element composition analysis, it was clear that this rock was compositionally similar to the S99 2006-2008 group of samples. After revisiting video footage, it became clear that the lava flows the ROV entered after collecting sample S99-R18 had larger, more developed benthic non-vent fauna and were likely older than the 2006-2008 eruption.

After exiting the 2006-2008 flow, most of the ROV SuBastian's dive path continued through older flows; however, it did encounter one patch of lava that appeared to be fresher and younger. Here, S99-R21 was collected. The major element composition of S99-R21 matches that of those rocks included in the NT 1 flow, so we consider it to be an eruptive product of the 2006-2008 NT 1 eruption. With the exception of S99-R21, all other samples after S99-R18 were determined to be from one or more older eruptions, and therefore are grouped with "NT 0." These rocks and sediments had more alteration than the youngest flows and were located outside of any depth differences. Because these rocks and sediments were collected outside of any depth differences, all of which occurred after 2006, they must be older than 2006. However, this does not mean that all rock included in the NT 0 group are from the same eruption. These older rocks and sediments may have come from multiple different eruptions prior to 2006, making NT 0 a sort of grab bag of older samples. Their compositions also do not match any of the rocks known to be from the 2006-2008 or 2010-2017 eruptions.

Eruptive Group	Location	Time of Eruption	Symbol in Figures	Expedition of Collection	Date of Collection
ST 1	South Tafu	2010-2017	●	FK 171110	December 2017
ST 0	South Tafu	<2006	●	FK 171110	December 2017
ST Outside Boundary	South Tafu	unknown	●	FK 171110	December 2017
NT 1	North Tafu	2006-2008	▲	FK 171110	December 2017
NT 2	North Tafu	2010-2017	▲	FK 171110	December 2017
NT 0	North Tafu	<2006	▲	FK 171110	December 2017
NT Dredge 1	North Tafu	TBD	■	KM 1008 and KM 1024	May 2010 and December 2010
NT Dredge 2	North Tafu	TBD	■	KM 1024	December 2010
Puipui	Puipui	2008	■	TN 234	May 2009

Table 8.1. Summary of eruptive groups used in this study. Eruption times that are labeled TBD will be explored further in section 9.4. and 9.6.

8.2. Analytical Results

8.2.1 Electron Microprobe Analysis of Major Elements in Glass

Major element compositions of the glasses span a range of compositions. They are primarily basalts but extend into the realms of trachybasalts and basaltic andesites (Figure 8.3). SiO_2 ranges from 47.5 to 53.4 wt.%. MgO ranges from 5.3 to 8.0 wt.%. K_2O ranges from 0.57 to 1.4 wt.%. FeO ranges from 7.9 to 10.0 wt.%. CaO ranges from 10.7 to 12.8 wt.%. Al_2O_3 ranges from 14.25 to 16.8 wt.%. TiO_2 ranges from 0.70 to 1.4 wt.%. Complete major element composition of the glasses for each sample are presented in Table 8.2.

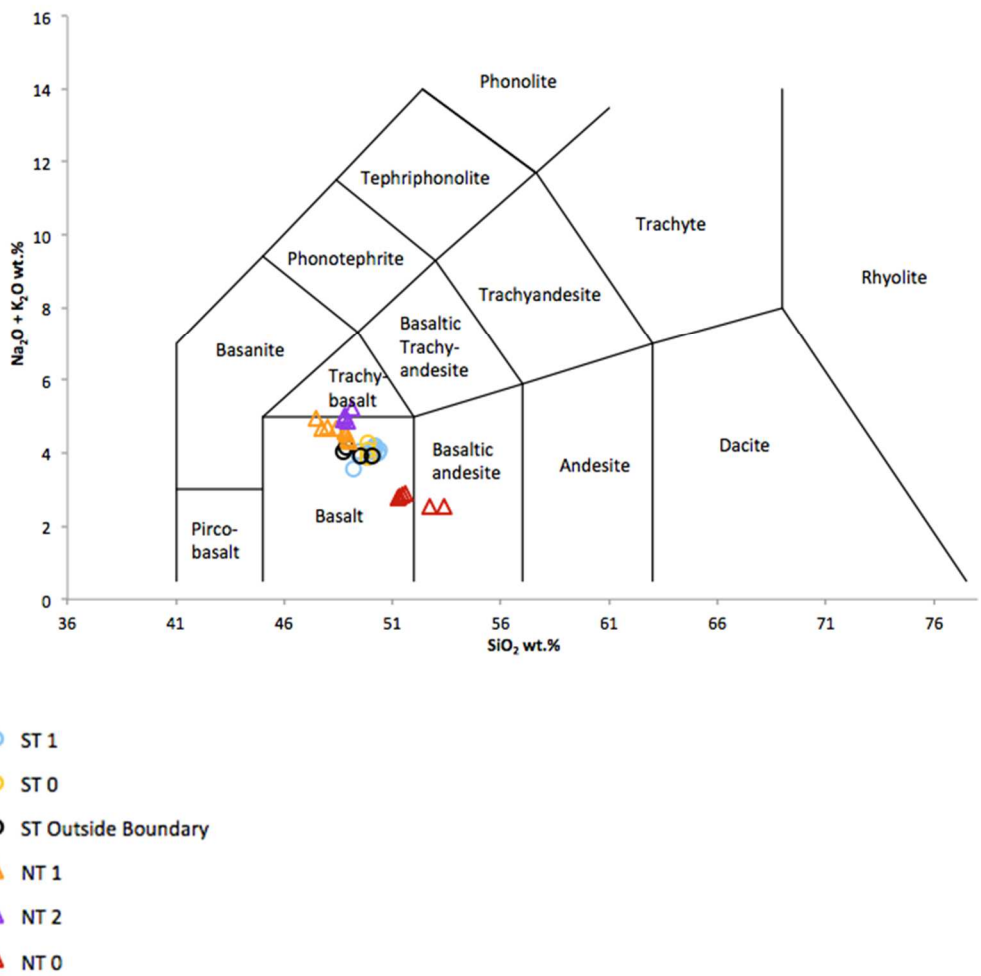

Figure 8.3. Total Alkali Silica (TAS) showing compositions of rock samples collected on dives S98 and S99 on expedition FK171110. TAS template is from Iacovino, 2017, modeled from Le Maitre et al., 2002.

Sample Name	SiO_2	TiO_2	Al_2O_3	FeO	MnO	MgO	CaO	Na_2O	K_2O	SO_3	P_2O_5	Cl	Total	Suspected Eruption Group	Eruption Timing
S98-S01	50.07	1.12	16.06	8.95	0.15	6.31	12.09	2.87	1.06	0.03	0.40	0.16	99.28	ST Outside Boundary	Unknown/Variable
S98-S02	49.54	1.11	15.83	8.66	0.17	6.32	12.15	2.85	1.05	0.03	0.40	0.16	99.52	ST Outside Boundary	Unknown/Variable
S98-R03	48.85	1.13	15.85	9.03	0.17	5.74	11.37	3.00	1.16	0.04	0.43	0.17	98.23	ST Outside Boundary	Unknown/Variable
S98-R04	48.71	1.04	15.94	8.66	0.17	5.86	11.64	2.94	1.12	0.02	0.41	0.17	97.96	ST Outside Boundary	Unknown/Variable
S98-R05	49.21	1.11	14.54	8.28	0.16	7.05	12.83	2.60	0.98	0.04	0.37	0.16	98.60	ST 1	2010-2017
S98-S06	50.10	1.08	16.45	9.16	0.17	6.05	11.73	3.01	1.12	0.04	0.43	0.17	99.50	ST 1	2010-2017
S98-R07	50.04	1.10	16.12	8.81	0.16	6.16	11.90	2.94	1.11	0.05	0.41	0.17	100.28	ST 1	2010-2017
S98-R08	50.10	1.06	16.31	8.91	0.17	6.02	11.76	2.94	1.11	0.04	0.41	0.17	100.31	ST 1	2010-2017
S98-R09	49.88	1.09	15.40	8.72	0.16	6.63	12.29	2.79	1.11	0.04	0.43	0.16	100.15	ST 1	2010-2017
S98-R11	49.85	1.16	15.25	8.73	0.16	6.77	12.40	2.79	1.11	0.04	0.42	0.17	100.20	ST 1	2010-2017
S98-R12	49.46	1.08	15.82	8.84	0.15	6.26	11.98	2.84	1.08	0.05	0.41	0.18	99.45	ST 1	2010-2017
S98-S13	50.30	1.12	16.10	8.96	0.16	6.43	12.13	2.92	1.06	0.03	0.41	0.16	101.01	ST 1	2010-2017
S98-R14	49.43	1.14	15.85	9.39	0.19	5.90	11.41	2.95	1.10	0.05	0.42	0.20	99.29	ST 1	2010-2017
S98-R15	50.19	1.23	15.97	9.36	0.17	5.94	11.32	3.01	1.13	0.04	0.41	0.17	100.17	ST 1	2010-2017
S98-S16	50.37	1.17	16.50	9.29	0.16	6.04	11.68	3.02	1.07	0.04	0.42	0.17	101.14	ST 1	2010-2017
S98-R17	50.22	1.23	15.83	9.57	0.18	5.92	11.10	3.03	1.16	0.04	0.43	0.18	100.20	ST 1	2010-2017
S98-R18	49.86	1.09	16.39	8.97	0.16	5.92	11.67	3.19	1.07	0.05	0.42	0.24	100.21	ST 0	<2006
S98-R21	49.88	1.10	15.88	8.86	0.16	6.41	12.20	2.82	1.06	0.02	0.39	0.15	100.17	ST 0	<2006
S98-R22	49.83	1.22	15.92	9.21	0.15	5.90	11.45	2.97	1.11	0.05	0.42	0.18	99.67	ST 0	<2006

Table 8.2a. Microprobe glass analyses for samples collected during dive FK171110-S98 on South Tafu. All values are reported in wt.%. Suspected eruption group is based on location (primarily) and geochemistry (secondarily; see section 8.1.2).

Sample Name	SiO_2	TiO_2	Al_2O_3	FeO	MnO	MgO	CaO	Na_2O	K_2O	SO_3	P_2O_5	Cl	Total	Suspected Eruption Group	Eruption Timing
S99-R01	51.29	0.91	16.09	8.38	0.15	6.72	12.10	2.24	0.58	0.04	0.16	0.12	100.31	NT 0	< 2006
S99-R02	51.46	0.94	16.09	8.51	0.15	6.64	12.02	2.28	0.59	0.06	0.17	0.12	100.47	NT 0	< 2006
S99-R03	51.58	0.96	16.20	8.45	0.17	6.71	11.98	2.29	0.60	0.05	0.17	0.11	100.76	NT 0	< 2006
S99-R04	48.90	1.19	16.77	9.41	0.17	5.46	11.20	3.60	1.26	0.05	0.56	0.23	100.14	NT 2	2010-2017
S99-R05	49.15	1.30	16.48	9.98	0.16	5.42	10.67	3.83	1.38	0.05	0.59	0.26	100.47	NT 2	2010-2017
S99-R06	48.80	1.38	16.45	9.82	0.17	5.32	10.82	3.68	1.32	0.06	0.59	0.25	100.02	NT 2	2010-2017
S99-R07	48.73	1.37	16.71	9.59	0.17	5.43	11.01	3.65	1.27	0.06	0.57	0.24	100.04	NT 2	2010-2017
S99-R08	48.78	1.32	16.56	9.70	0.17	5.37	10.84	3.72	1.31	0.05	0.59	0.24	99.84	NT 2	2010-2017
S99-S09	48.96	1.11	15.91	9.21	0.16	6.63	12.53	3.48	0.92	0.05	0.52	0.18	100.92	NT 1	2006-2008
S99-R10	48.86	1.14	16.16	9.13	0.15	6.55	12.41	3.57	0.94	0.06	0.48	0.20	100.86	NT 1	2006-2008
S99-R12	47.99	1.08	16.23	9.31	0.16	6.25	12.26	3.79	0.93	0.06	0.54	0.22	99.78	NT 1	2006-2008
S99-R13	47.73	1.15	16.27	9.14	0.16	6.21	12.31	3.73	0.94	0.06	0.52	0.22	99.69	NT 1	2006-2008
S99-R14	49.00	1.11	16.63	9.28	0.18	6.00	12.10	3.40	0.93	0.04	0.50	0.18	100.55	NT 1	2006-2008
S99-S15	48.82	1.16	16.33	9.26	0.17	5.82	11.66	3.61	0.98	0.05	0.51	0.19	99.80	NT 1	2006-2008
S99-R18	48.39	1.14	16.50	9.43	0.17	6.01	12.05	3.69	0.96	0.05	0.57	0.21	100.39	NT 1	2006-2008
S99-R20	51.25	0.79	15.70	8.04	0.13	7.14	12.23	2.19	0.57	0.02	0.16	0.15	99.78	NT 0	< 2006
S99-R21	47.50	1.20	16.49	9.48	0.17	5.80	11.79	3.95	1.00	0.05	0.56	0.23	99.36	NT 1	2006-2008
S99-S25	52.75	0.70	15.01	7.92	0.15	7.33	12.14	1.92	0.60	0.02	0.15	0.14	100.20	NT 0	< 2006
S99-R26	53.38	0.72	14.15	8.00	0.15	8.02	12.82	1.75	0.79	0.01	0.16	0.14	101.33	NT 0	< 2006

Table 8.2b. Microprobe glass analyses for samples collected during dive FK171110-S99 on North Tafu. All values are reported in wt.%. Suspected eruption group is based on location (primarily) and geochemistry (secondarily; see section 8.1.2).

Figure 8.4 below shows various elemental oxides plotted against wt.% MgO as measured by electron microprobe and grouped by suspected eruption. The ST 1 group is the largest in sample numbers. It clusters with medium MgO comparatively, ranging from 5.90 to 7.05 wt.%. The geochemical ranges of both the ST 0 and ST Outside Boundary groups overlap that of the 2010-2017 ST 1 eruption group in all elements.

Geochemical variation amongst eruptions on North Tafu tends to be much higher than that on South Tafu. The NT 1 eruption group also lies within the mid-MgO spectrum of the samples being studied here but differs from the ST 1 eruption in other oxide concentrations. The NT 2 eruption group is the lowest in MgO and has very little internal variation in MgO (standard deviation of MgO in the NT 2 eruption group is 0.057, and values range from 5.32 to 5.46 wt.%). However, this group varies more greatly in concentrations of other oxides compared to its variation in MgO. The NT 0 eruptive group has the highest MgO wt.% of all groups, ranging from 6.64 to 8.02 wt.%.

NT 2 has the highest wt.% Al_2O_3. ST 1 and NT 0 overlap in Al_2O_3 wt.%, though NT 0 has the lowest wt.% Al_2O_3 of all the FK171110 samples. NT 1 and ST 0 have similar ranges in Al_2O_3, spanning from about 15.8 to 16.7 wt.% Al_2O_3. The ST Outside Boundary group has a narrow range in Al_2O_3 from about 15.8 to 16.0 wt.%.

NT 2 has the lowest wt.% CaO, while ST 1 and NT 0 have the highest wt.% CaO. ST1 spans the widest range of CaO compositions. All samples display a trend of increasing CaO with increasing MgO. NT 1 lies in the mid to upper range of CaO with respect to the other Tafu samples.

In K_2O, once again NT 2 and NT 0 are the end members in a range of compositions; NT 2 has the highest wt.% K_2O, while NT 0 has the lowest wt.% K_2O. Most NT 0 samples have about 0.6 wt.% K_2O, except for S99-R26, which has about 0.8 wt.% K_2O. NT 1 has a fairly narrow range of K_2O from 0.916 to 1.003 wt.%. Once again, the South Tafu groups overlap in K_2O composition.

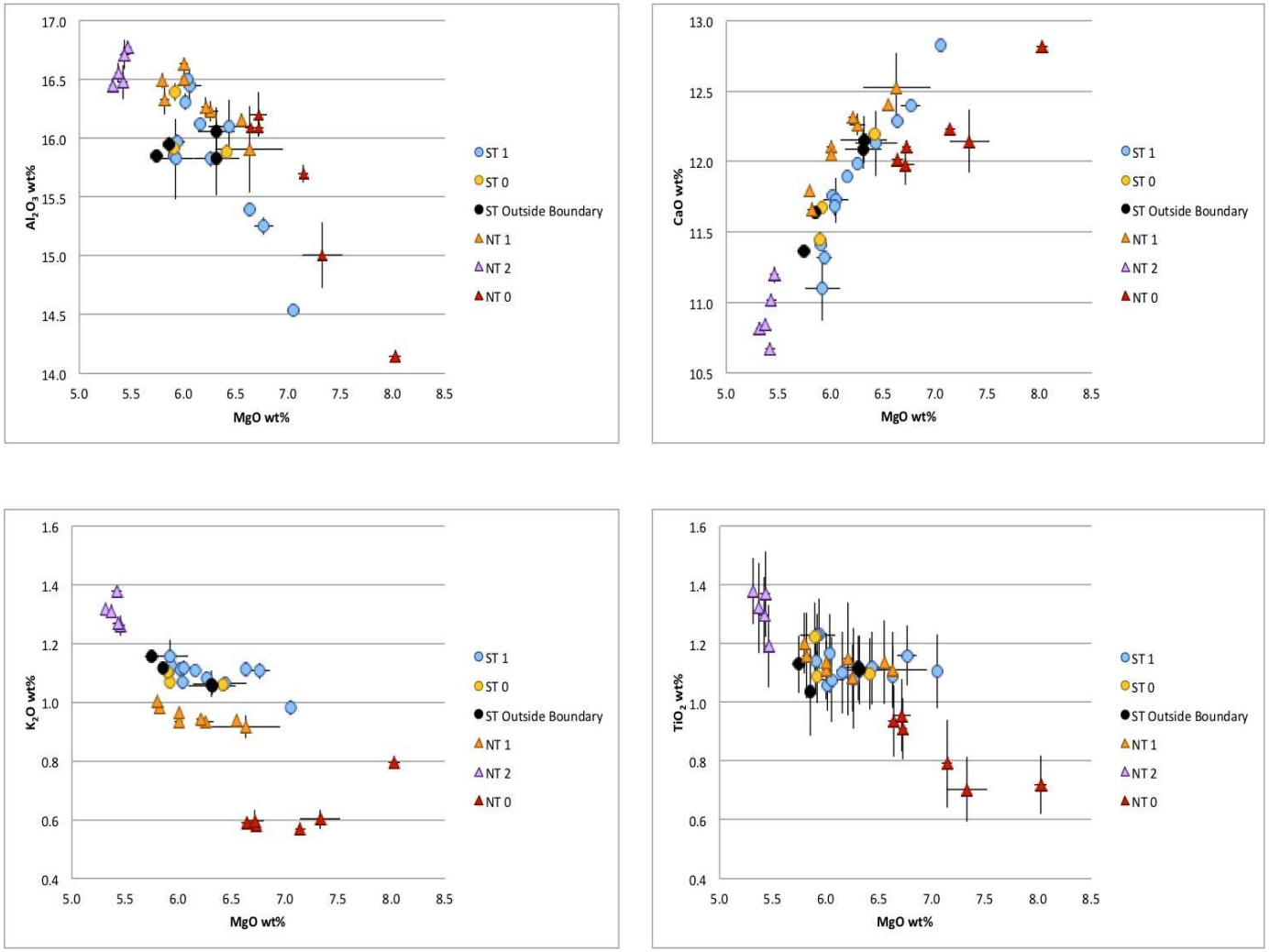

Figure 8.4. Results of electron microprobe analysis of all rock and sediment samples from dives S98 and S99. Circles indicate results from samples collected at South Tafu, while triangles indicate results from samples collected from North Tafu. Colors refer to different suspected eruption groups as described in Table 8.1. Error bars are one standard deviation. Graphs showing composition of SiO_2 and FeO are in section 11.4 in Appendix D.

NT 2 has the highest wt.% TiO_2, while NT 0 has the lowest wt.% TiO_2. TiO_2 compositions in NT 0 are bimodal: one group close to 0.9 wt.%, and the second from 0.703 to 0.792 wt.% TiO_2. All South Tafu groups as well as the NT1 group overlap in TiO_2 composition, ranging from 1.035 to 1.233 wt.%.

8.2.2. Visual observations of glasses under backscattered electron imaging

Backscattered electron images were taken of each glass chip during electron microprobe analysis. Selected images of glass chips can be found in Appendix C. Though the objective of electron microprobe analysis was to measure glass composition, observations of whole chip texture, including crystals, were still made. Glass chips varied from entirely glass to crystal-rich, both with relatively large crystals (up to approximately 1mm in diameter) and microlites. Several crystals showed evidence of zoning (Figure 8.5 and 8.6). Additional photomicrographs will be presented in section 9.3.

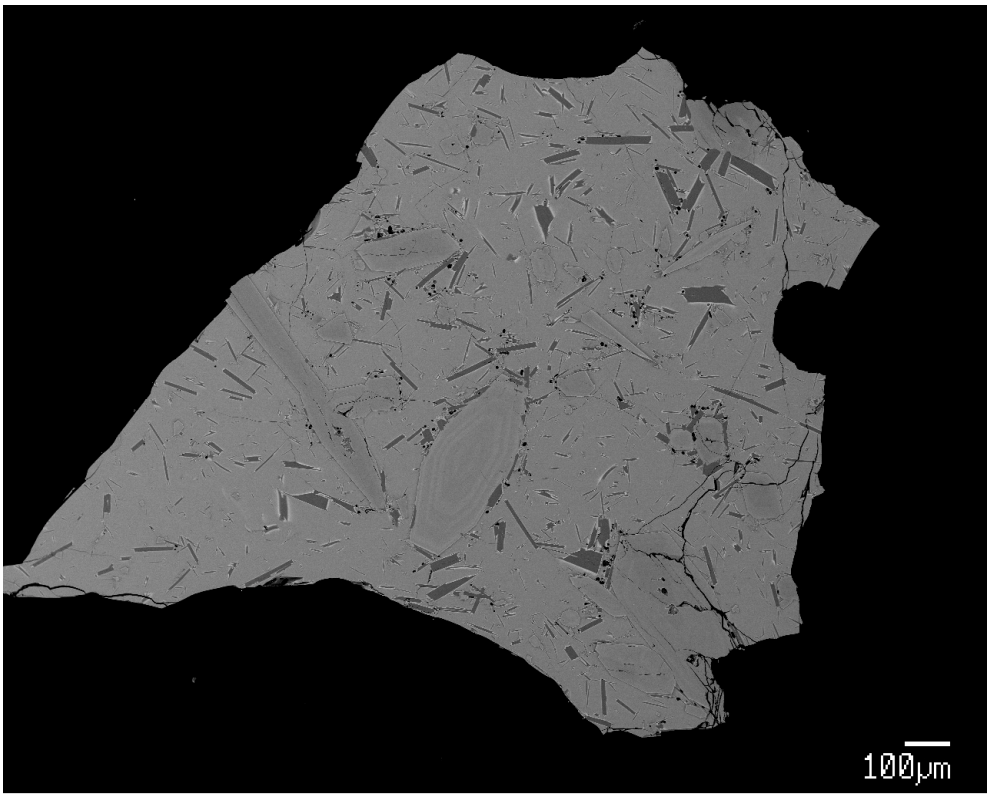

Figure 8.5. Rock S99-R06, glass chip 03.

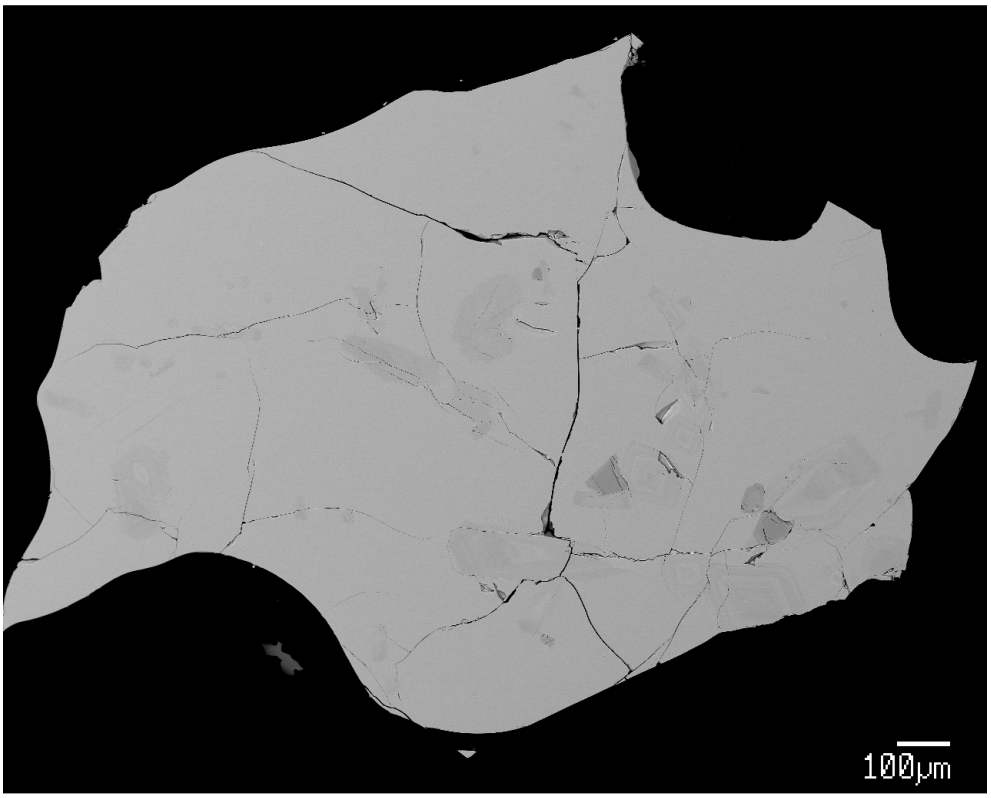

Figure 8.6. Rock S99-R12, glass chip 03.

8.2.3 Raman Spectroscopy

Water varied from 1.14 to 1.51 wt.% prior to any rejection and varied 1.15 to 1.51 wt.% after rejection using the >7.6% variation from mean procedure described in section 7.3.2. After the >5.5% variation from mean rejection procedure, water varied from 1.17 to 1.51 wt.%. Complete water content given in wt.% is shown in Table 8.3.

Sample Name	Before Rejection			After Rejection of % variation > 7.6%			After Rejection of % variation >5.5%			Suspected Eruption Group
	Average H_2O wt.%	Standard Deviation	Percent Variation	Average H_2O wt.%	Standard Deviation	Percent Variation	Average H_2O wt.%	Standard Deviation	Percent Variation	
S98-S01	1.272	0.066	5.021	1.272	0.066	5.021	1.271	0.063	4.804	ST Outside Boundary
S98-S02	1.249	0.064	4.905	1.240	0.056	4.331	1.233	0.051	3.963	ST Outside Boundary
S98-R03	1.297	0.047	3.521	1.297	0.047	3.521	1.297	0.047	3.521	ST Outside Boundary
S98-R04	1.290	0.072	5.369	1.304	0.061	4.513	1.304	0.061	4.513	ST Outside Boundary
S98-R05	1.280	0.078	5.855	1.297	0.064	4.744	1.297	0.064	4.744	ST 1
S98-S06	1.281	0.053	3.952	1.284	0.051	3.813	1.280	0.047	3.500	ST 1
S98-R07	1.304	0.047	3.447	1.304	0.047	3.447	1.304	0.047	3.447	ST 1
S98-R08	1.322	0.091	6.626	1.349	0.045	3.225	1.349	0.045	3.225	ST 1
S98-R09	1.446	0.122	8.150	1.446	0.122	8.150	1.484	0.097	6.323	ST 1
S98-R11	1.364	0.044	3.131	1.364	0.044	3.131	1.364	0.044	3.131	ST 1
S98-R12	1.274	0.066	5.017	1.274	0.066	5.017	1.274	0.066	5.017	ST 1
S98-S13	1.228	0.054	4.194	1.222	0.046	3.593	1.224	0.046	3.598	ST 1
S98-R14	1.250	0.042	3.202	1.250	0.042	3.202	1.250	0.042	3.202	ST 1
S98-R15	1.233	0.043	3.381	1.233	0.043	3.381	1.247	0.023	1.768	ST 1
S98-S16	1.208	0.079	6.281	1.223	0.052	4.095	1.220	0.049	3.868	ST 1
S98-R17	1.317	0.058	4.223	1.317	0.058	4.223	1.317	0.058	4.223	ST 1
S98-R18	1.206	0.114	9.045	1.206	0.114	9.045	1.209	0.121	9.598	ST 0
S98-R21	1.198	0.057	4.536	1.198	0.057	4.536	1.198	0.057	4.536	ST 0
S98-R22	1.268	0.078	5.938	1.268	0.078	5.938	1.279	0.075	5.890	ST 0

Table 8.3a. Wt.% of H_2O in glass samples determined by Raman spectroscopy. Rejection was conducted based on the procedures described in section 7.3.2. Samples whose percent variation was higher than 7.6% or 5.5% had point measurements rejected to reduce noise in the data set.

Sample Name	Before Rejection			After Rejection of % variation > 7.6%			After Rejection of % variation >5.5%			Suspected Eruption Group
	Average H_2O wt.%	Standard Deviation	Percent Variation	Average H_2O wt.%	Standard Deviation	Percent Variation	Average H_2O wt.%	Standard Deviation	Percent Variation	
S99-R1	1.514	0.064	4.070	1.514	0.064	4.070	1.514	0.064	4.070	NT 0
S99-R2	1.450	0.066	4.374	1.450	0.066	4.374	1.450	0.066	4.374	NT 0
S99-R3	1.494	0.129	8.333	1.494	0.129	8.333	1.494	0.129	8.333	NT 0
S99-R4	1.323	0.076	5.527	1.336	0.070	5.067	1.336	0.070	5.067	NT 2
S99-R5	1.189	0.068	5.479	1.189	0.068	5.479	1.189	0.068	5.479	NT 2
S99-R6	1.330	0.229	16.607	1.254	0.040	3.070	1.254	0.040	3.070	NT 2
S99-R7	1.180	0.149	12.118	1.228	0.049	3.845	1.214	0.033	2.631	NT 2
S99-R8	1.186	0.046	3.733	1.186	0.046	3.733	1.186	0.046	3.733	NT 2
S99-S9	1.285	0.082	6.146	1.294	0.068	5.024	1.287	0.059	4.392	NT 1
S99-R10	1.226	0.042	3.324	1.226	0.042	3.324	1.226	0.042	3.324	NT 1
S99-R12	1.266	0.045	3.400	1.266	0.045	3.400	1.266	0.045	3.400	NT 1
S99-R13	1.313	0.138	10.113	1.270	0.051	3.896	1.270	0.051	3.896	NT 1
S99-R14	1.192	0.047	3.763	1.192	0.047	3.763	1.192	0.047	3.763	NT 1
S99-S15	1.223	0.061	4.815	1.223	0.061	4.815	1.215	0.044	3.450	NT 1
S99-R18	1.226	0.129	10.070	1.187	0.053	4.301	1.187	0.053	4.301	NT 1
S99-R20	1.422	0.042	2.862	1.422	0.042	2.862	1.422	0.042	2.862	NT 0
S99-R21	1.141	0.070	5.915	1.151	0.068	5.621	1.169	0.047	3.840	NT 1
S99-S25	1.370	0.082	5.762	1.375	0.079	5.563	1.375	0.079	5.563	NT 0
S99-R26	1.254	0.033	2.545	1.254	0.033	2.545	1.254	0.033	2.545	NT 0

Table 8.3b. Wt.% of H_2O in glass samples determined by Raman spectroscopy. Rejection was conducted based on the procedures described in section 7.3.2. Samples whose percent variation was higher than 7.6% or 5.5% had point measurements rejected to reduce noise in the data set.

Variation of wt.% of H_2O with K_2O, MgO, and water depth are displayed in Figures 8.5-8.7. Once again, samples are labeled based on the suspected eruption group. Figures shown below include H_2O wt.% data after rejection of points outside of the 5.5% variation criteria; figures with data before rejection and after rejections of points outside of the 7.6% variation criteria can be found in section 11.5.

Figure 8.7 compares H_2O wt.% to MgO wt.%; here, all South Tafu samples combined with the NT 1 eruption samples overlap due to their similar compositions; NT 1 has slightly lower water content. The NT 0 eruptive group has a negative trend, and the NT 2 eruption appears to have no significant trend because of its narrow range of MgO wt.%.

Figure 8.8 compares H_2O wt.% to K_2O wt.%. There is little variation in K_2O wt.% amongst all South Tafu samples with the exceptions of S98-R05 and S98-S16; because of this, it is difficult to conclude if there is any significant trend. If outliers S98-R05 and S98-S16 are considered, one could see H_2O wt.% increasing with K_2O wt.%. The NT 0 eruption has a narrow range of K_2O wt.% with the exception of outlier S99-R26.

Comparing water depth with H_2O wt.% in Figure 8.9 generally indicates an increase in H_2O wt.% with increase in water depth for individual eruption groups. The only exceptions are the ST 0 and ST Outside Boundary eruptive groups, if considered individually and not grouped with the ST 1 eruption.

Analytical uncertainty of +/- ~0.6 wt.% H_2O makes any trends less reliable. This will be further explored in section 9.3.1.1.

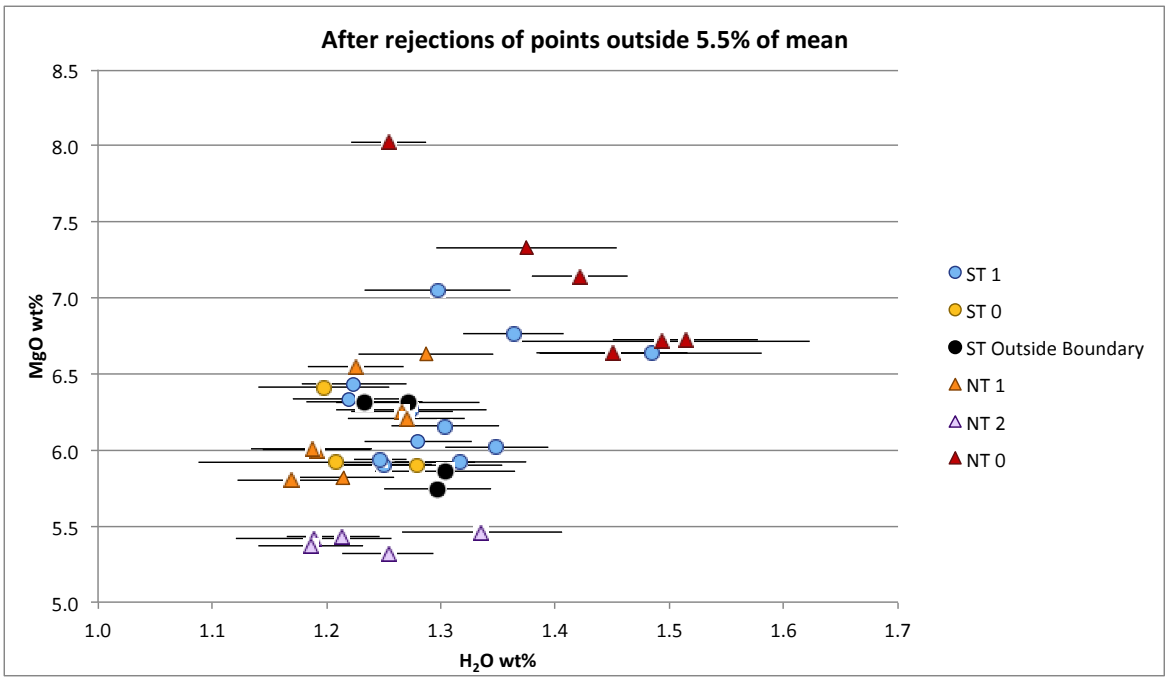

Figure 8.7. H_2O wt.% vs. MgO wt.% of samples labeled by eruption group. Error bars represent one standard deviation. Each point represents the average of all points measured on one sample.

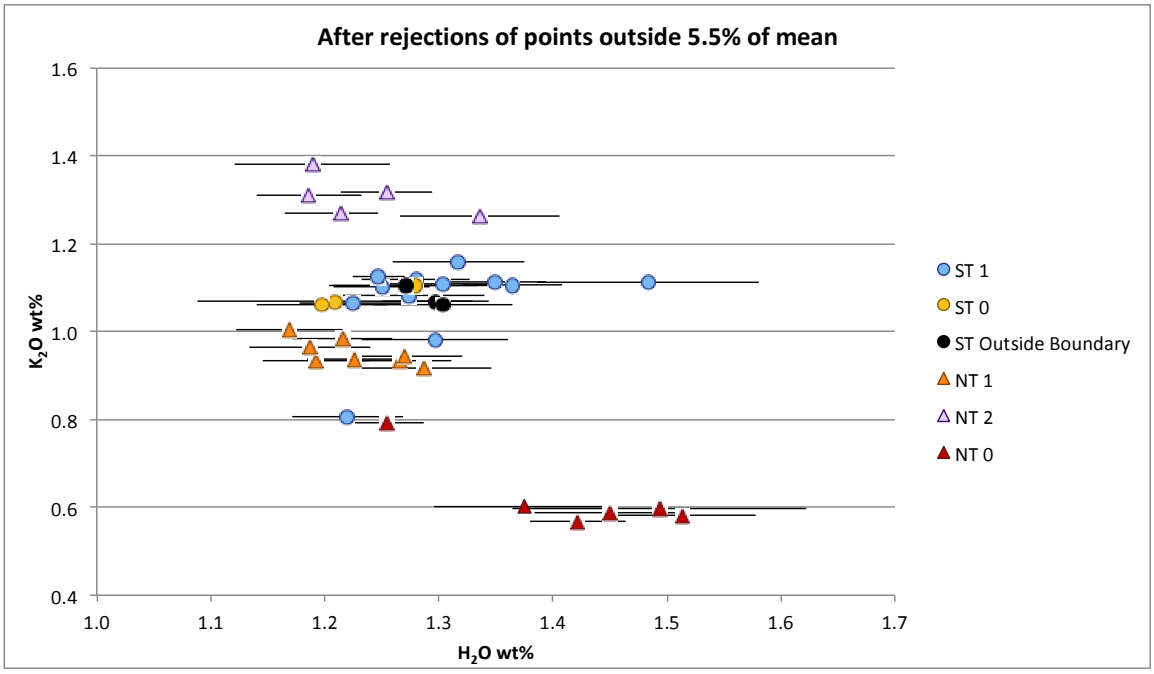

Figure 8.8. H_2O wt.% and K_2O wt.% of samples labeled by eruption group. Error bars represent one standard deviation. Each point represents the average of all points measured on one sample.

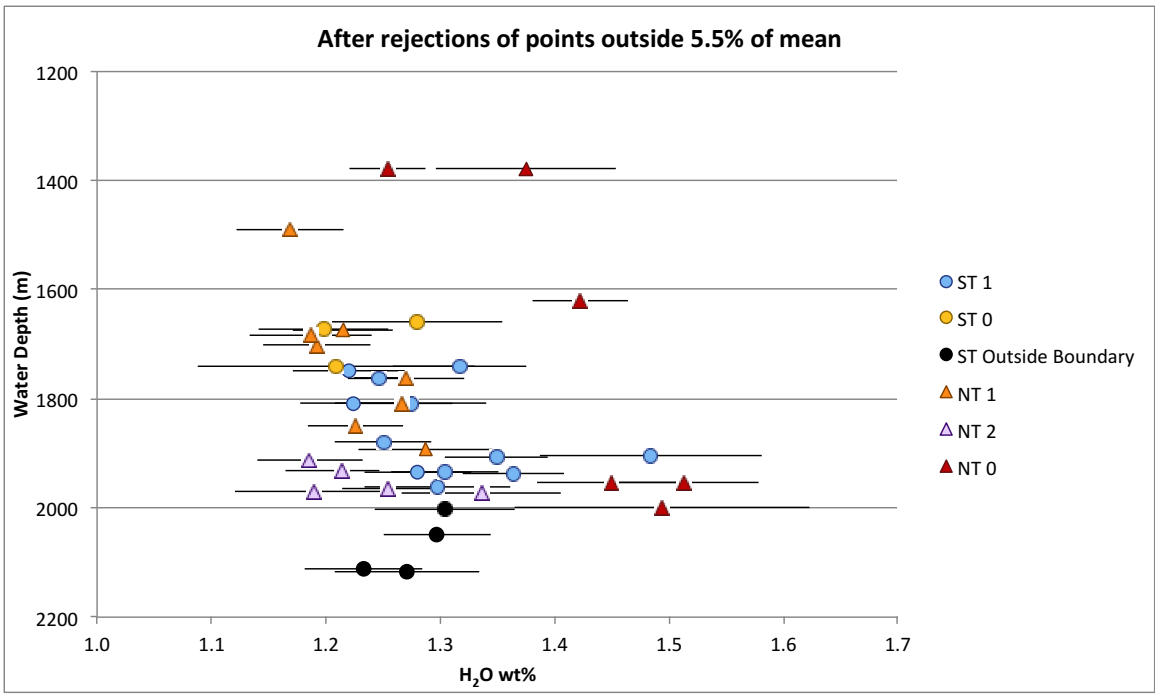

Figure 8.9. H_2O wt.% and water depth in meters of samples labeled by eruption group. Error bars represent one standard deviation. Each point represents the average of all points measured on one sample.

H_2O wt.% was also compared to the flow morphology from which each sample was collected (Figure 8.10). There is much less variation between flow morphologies than within them, although the highest water contents measured tend to be in the morphologies for which we interpret higher effusion rates (i.e., jumbled sheet flows). In contrast, tephra fragments (sediment) tend to have the lowest range of water contents.

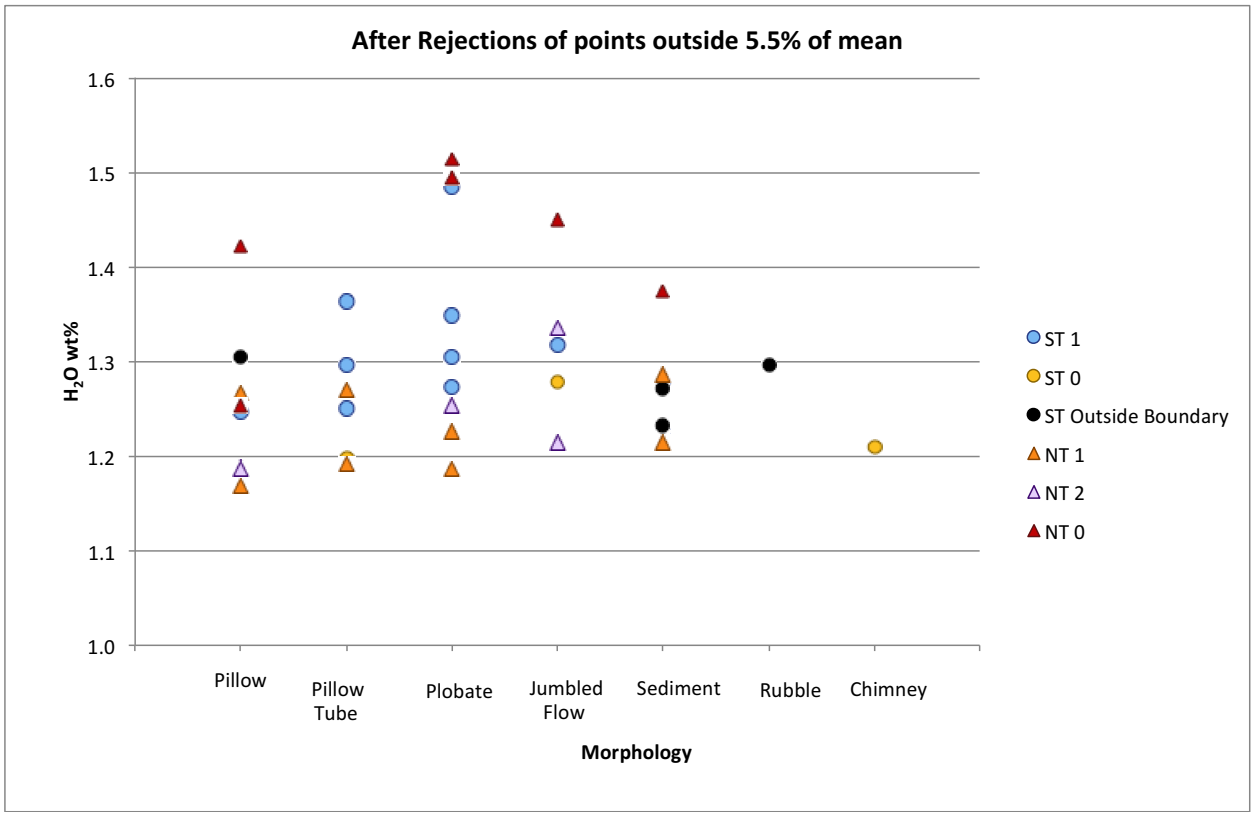

Figure 8.10. Comparison of H_2O wt.% with morphology type. No error bars for wt.% H_2O are included for the sake of legibility.

8.2.3.1. VolatileCalc 2.0

To evaluate if the relationship between wt.% H_2O and water depth in some of the sample groups was due to hydrostatic pressure at the vent (as opposed to differences in the amounts of juvenile H_2O), we needed to confirm that the wt.% H_2O in the samples was in equilibrium with the depth and therefore saturated in H_2O. The software package VolatileCalc 2.0 allowed us to make this determination (Newman and Lowenstern, 2002). By inputting variables like SiO_2 content, final water content, CO_2 content, and temperature, VolatileCalc 2.0 models at what pressure the samples should have erupted.

The following conditions were used for the "Calculate Saturation Pressure" function under "Basalt Calculations": 49.00 wt.% SiO_2 (VolatileCalc 2.0 only allows for wt.% SiO_2 between 40.00 and 49.00), 1.00 wt.% H_2O, CO_2 concentration of 200 ppm (a rough estimate considering CO_2 was not measured in the Tafu samples), and temperature of 1200°C. Figure 8.11 shows the results of this model for depths of all FK171110 Tafu samples along with the measured water compositions and depths of the samples. Wt.% H_2O of eruption samples shown in this figure have had the >5.5% variation from mean wt.% H_2O rejection procedure applied. Figures using wt.% H_2O before rejection and after >7.6% variation from mean wt.% H_2O can be found in section 11.5 in Appendix E.

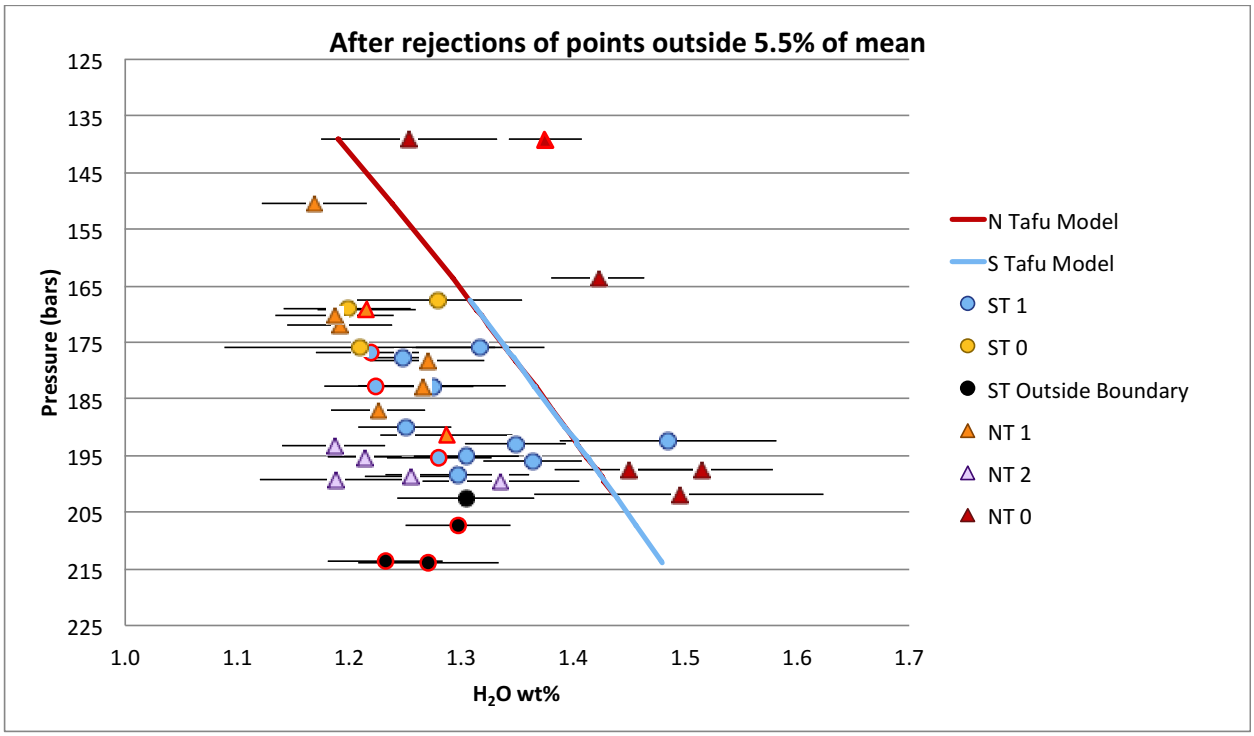

Figure 8.11. Wt.% H_2O after rejection of data >5.5% variation from mean v. pressure in bars. Water pressure (in bars) at each sample location was derived from the CTD pressure sensor on the ROV SuBastian. Error bars indicate one standard deviation. Both S Tafu and N Tafu models are from VolatileCalc 2.0 (Newman and Lowenstern, 2002). These model lines indicate where water content is considered saturated at a given depth.

9. Discussion

9.1. MELTS modeling

MELTS is a software package that uses experimental data and thermodynamic models to model phase equilibriums within magmatic systems (Gualda et al., 2012; Ghiorso and Gualda, 2015). One can set variables such as the major element composition of a parent melt, initial and final melt temperatures, oxygen fugacity, increment of change in temperature, and water content. Given these variables, MELTS will calculate the composition and proportion of each component at each temperature step within the system being modeled. Composition of the liquid melt is the only component being examined for the purposes of this study. This is because our major element compositions were determined in glasses, which represent the composition of the liquid melt.

Rhyolite-MELTS was used for these studies (Gualda et al., 2012; Ghiorso and Gualda, 2015); although the name may be deceiving as none of the FK171110 samples are rhyolites, this MELTS version yields results for mafic systems that are identical to those produced by the original MELTS calibration. Using rhyolite-MELTS was preferable to using MELTS because algorithmic modifications in rhyolite-MELTS cause fewer numerical failures (Gualda et al., 2012; Ghiorso and Gualda, 2015).

MELTS can be used in countless ways to understand a magmatic system. For the purpose of this study, its function is to use the modeled differentiation paths to understand how parent melt composition, fractional crystallization, and magma mixing occur at Tafu and interact to create the samples being studied.

The conditions used for each MELTS model are listed in Table 9.1, and the parent melt compositions used for our MELTS models are given in Table 9.2. Parent Melt 1

composition was determined by interpolating oxide trends in the ST 1 composition out to 10 wt.% MgO. This interpolation was done for all elements. Depending on the oxygen fugacity selected for the model, normalization changes these values slightly for each model. All MELTS models completed used a temperature range of 1300°C-1050°C and a temperature step of 1°C. Although different pressures (400-500 bars) were used for different models, pressure remained constant within each model. The complete results of our MELTS models are shown in Appendix F, section 11.6, as wt.% MgO vs. various other oxides; the best models chosen are shown here in Figure 9.1. This figure includes lines that represent the path of the liquid melt composition as it cools and differentiates due to fractional crystallization (i.e., from high to low MgO wt.%, right to left). Slope changes indicate where different phases begin to crystallize out of the melt and dilute or concentrate elements in the melt depending on the crystallizing phases. The major element compositions of each rock and sediment sample from the three known eruptions at Tafu are included in these figures.

Model Name	**Parent Melt Composition**	**Oxygen Fugacity Buffer**	**Pressure (bars)**	**wt.% FeO***	**wt.% Fe_2O_3***	**wt.% SiO_2***
D1	Parent Melt 2	QFM-3	500	-	-	-
D2	Parent Melt 3	QFM-3	400	-	-	-
E1	Parent Melt 1	QFM-3	400	8.00	-	-
E2	Parent Melt 1	QFM-3	400	-	1.30	-
E3	Parent Melt 1	QFM-3	400	8.00	-	48.50
E4	Parent Melt 1	QFM-3	400	8.00	-	50.00

Table 9.1. Conditions used for the MELTS models that best fit our data. All MELTS models and their conditions are in Appendix F. * indicates that a wt.% is only given here if it has been adjusted from the parent melt composition. Models with no entries in these columns have the same parent melt compositions as those listed in Table 9.2 for that elemental oxide.

	SiO_2	TiO_2	Al_2O_3	Fe_2O_3	FeO	MnO	MgO	CaO	Na_2O	K_2O	P_2O_5	H_2O	SO_3	Cl_2O^{-1}
Parent Melt 1	45.78	0.89	12.00	0.70	7.00	0.07	10.00	15.00	1.69	0.71	0.31	3.00	0.059	0.07
Parent Melt 2	45.78	0.89	12.00	1.50	7.00	0.07	9.00	12.00	1.69	0.71	0.31	3.00	0.059	0.07
Parent Melt 3	45.78	0.89	12.00	1.50	7.00	0.07	10.00	11.00	1.69	0.71	0.31	3.00	0.059	0.07

Table 9.2. Compositions of parent melts chosen for MELTS models. All oxide values are given in wt.%. The composition of Parent Melt 1 was chosen by extrapolating trends seen in the ST 1 major element compositions out to 10.00 wt.% MgO and choosing wt.% of other oxides by what they would be at 10.00 wt.% MgO. Values highlighted in red indicate an oxide wt.% that was adjusted relative to Parent Melt 1 to find a better fit to the Tafu major element composition data.

Of all the MELTS results (Figures 11.12 in Appendix F), 6 models of best fit were chosen to study further. These 6 models are shown in Figure 9.1. No single model perfectly fits the major element composition data for the ST 1 flow; however, these six models came the closest, and their trends can help decipher the magma history of Tafu. Position of the MELTS model on the graph is controlled by the user-set conditions (Table 9.1) of the MELTS run and can be adjusted to better fit certain data sets. However, because this study maintained similar parent melts and only varied conditions slightly between runs, the slope of the models stays similar from model to model. This slope is the most important result of the MELTS models, as slope indicates the change in composition of the liquid melt as fractional crystallization occurs. By comparing slope of the MELTS models to the average slope projected within each eruption group, it is possible to see if fractional crystallization of a single parent melt could have produced many different samples collected from Tafu.

Beginning with Figure 9.1a showing wt.% SiO_2 vs. wt.% MgO, the D1 model best fits the ST 1 SiO_2 data. If assuming this model's path represents the composition of the liquid melt of the ST 1 eruption, then SiO_2 initially increases with decreasing MgO as majority forsterite (Mg_2SiO_4) olivine crystallizes. Only olivine crystallizes until MgO is at about 7.3 wt.%. The SiO_2 wt.% in the melt then decreases and increases once more as clinopyroxene and olivine fractionate out of the melt at different rates. Following this MELTS-derived

path, it would be impossible for the NT 2 eruption from 2010-2017 to have come from the same source as the ST 1 eruption group, as they cannot sit along the same differentiation path. Likewise, the ST 1 melt from 2010-2017 could not have differentiated from the same melt that produced NT 1. However, the NT2 samples can sit along the same differentiation path as the NT 1 samples. This indicates that the NT 2 lavas could have fractionally crystallized from the same melt as the NT 1 lavas, at least with respect to SiO_2 and MgO. We will soon see that this is not the case in all oxides.

Figure 9.1b shows wt.% Al_2O_3 vs. wt.% MgO. With decreasing MgO, Al_2O_3 increases gradually at first, and then more quickly as clinopyroxene fractionates and removes non-Al atoms from the melt. When MgO reaches ~5 wt.%, Al_2O_3 starts to decrease as plagioclase feldspar is crystallized.

In this case, model E3 best fits the trend in ST 1 seen between MgO and Al_2O_3. NT 1 looks similar and even overlaps with the ST 1 Al_2O_3/MgO compositions. If the E3 model represents the differentiation path of one parent melt, then it could be possible to get some of the lava samples from ST 1 and NT 1 via fractional crystallization of the same parent melt. However, numerous ST 1 lavas are too low in Al_2O_3 with respect to MgO to lie along that differentiation path. The NT 2 melt is also too low in Al_2O_3 to sit on the differentiation path given by model E3 and likely did not fractionate from the same parent melt as ST 1 and NT 1 with respect to aluminum.

Figure 9.1c displays wt.% MgO vs. wt.% FeO and how the different melt compositions in MELTS models change with decreasing MgO. Initially, FeO decreases gradually with decreasing MgO as forsterite (Mg_2SiO_4) and fayalite (Fe_2SiO_4) crystallize. At this point, more forsterite is crystallizing than fayalite. In model E4, olivine begins to

crystallize at 1204°C (at this temperature, there is 9.77 wt.% MgO); the olivine being crystallized is 83.57 mol% forsterite and 14.59 mol% fayalite, so wt.% MgO in the melt decreases more quickly than wt.% FeO in the melt. FeO begins to increase with decreasing MgO once clinopyroxene crystallization begins. This is because the clinopyroxene being crystallized at 1174°C (at this temperature, there is 8.66 wt.% MgO) in model E4 is 69.37 mol% diopside ($MgCaSi_2O_6$). Mg atoms are now leaving the melt to form both diopside and forsterite crystals; this loss of Mg causes the relative wt.% of FeO to increase as it makes up a larger proportion of the melt. Finally, feldspar begins crystallizing at 1102°C in model E4 (at this temperature, there is 4.79 wt.% MgO) and proportions of MgO and FeO in the melt begin to change once more as other elements such as Ca, Al, Na, and K are used to crystallize feldspar.

None of the MELTS models shown here perfectly fit the South Tafu 2010-2017 MgO and FeO data. However, models E2 and E3 come the closest. For simplicity, model E2 will be the focus of this section. There is a wide range of FeO compositions within the samples collected, meaning that it would be difficult even in a single eruption to get all of these compositions via differentiation from a single parent melt. It is possible that magma mixing and multiple parent magmas within eruptions are required to explain the wide range in FeO wt.%, especially in both 2010-2017 eruptive groups (ST 1 and NT 2). Regardless, it is certainly unlikely that ST 1, NT 1, or NT 2 could have differentiated from the same parent melt with respect to FeO. The trend of the NT 2 data is much too steep to be part of a differentiation path, and no differentiation paths tie together all compositions of different eruptions in MgO and FeO. The lower FeO rock samples of the NT 2 group could lie along

the NT 1 differentiation path, but this does not account for the higher FeO NT 2 rock samples.

Figure 9.1d plots CaO wt.% vs. MgO wt.% and it is clear for all models that CaO initially increases with decreasing MgO, and then decreases with decreasing MgO. Once again focusing on model E4, CaO initially increases with decreasing MgO as forsterite crystallizes. Forsterite takes Mg atoms from the melt as it crystallizes (Mg_2SiO_4), leaving more CaO in the melt relative to MgO. CaO begins to decrease with decreasing MgO as Ca atoms are used to crystallize clinopyroxene (69.37 mol% diopside and 12.27 mol% hedenbergite at 1174°C).

Both ST 1 and NT 1 follow the slope of decreasing CaO with decreasing MgO. NT 1 has the highest wt.% CaO of the eruptive groups, but all three groups follow a similar path of differentiation with respect to CaO. These samples have CaO contents that behave as we would expect as fractional crystallization occurs.

Finally, Figure 9.1e compares MgO wt.% to K_2O wt.% in liquid melt composition. K_2O increases slightly with decreasing MgO as, once again, Mg is used to crystallize forsterite at 1204°C in model E4. K_2O sharply increases relative to decreasing MgO once Mg moves into diopside and clinoenstatite crystals. Lastly, K_2O increases relative to MgO at an even higher rate once feldspar begins to crystalize and use various other elements like Ca, Al, Na, and Si. This increases the K_2O in the melt relative to the total melt composition. Some K is used in creating sanidine variety feldspar at this point; however, in model E4 at 1102°C, only 0.35 mol% of the feldspar crystallized is sanidine. This amount is nearly negligible and has little effect on the total K_2O wt.% in the melt. It is worth noting that K is incompatible in nearly all the minerals crystallizing, meaning that K atoms are not the

correct size and charge to take cation sites in crystals that are fractionating. Because of this, K largely stays in the melt even as the melt cools and crystallizes, making it a good indicator of parent melt composition.

NT 1 has a much lower wt.% K_2O than the other two eruptive groups and could not lie along the same liquid line of descent as ST 1 or NT 2. Therefore the 2010-2017 magmas (ST 1 and NT 2) could not have fractionated from the same parent melt as the NT 1 eruption from 2006-2008. However, ST 1 and NT 2 do lie along similar paths of differentiation (see E1 and E2 in Figure 9.1e). This means that with respect to K_2O, NT 2 could have fractionated from the same parent melt as ST 1.

With respect to all elements and differentiation trends, it is worth noting that anywhere from 2 to 11 years separates these eruptions. Some of the narratives proposed regarding fractionation of a single parent melt feeding multiple eruptions could be difficult to justify with the timeline required. Even with 2 to 11 years' time, it could be difficult for a remaining magma stored in the crust to cool and differentiate enough to validate some of these differentiation trends.

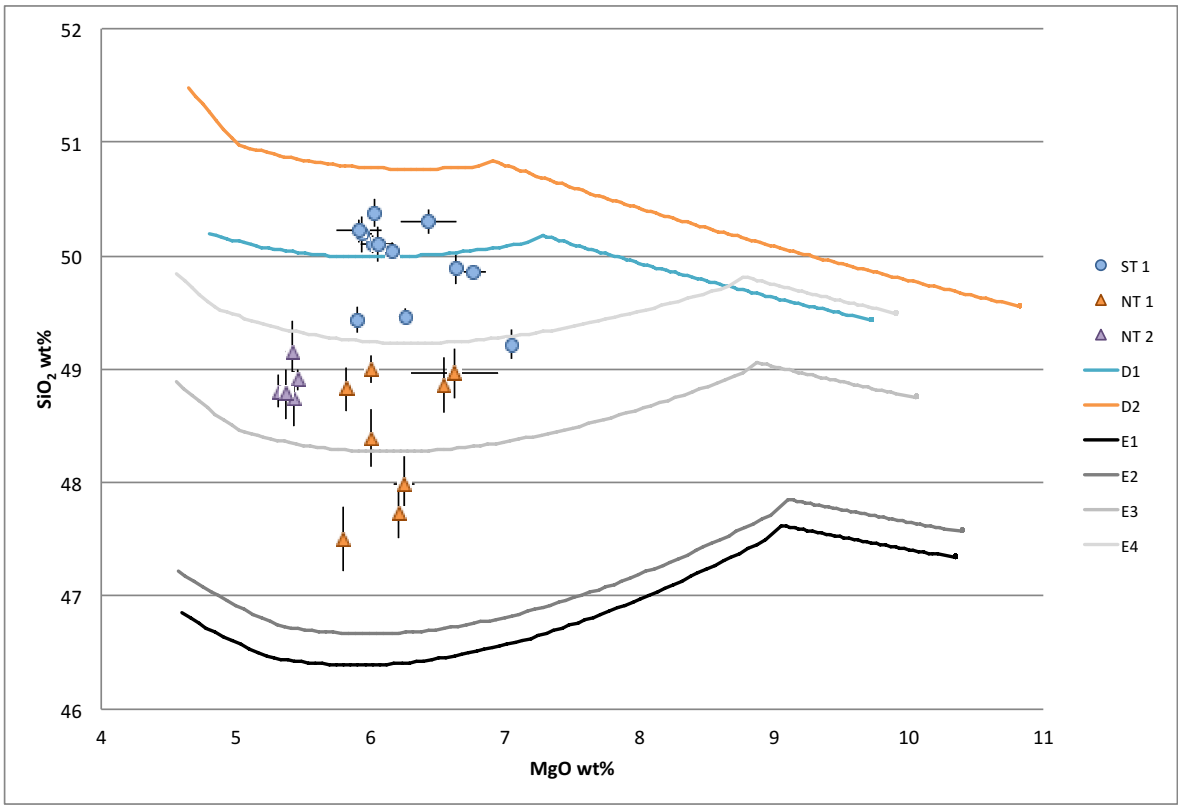

Figure 9.1a.

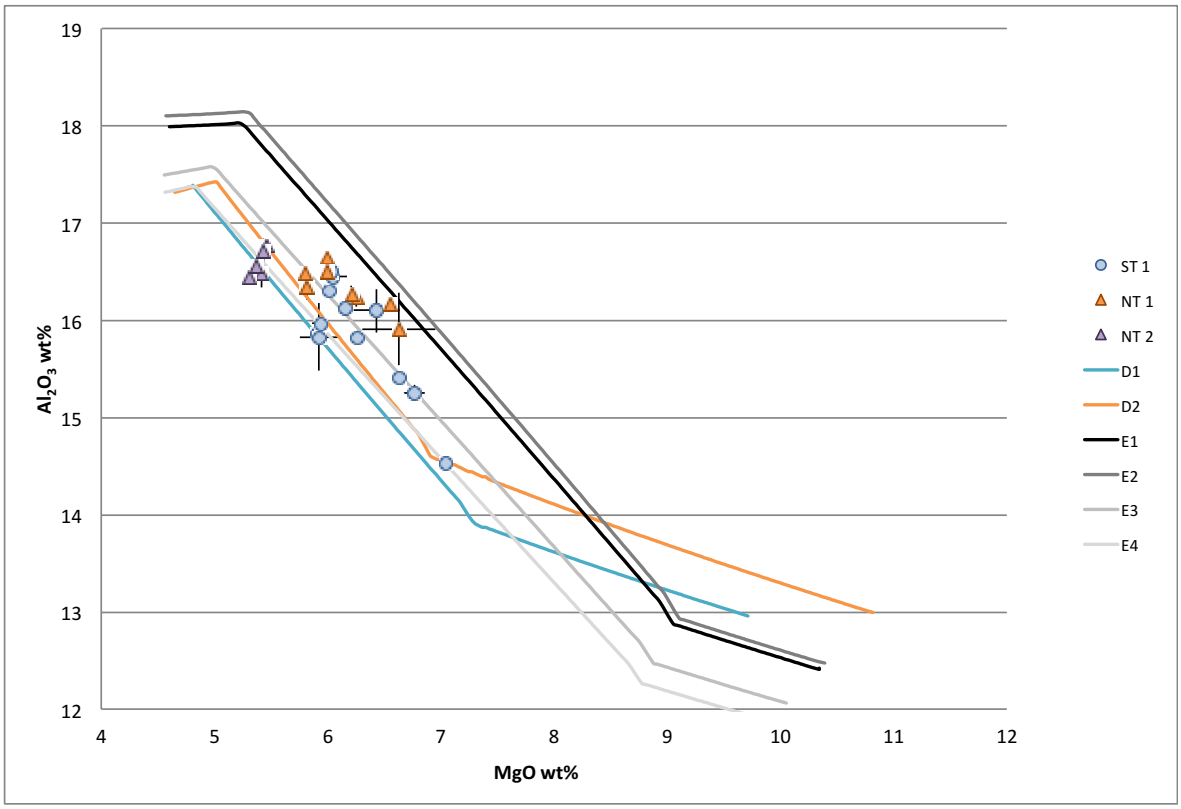

Figure 9.1b.

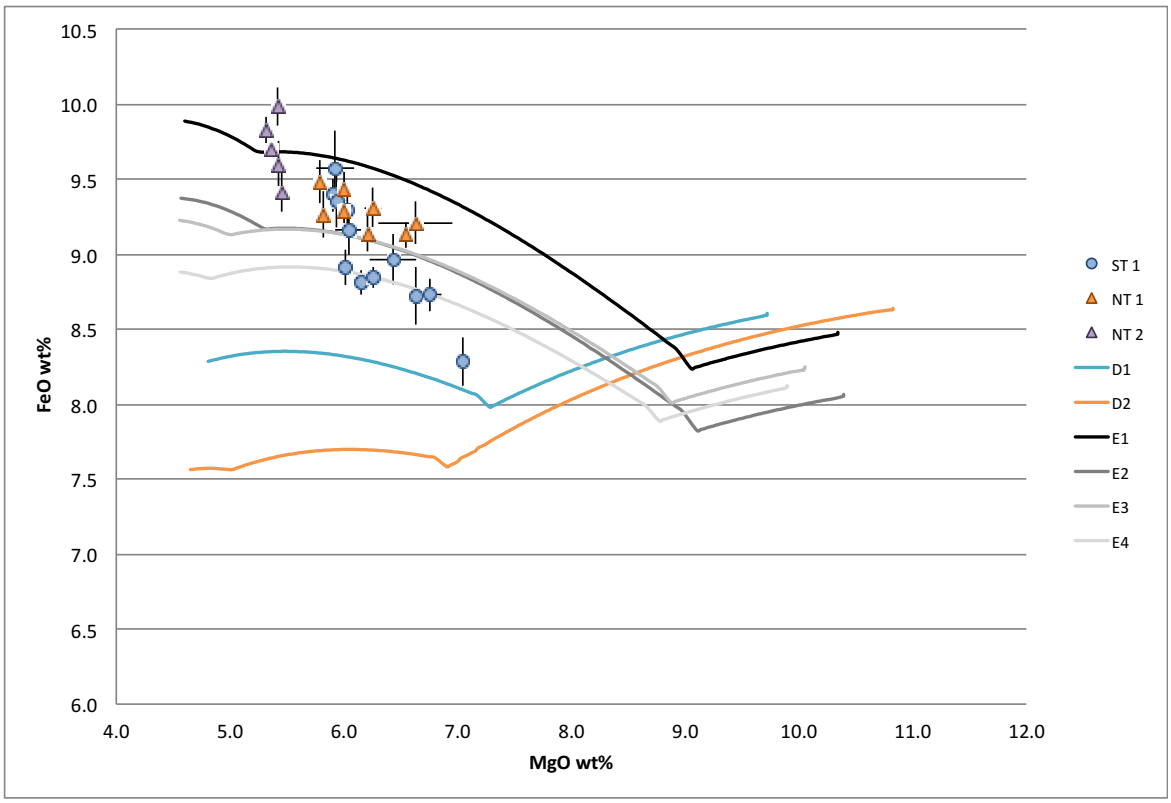

Figure 9.1c.

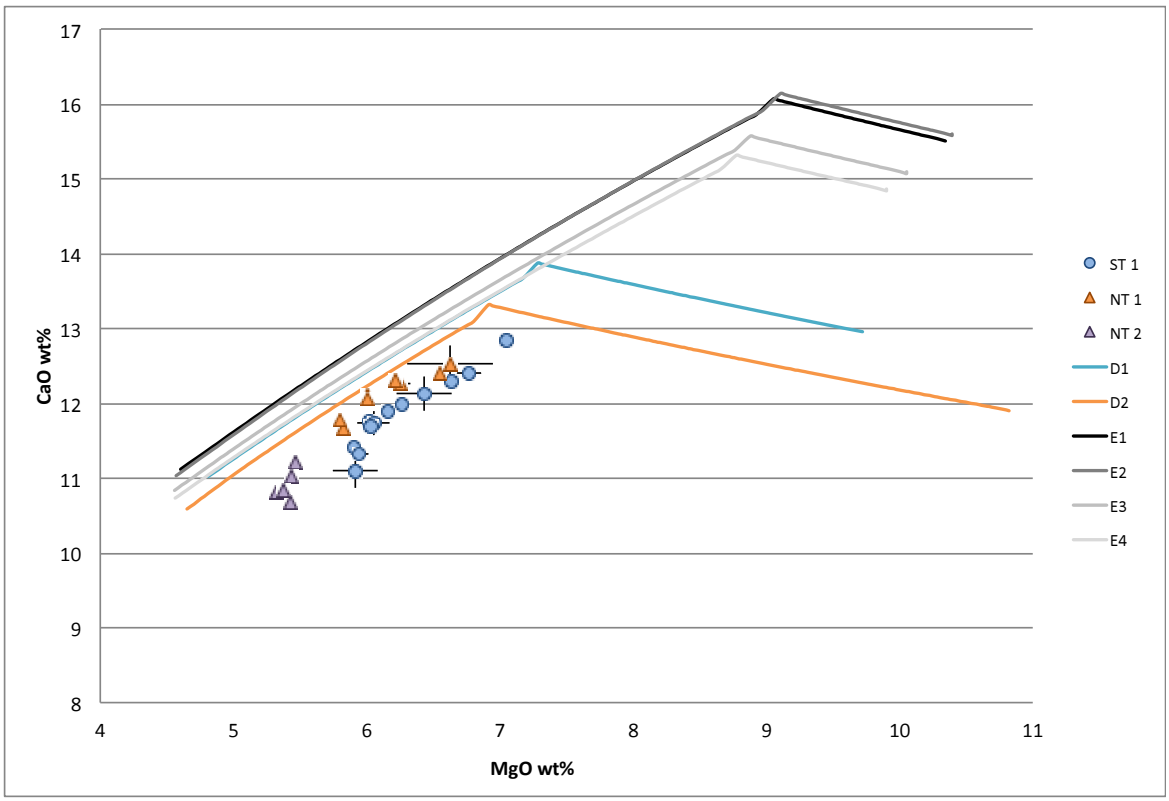

Figure 9.1d.

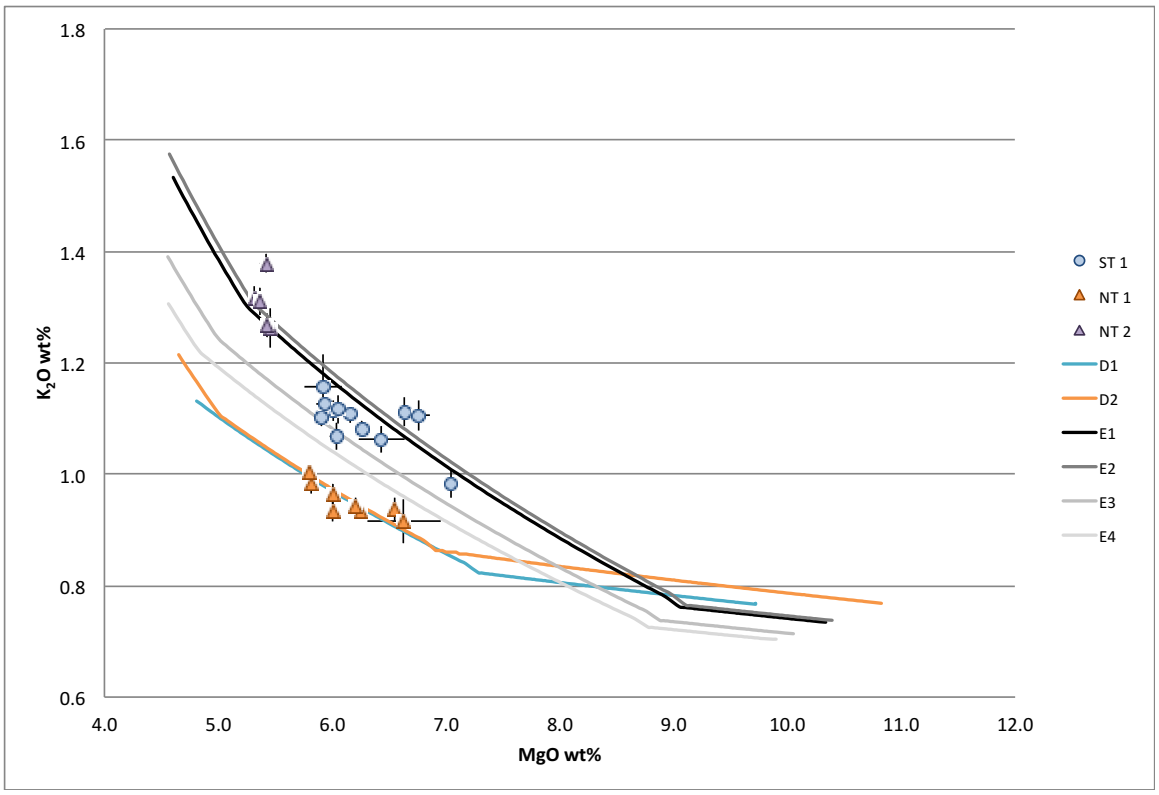

Figure 9.1e.

Figure 9.1. Comparing MgO wt.% with wt.% of various oxides of MELTS models that were decided to best fit known major element composition data of the ST 1 eruption. Error bars indicate one standard deviation. Parental melt compositions correspond to the right-hand end of each line. As differentiation occurs, MgO wt.% decreases and the y-axis oxide varies as different phases fractionate out of the melt. Compositions of the samples collected from the three main eruptions at Tafu are plotted. The significance of these differentiation paths will be explored further in section 9.1.

9.2. Water content as determined by Raman spectroscopy

The strength of many of the trends seen within eruption groups in "*parameters v. H_2O*" may be called into question because differences within the trends vary by less than one standard deviation of error. Though these trends may be questionable in terms of error, they are still consistently seen within the majority of "*parameters v. H_2O*" data. For this reason, they will be explored further in the following sections.

9.2.1. Change in water content with depth

Figure 9.2 shows the change in wt.% H_2O with the depth of the location the sample was taken from, similarly to Figure 8.7. However, Figure 9.2 highlights any data points representing a sample that was either sediment or talus and could have erupted at a depth that was different from the one the sample was collected from. These data points are highlighted with a bright red outline.

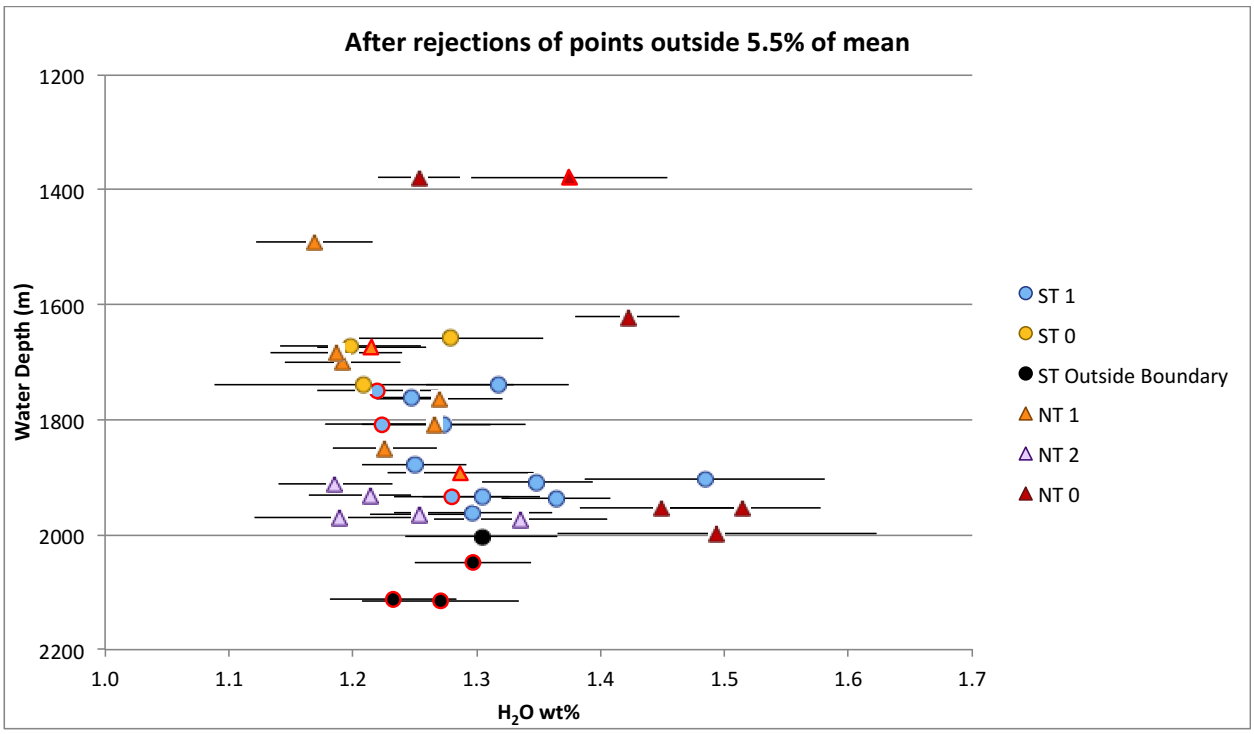

Figure 9.2. H_2O wt.% and water depth in meters below sea level of samples grouped by suspected eruption. Error bars indicate one standard deviation. Bright red outlines indicate samples that are sediment or talus and therefore could have erupted at a different depth than the one they were collected from.

In almost all eruption groups, except for the ST 0 eruptive group, which only has 3 data points, wt.% H_2O increases with depth. This is to be expected, as increasing depth within the water column means increasing pressure and more volatiles staying in solution in the melt.

9.2.1.1. VolatileCalc 2.0

As covered in section 8.2.3.1, VolatileCalc 2.0 (Newman and Lowenstern, 2002) was used to evaluate if water content in the FK171110 North and South Tafu rock samples were at saturation for their depth of collection. Results are provided one again in Figure 9.3 for accessibility. All samples measured, with the exception of the NT 0 eruptive group and S98-R09 from the ST 1 eruptive group, have a lower wt.% H_2O than the VolatileCalc 2.0 model predicts for the given conditions.

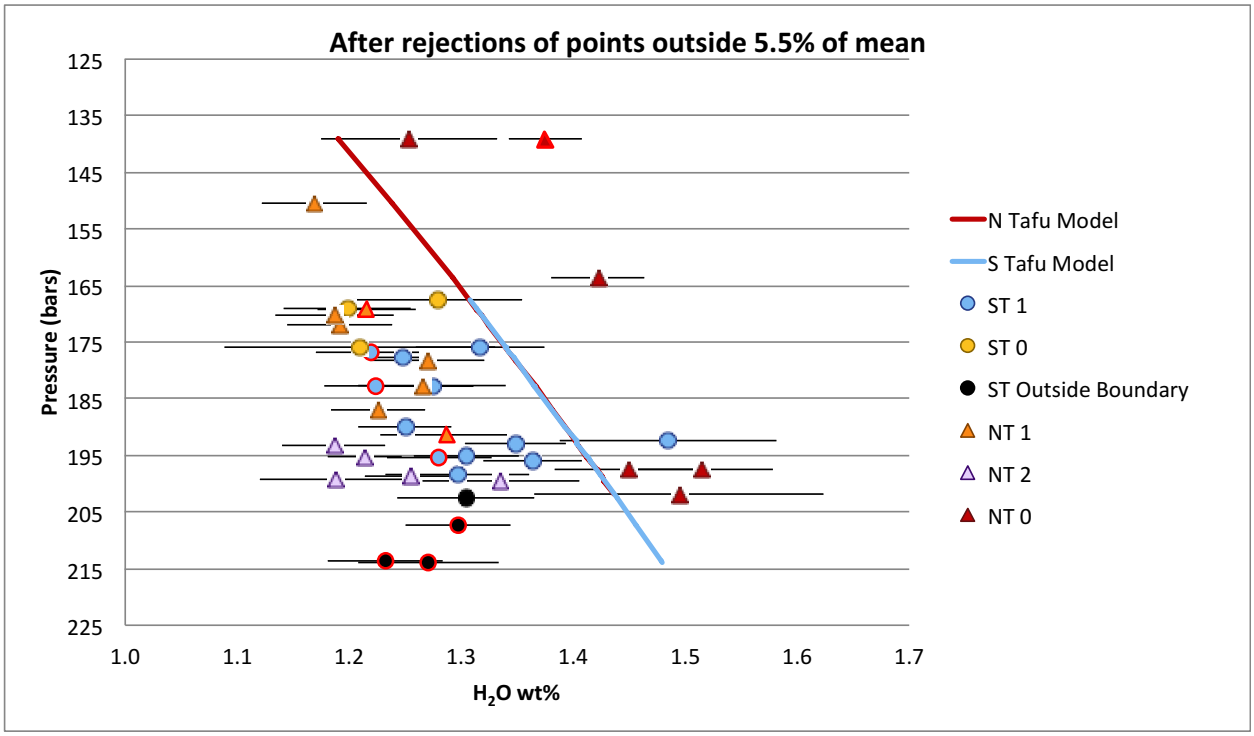

Figure 9.3. Wt.% H_2O with points rejected for samples whose percent variation is greater than 5.5% vs. pressure in bars. Pressure in bars of location of collection of samples was taken from the CTD pressure sensor on the ROV SuBastian. Error bars indicate one standard deviation. Bright red outlines indicate a sample that is either sediment or talus, and therefore could have been erupted at a depth (and therefore pressure) different from the depth the sample was collected. Both North and South Tafu models are from VolatileCalc 2.0 (Newman and Lowenstern, 2002).

The NT 1 eruption group has the largest range in depth (and therefore largest range in pressure), which makes the trend of increasing water with increasing pressure more visible in NT 1 than any other eruption group. The sample with the shallowest depth (and therefore lowest pressure) has the lowest wt.% H_2O, and the sample with the deepest depth (and therefore highest pressure) has the highest wt.% H_2O. Though this trend is a bit messy, it clearly shows that this method of measuring water works, and water content increases as expected with increasing pressure. The trend is slightly offset from the VolatileCalc 2.0 model towards lower wt.% H_2O. This could be due to one of the following: an issue with calibration of the method causing less than perfect accuracy, or the magmas truly being undersaturated in water. If the latter is the case, one cause could be that the magmas came from a very dry mantle source and never gained enough water to reach saturation and degas. This is not likely, as mantle sources for the surrounding area do not show any indication that the melt should be low in water (e.g., Caulfield et al., 2012; Lupton et al., 2015). A second option could be that the magma may have been stored at a shallower depth within the edifice of Tafu and degassed before travelling downrift and being erupted at the depth of collection. This would cause the erupted lavas to preserve the lower water content that indicated equilibration at that shallower depth.

The blue circles indicating the ST 1 eruption group from 2010-2017 overlap with the orange triangles representing the NT 1 eruption group from 2006-2008, extending their trend into higher pressure and higher wt.% H_2O as expected. The high wt.% H_2O outlier in this ST 1 group has a high error bar and likely does not have as high of water content as measured.

The yellow circles indicating the ST 0 eruption group overlap with the NT 1 eruptive group (orange triangles). There are only three data points in this group and therefore it is difficult to interpret much from their water content. However, they generally fall within the expected trend of increasing water content with increasing depth as they overlap with the NT 1 data.

The NT 2 eruptive group from 2010-2017, in comparison, has the lowest water content of all eruptive groups. In the process of completing the rejection procedure described in section 7.3.2., the water content in one NT 2 sample decreased due to rejection of a high wt.% H_2O measurement point that was outside of the 7.6% variation from mean criteria. This could indicate that measurements tend to err on the higher side of wt.% H_2O, and the sample (S99-R04) with highest water content (and additionally, with large error) might not actually have as high of water content as measured. This is difficult to determine due to the low precision of these measurements. Regardless of this outlier, NT 2 has the lowest water content relative to pressure of the samples collected from Tafu. These samples are significantly undersaturated in water for their depth. The NT 2 samples were collected at a depth of 1913-1974 meters, where the pressure is 193-200 bars. However, the measured water content of the NT 2 samples means the samples would be saturated at closer to 145-175 bars, or 1436-1732 meters depth. There are several possible explanations for this. One could be that the measurements are inaccurate and do not correctly represent the samples' water content. This is not likely since none of the samples' error overlaps with the VolatileCalc 2.0 model that represents saturation. They all have low water content, and even with uncertainty accounted for, they tend to group closely in water content except for the S99-R04 outlier. It seems more likely that this low water content is

real and not an analytical error. In that case, one cause for undersaturation in the lavas could be that lava was erupted at a shallower depth and then travelled downslope to its final depth. The initially shallow eruption would have allowed the lava to degas at a lower pressure, causing it to lose more dissolved water and preserve the water content of a shallower depth. This is not plausible since the area of the NT 2 eruption is small and covers a narrow range in depth. There is no area of the NT 2 depth difference that lies between 1436 and 1732 meters depth, so these lavas could not have erupted at a shallow depth and flowed downslope. Alternatively, a process of events similar to those described with the NT 1 eruptive group (orange triangles) could have occurred. The magma may have ascended to a shallow reservoir anywhere from approximately 1436 to 1732 meters within the edifice of Tafu, degassed, and then moved downrift within the volcano and erupted at the deeper location it was collected from.

The ST Outside Boundary group is unique in that three of the four samples were either talus or sediment, indicating that they probably did not erupt at the location they were found. This means that the depth, and therefore pressure, of their location of collection does not correlate to the water content measured in the samples. These three out-of-place samples are highlighted with a bright red outline in Figure 9.3. If following the trend seen in the other South Tafu eruptive groups (as well as the trend shown by the models), the actual pressure of the samples collected could be anywhere from 170 to 200 bars; this equates to an approximate range in depth of 300m, from 1680 to 1980 meters below sea level. The similar wt.% H_2O to other samples, but at significantly deeper depth, suggests that these samples preserve a signature of equilibrium and eruption at a shallower depth.

Lastly, the NT 0 eruptive group consistently has the highest water content of all eruptive groups and are supersaturated with respect to the pressure at depth of their collection. Because of the consistency of the high water content within this group, this high water content is likely real and not an analytical ghost. This could be an indication that the magma feeding this eruption erupted quickly and did not have enough time to degas to equilibrium. However, the morphology of the NT 0 rocks is mostly pillows and plobate lavas, with one sediment and one rock from a jumbled sheet flow. Pillows and plobate lavas are characteristic of lower effusion rates (Ballard et al., 1979; Luyendyk and Macdonald, 1985; Fox et al., 1987; Gregg and Fink, 1995). These morphologies do not support the idea that the magma was erupted quickly. Additionally, as stated in section 8.1.2., NT 0 is a grab bag of older lavas that could have come from different eruptions, each with possibly different eruptive rates. If these rocks did come from different eruptions, it is unlikely that all of these eruptions would have erupted abnormally quickly, causing the supersaturation in water. The group's high water content could instead have been caused by something compositionally that this study has not detected, like rehydration of the rocks and sediments after eruption.

9.2.2. Change in water content with MgO

Figure 9.4 once again shows H_2O wt.% of rock and sediment samples collected on FK171110 dives S98 and S99 compared to measured wt.% of MgO. Overall, there is no consistent trend between eruption groups indicating that wt.% H_2O correlates with wt.% MgO. The only significant trend that appears between wt.% H_2O and wt.% MgO is in the NT 0; however, this eruption group contains two subgroups: one with higher MgO, and one

with lower MgO. These MgO groups were collected from different locations, and therefore different depths. For this reason, this correlation may seem to imply that wt.% H_2O decreases with increasing MgO; however, this correlation actually represents the different depths the samples were collected from. This lack of true correlation between MgO and H_2O gives confidence to the discussion presented in section 9.2.1: water is more closely related to equilibrium with pressure and therefore depth of eruption than it is with major element composition.

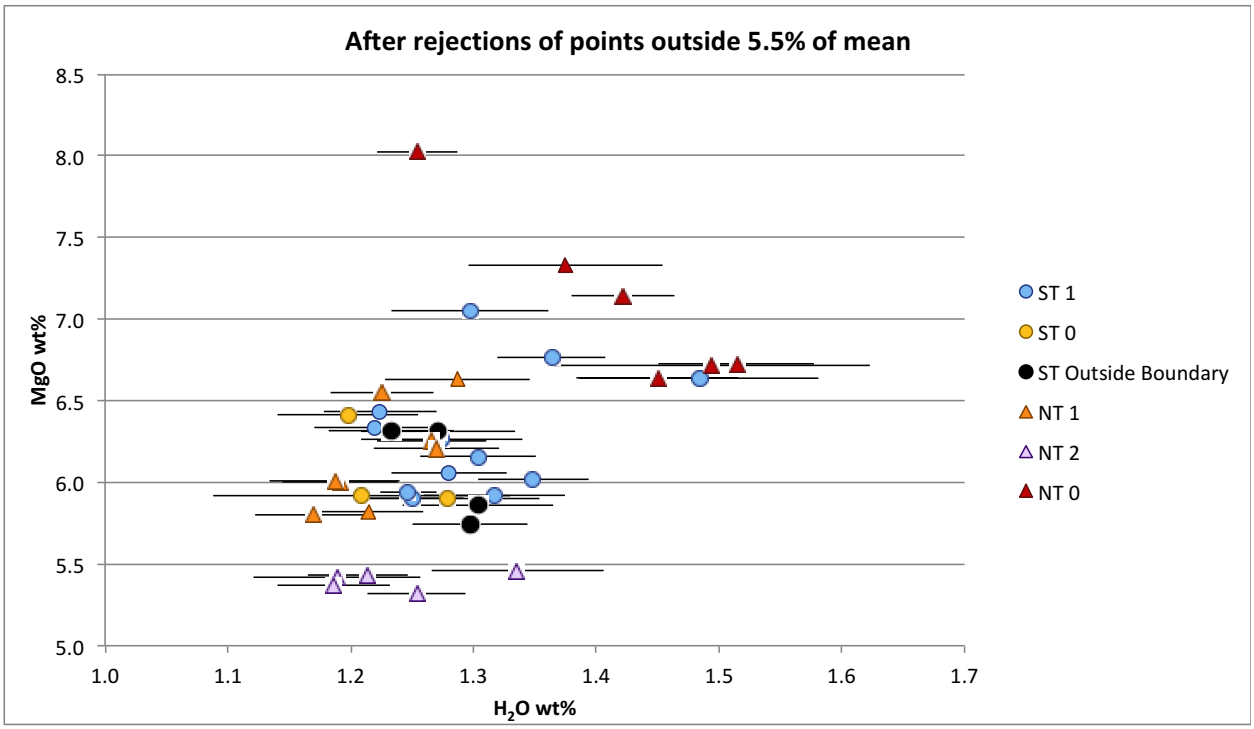

Figure 9.4. Wt.% H_2O and wt.% MgO of samples grouped by suspected eruption. Error bars indicate one standard deviation.

9.2.3. Change in water content with K_2O

Figure 9.5 shows comparisons of wt.% H_2O of samples with wt.% K_2O. As with MgO, there is no significant and consistent correlation of wt.% H_2O with wt.% K_2O. Once again, this helps to reinforce that water content in the samples is not significantly influenced by

composition. There may be some difference in solubility of water with composition; however, it is likely minor and unfortunately cannot be modeled using VolatileCalc 2.0 (Newman and Lowenstern, 2002) due to the software's restriction of varying composition only with respect to SiO_2 wt.% below 49.00 wt.%.

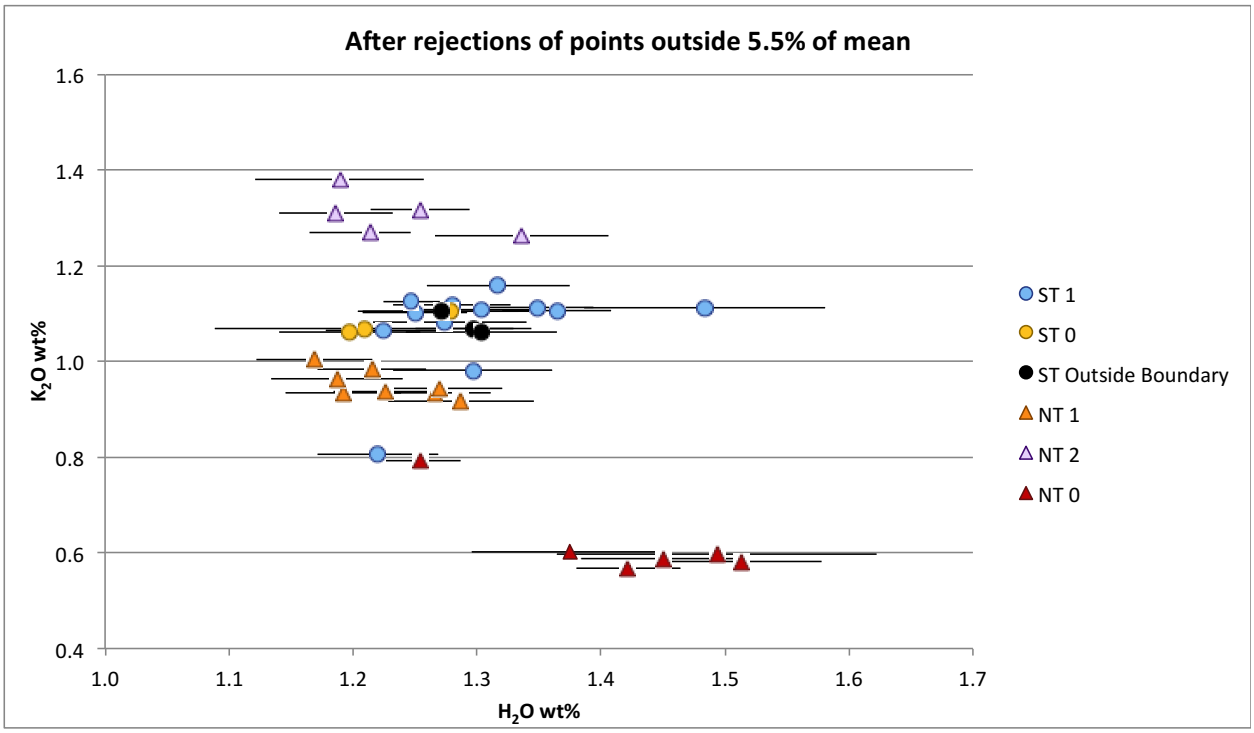

Figure 9.5. H_2O wt.% and K_2O wt.% of samples grouped by suspected eruption. Error bars indicate one standard deviation.

9.2.4. Water content with morphology

Figure 9.6 shows variation in water content with morphology. There is no apparent correlation between morphology type and water content. This supports the idea that water content is primarily controlled by pressure, and therefore, depth.

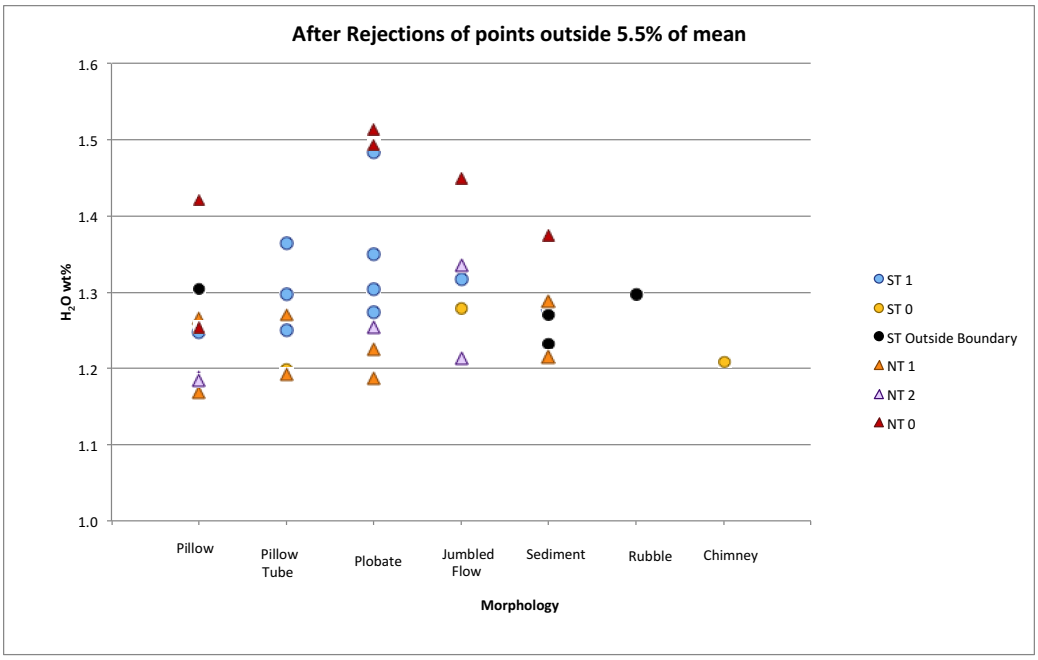

Figure 9.6. comparison of H_2O wt.% with morphology type.

9.3. Magma history: parent melts, mixing, and fractional crystallization

As addressed in section 9.1, MELTS can be used to determine how different parent melts, fractional crystallization, and mixing can cause the variation seen within and between eruptions; this, along with water content, is vital for understanding magma history. Figure 9.7 shows two chosen MELTS models (models E3 and E4) compared with all eruption groups from dives FK171110-S98 and S99, as well as North Tafu dredge samples from expedition KM1024 in December 2010, North Tafu camera tow rock samples from expedition KM1008 in May 2010, and Puipui samples from dives J415 and J416 on expedition TN234 in May 2009.

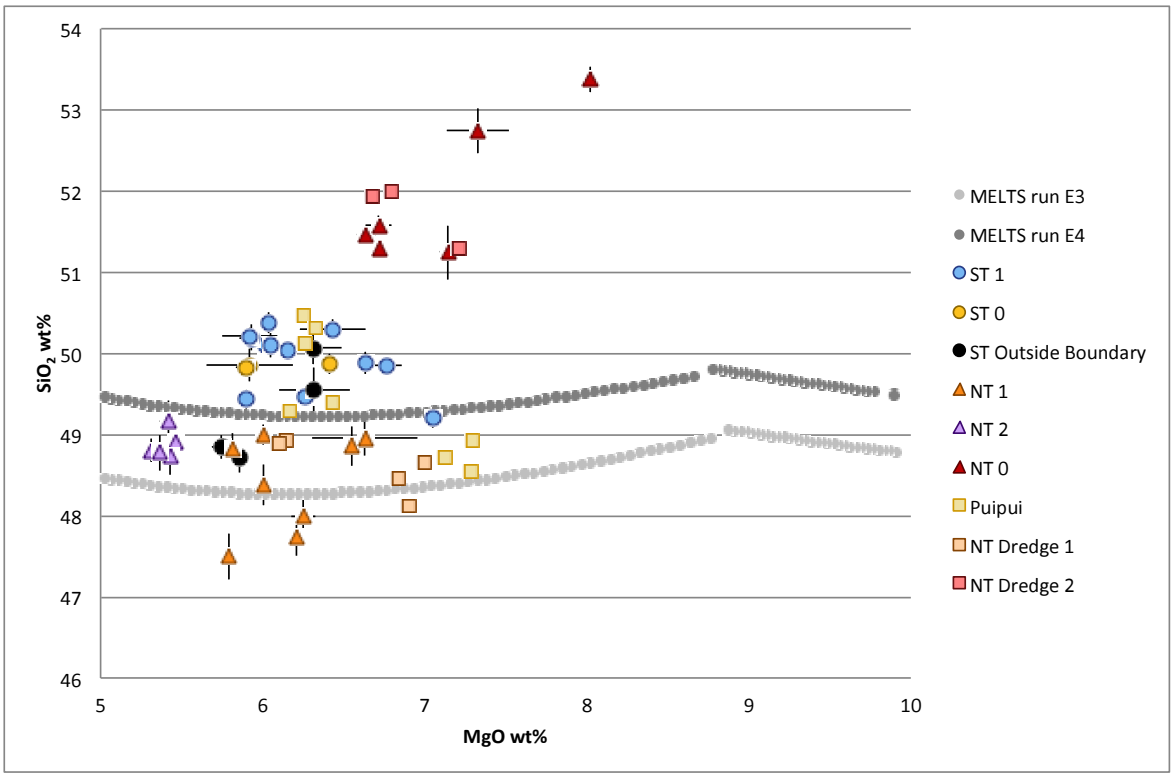

Figure 9.7a.

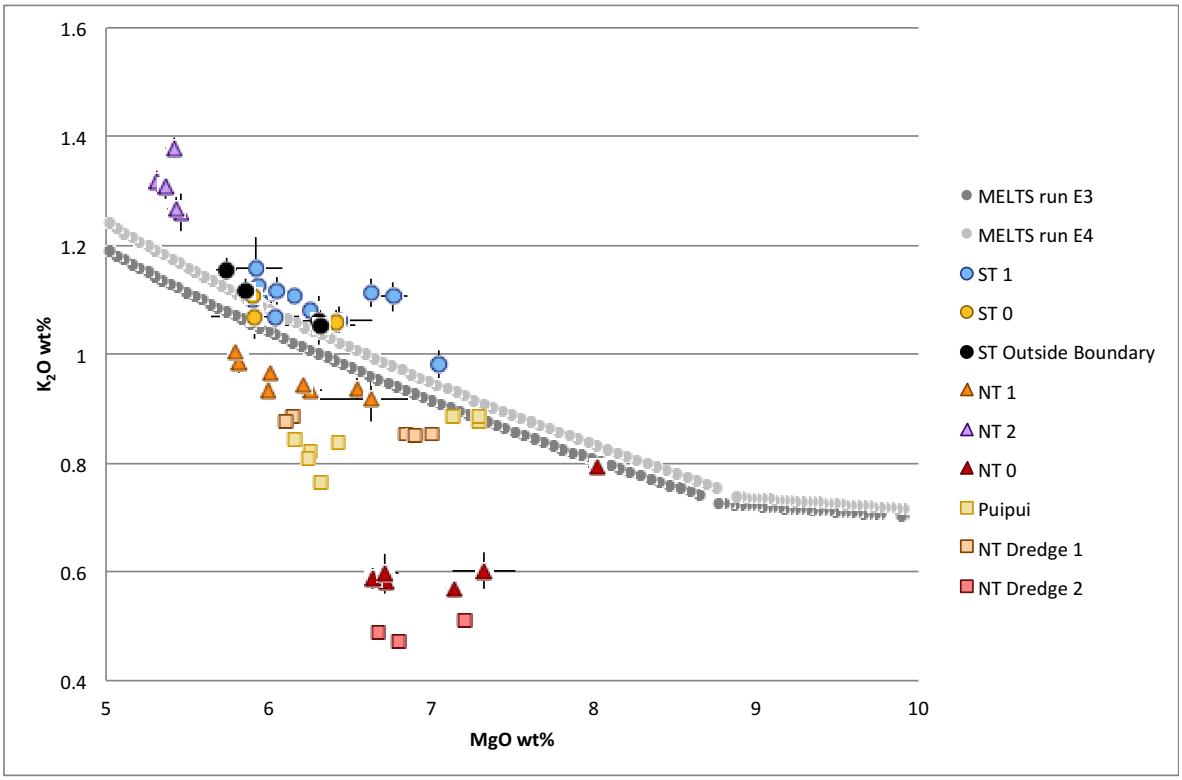

Figure 9.7b

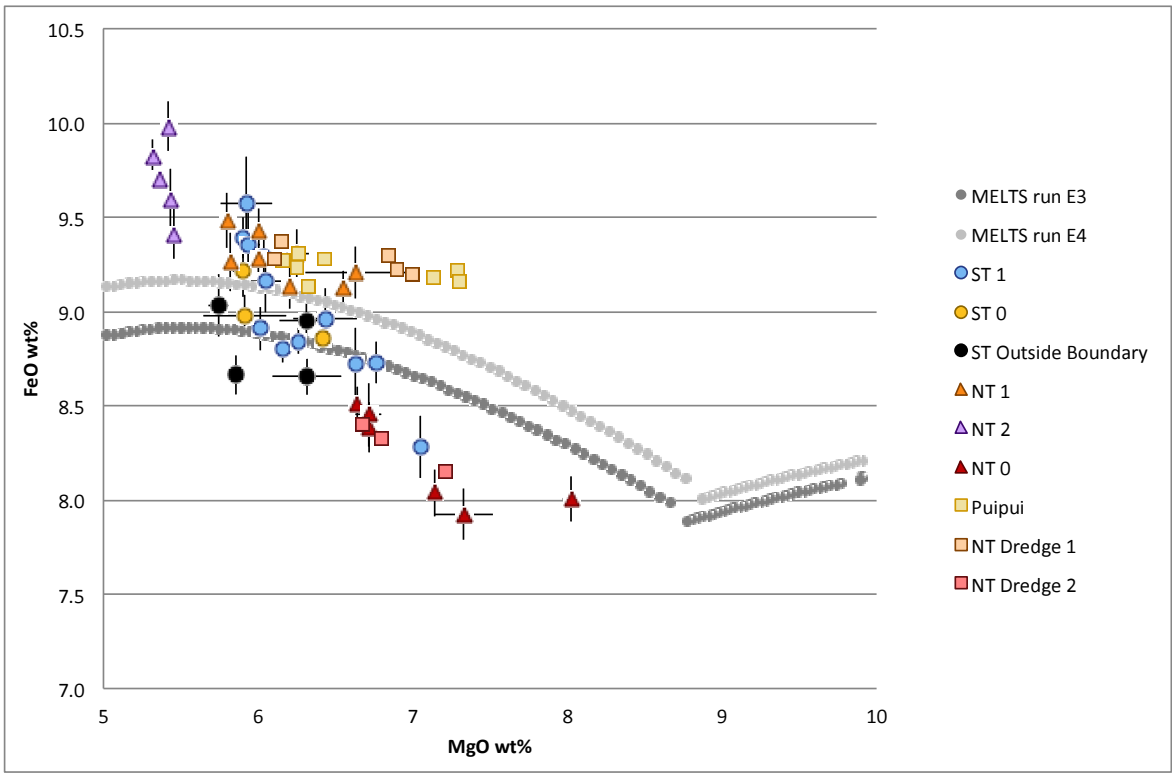

Figure 9.7c

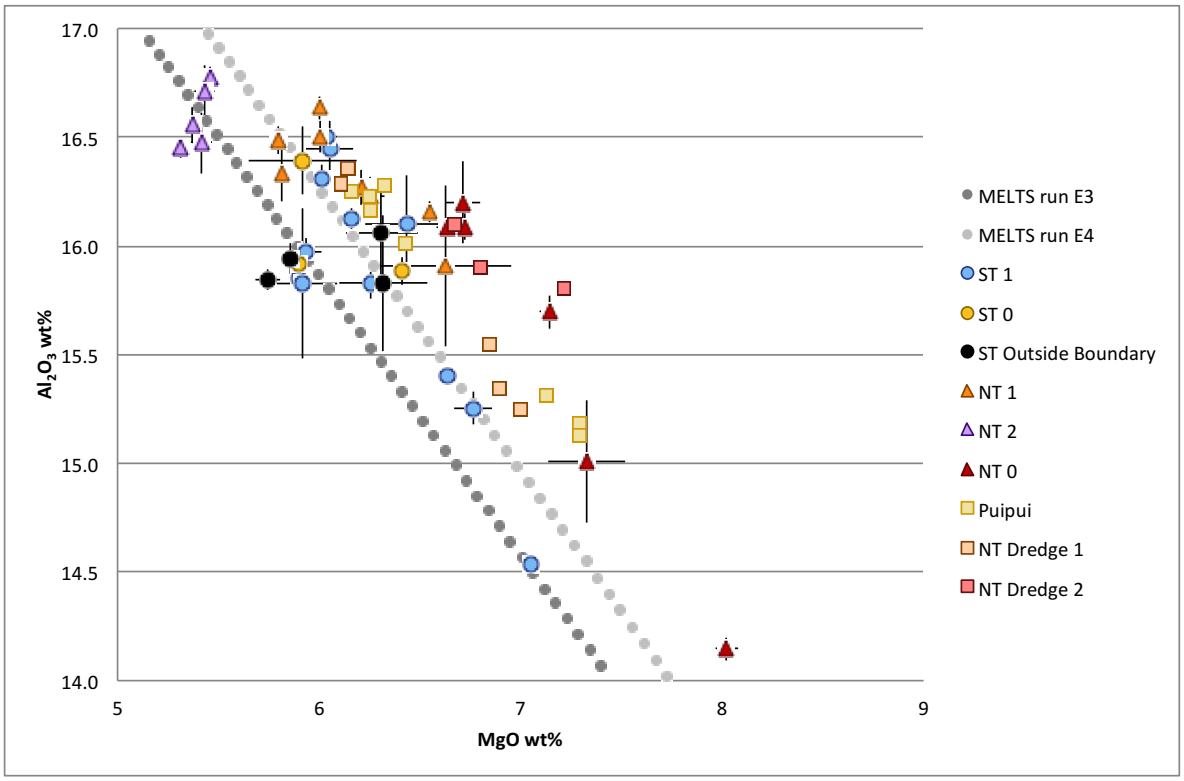

Figure 9.7d

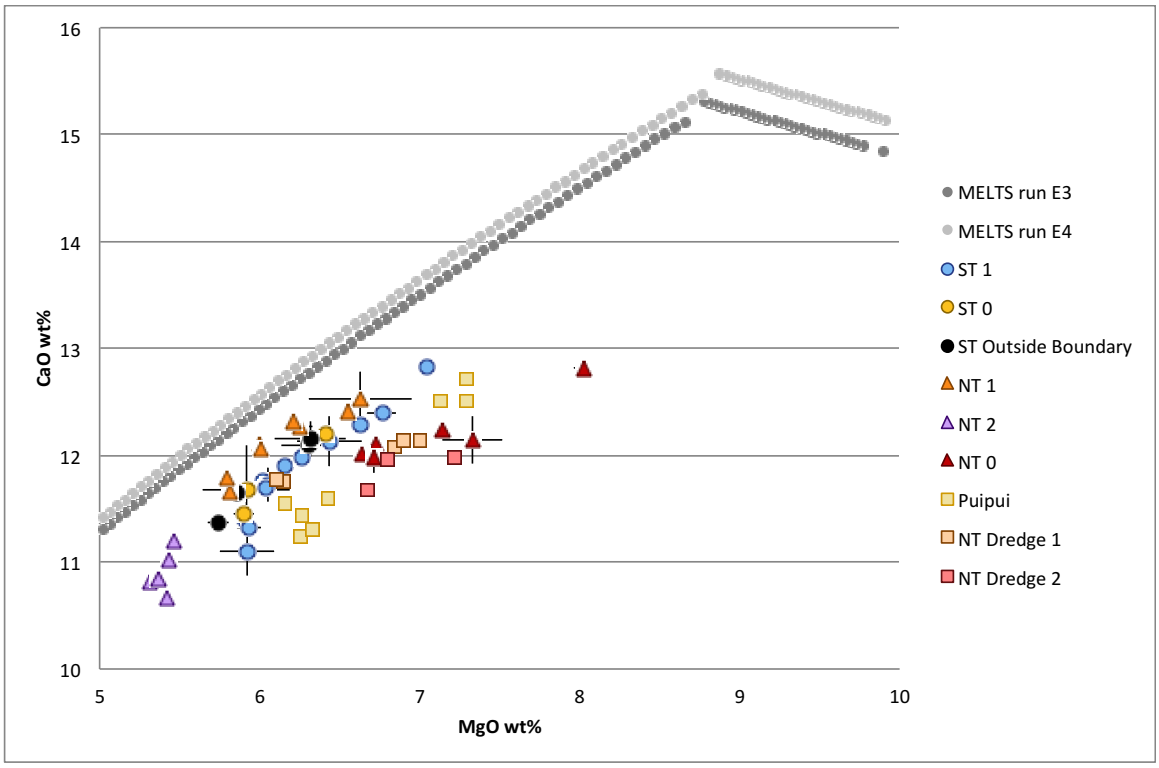

Figure 9.7e

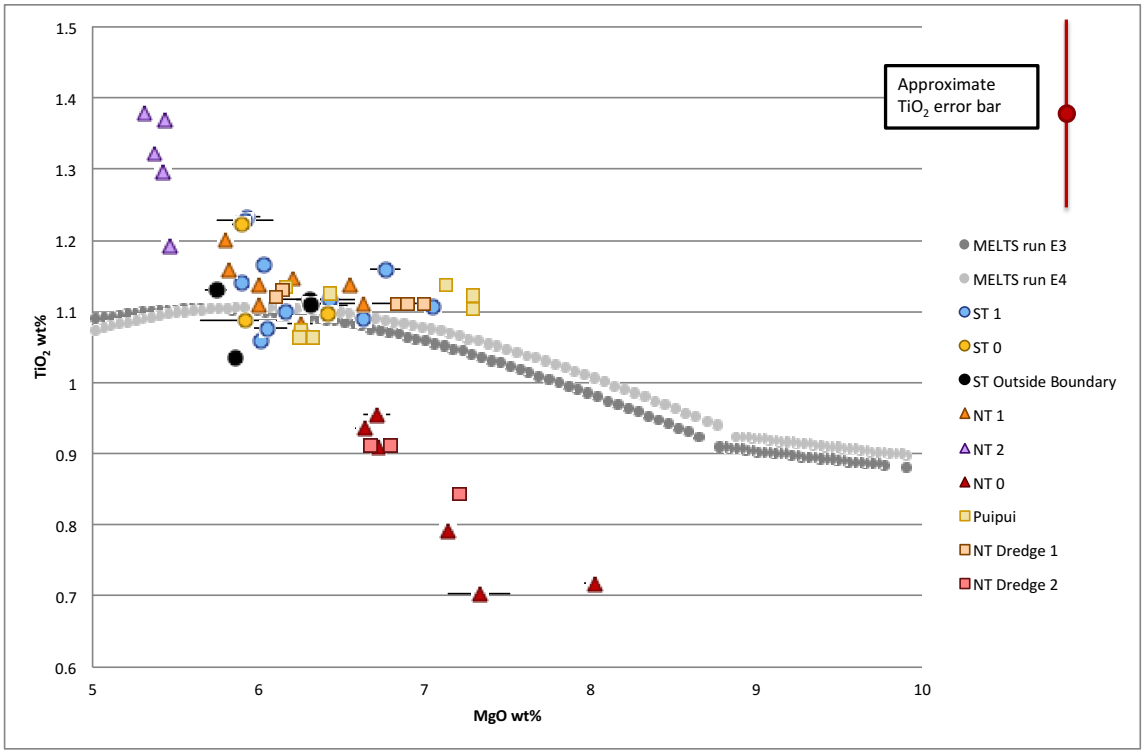

Figure 9.7f.

Figure 9.7. MgO wt.% and wt.% of various oxides of samples grouped by suspected eruption. Error bars indicate one standard deviation. "Puipui" group represents rock samples collected on dives J415 and J416 on expedition TN234 in May 2009. NT Dredge 1 and NT Dredge 2 represent rock samples collected on two dredges during expedition KM1024 and one camera tow during expedition 1008. Their grouping as NT Dredge 1 and NT Dredge 2 is determined by their similar major element composition, not their method or timing of collection.

As introduced in sections 9.1 and 9.2, examining modeled differentiation paths and solubility of water at different depths can provide insight on the history of the magmas that created the rock samples collected. In investigating the magma history of these samples, there are three main processes at play: parent melt composition, fractional crystallization, and magma mixing. Using these MELTS models, I will be looking for evidence of these processes occurring in the Tafu and Puipui eruptions and interpret if these processes indicate shared magma history between the eruptive groups.

Major element compositions initially indicated that the NT 2 eruption could have evolved from the same melt as the NT 1 eruption (section 9.1). This hypothesis is supported by the MELTS differentiation trends in SiO_2 and in FeO for lower FeO NT 2 rock samples. However, the NT 2 eruption group does not lie directly along the differentiation trend for all other major element oxides (i.e., K_2O, Al_2O_3, CaO, TiO_2). The eruptive groups have similarities but are not similar enough to have fractionated from the exact same parent melt. Instead, the two eruption groups' compositions could represent a similar or same parent melt, but with a second magma composition mixing with residual melt prior to the NT 2 eruption. This would help account for variance from the expected differentiation trends. This idea is compatible with the story told by the water content in both eruptions. The NT 2 eruption has the lowest water content of all eruptions relative to its depth (Figure 9.2); recall that a situation that would allow for this low water content with depth would be the magma rising to a shallow depth within the edifice of Tafu, then migrating downrift and

erupting in its final location where the erupted lava would be undersaturated for its depth. A portion of the same parent magma that fed the NT 1 eruption could have migrated to a shallow depth within Tafu where it was able to degas for several years. Sometime before the NT 2 eruption in 2010-2017, a new magma could have been injected, mixed with the parent magma, and erupted downrift as the NT 2 lava. Crystal zoning shown in backscattered electron images (Figure 9.8) supports this theory, as a varying melt composition caused by mixing would cause slightly different compositions in rims of crystals as they grow.

This situation presents three possibilities for Tafu's magma system: one case in which lava rises beneath the summit and is transported downrift where it erupts, a second case in which lava rises directly beneath the rift zones where it is erupted, or a third case that is some combination of the two. It is not completely known which of these cases is happening at Tafu, but the geochemical evidence provided by the NT 2 samples suggests that magma can rise within Tafu, degas, and continue downrift where it erupts. This would make case one or three most probable at Tafu.

South Tafu, however, behaves much differently from North Tafu with respect to magma history and mixing. The major element compositions of ST 0 and ST Outside Boundary, as well as their water content, overlap with that of ST 1 in nearly every element. The only exceptions are S98-R03 and -R04 being about 0.50 wt.% low in SiO_2 (Figure 9.7a), and S98-R04 being low in FeO relative to its wt.% MgO (Figure 9.7c). There is no substantial evidence to prove that these samples came from the same parent melt or magma as the ST 1 eruption; however, all of these rocks collected from South Tafu on average have remarkably similar compositions. This sets South Tafu apart from North Tafu,

whose three eruptions are significantly more heterogeneous and show variation in the types of lavas erupted on Tafu's northern rift zone. The homogeneity of South Tafu suggests that magmas supplying eruptions at South Tafu could be fairly constant in composition. Alternatively, if this is not the case and parent melts vary in composition at South Tafu, the mixing at South Tafu would need to be complete and result in homogeneous lava compositions. Crystals in the South Tafu rock and sediment samples show some crystal zoning (Figure 9.9), though to a lesser extent than the North Tafu samples. This indicates that there could be some mixing at South Tafu, but it would result in significantly more homogeneous erupted lavas due to more complete mixing.

However, it is known that not all Tafu lavas, north and south, rise within the center of Tafu, mix, and continue downrift. If this were the case, we might expect the two 2010-2017 eruptions (ST 1 and NT 2) to look more similar in their major element compositions. Instead, they overlap in some compositions like FeO, Al_2O_3, TiO_2, and CaO, but not in SiO_2 or K_2O. This is significant because, as mentioned previously, K is highly incompatible and is a good indicator for parent melt composition. This discrepancy in K_2O implies that the two 2010-2017 eruptions did not come from the same parent melt, did not undergo the same eruptive processes, and did not mix at a shallow depth. This is supported by the saturation of the ST 1 rocks at their depth of eruption, which indicates they did not degas at a shallower depth of 1436-1732 meters as the NT 2 magma may have.

Moving on to the rock samples not collected during dives FK171110-S98 and S99, the eruptive group NT Dredge 1 consists of rock samples collected on both the KM1008 camera tow and the KM1024 dredge 2 (major element composition data can be found in Table 9.3). NT Dredge 1 and NT Dredge 2 together make up all rock samples collected on

Tafu prior to the FK171110 expedition. They are grouped into NT Dredge 1 and NT Dredge 2 by geochemistry rather than by collection method or exact location of collection since all rocks were retrieved by dredge or camera tow. NT Dredge 1 is most similar in composition to the rock samples from NT 1. There are two MgO groups within NT Dredge 1: a high MgO group and a low MgO group. If grouped with the NT 1 eruption, the high MgO group extends the MgO range by 0.37 wt.% to a high MgO end member of 7.00 wt.%. These high MgO samples represent more primitive, less differentiated samples of the same parent magma for NT 1. The NT Dredge 1 major element compositions appear to lie along MELTS differentiation trends for nearly every major element composition. The only exception is in CaO (Figure 9.7e), where the NT Dredge 1 group is approximately 0.50-0.75 wt.% lower than the NT 1 group in wt.% CaO. However, there is no standard deviation data for the NT Dredge 1 rock samples from which error can be determined, as these rock samples had major element compositions measured using a different microprobe in a different location with a different user. All of these variables could account for this discrepancy in wt.% CaO. Despite this divergence, the NT Dredge 1 group will be considered to be from the same eruption and same parent melt as the NT 1 eruption. This is congruent with known timing of the NT 1 eruption, as the NT Dredge 1 rocks were collected in May and December of 2010, well after their eruption sometime between 2006 and 2008. There is no water content data for the NT Dredge 1 rock samples, so comparisons cannot be evaluated with respect to water content.

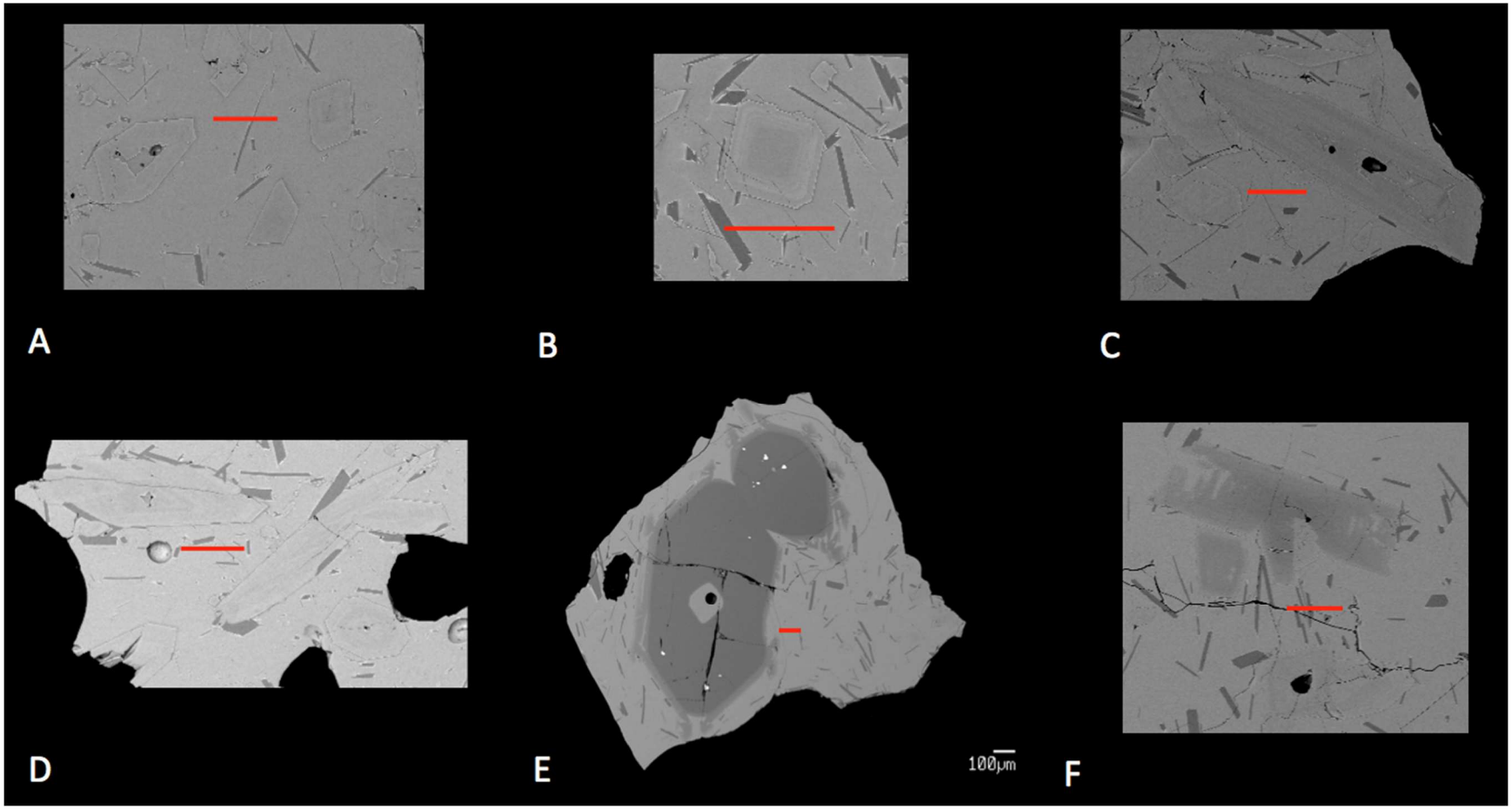

Figure 9.8. Crystal zoning in NT 2 rocks. Red lines are 100 microns in length for scale. A. S99-R4 glass chip 3. B. S99-R05 glass chip 4. C. S99-R06 glass chip 2. D. S99-R07 glass chip 2. E. S99-R08 glass chip 1. F. S99-R08 glass chip 4.

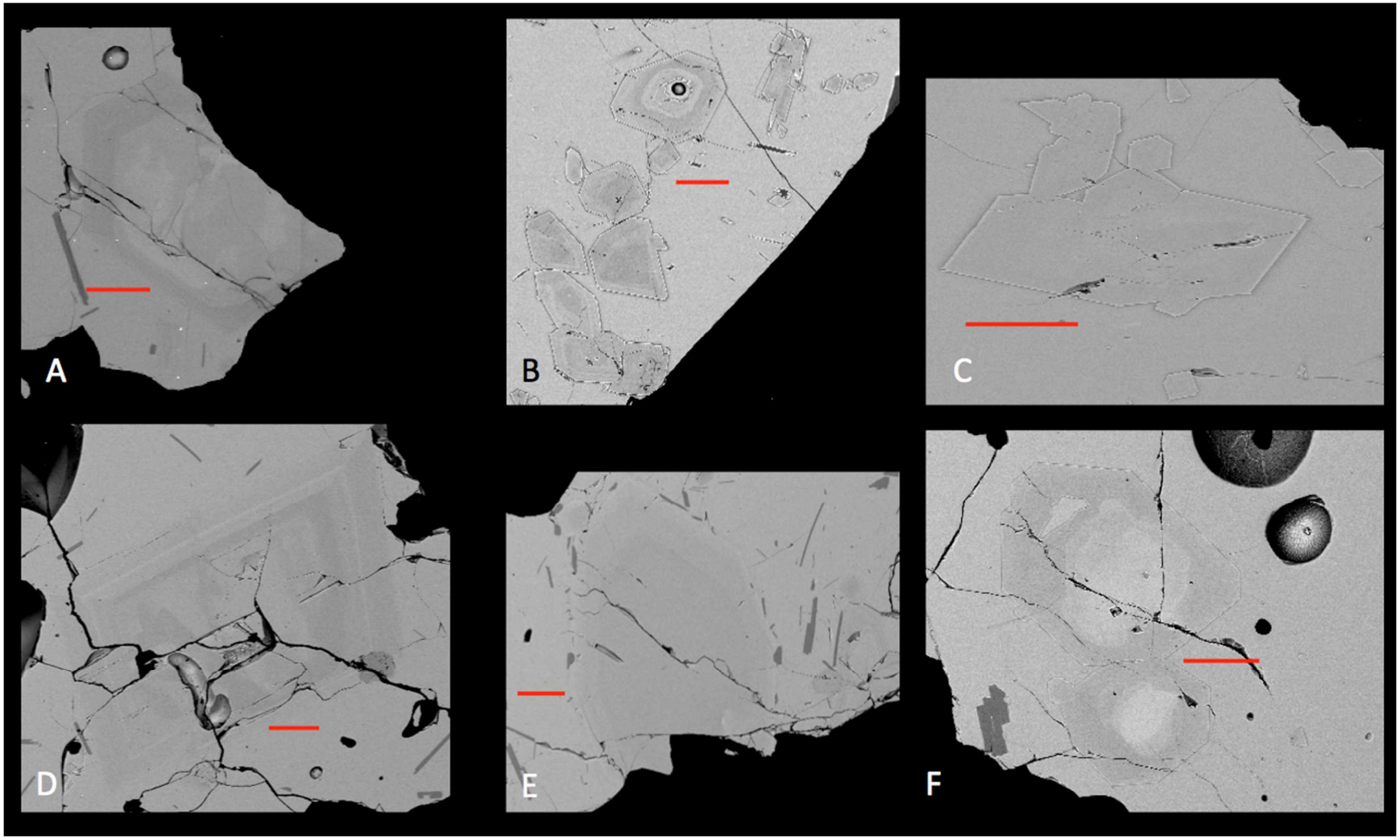

Figure 9.9. Crystal zoning in South Tafu rocks. Red lines are 100 microns in length for scale. A. S98-R03 glass chip 3. B. S98-R05 glass chip 4. C. S98-R12 glass chip 5. D. S98-S13 glass chip 10. E. S98-R14 glass chip 2. F. S98-R18 glass chip 3.

Sample Name	Eruption Group	SiO_2 Wt.%	TiO_2 Wt.%	Al_2O_3 Wt.%	FeO Wt.%	MnO Wt.%	MgO Wt.%	CaO Wt.%	Na_2O Wt.%	K_2O Wt.%	P_2O_5 Wt.%	Total
KM1008 CT07-1A	NT Dredge 1	48.92	1.13	16.36	9.37	0.15	6.14	11.76	3.49	0.89	0.53	98.74
KM1008 CT07-1B	NT Dredge 1	48.89	1.12	16.28	9.28	0.17	6.11	11.78	3.38	0.88	0.52	98.41
KM1024 D2-Rock01	NT Dredge 1	48.65	1.11	15.25	9.20	0.18	7.00	12.14	3.59	0.85	0.58	98.55
KM1024 D2-Rock02	NT Dredge 1	48.47	1.11	15.55	9.30	0.15	6.84	12.08	3.54	0.85	0.55	98.44
KM1024 D2-Rock04	NT Dredge 1	48.12	1.11	15.35	9.23	0.18	6.90	12.15	3.49	0.85	0.58	97.95
KM1024 D1-Rock01	NT Dredge 2	51.93	0.91	16.10	8.40	0.15	6.67	11.67	2.25	0.49	0.27	98.84
KM1024 D2-Rock03	NT Dredge 2	51.29	0.84	15.80	8.15	0.15	7.21	11.97	2.18	0.51	0.24	98.35
KM1024 D2-Rock05	NT Dredge 2	52.00	0.91	15.90	8.33	0.15	6.80	11.96	2.25	0.47	0.22	99.00
J2-415-R01	Puipui	49.41	1.13	16.01	9.28	0.17	6.43	11.59	3.00	0.838	0.43	98.79
J2-415-R02	Puipui	50.13	1.07	16.16	9.31	0.16	6.26	11.44	3.03	0.82	0.40	98.79
J2-415-R03	Puipui	50.47	1.06	16.23	9.23	0.18	6.25	11.23	2.97	0.81	0.47	98.91
J2-415-R06a	Puipui	50.31	1.06	16.28	9.13	0.24	6.32	11.31	2.99	0.764	0.32	98.91
J2-415-R7	Puipui	48.55	1.12	15.19	9.22	0.18	7.29	12.72	2.97	0.875	0.44	98.63
J2-415-R8	Puipui	48.92	1.10	15.13	9.16	0.18	7.29	12.51	2.98	0.88	0.47	98.63
J2-415-R18	Puipui	48.72	1.14	15.31	9.18	0.18	7.13	12.51	3.07	0.885	0.45	98.29
J2-415-R20	Puipui	49.30	1.13	16.25	9.27	0.17	6.16	11.55	3.19	0.84	0.41	98.29

Table 9.3. Major element compositions of all Tafu rock samples not collected during the FK-171110 S98 and S99 dives as well as Puipui samples relative to this study. Within the Tafu sample names, KM_____ refers to the expedition during which the rocks were collected. "CT-___" refers the camera tow number, while "D-___" refers to the dredge number. KM1008 samples were collected in May 2010, while KM1024 samples were collected in December 2010. "J2-415" in the Puipui samples refers to dive 415 made on the ROV Jason2 on research expedition TN 234 in May 2009.

Likewise, the NT Dredge 2 rock samples show similarities in major element composition to the NT 0 group. Major element compositions can be found in Table 9.3. The NT Dredge 2 rock samples lie on the higher end of wt.% MgO for the Tafu samples, and the NT 0 group has the highest wt.% MgO of all rock samples. Major element compositions in NT Dredge 2 overlap with the NT 0 in wt.% SiO_2, FeO, Al_2O_3, CaO, and TiO_2 (Figure 9.7, b, d-f). The wt.% K_2O for NT Dredge 2 is about 0.05-0.10 wt.% lower than that of the NT 0 Group. Again, the NT Dredge 2 rock samples were measured for major element composition on a different microprobe by a different user, and do not have data for error. Because of these similarities, the NT Dredge 2 will be considered as part of the NT 0 eruptive group. The eruption or eruptions of these rocks and sediments occurred sometime before 2006; the collection of the NT Dredge 2 rocks was in December 2010, which makes it consistent with the timeline of eruptions. Again, water content data is not available for the NT Dredge 2 rocks, so no comparisons will be made with regards to water content.

9.4. Puipui

As stated in section 6.5, cruise TN234 visited Puipui, Tafu's next door neighbor, during two dives and collected rock and sediment samples from its 2008 eruption. 7 of these rock samples are shown along with major element compositions of Tafu's eruptions in Figure 9.7, and their major element compositions are listed in Table 9.3. The Puipui samples are divided into two different geochemical groups by their MgO content: J2-415-R01, R02, R03, and R06A are the low MgO group, and J2-415-R07, R08, and R18 are the higher MgO group.

The low MgO group overlaps with the ST 1 eruption in SiO_2, FeO, Al_2O_3, and TiO_2; it overlaps with the NT 1 eruption in FeO, Al_2O_3, and TiO_2 compositions. The low MgO group is similar to the ST 1 compositions in several ways but does not overlap in composition with it in K_2O, a main indicator for parent melt similarities. It does not share any similarities with the NT 2 eruption.

The higher Mg group does not overlap with any of the Tafu groups except with ST 1, but only in TiO_2. However, it does lie along remarkably similar differentiation trends as NT 1 for all elements other than CaO with respect to MELTS model E3. This suggests that NT 1 could have differentiated from the same melt that erupted at Puipui. If this is the case, the NT 1 magma would have needed to differentiate within an incredibly short time frame (<1 year), which does not seem plausible. If stretching the imagination, a similar parent melt composition may have fed both eruptions but been injected at different times. An earlier parent melt injection at Tafu would allow for the NT 1 lavas to have had more time to differentiate. Finally, a single sea floor rifting event could have triggered the eruption of both Tafu and Puipui in the 2006-2008 time frame. A simpler and more probably explanation for these similarities could be that Tafu and Puipui's close geographic proximity (approximately 1km distance) allows the two volcanoes to receive similar parent melt compositions from the mantle.

The similarities in major element compositions between Puipui's low MgO group and the ST 1 lavas indicate that these separate volcanoes are capable of erupting very similar lavas. Puipui is also located less than one kilometer south-southeast of Tafu, erupting during nearly the same time frame (2008) as Tafu. However, the discrepancy in wt.% K_2O prevents the lavas from having the exact same parent melt. These differences in

lava compositions reinforce that the individual eruptions of Tafu and Puipui are probably not coming from one singular, large, homogeneous magma chamber that is continuously being fed from the mantle. Instead, it seems more likely that small portions of melt come up individually from a heterogeneous mantle across the two volcanoes, and their heterogeneities are preserved in the final lava compositions.

Though Puipui is similar to Tafu in some compositions and differentiation trends, it is not likely that Puipui is connected to Tafu by magma storage or plumbing, nor does it receive the exact same parent melt injections. However, the similarities in composition as well as timing of eruptions cannot be ignored and indicates that the same mantle compositions could be supplying eruptions at both Tafu and Puipui.

9.5. Summary

Tafu and Puipui have been shown to erupt a wide variety of different compositions across just 11 years. Those eruptions, their compositions, their relations to each other, and their significance will be reviewed here. Table 9.4 consists of a brief summary of each eruption group as well.

The eruptive products of South Tafu (ST 1, ST 0, and ST Outside Boundary) are similar in terms of major element composition and are therefore grouped together. These lavas range from 5.74 to 7.05 wt.% MgO and all lie along similar differentiation trends. Geochemistry of the South Tafu samples indicates that South Tafu magmas either originate from similar parent melts compositions or mix homogeneously before eruption. Their water content spans 1.198 to 1.484 wt.% H_2O when using the >5.5% variation rejection procedure. These lavas are slightly undersaturated in water for their depth, but their water content with pressure follows the trend projected by VolatileCalc 2.0 (Newman and

Lowenstern, 2002) as expected. The only exceptions are S98-S01, S02, and R03, which are significantly more undersaturated and do not fit this projected trend. However, this is likely because they were collected from a location deeper than their actual depth of eruption and degassing.

The NT 1 eruption group from 2006-2008 has similarities to the NT Dredge 1 group, which overlaps it in nearly every major element composition. For this reason, they will be grouped together. The only major difference in their composition is in CaO, in which the higher MgO group from NT Dredge 1 is about 0.50-0.75 wt.% low in CaO relative to their MgO content. This could be because the NT Dredge 1 rocks were analyzed for major element composition using a different microprobe at a different location than the FK171110 Tafu rocks and sediments. This group erupted in the time between the 2006 KORDI survey and the 2008 TN227 expedition; it spans 5.80 to 7.00 wt.% MgO when including NT Dredge 1. There is no water content data for the NT Dredge 1 group, but the NT 1 eruption group has water contents between 1.15 and 1.29 wt.% H_2O (once again using the >5.5% variation from mean rejection). These rocks are undersaturated in water for their depth, but also follow the projected trend for water content with depth predicted by VolatileCalc 2.0 (Newman and Lowenstern, 2002).

The NT 2 is the most differentiated eruption group of all examined in this study and covers a narrow range in MgO of just 5.32 to 5.46 wt.% MgO. This narrow range in MgO but larger variation in all other oxides makes it difficult to place this group along any differentiation trend. However, it is most similar in differentiation to the NT 1 eruption group. The two groups lie along similar differentiation trends in SiO_2, FeO, and CaO, but not in K_2O, TiO_2, or Al_2O_3. The NT 2 eruption group has the lowest water content of all eruptive

groups, with water content between 1.19 and 1.34 wt.% H_2O using >5.5% variation from mean rejection criteria. This makes these lavas significantly undersaturated for their depth, especially compared to all other eruptive groups. By combining this with the known major element compositions and differentiation trends discussed above, it is believed that the magma supplying the NT 2 eruption was the same, or similar to, melt from the NT 1 eruption. At some point, melt remaining from the NT 1 eruption could have mixed with a second, new parent melt and risen to a shallower depth to degas. After this, it was transported downrift and erupted at its final depth of about 1900-2000 meters below sea level.

The NT 0 group spans a wide range of major element compositions and is a grab bag of samples older than 2006; due to consistent similarities in major element compositions, the NT Dredge 2 group is included with this NT 0 eruptive group. These lavas were erupted sometime before the KORDI survey conducted in 2006 and may have come from different eruptions. Together, their MgO content ranges from 6.64 to 8.02 wt.% MgO. The water content of the NT 0 group is unique in that it is significantly supersaturated for its depth. This could be due to not having enough time to degas before solidifying or could have been caused by something compositionally that has not been detected or investigated during this study like rehydration.

The North Tafu samples differ from each other much more than the South Tafu samples. This heterogeneity in the North Tafu samples indicates that if there is magma mixing occurring as we suspect, there is no complete homogenization of mixing occurring. This causes the variation between eruption groups that is unique to the north ridge of Tafu. It is possible that South Tafu either receives a consistent melt composition from the mantle,

or if it receives different melt compositions, these melts mix completely and homogenize before eruption.

Lastly, the Puipui eruptive group has two groups that are compositionally distinct from each other: one with low MgO (6.16-6.43 wt.% MgO), and one with high MgO (7.13-7.29 wt.% MgO). The high MgO group appears to be a more primitive composition along a similar differentiation trend as the NT 1 lava in all major element compositions except CaO. This indicates that the magma histories of Puipui and the NT 1 eruption could be related either through crystal fractionation of a single parent melt or simply having similar parent melt compositions. Similarly, the lower MgO group overlaps with the ST 1 eruptive group in several major element compositions (SiO_2, Al_2O_3, FeO, and TiO_2). However, these groups do not overlap in K_2O, a strong indicator for parent melt compositions. Together, the low and high MgO groups of Puipui help illuminate that the compositions of lavas erupted at Tafu and Puipui are similar but not the same. It is not likely that these two volcanoes have connected magma plumbing or share a magma chamber. It is more likely that their proximity allows both to receive similar parent melt compositions from the mantle.

Eruption Group	Location	Time of Eruption	Symbol in Figures	Geochemistry	Water Content	Similar Groups?
ST 1	South Tafu	2010-2017	●	mid differentiation	undersaturated, follows trend	ST 0 ST Outside Boundary Low MgO Puipui
ST 0	South Tafu	<2006	●	mid differentiation	undersaturated, follows trend	ST 1 ST Outside Boundary
ST Outside Boundary	South Tafu	unknown	●	mid differentiation	very undersaturated for depth	ST 1 ST 0
NT 1	North Tafu	2006-2008	▲	mid differentiation	undersaturated, follows trend	High MgO Puipui by differentiation NT Dredge 1
NT 2	North Tafu	2010-2017	△	most differentiated	very undersaturated for depth	NT 1 by differentiation
NT 0	North Tafu	<2006	▲	least differentiated	supersaturated	NT Dredge 2
NT Dredge 1	North Tafu	2006-2008?	□	mid differentiation	no data	NT 1
NT Dredge 2	North Tafu	<2006?	■	least differentiated	no data	NT 0
Puipui	Puipui	2008	□	mid differentiation	no data	ST 1 in low MgO NT 1 in high MgO by differentiation

Table 9.4. Summary of features of each eruptive group. Blue text indicates suspected time of eruption by comparison to other eruptions with known eruption dates.

10. Appendices

10.1 Appendix A: Photographs of rock and sediment samples

The following photographs are of rock and sediment samples collected from Tafu during dives S98 and S99 on cruise FK171110. All black and white squares in the photographs are 1cm for scale

Figure 10.1a. Sediment S98-S01.

Figure 10.1b. Sediment S98-S02.

Figure 10.1c. Rock S98-R03.

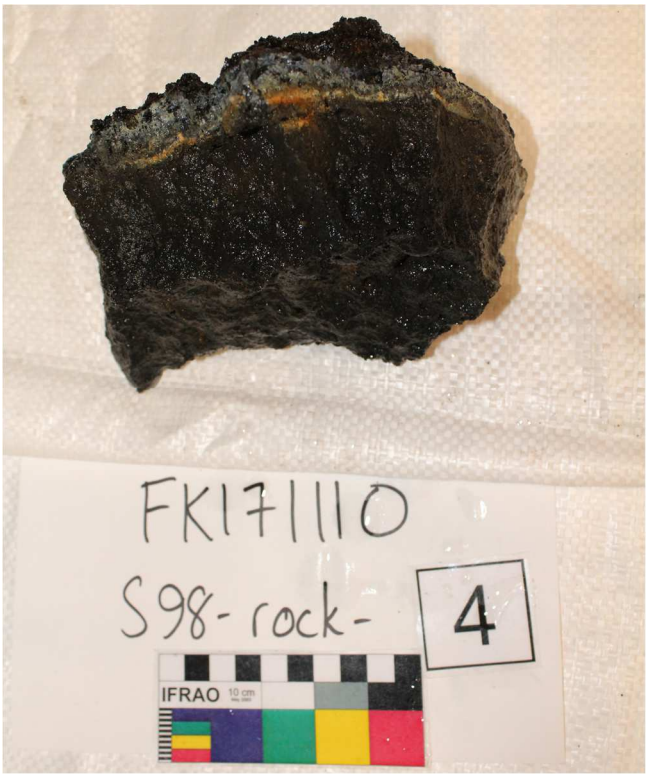

Figure 10.1d. Rock S98-R04.

Figure 10.1e. Rock S98-R05

Figure 10.1f. Sediment S98-S06.

Figure 10.1g. Rock S98-R07.

Figure 10.1h. Rock S98-R08.

Figure 10.1i. Rock S98-R09.

Figure 10.1j. Rock S98-R11.

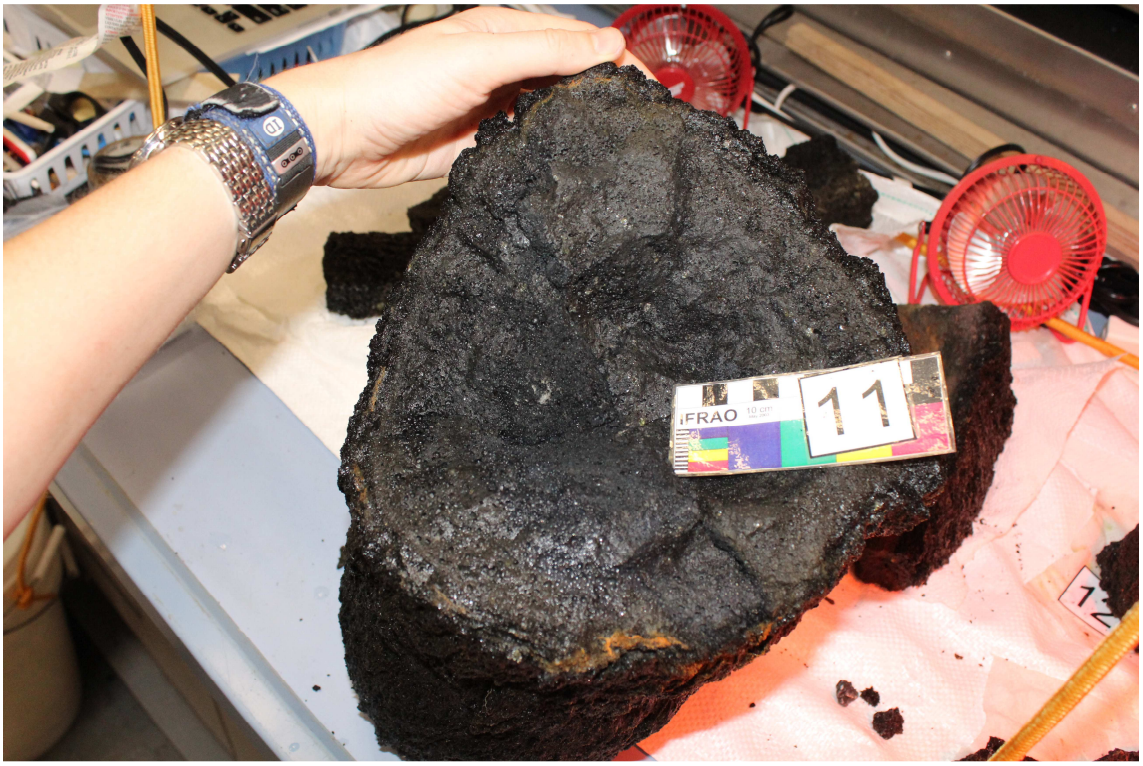

Figure 10.1k. Rock S98-R11 in cross section.

Figure 10.1l. Rock S98-R12.

Figure 10.1m. Sediment S98-S13.

Figure 10.1n. Rock S98-R14.

Figure 10.1o. Rock S98-R15.

Figure 10.1p. Sediment S98-S16.

Figure 10.1q. Rock S98-R17.

Figure 10.1r. Rock S98-R18.

Figure 10.1s. Rock S98-R21.

Figure 10.1t. Rock S98-R22.

Figure 10.2a. Rock S99-R01.

Figure 10.2b. Rock S99-R02.

Figure 10.2c. Rock S99-R03.

Figure 10.2d. Rock S99-R04.

Figure 10.2e. Rock S99-R05.

Figure 10.2f. Rock S99-R06.

Figure 10.2g. Rock S99-R07.

Figure 10.2h. Rock S99-R08.

Figure 10.2i. Sediment S99-S09.

Figure 10.2j. Rock S99-R10.

Figure 10.2k. Rock S99-R12.

Figure 10.2l. Rock S99-R12 in cross section.

Figure 10.2m. Rock S99-R13.

Figure 10.2n. Rock S99-R14.

Figure 10.2o. Sediment S99-S15.

Figure 10.2p. Rock S99-R18.

Figure 10.2q. Rock S99-R20.

Figure 10.2r. Rock S99-R21.

Figure 10.2s. Sediment S99-S25.

Figure 10.2t. Rock S99-R26.

10.2 Appendix B: Photographs of locations of sample collection

The following figures are photographs of all in-situ rock and sediment samples on dives S98 and S99 before collection.

Figure 10.3a. Sediment S98-S01 after collection to show both surface and sub-surface structure of sediments.

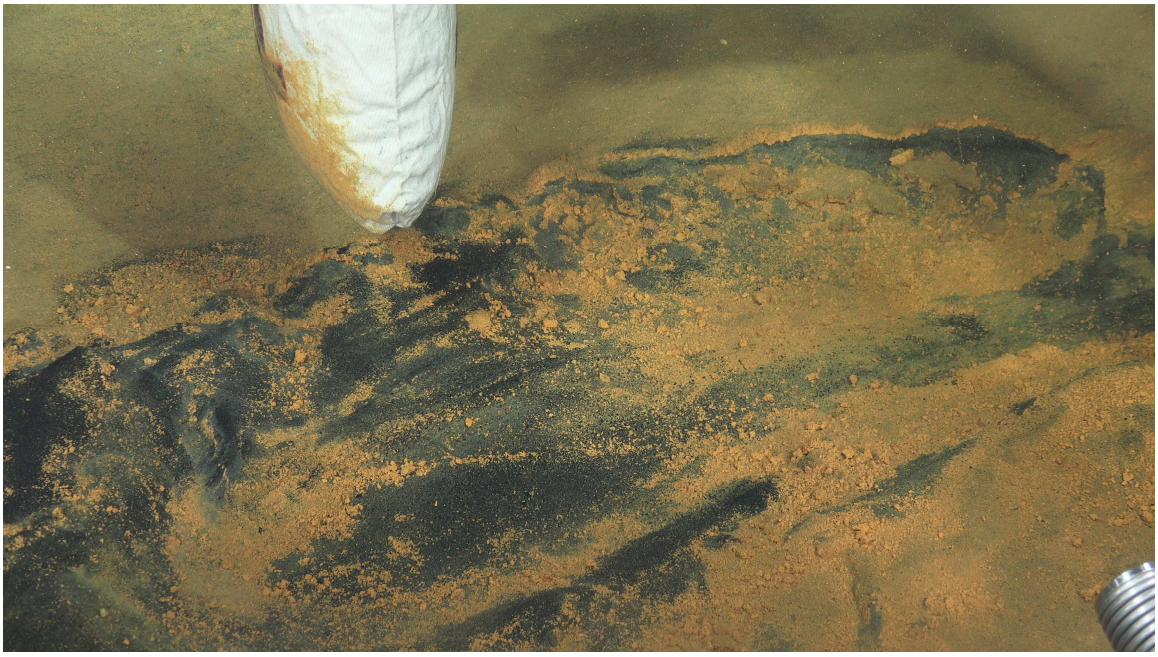

Figure 10.3b. Sediment S98-S02 after collection to show sediments below the layer of iron floc.

Figure 10.3c. Rock S98-R03.

Figure 10.3d. Rock S98-R04.

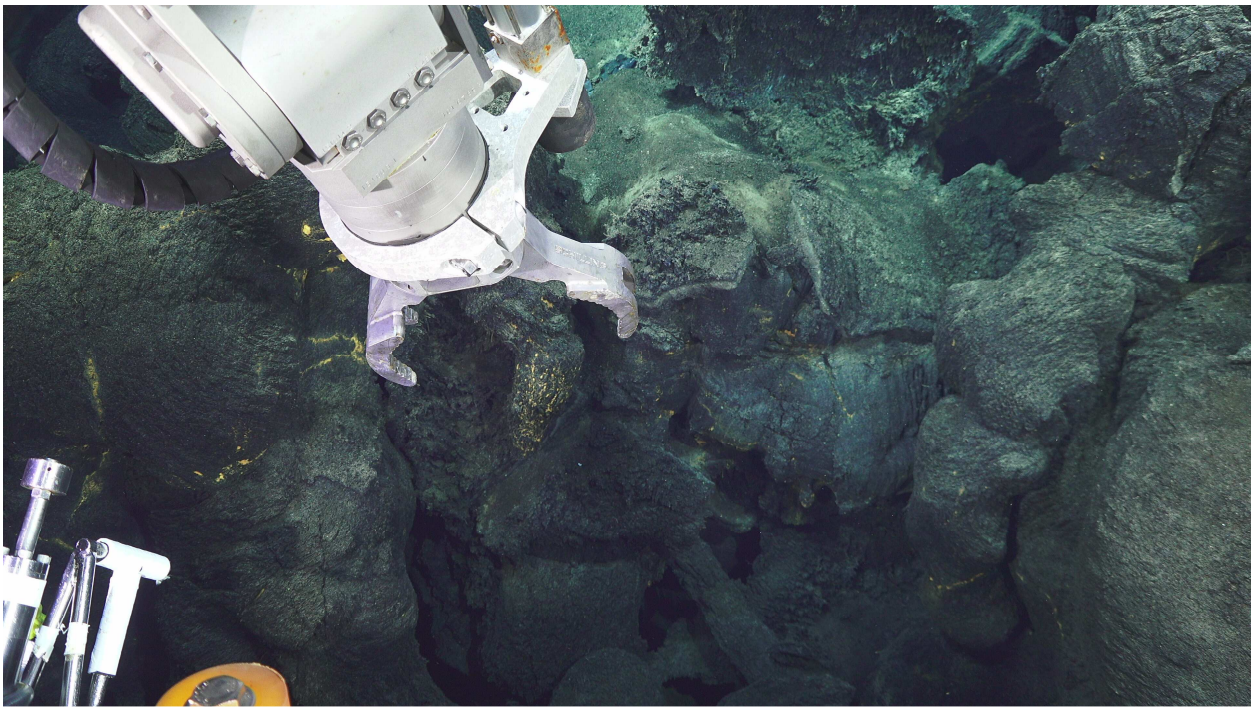

Figure 10.3e. Rock S98-R05.

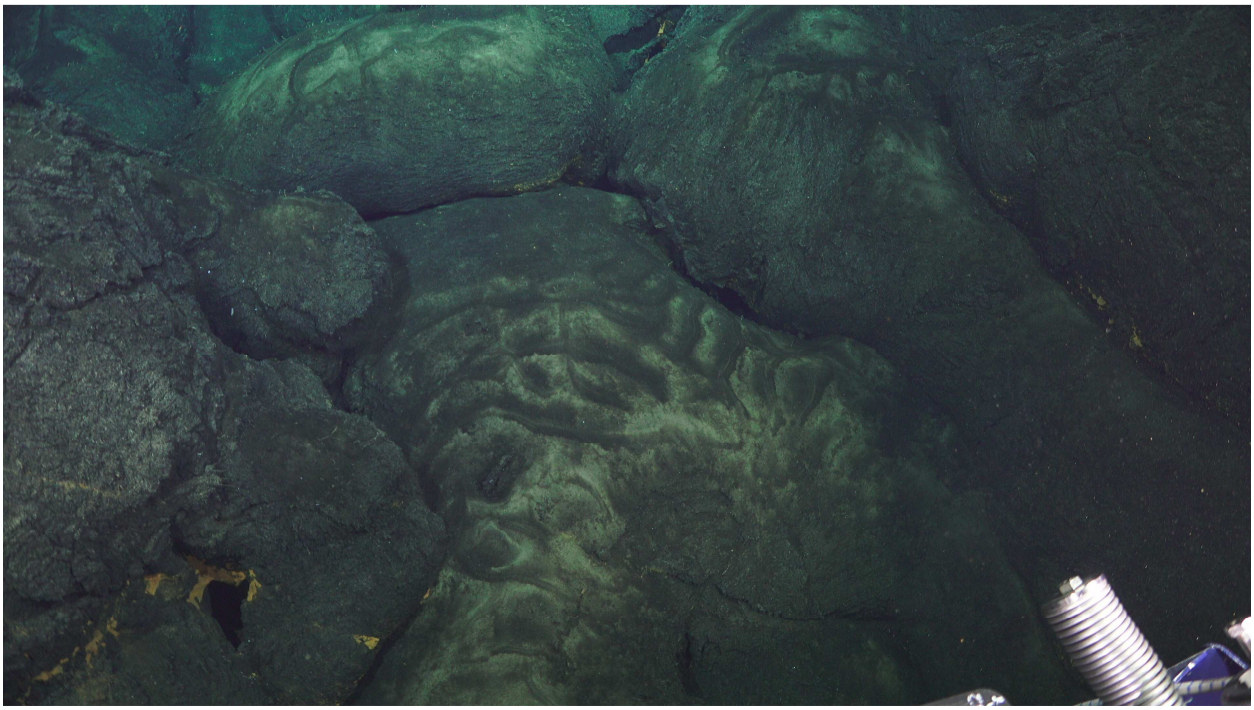

Figure 10.3f. Sediment S98-S06.

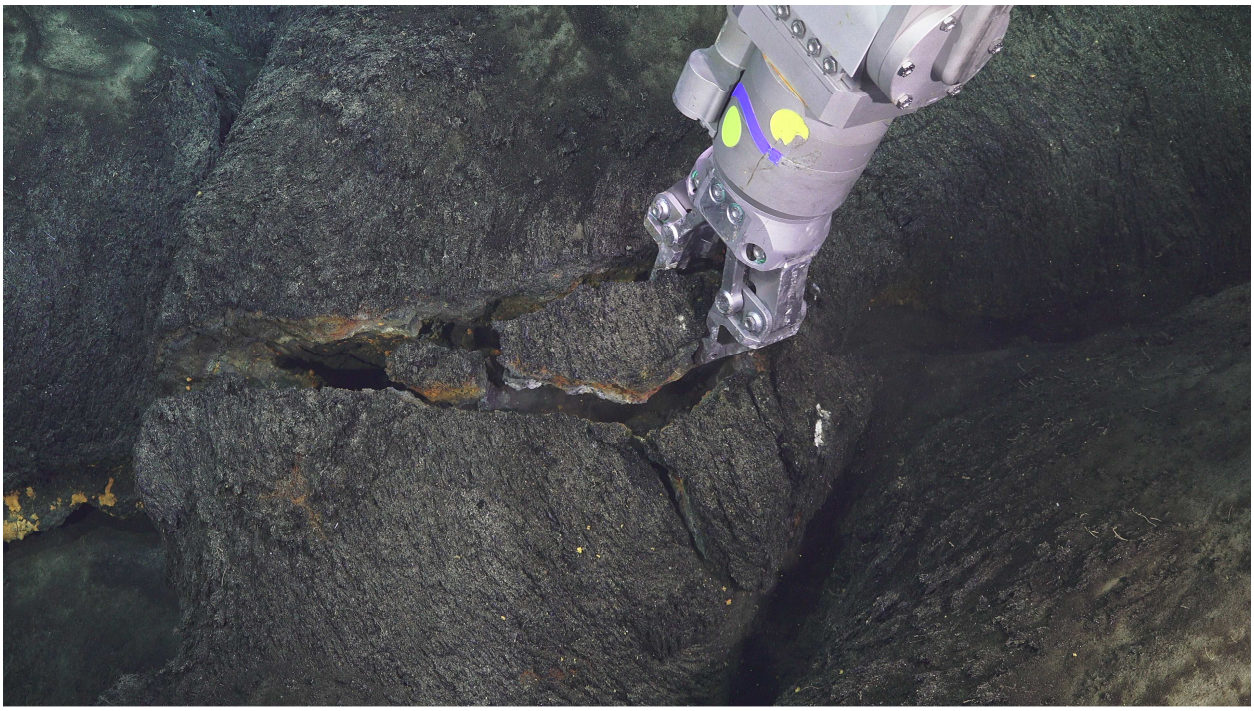

Figure 10.3g. Rock S98-R07.

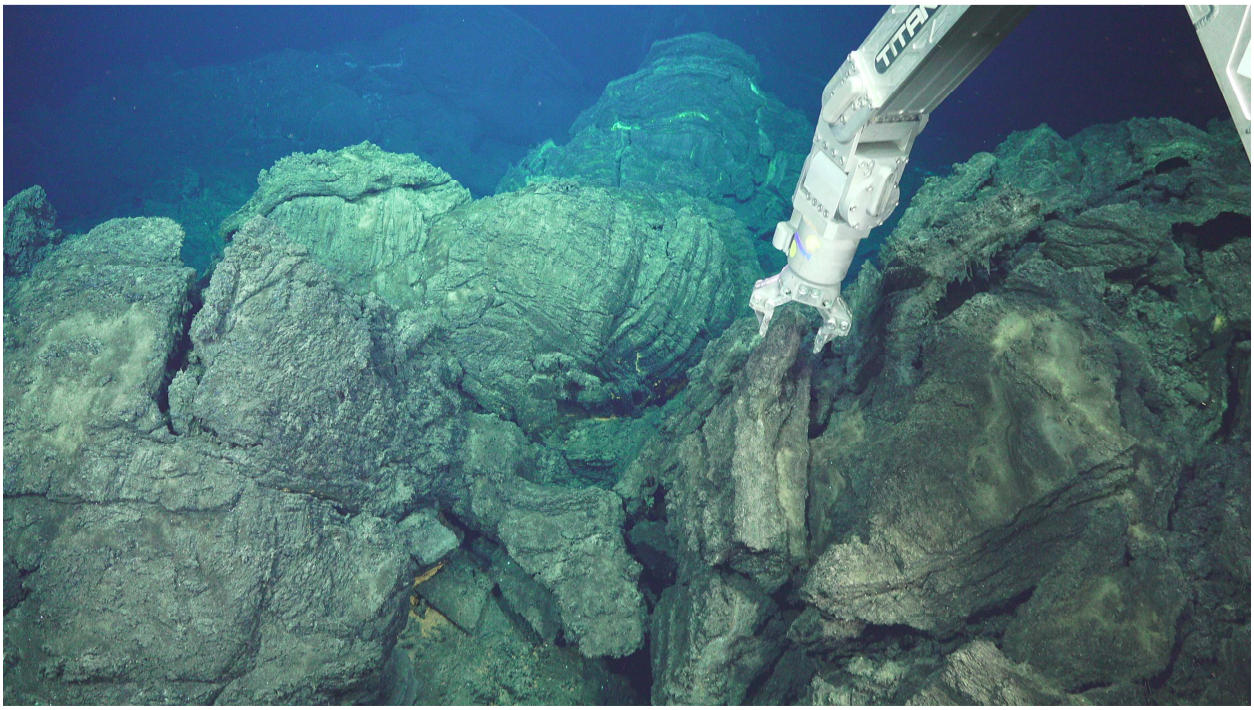

Figure 10.3h. Rock S98-R08.

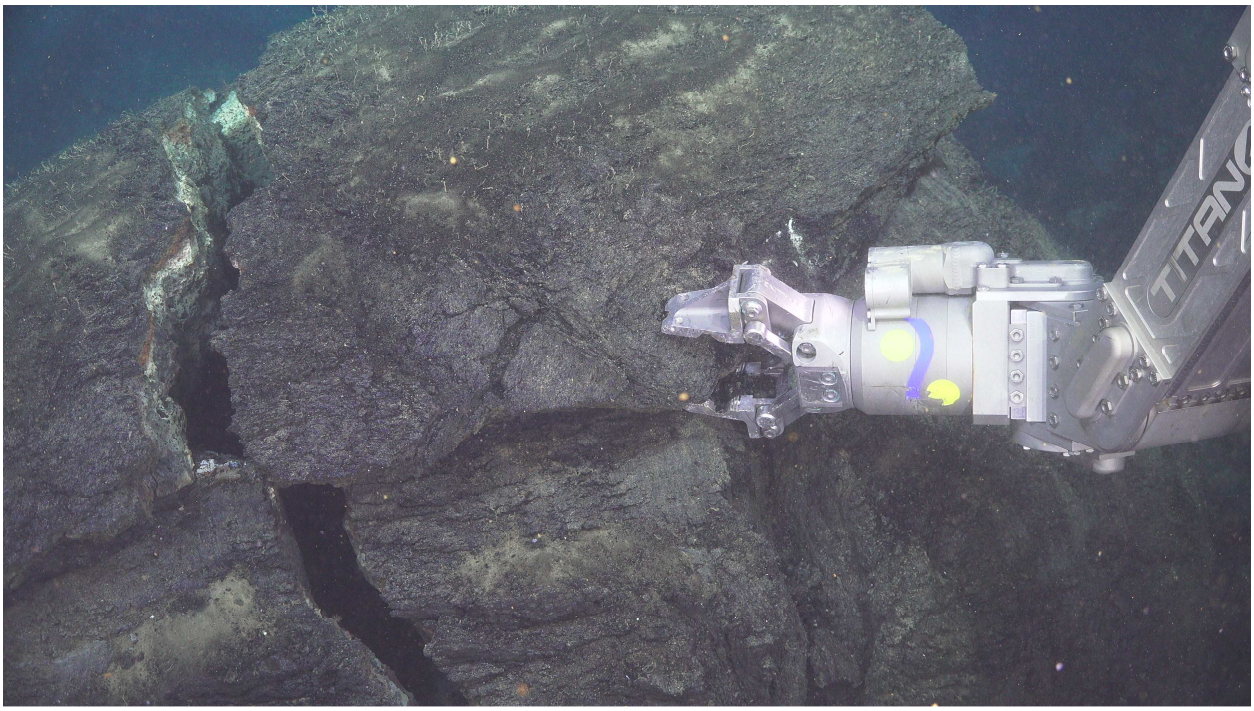

Figure 10.3i. Rock S98-R09.

Figure 10.3j. Rock S98-R11.

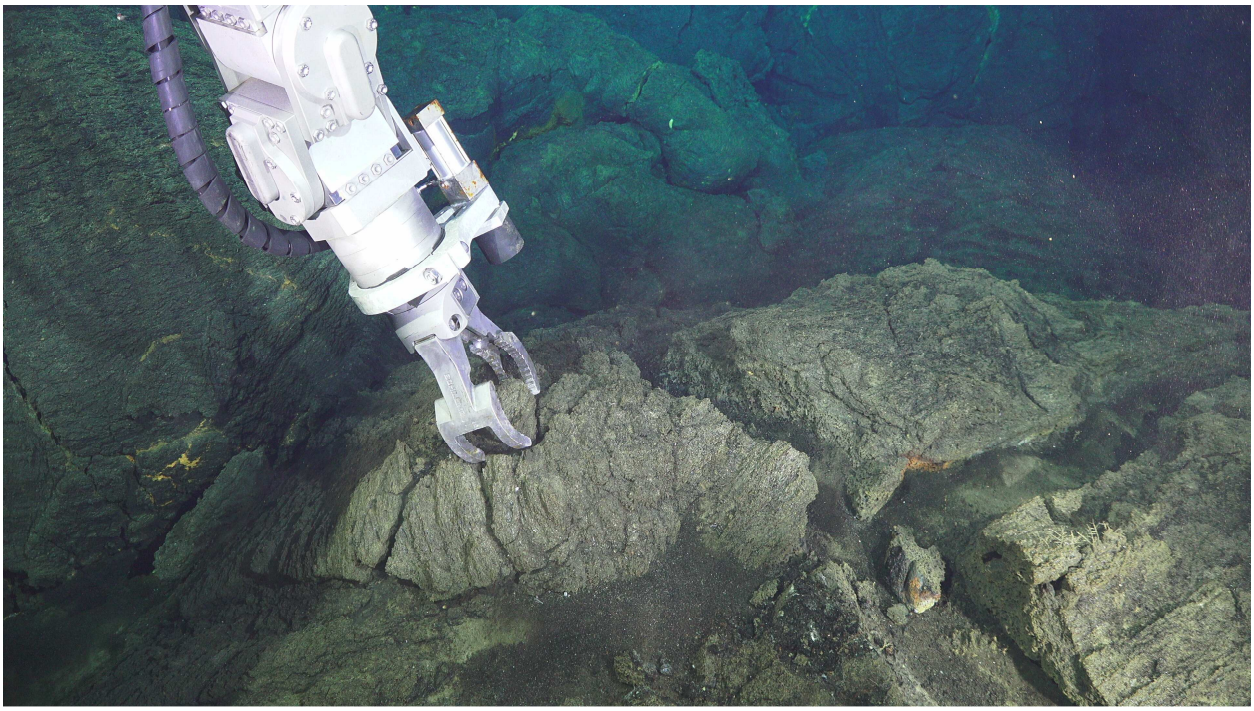

Figure 10.3k. Rock S98-R12.

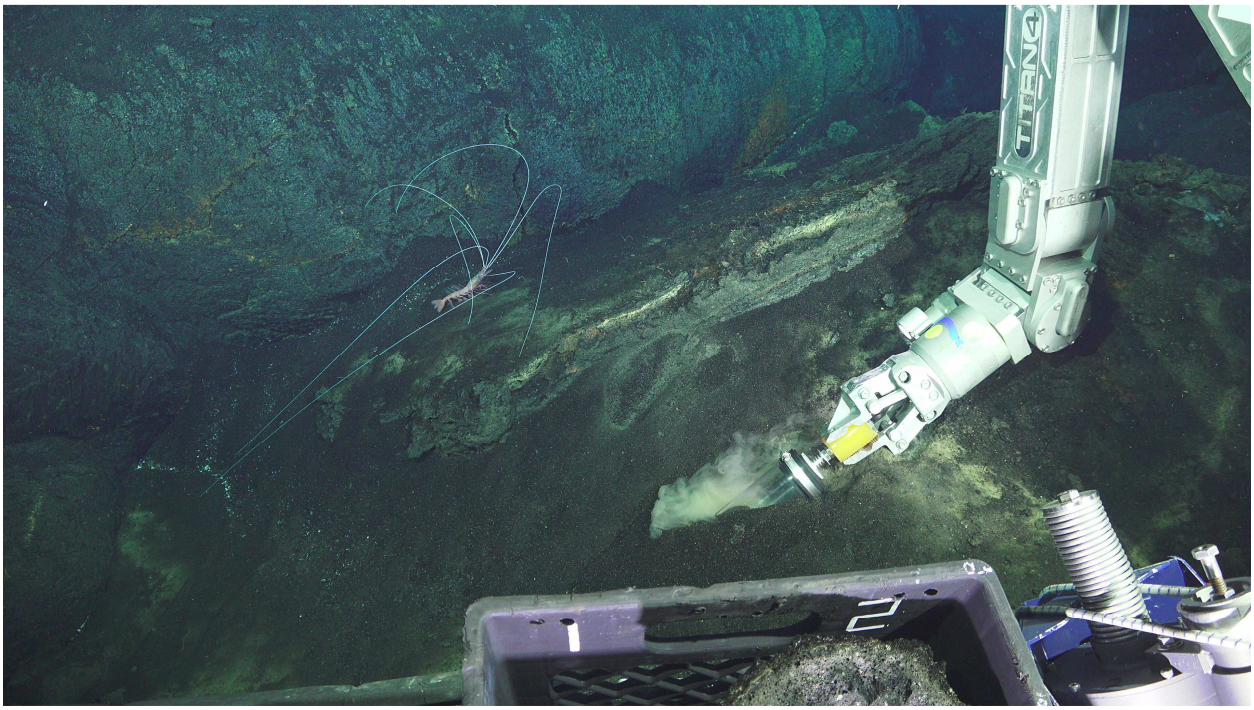

Figure 10.3l. Sediment S98-S13 being collected via push core. A deep-sea shrimp makes an appearance.

Figure 10.3m. Rock S98-R14.

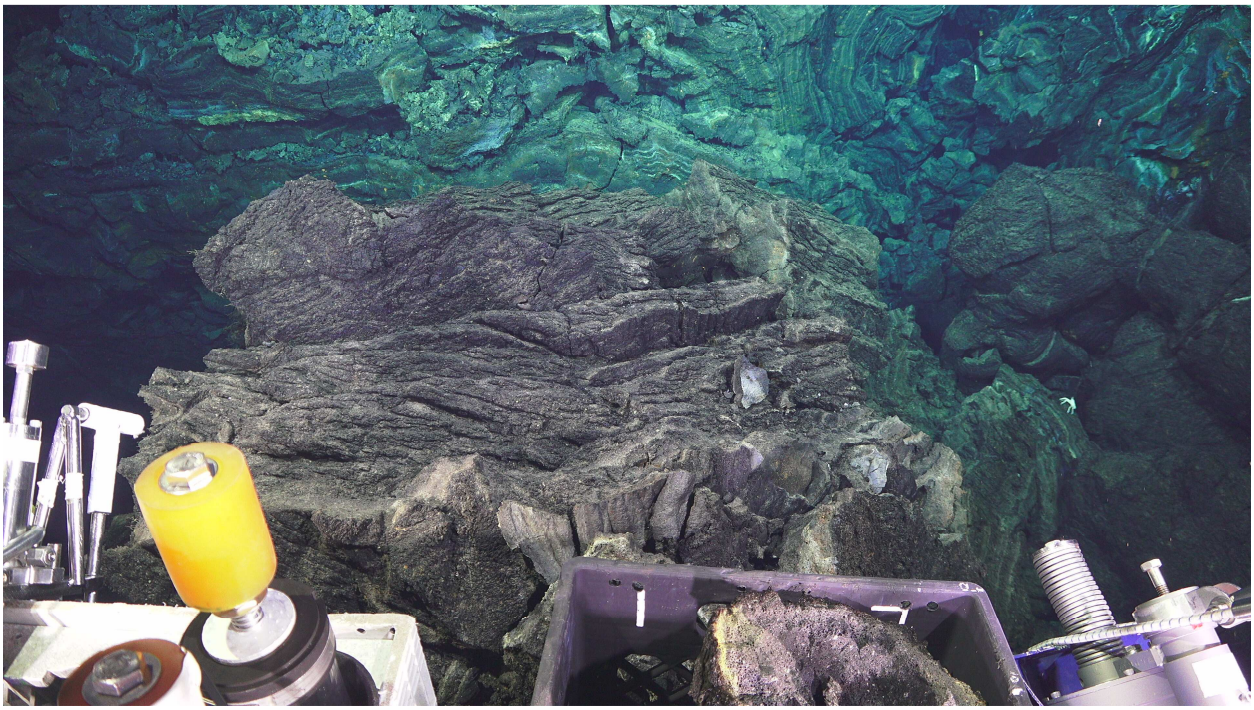

Figure 10.3n. Rock S98-R15.

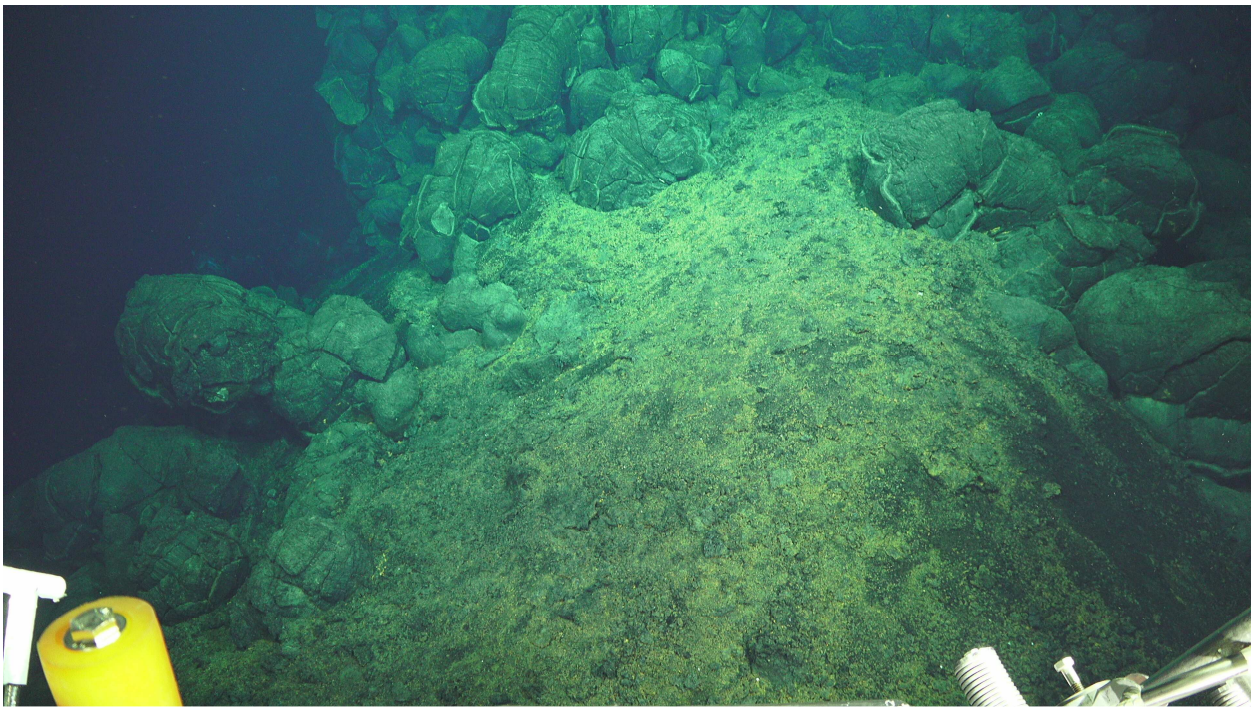

Figure 10.3o. Sediment S98-S16.

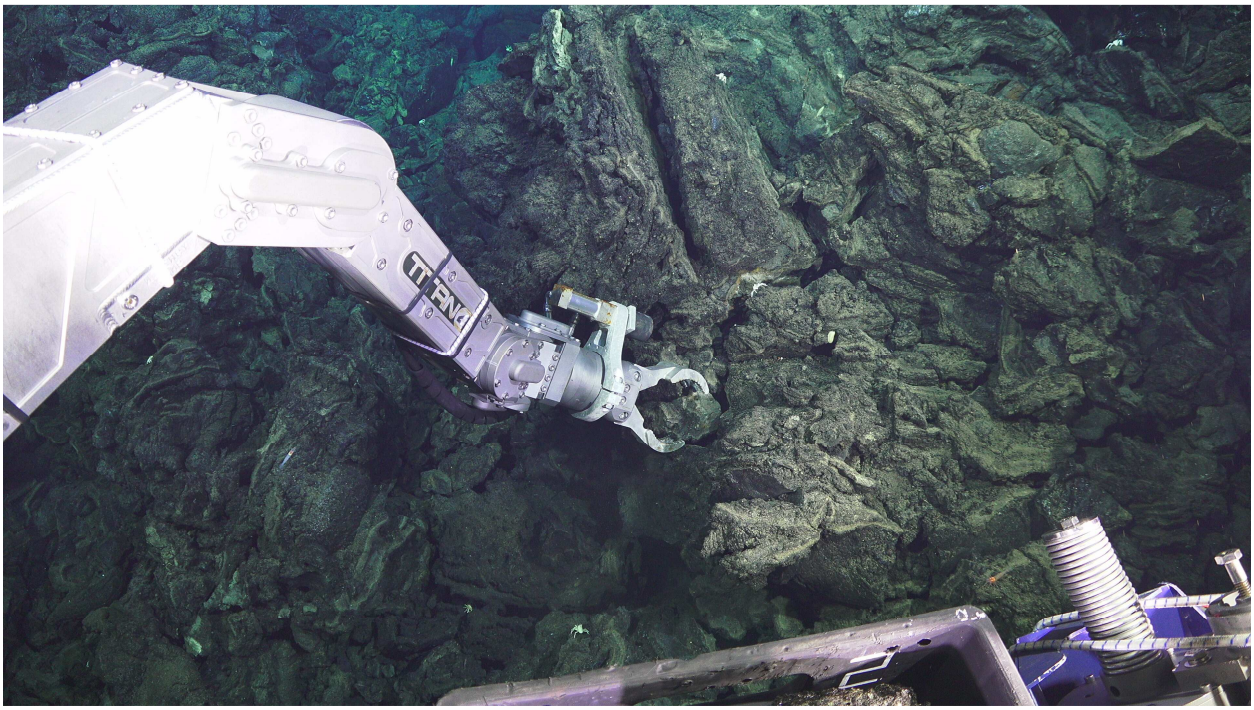

Figure 10.3p. Rock S98-R17.

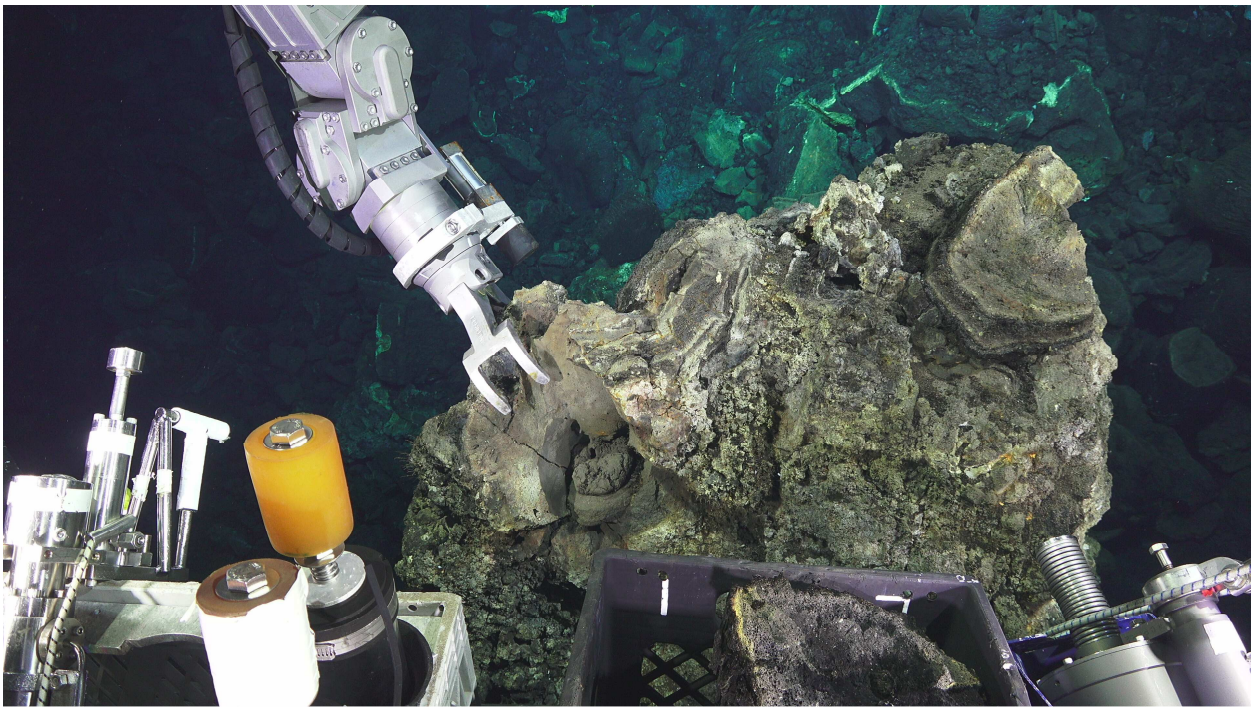

Figure 10.3q. Rock S98-R18.

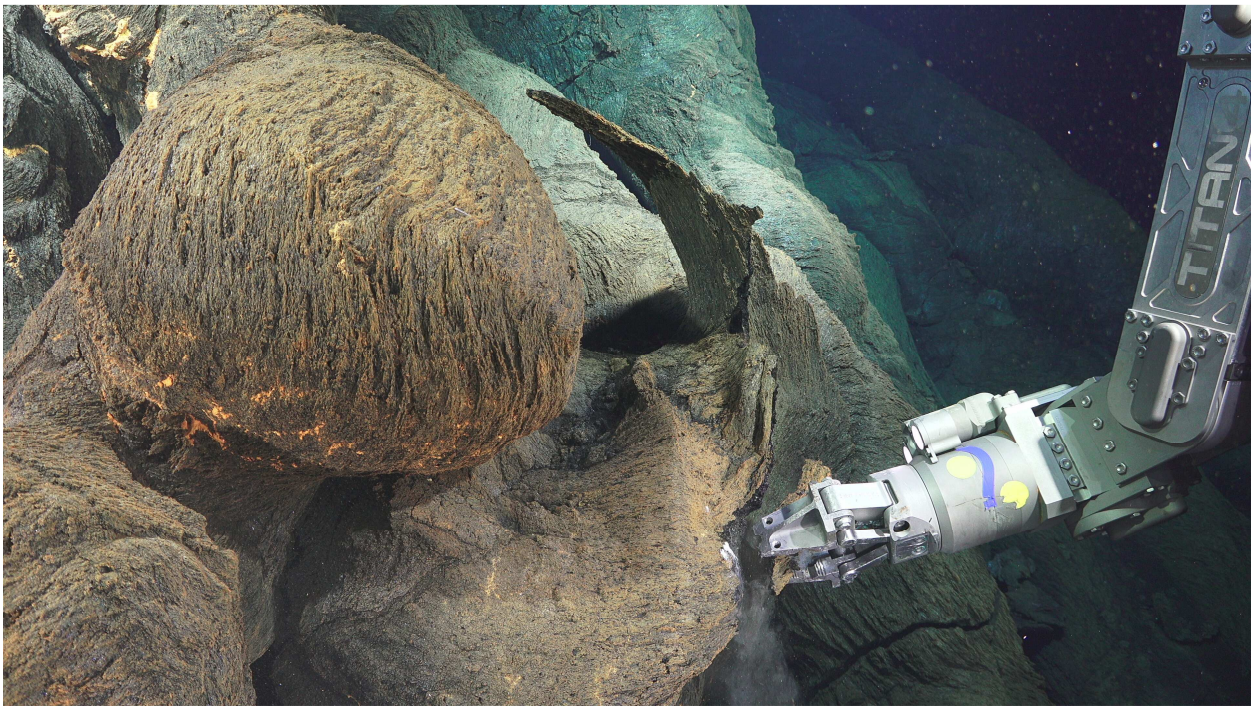

Figure 10.3r. Rock S98-R21.

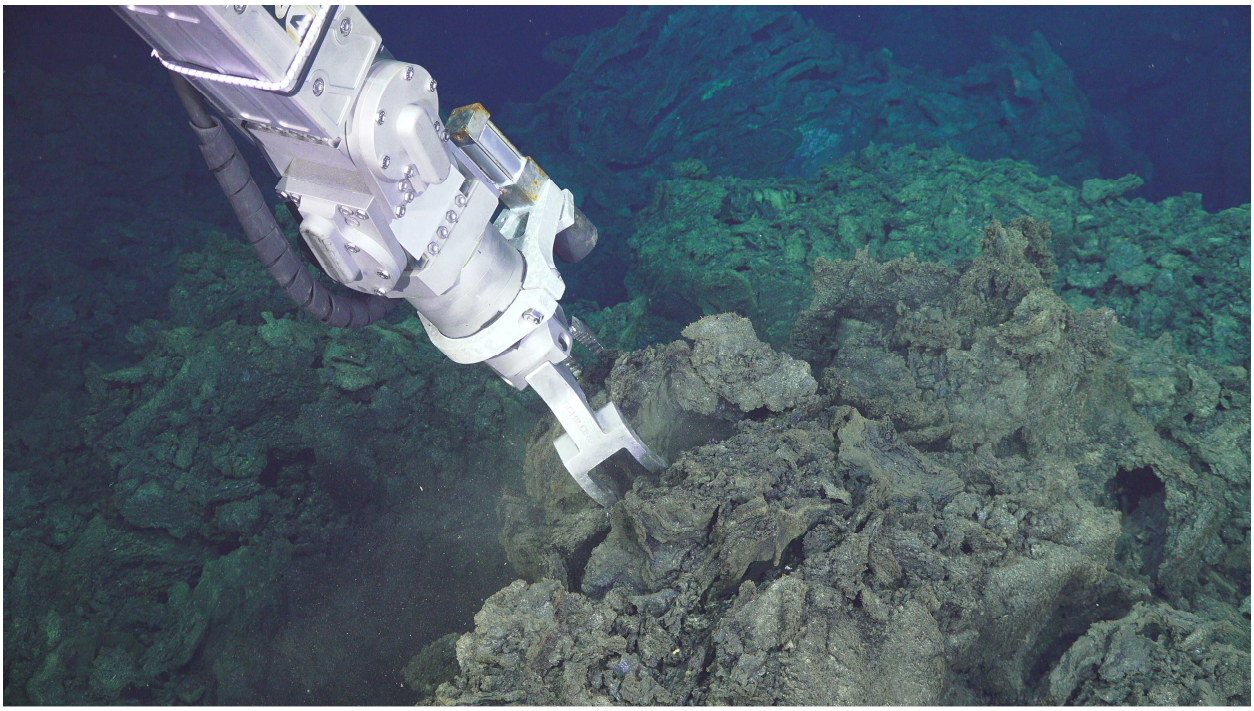

Figure 10.3s. Rock S98-R22.

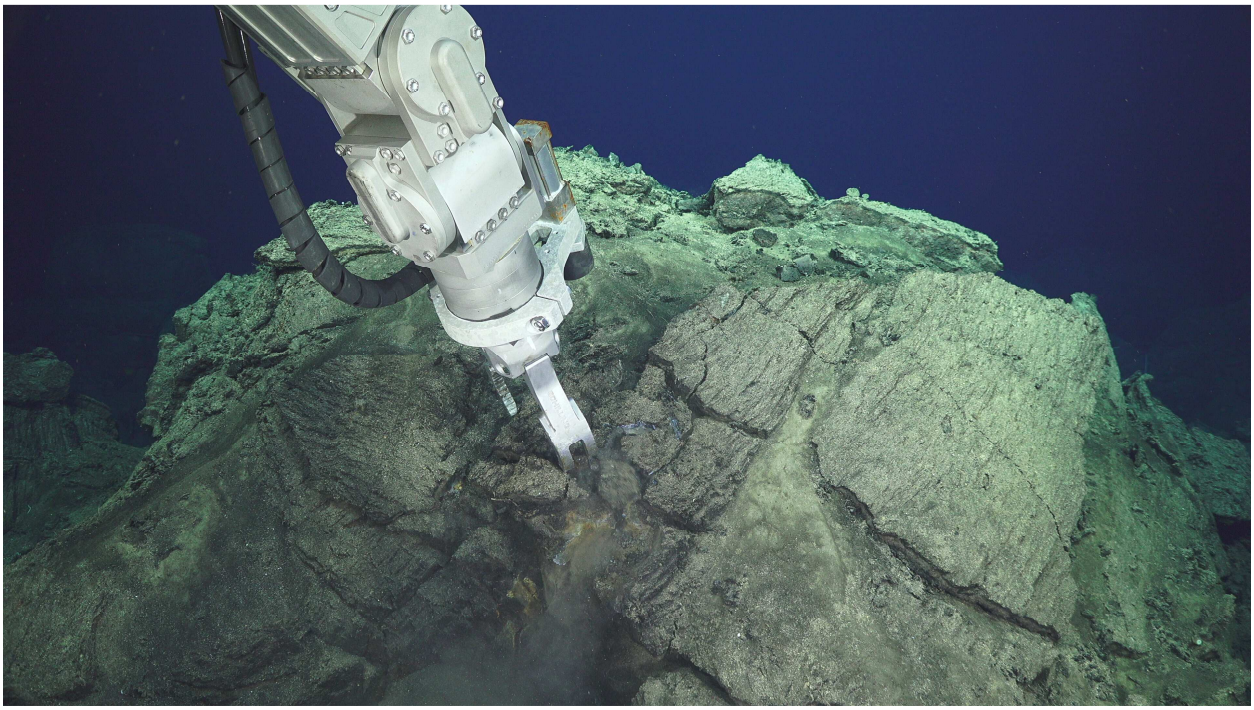

Figure 10.4a. Rock S99-R01.

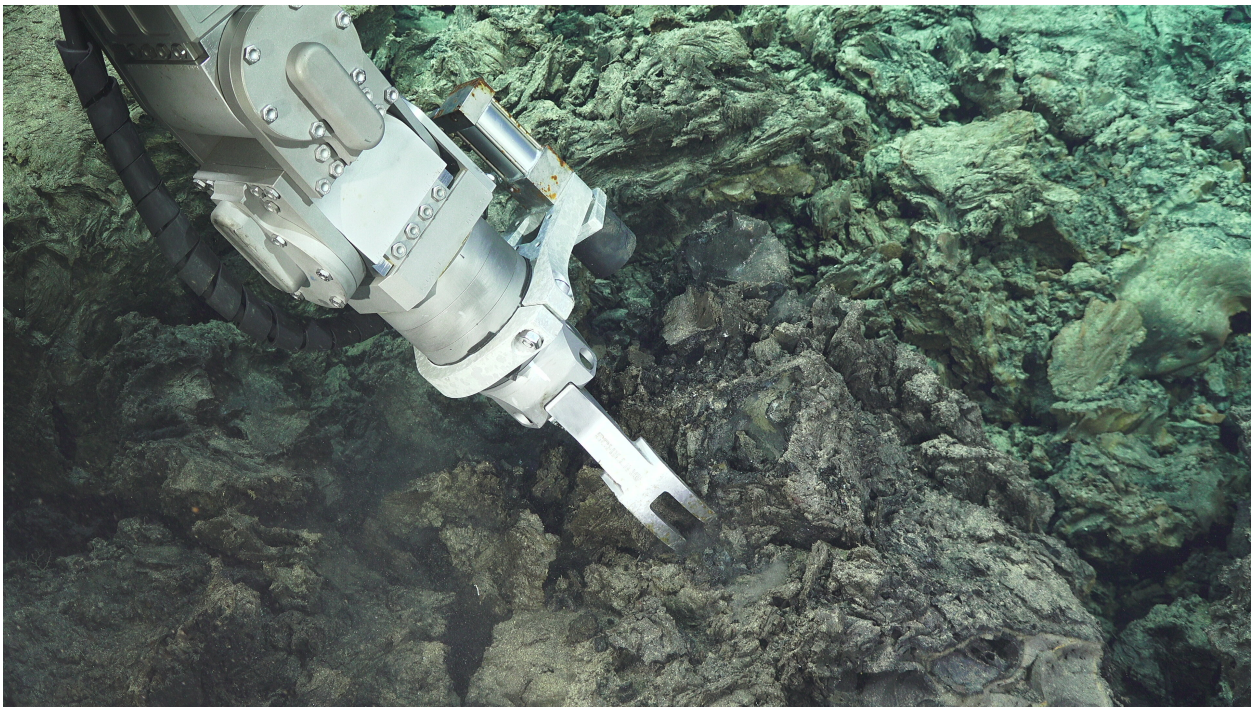

Figure 10.4b. Rock S99-R02.

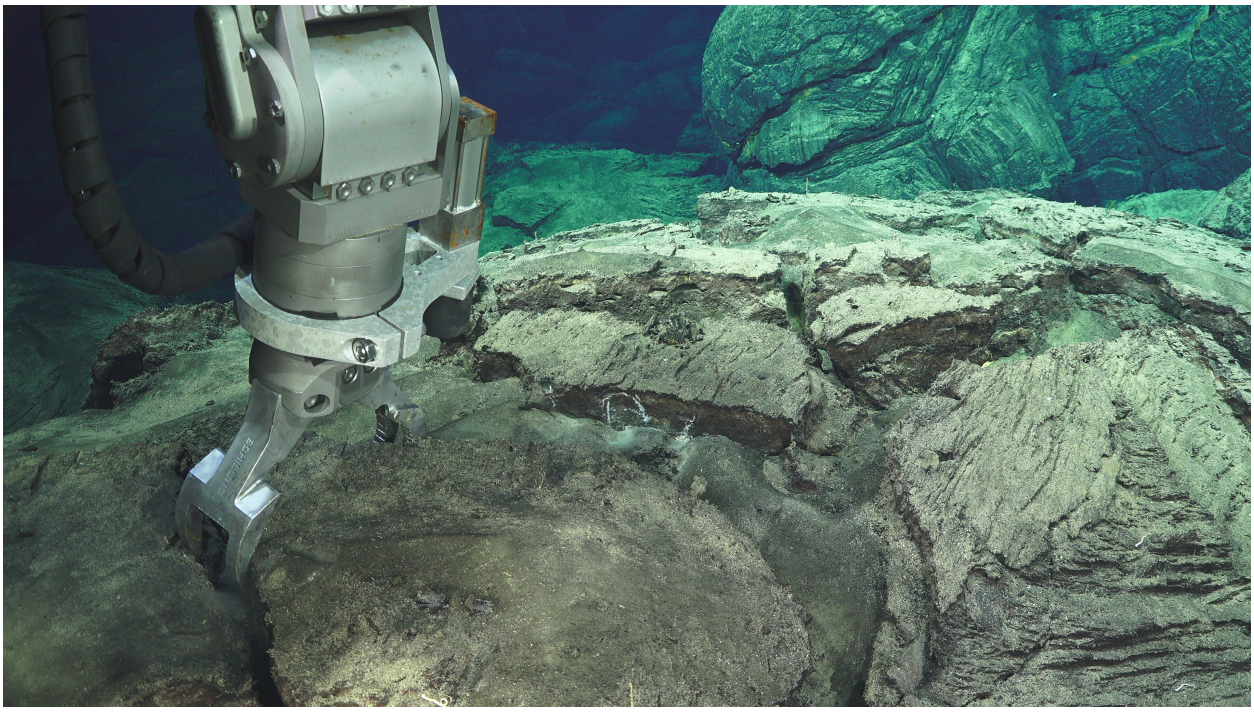

Figure 10.4c. Rock S99-R03.

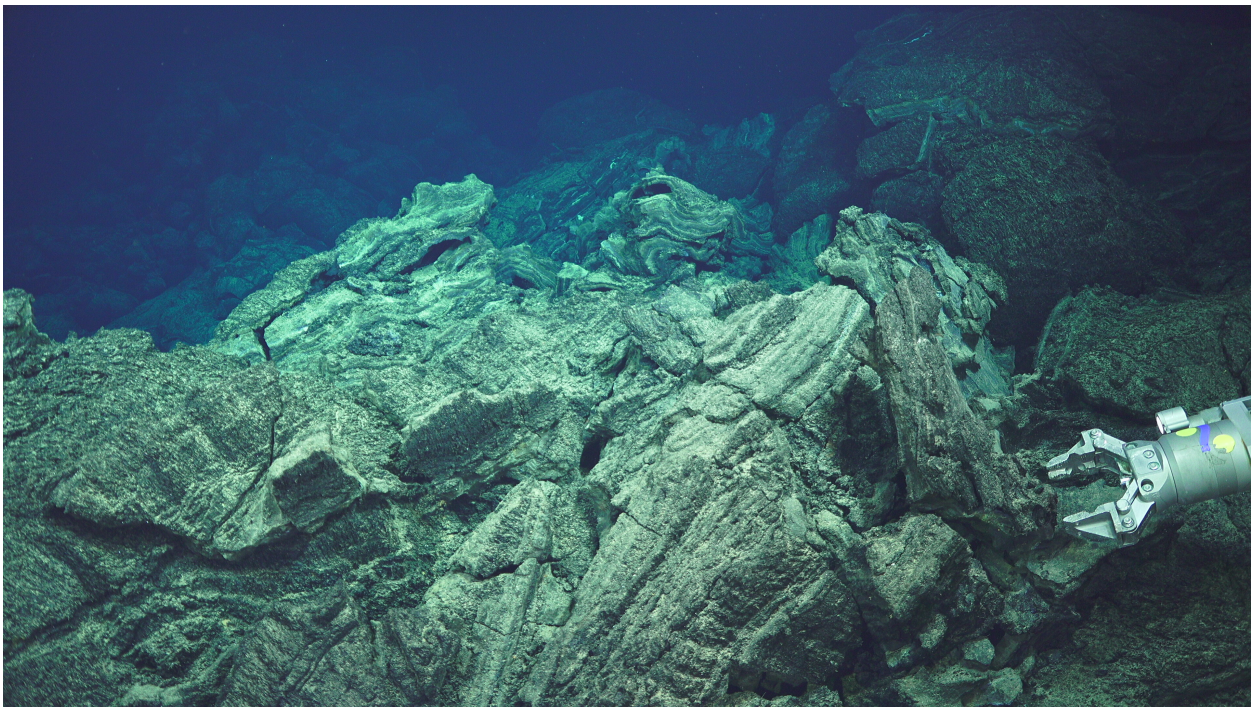

Figure 10.4d. Rock S99-R04.

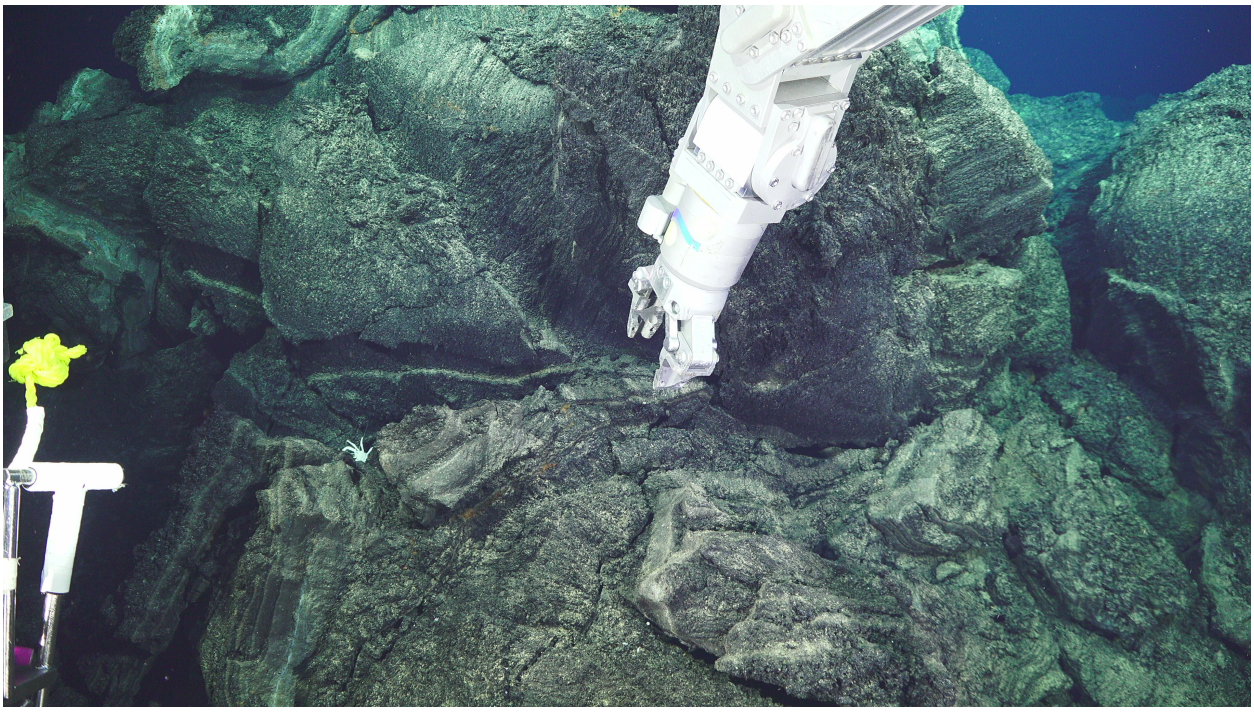

Figure 10.4e. Rock S99-R05.

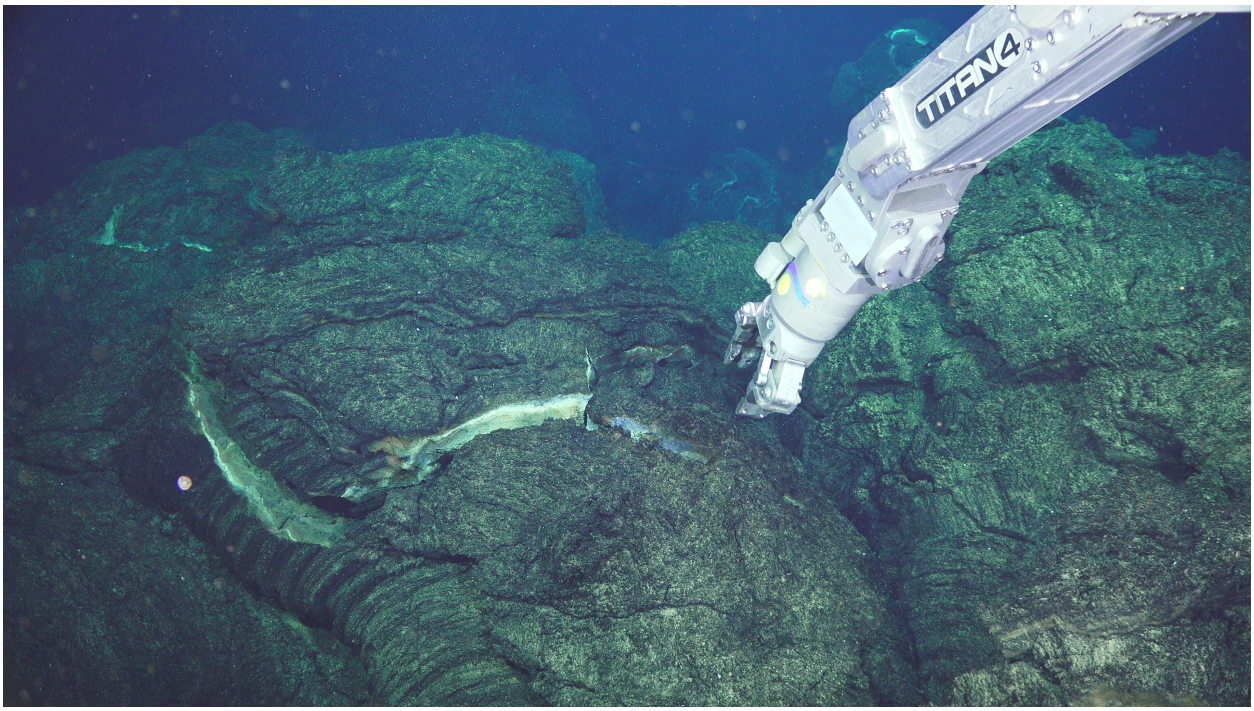

Figure 10.4f. Rock S99-R06.

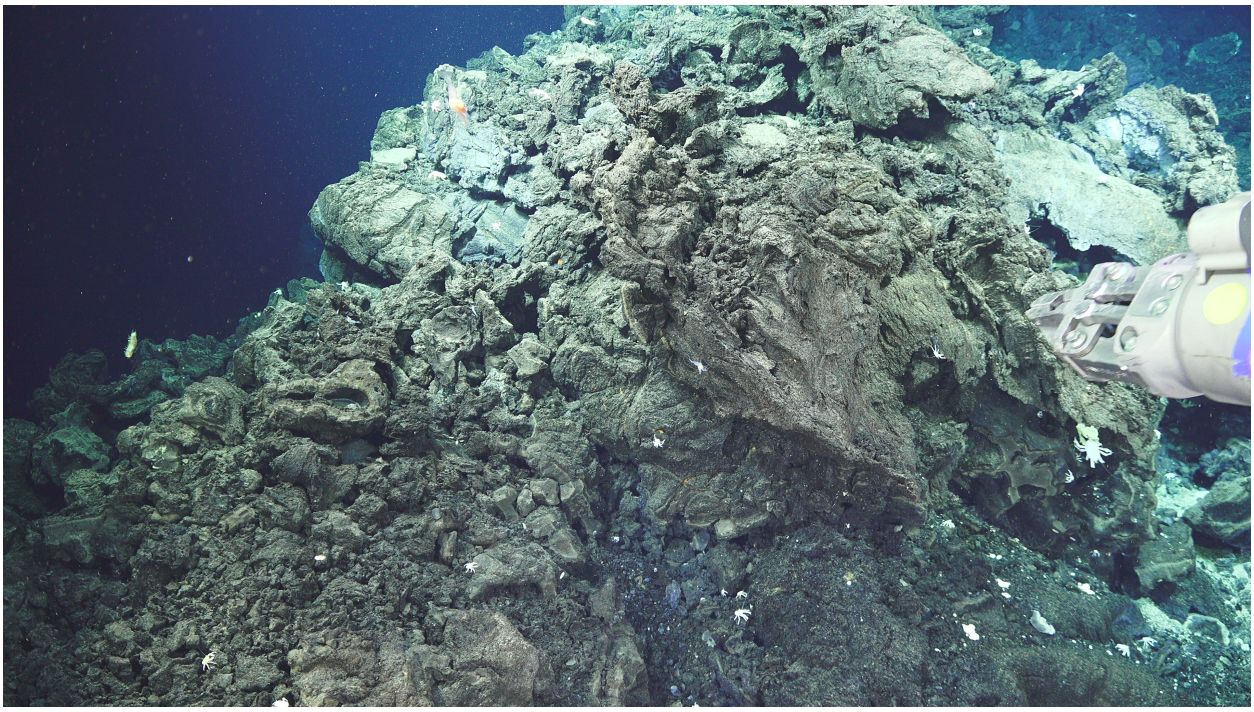
Figure 10.4g. Rock S99-R07.

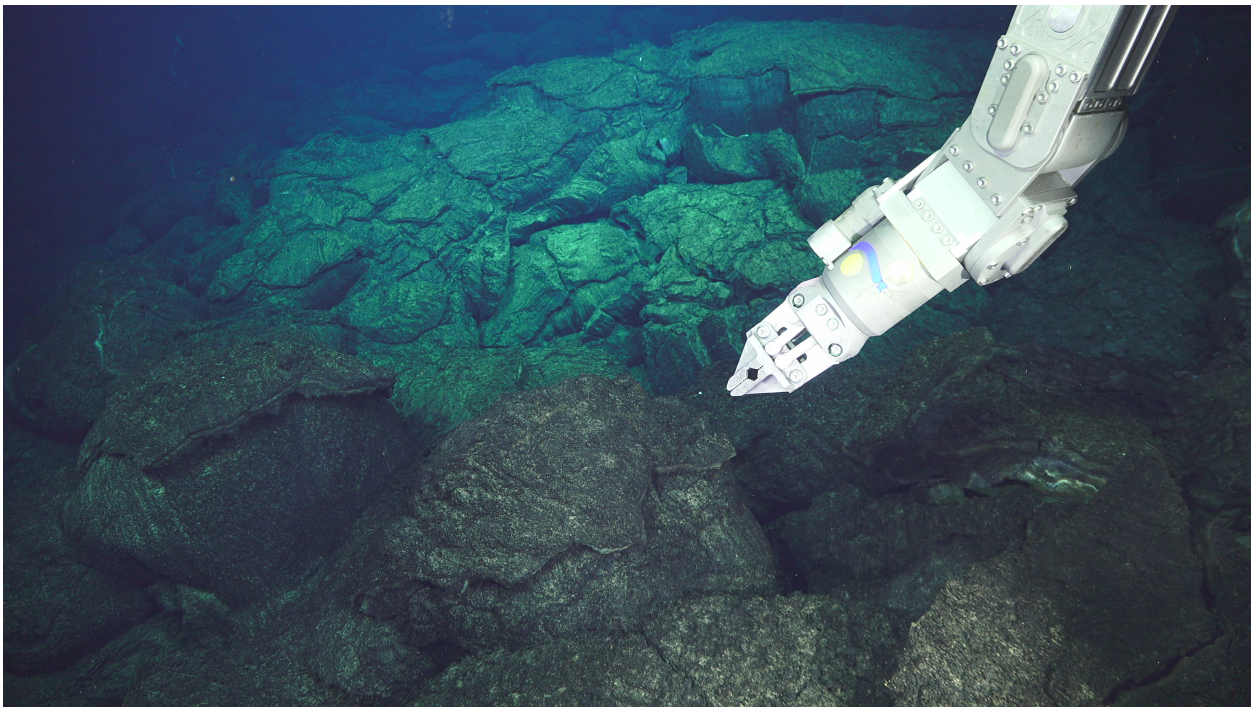

Figure 10.4h. Rock S99-R08.

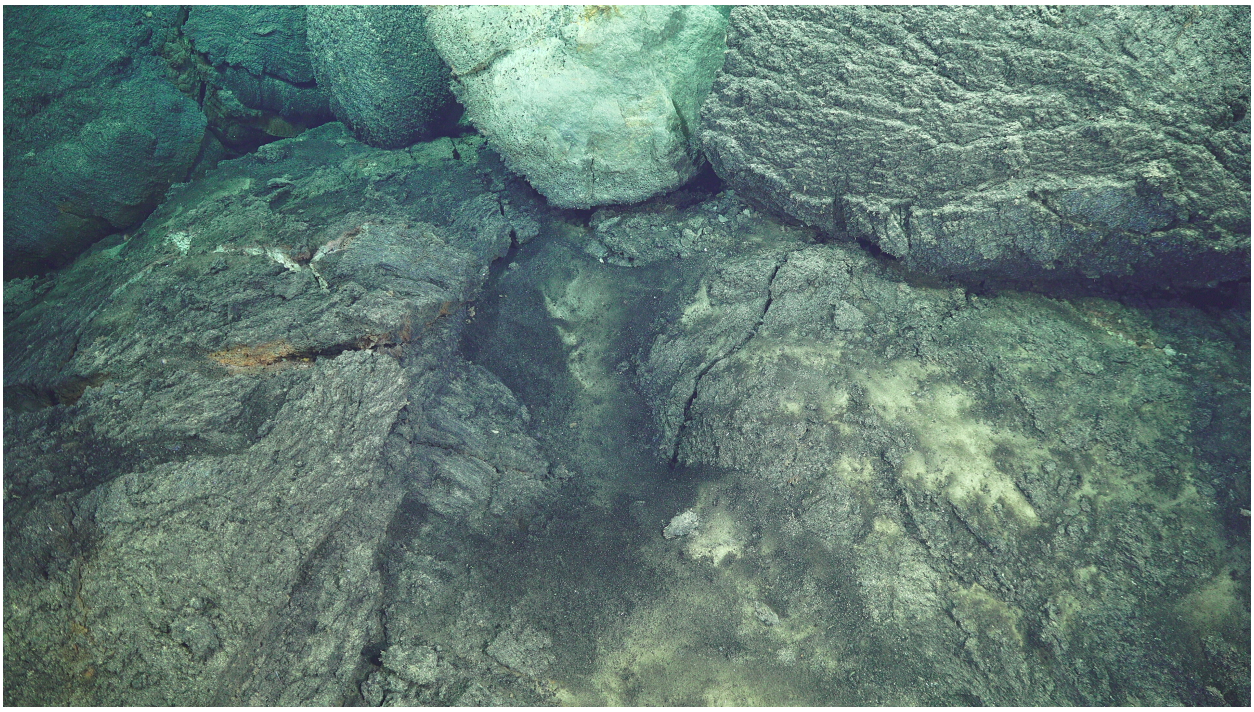

Figure 10.4i. Sediment S99-S09.

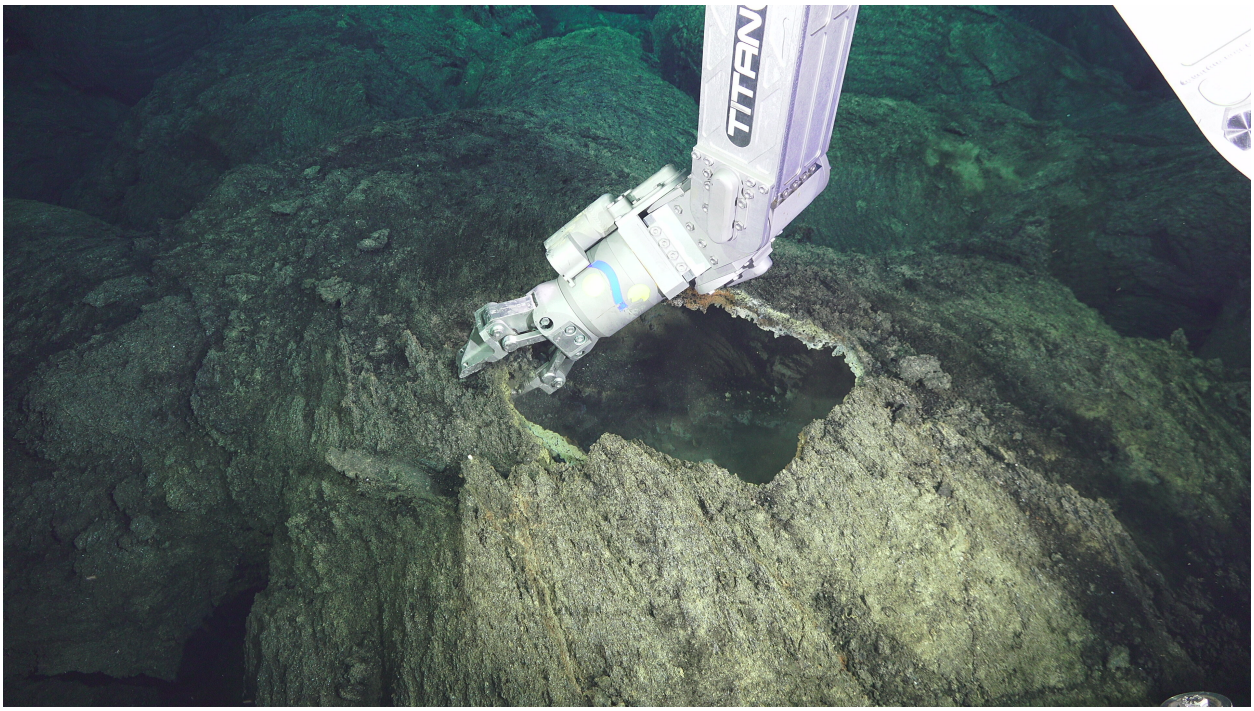

Figure 10.4j. Rock S99-R10.

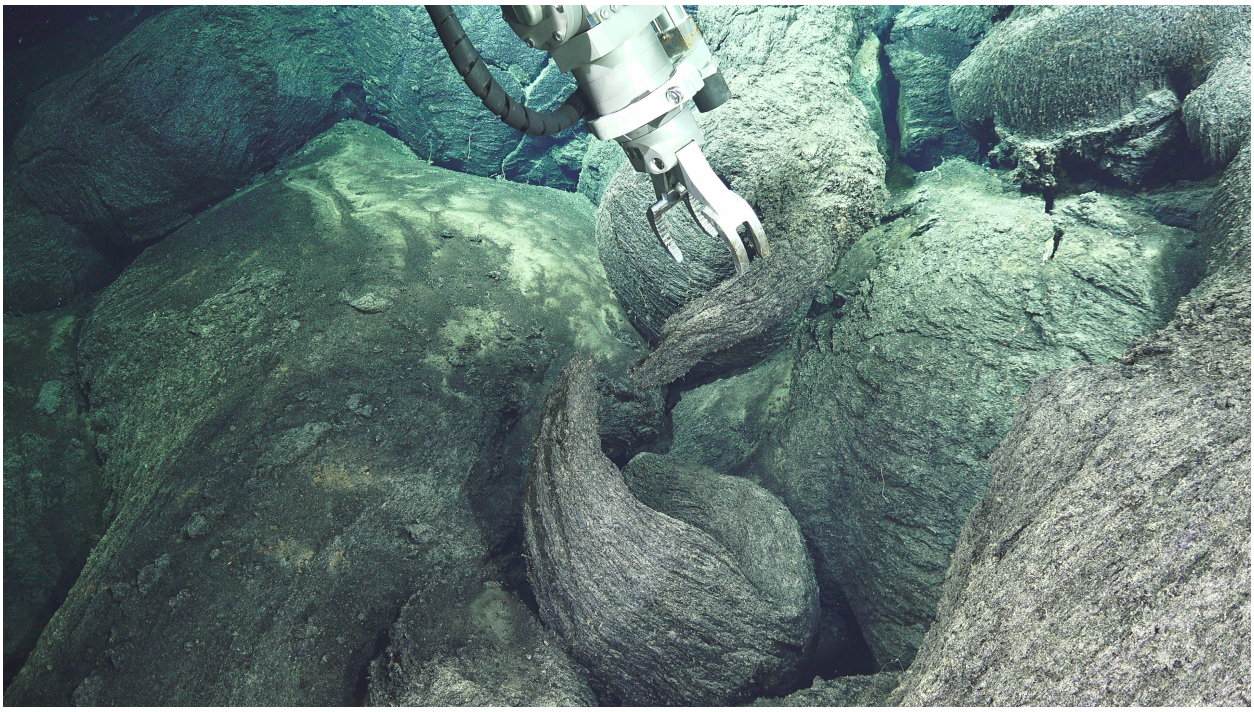
Figure 10.4k. Rock S99-R12.

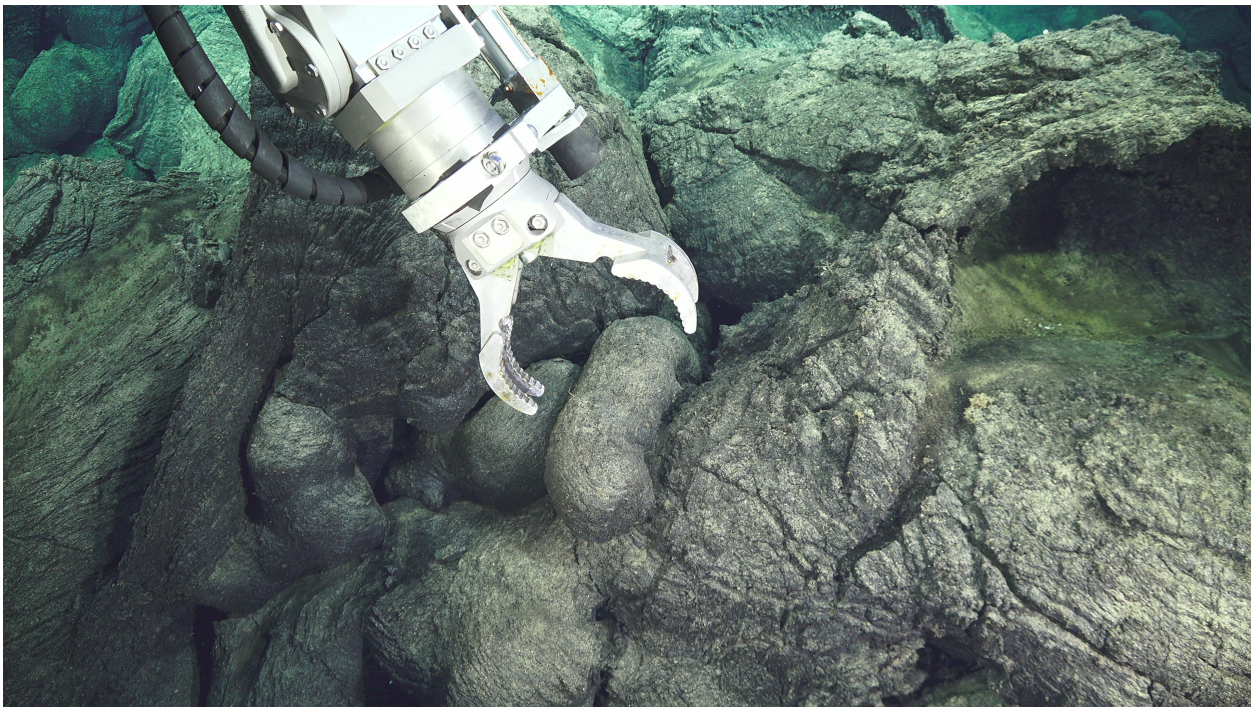

Figure 10.4l. Rock S99-R13.

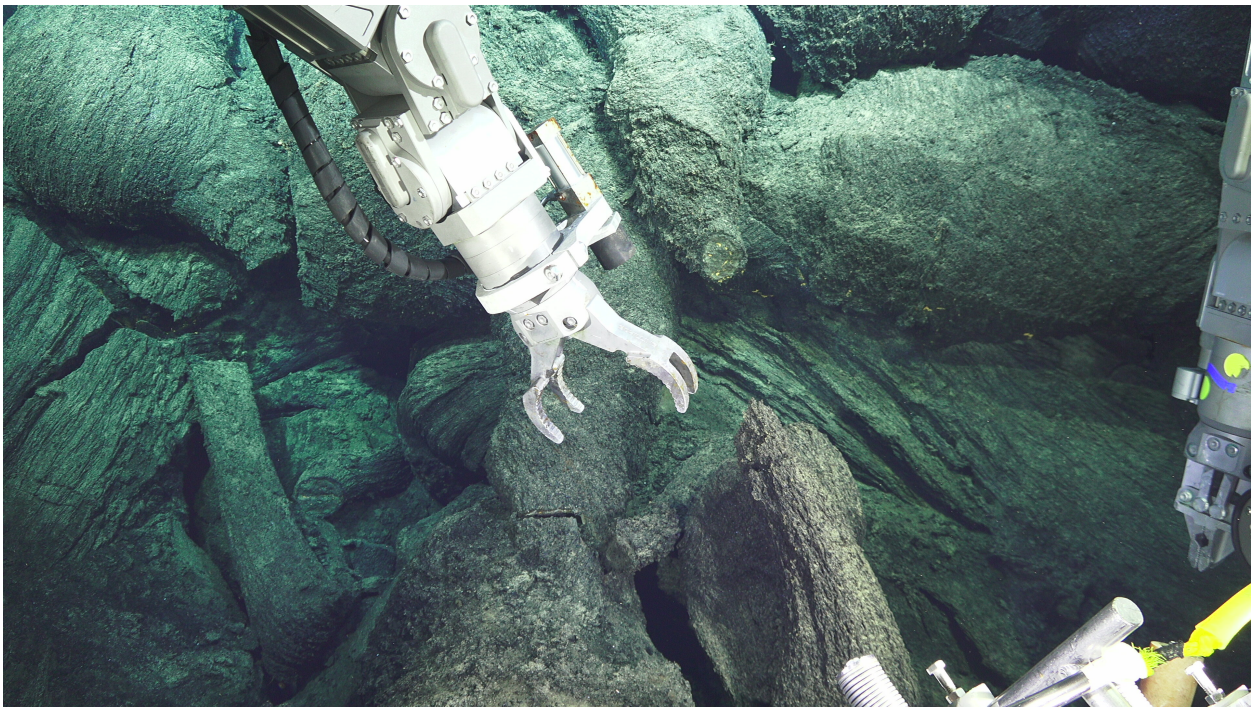

Figure 10.4m. Rock S99-R14.

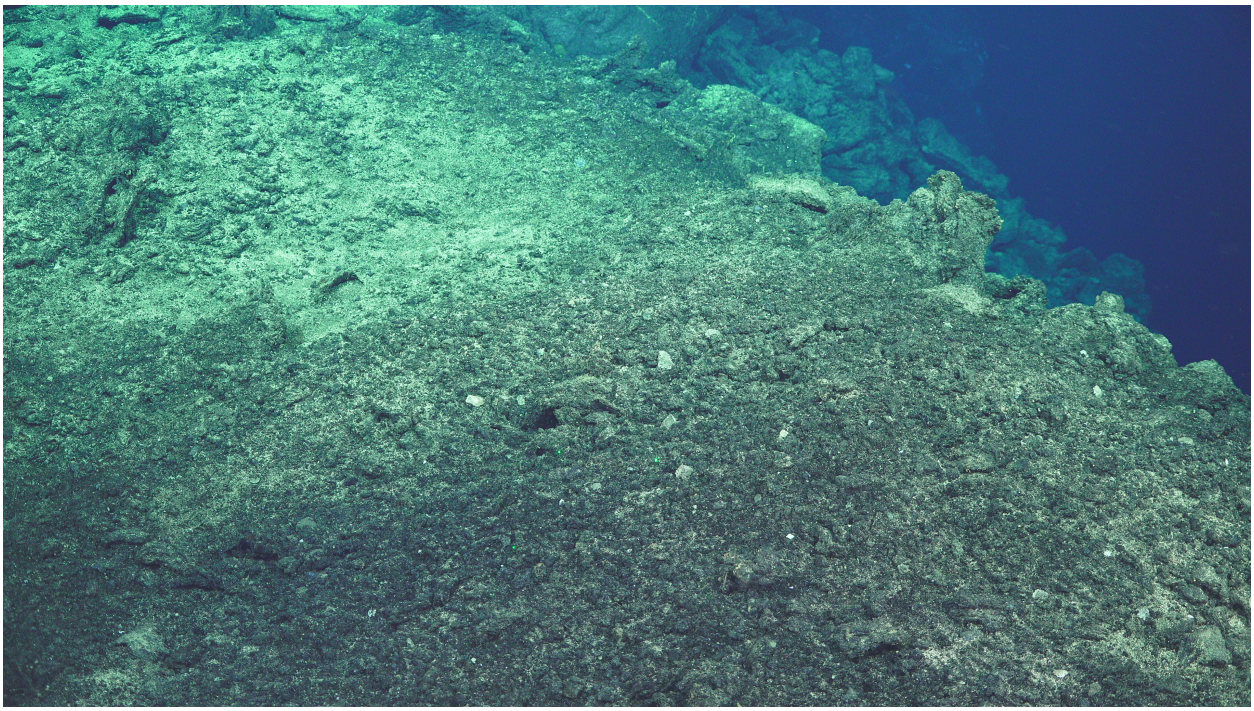

Figure 10.4n. Sediment S99-S15.

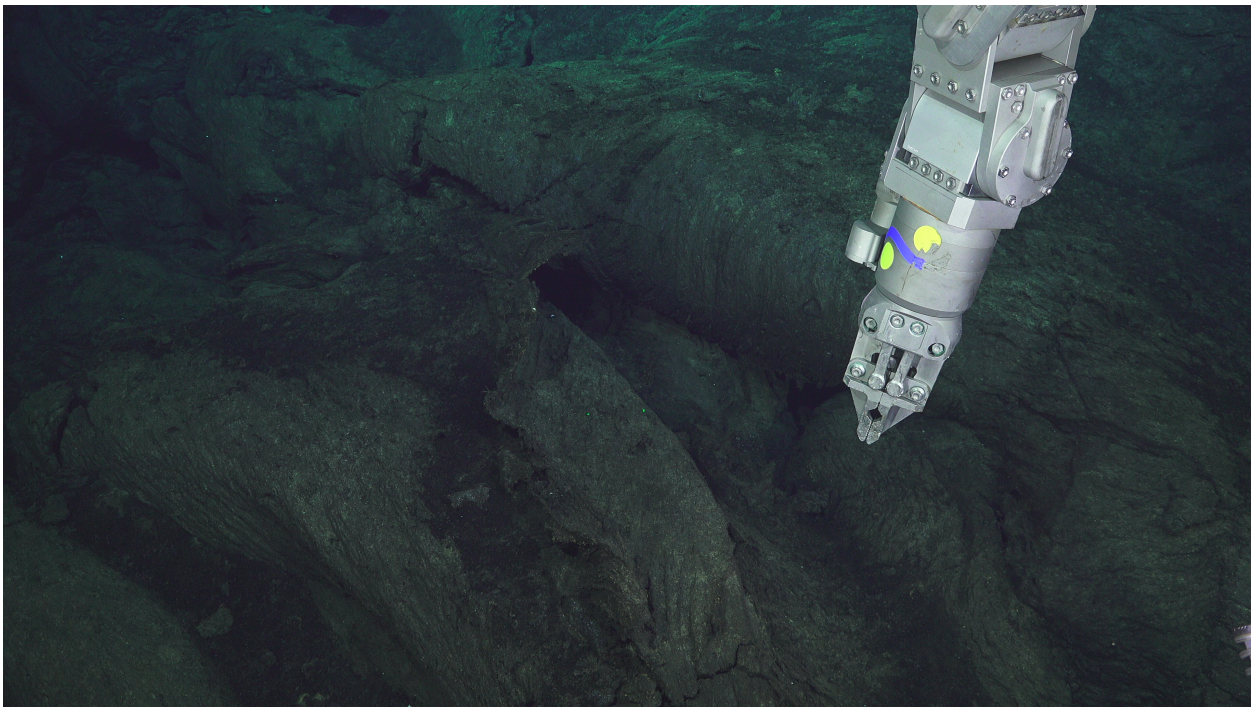

Figure 10.4o. Rock S99-R18.

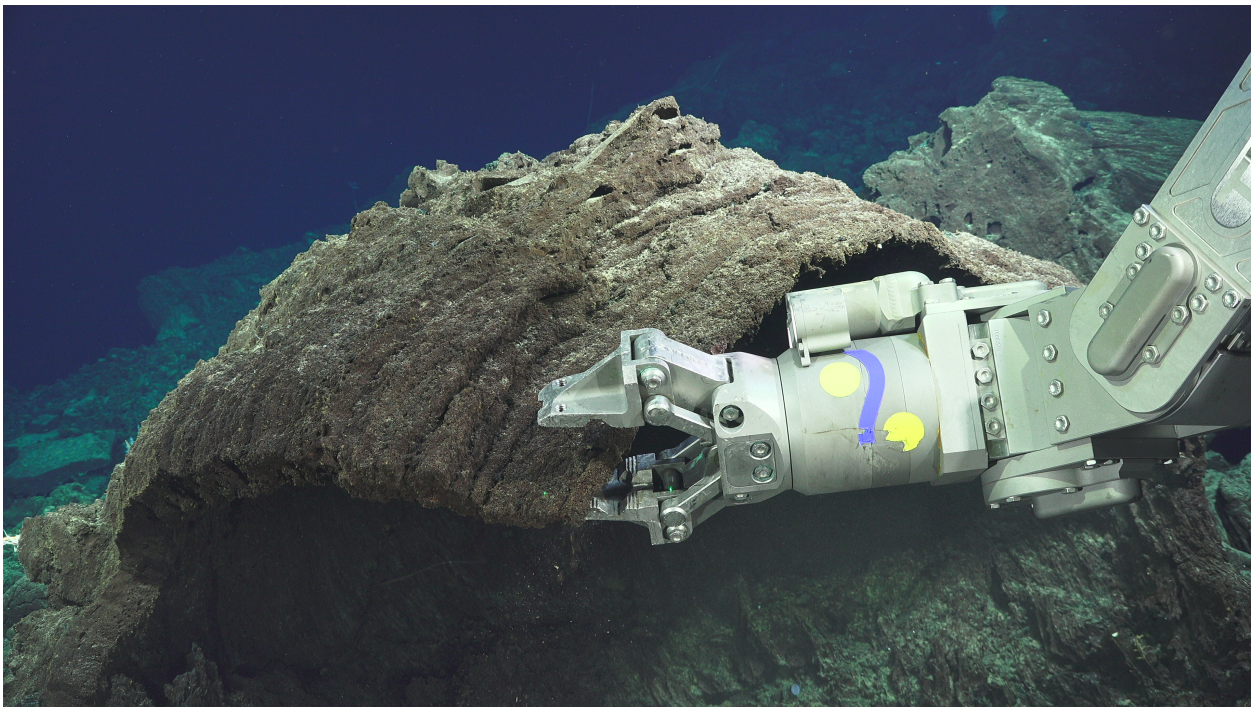

Figure 10.4p. Rock S99-R20.

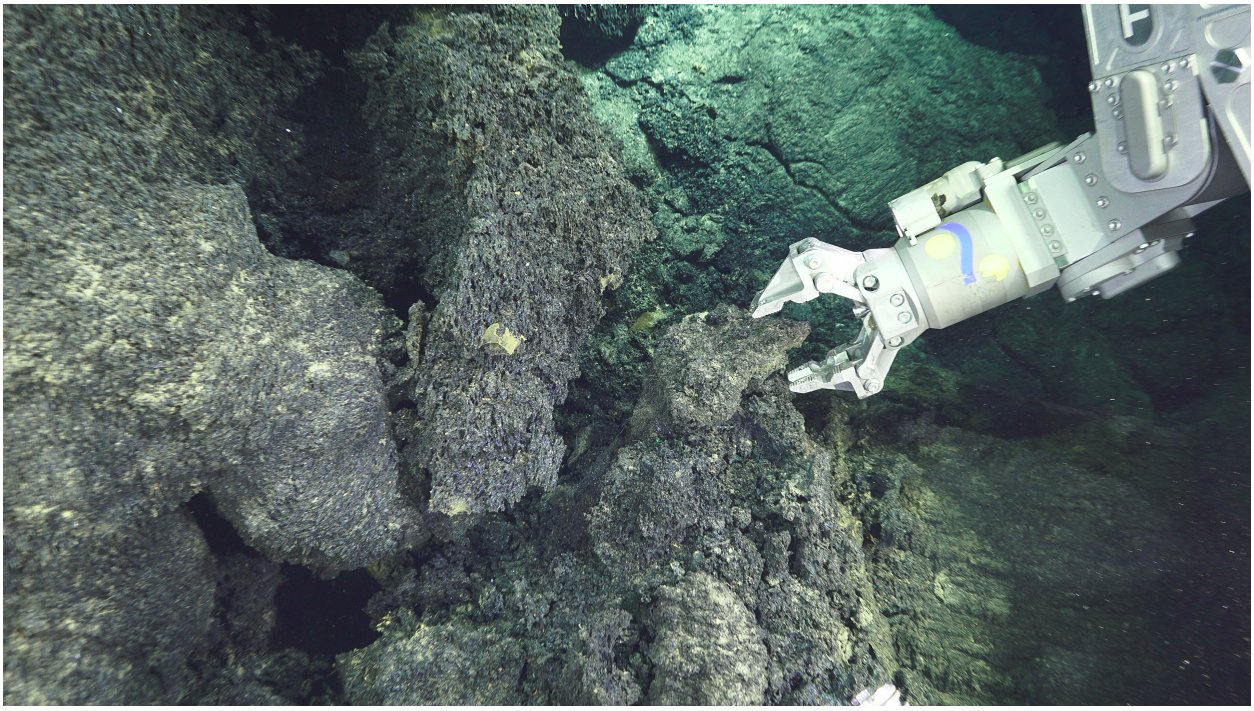

Figure 10.4q. Rock S99-R21.

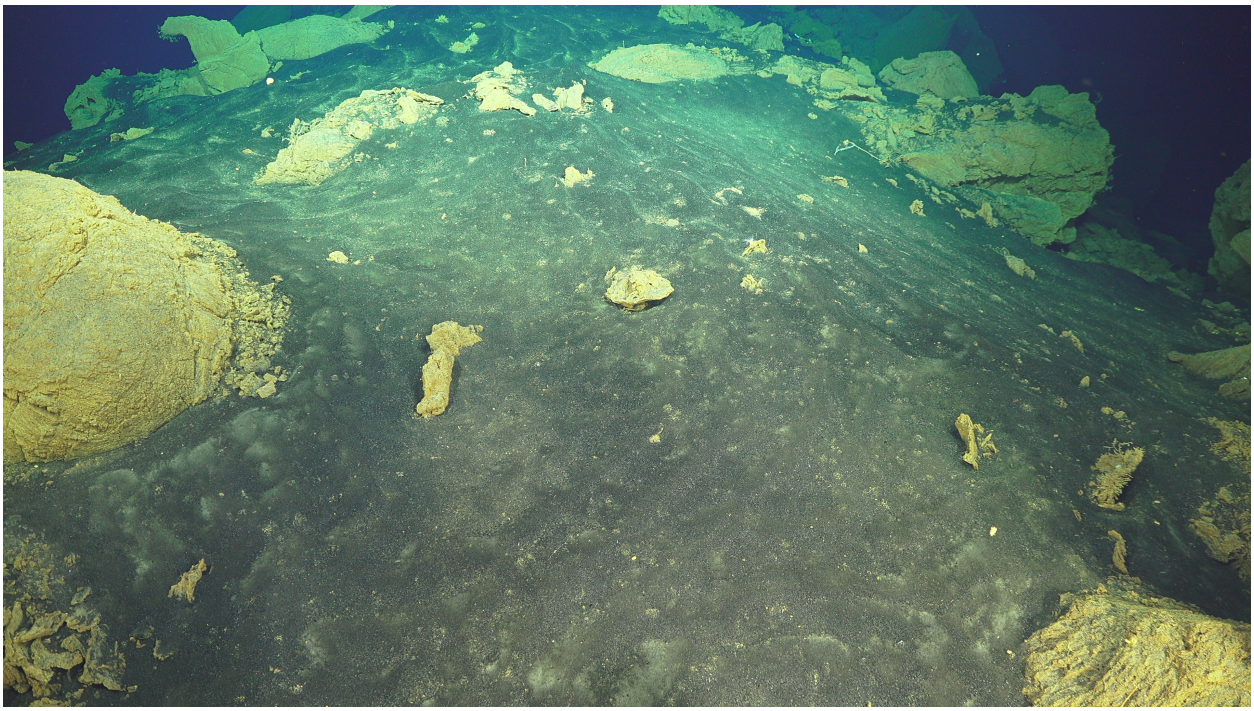

Figure 10.4r. Sediment S99-S25.

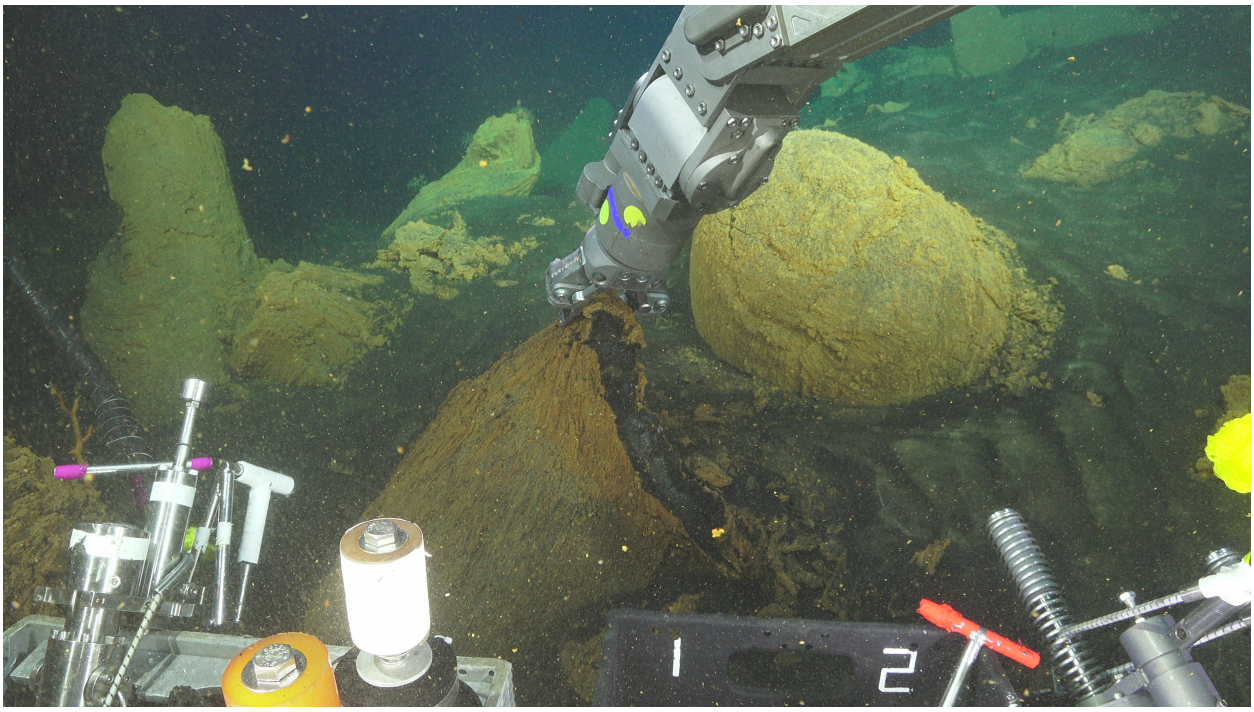

Figure 10.4s. Rock S99-R26.

10.3 Appendix C: Photomicrographs of glass chips

Over 235 backscattered electron images were taken of the glass chips studied in this body of work. Selected glass chips are shown in this appendix; if interested in any additional photomicrographs, contact the author at mzinn@hawaii.edu. Lighter colors in these photomicrographs indicate a higher average atomic number, while darker colors represent a lower average atomic number.

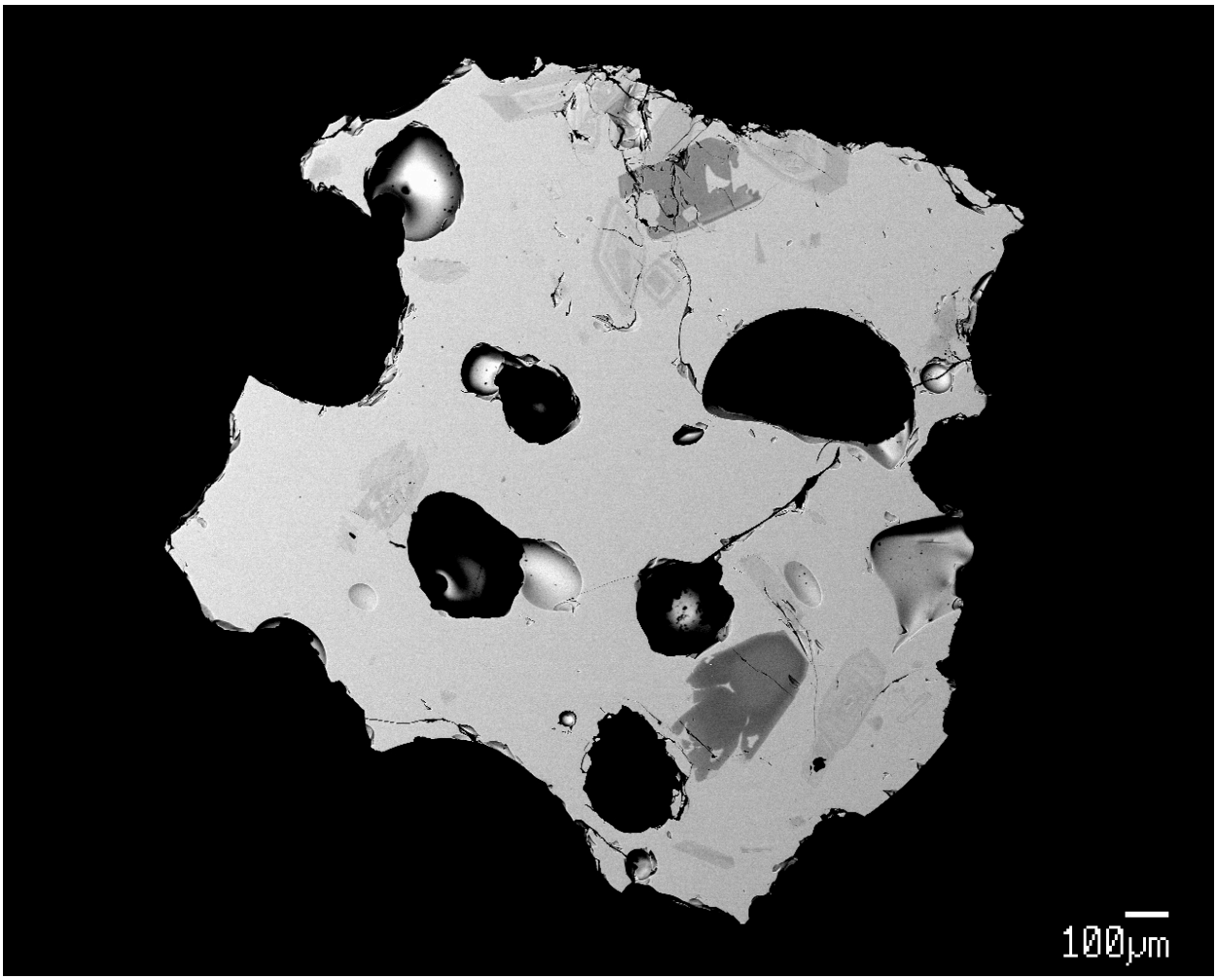

Figure 10.5a. Sediment S98-S01, glass chip 07.

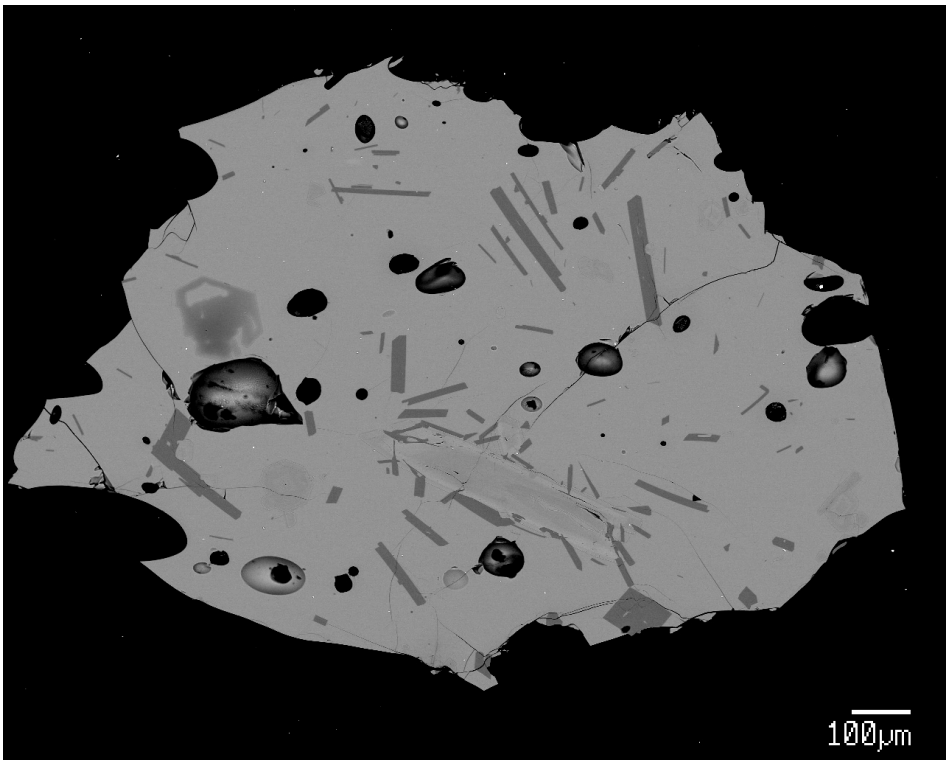

Figure 10.5b. Rock S98-R03, glass chip 02.

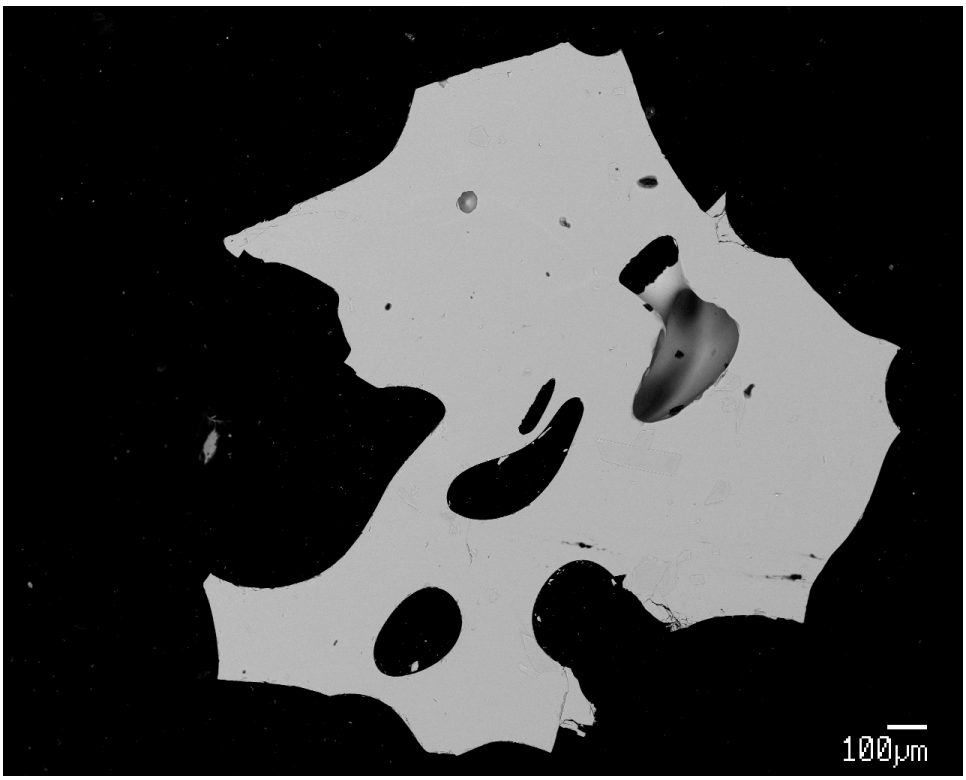

Figure 10.5c. Rock S98-R12, glass chip 03.

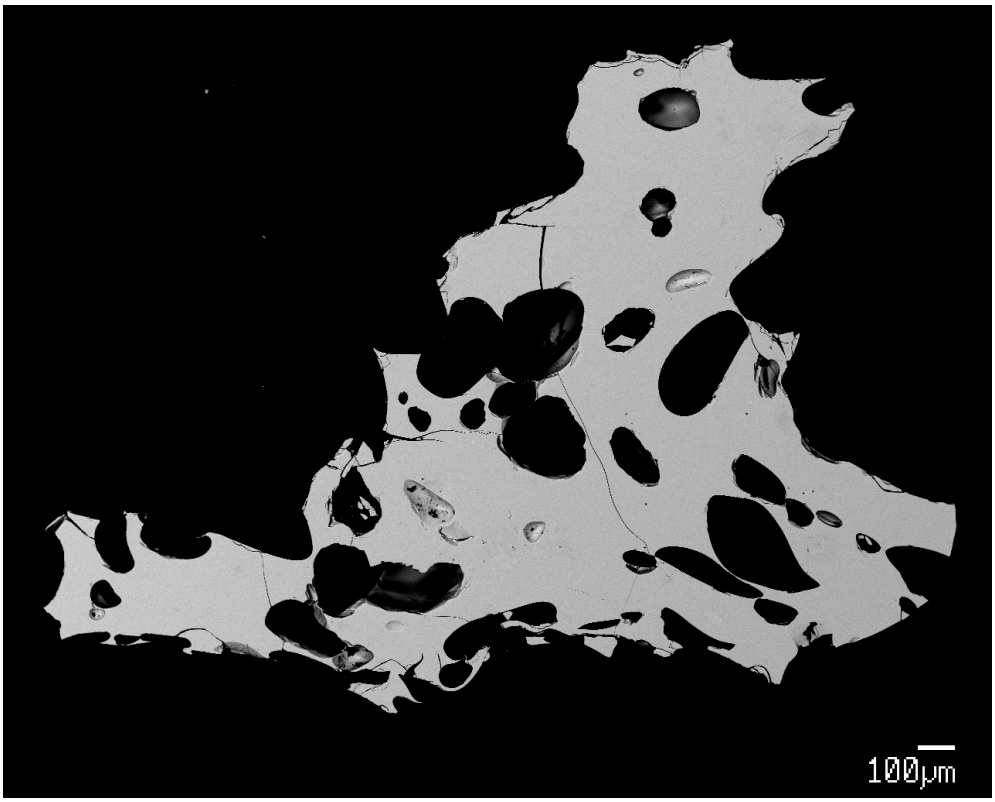

Figure 10.5d. Rock S98-R13, glass chip 03.

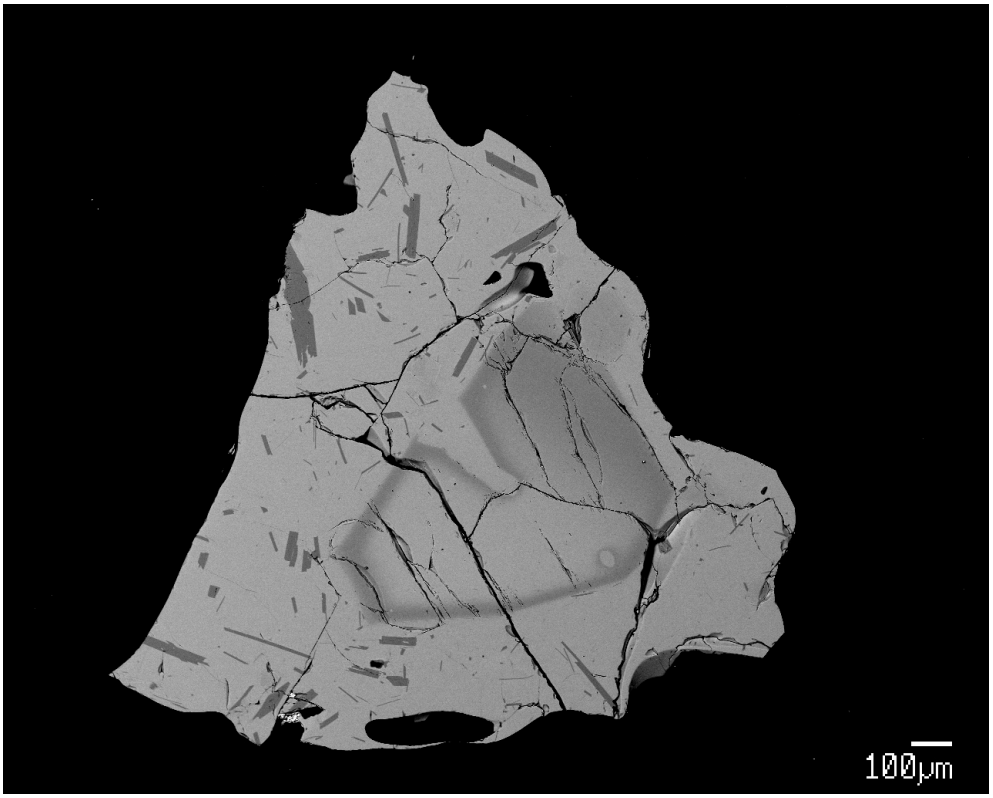

Figure 10.5e. Rock S98-R15, glass chip 03.

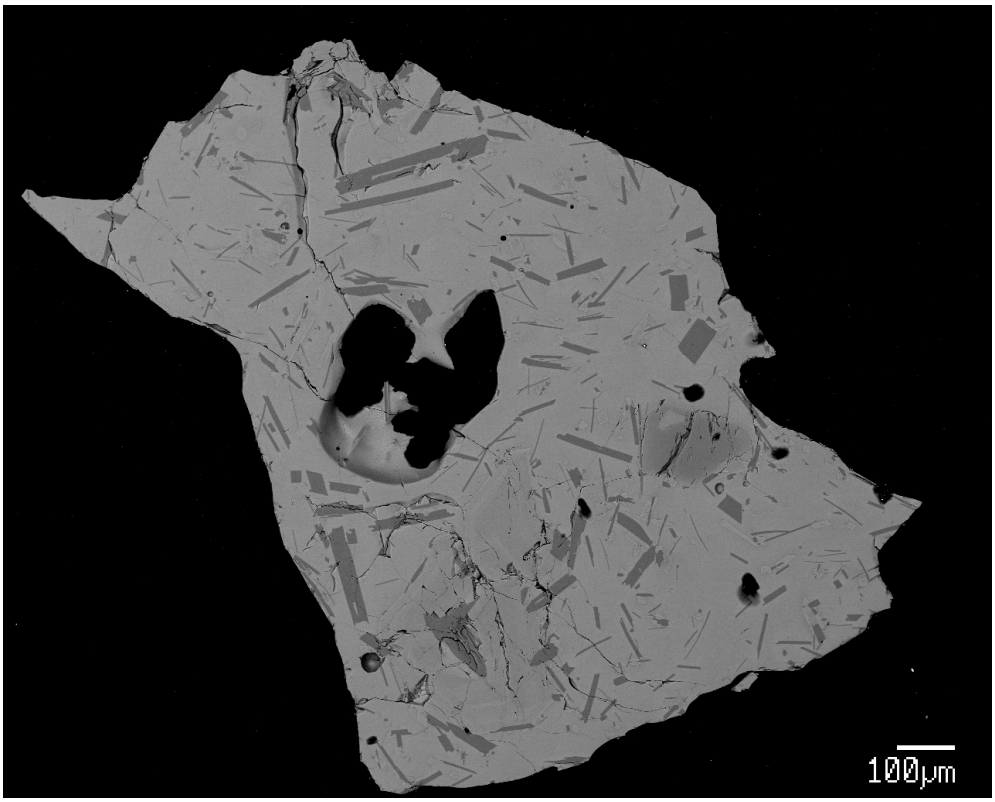

Figure 10.5f. Rock S98-R17, glass chip 02.

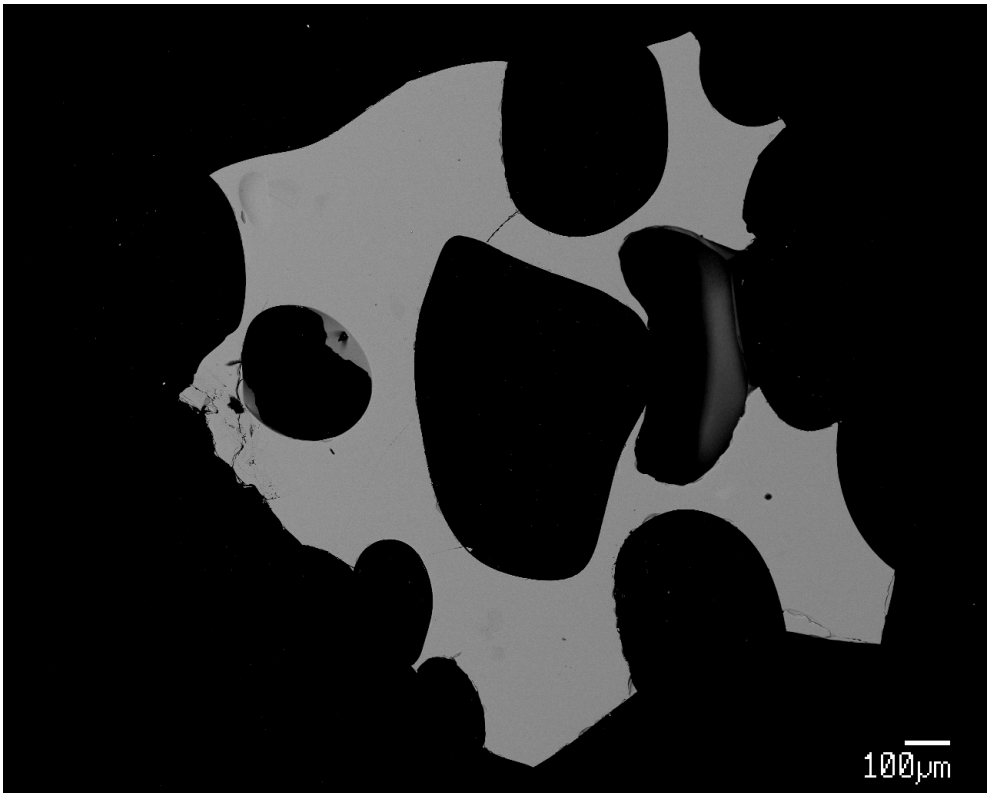

Figure 10.5g. Rock S98-R21, glass chip 02.

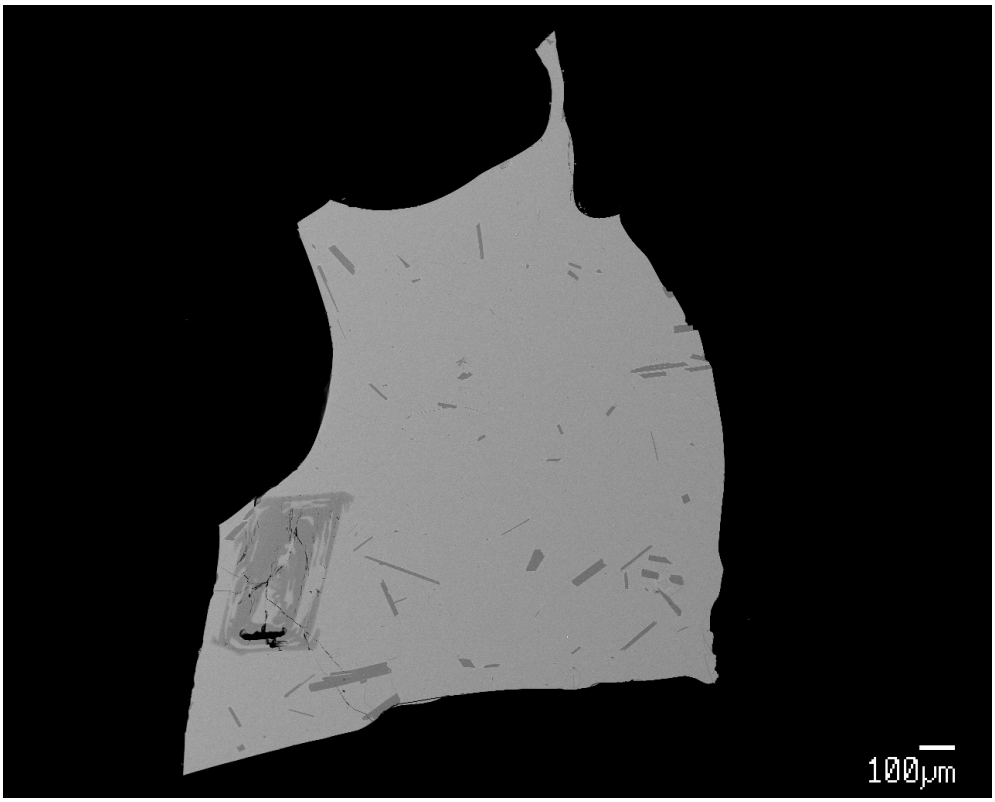

Figure 10.6a. Rock S99-R01, glass chip 02.

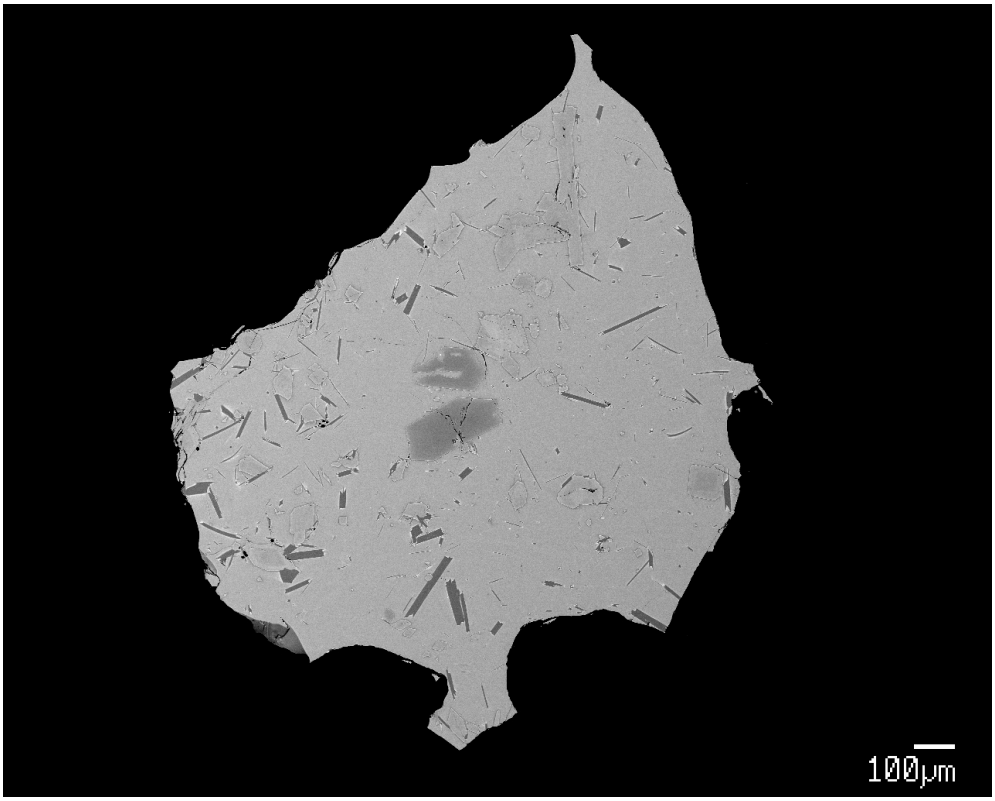

Figure 10.6b. Rock S99-R04, glass chip 01.

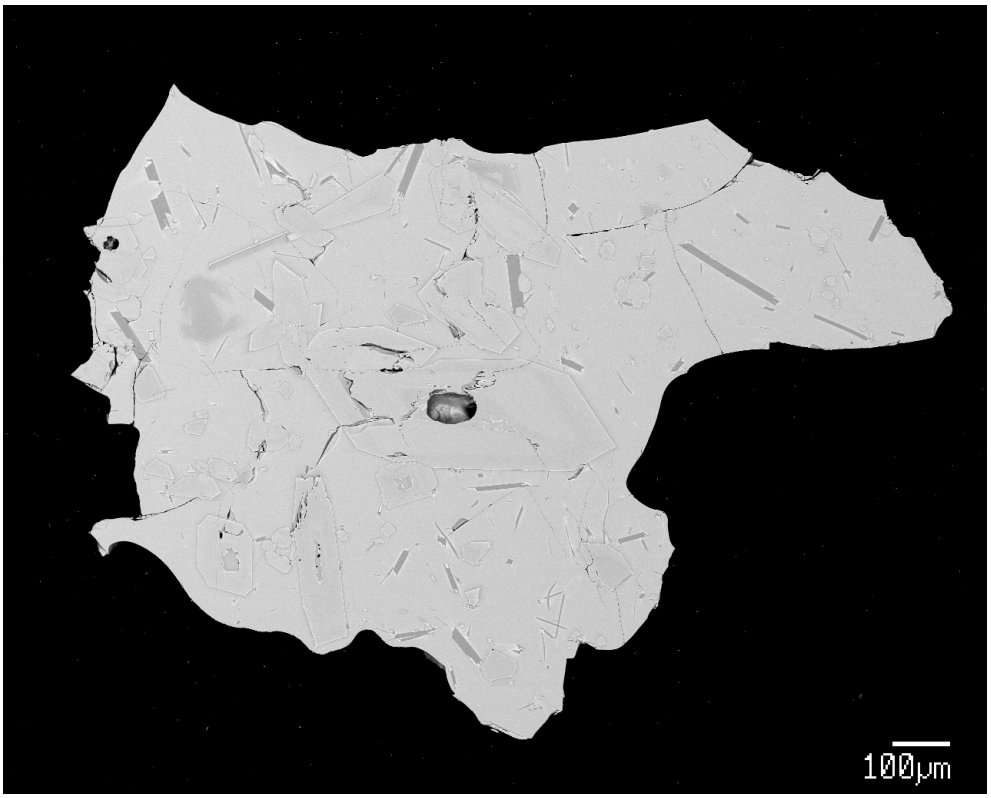

Figure 10.6c. Rock S99-R04, glass chip 05.

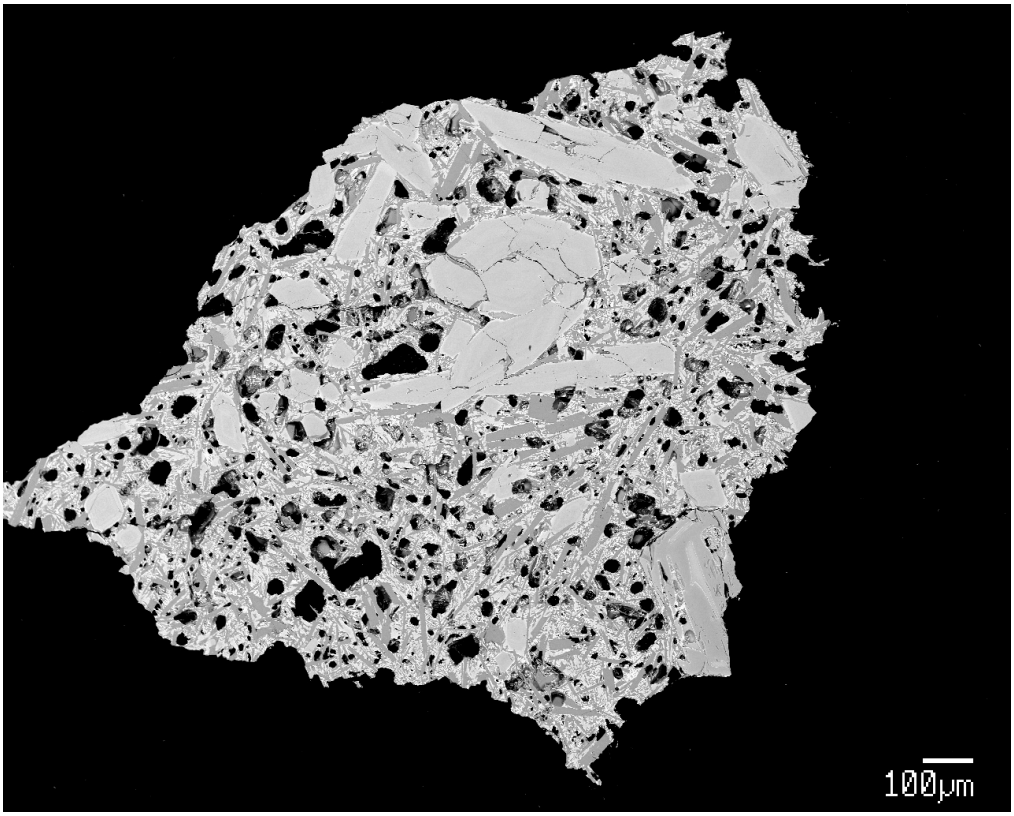

Figure 10.6d. Rock S99-R05, glass chip 03.

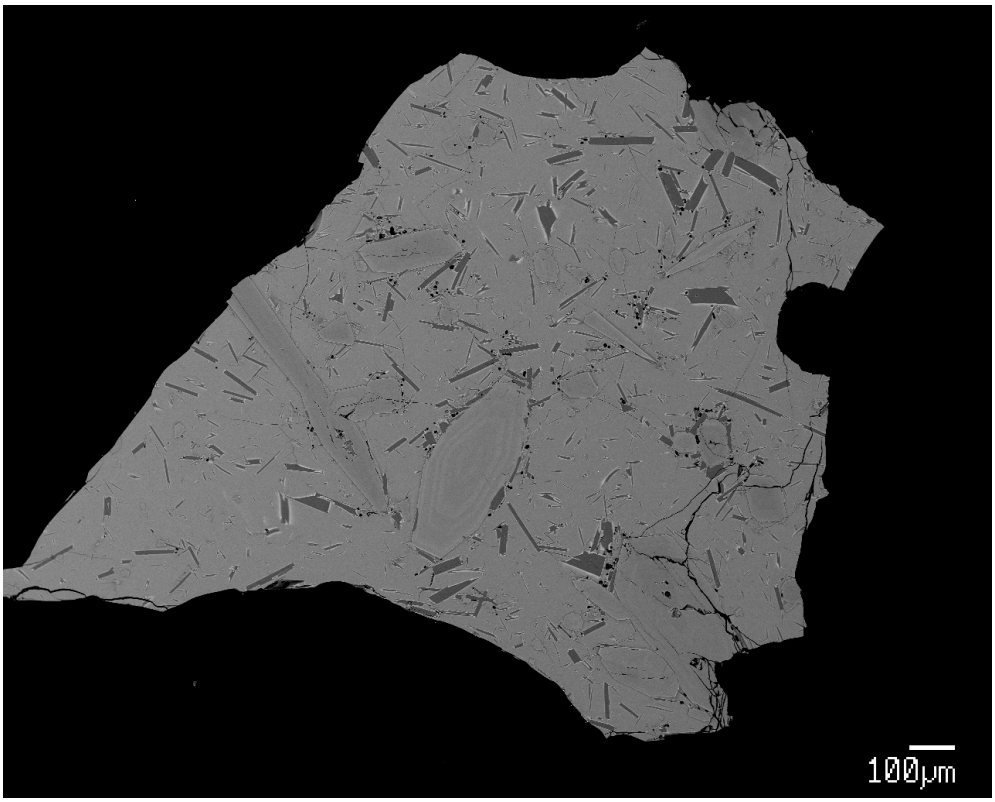

Figure 10.6e. Rock S99-R06, glass chip 03.

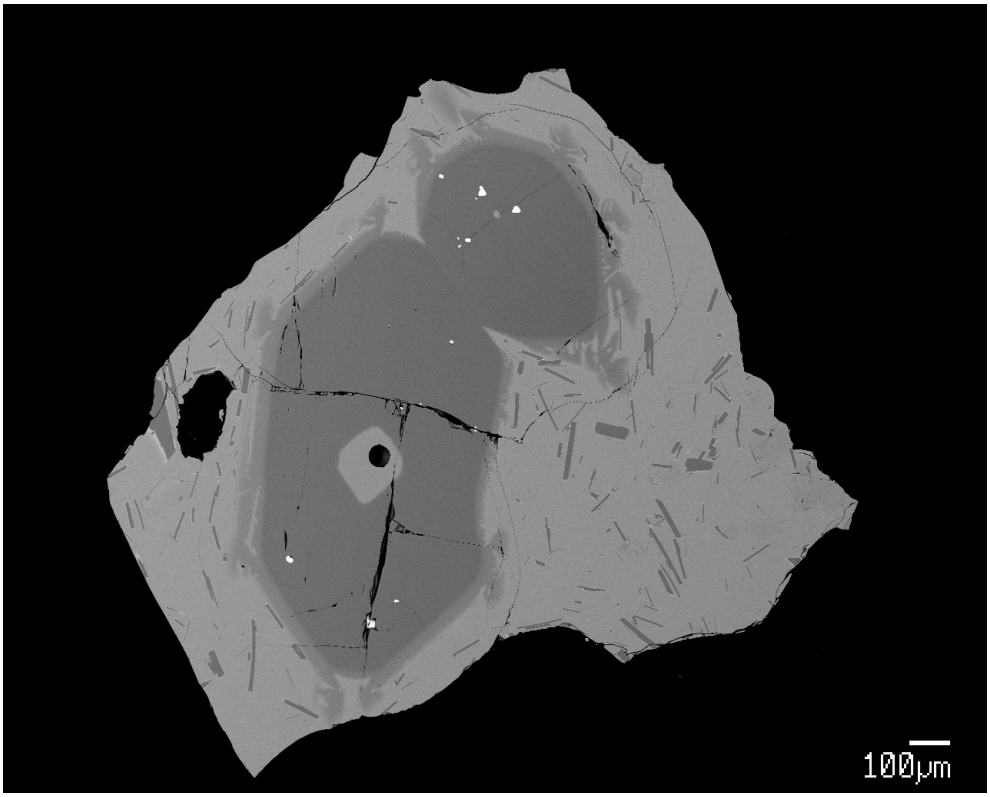

Figure 10.6f. Rock S99-R08, glass chip 01.

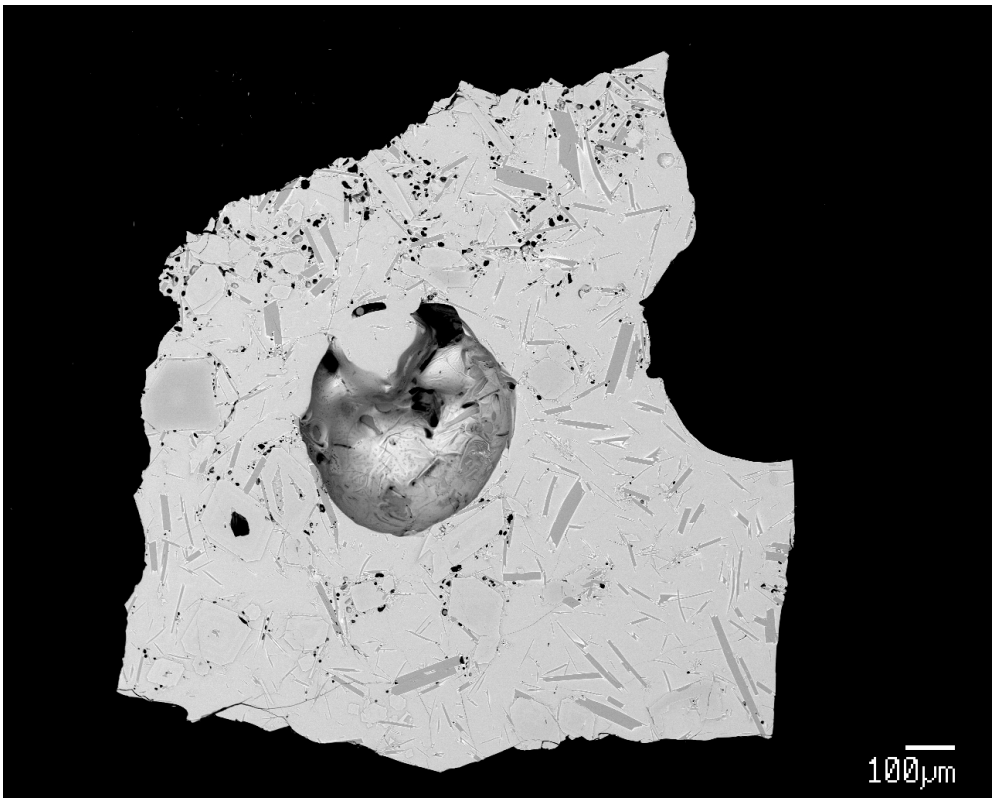

Figure 10.6g. Rock S99-R08, glass chip 05.

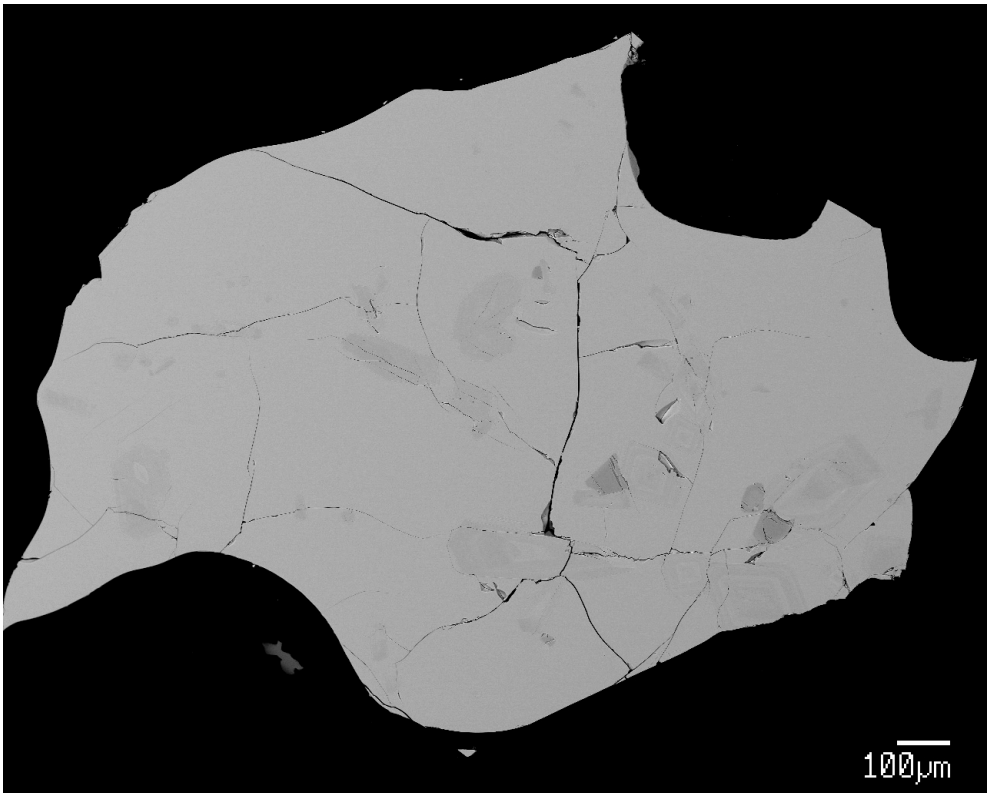

Figure 10.6h. Rock S99-R12, glass chip 03.

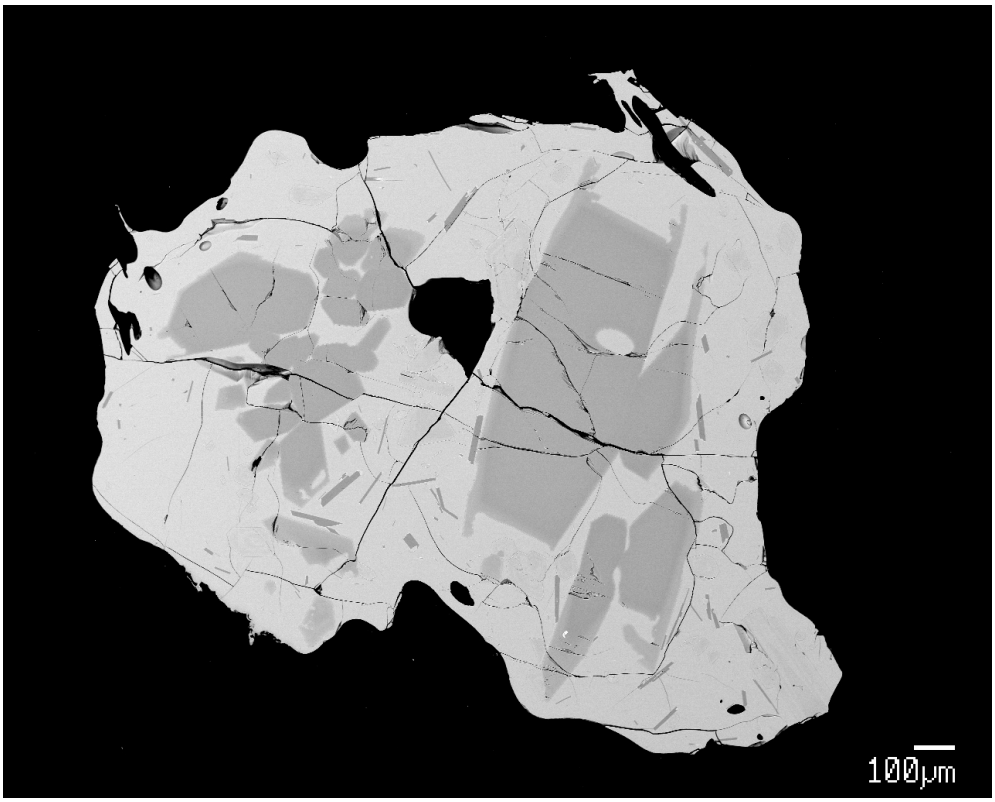

Figure 10.6i. Sediment S99-S15, glass chip 05.

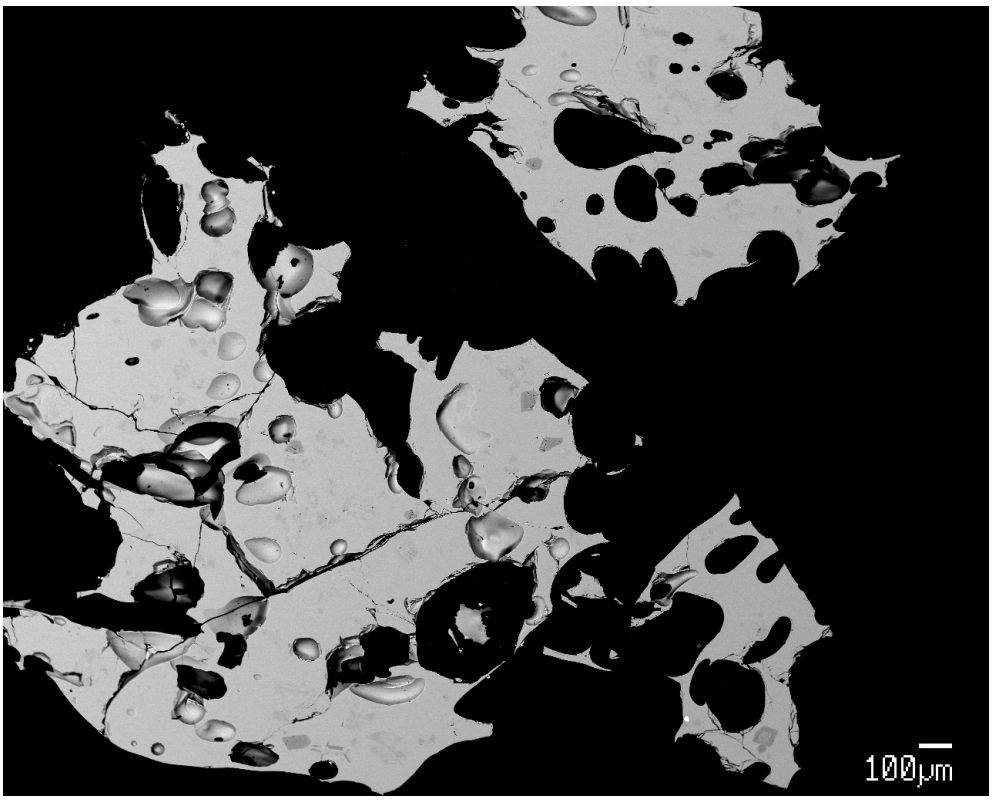

Figure 10.6j. Sediment S99-S25, glass chip 07.

10.4. Appendix D: Additional major element chemistry figures

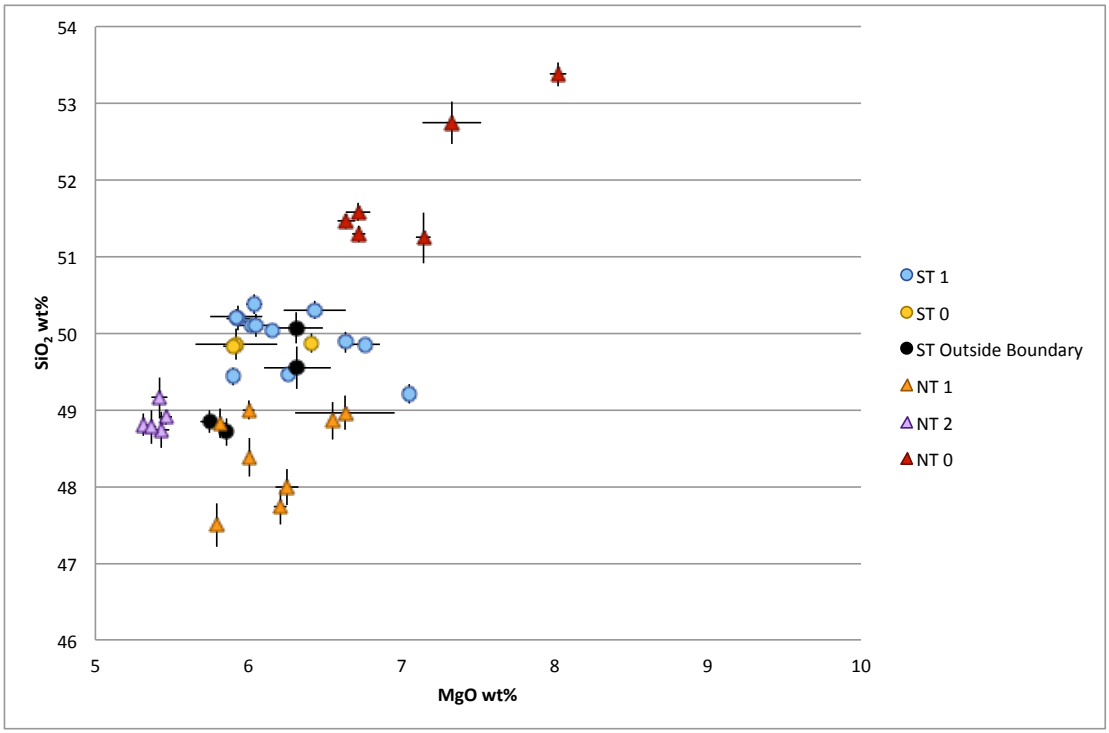

Figure 10.7a. wt.% MgO vs. wt.% SiO2.

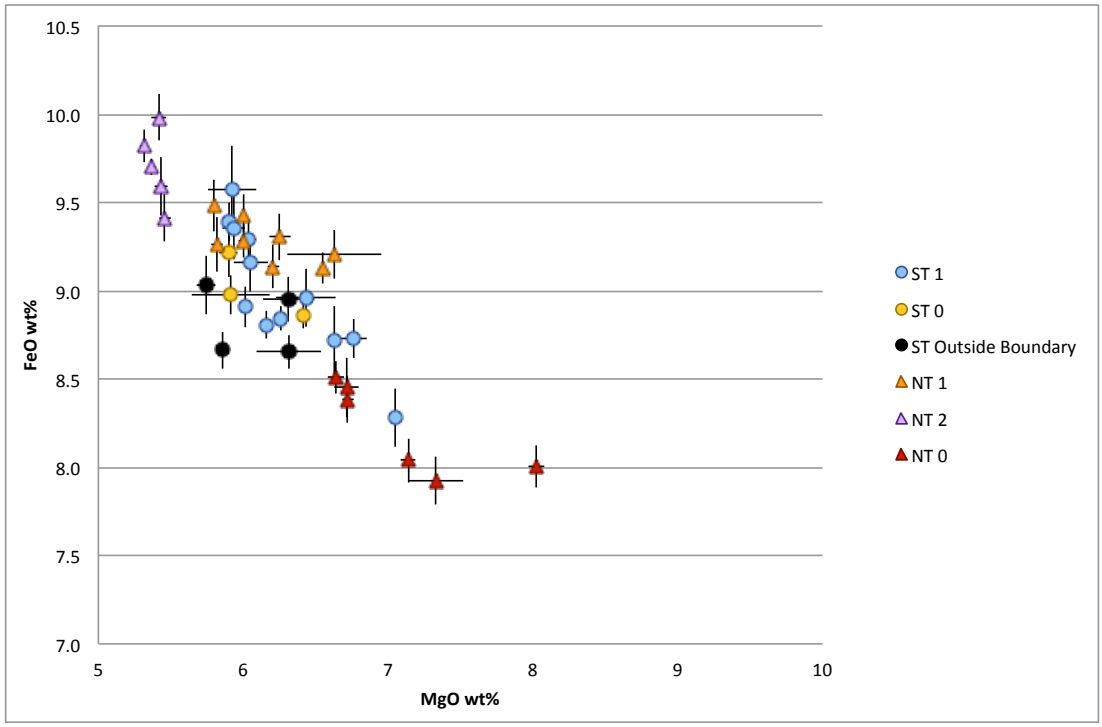

Figure 10.7b. wt.% MgO vs. FeO.

Figure 10.7. Major element compositions of Tafu samples collected from dives S98 and S99.

10.5 Appendix E: Water content figures using >7.6% variation rejection criteria, and no rejection criteria

Procedures for reducing noise in the measured water content of the Tafu samples are described in section 7.3.2. Three procedures were conducted: no rejection, rejection of points outside of 7.6% variation of the mean, and rejection of points outside of 5.5% variation of the mean. Figures showing water content in the main body of text all use the >5.5% variation rejection procedure. Figures using no rejection and >7.6% variation rejection are shown here.

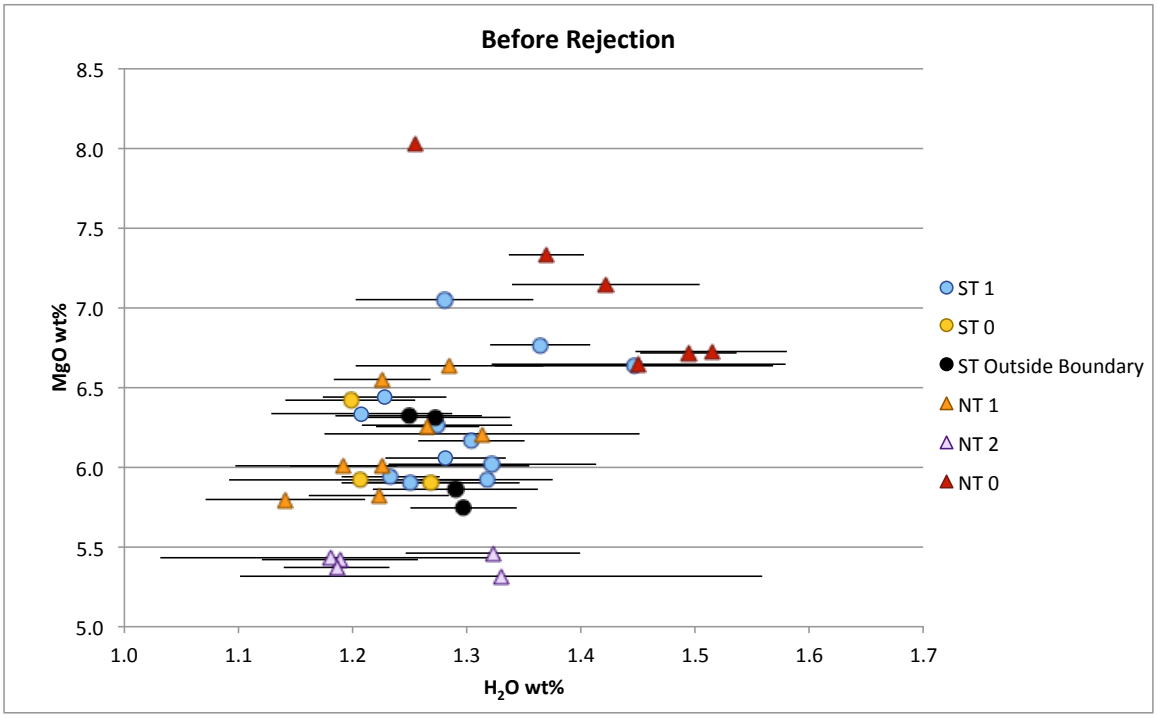

Figure 10.8a.

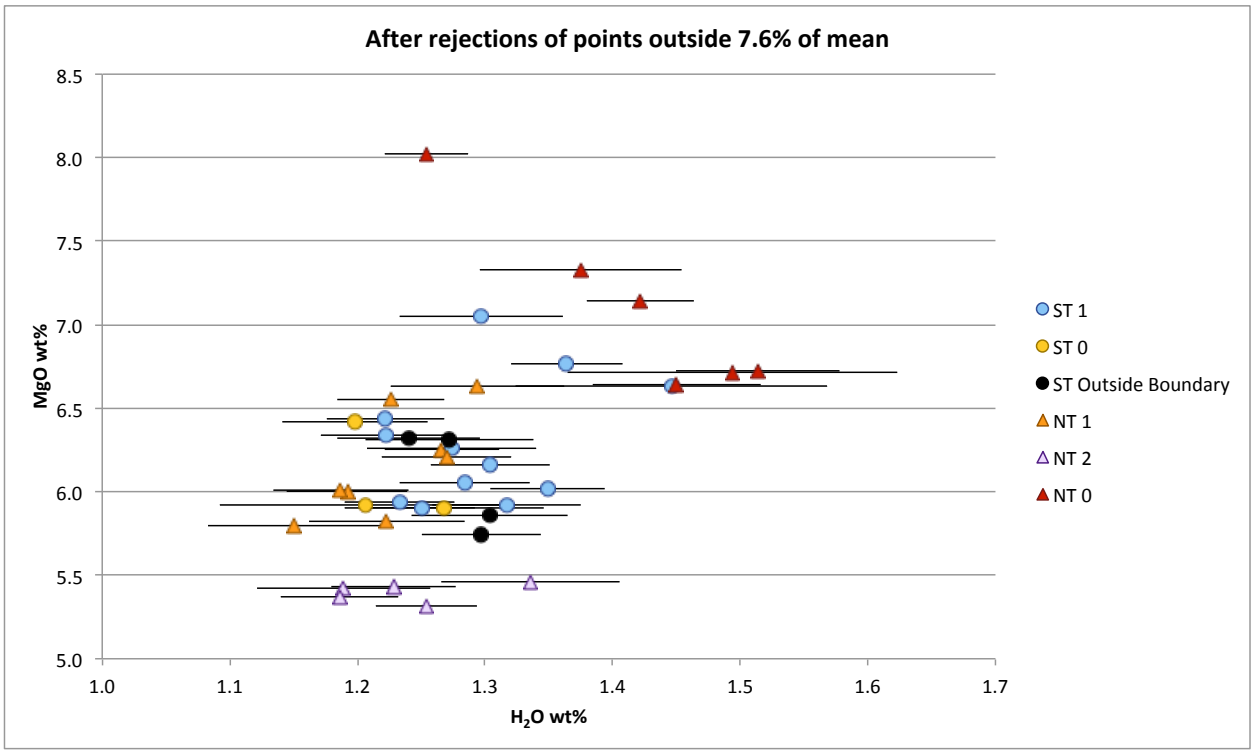

Figure 10.8b. wt.% H_2O vs. wt.% MgO. A has no rejection procedure applied, and B has points rejected for samples whose percent variation is greater than 7.6%. Error bars are one standard deviation.

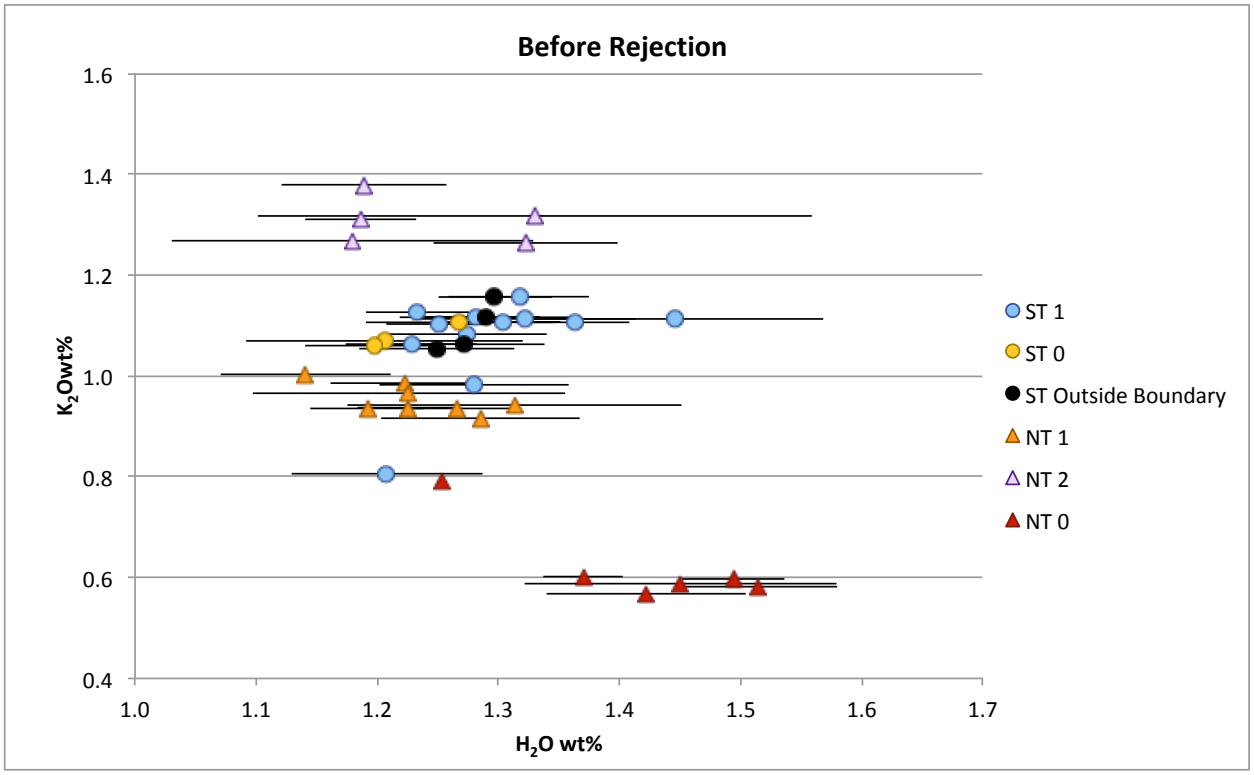

Figure 10.9a.

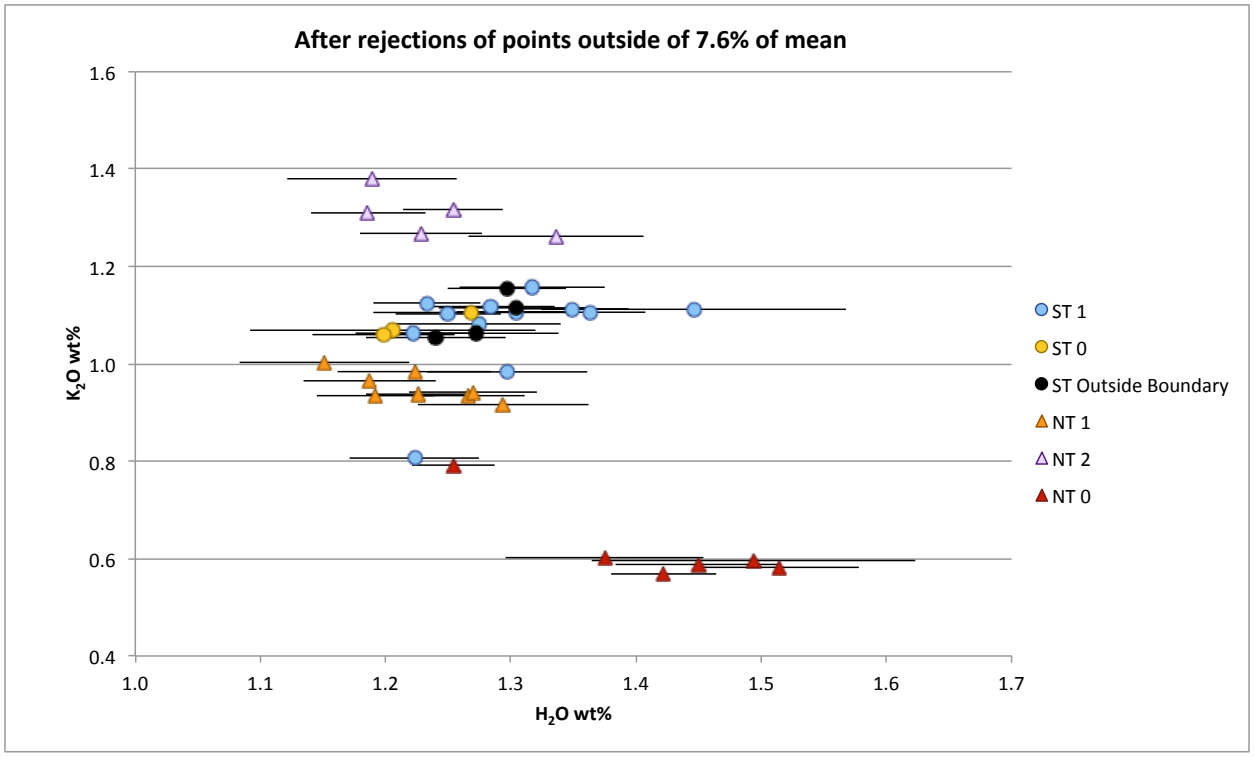

Figure 10.9b. wt.% H_2O vs. wt.% K_2O. A has no rejection procedure applied, and B has points rejected for samples whose percent variation is greater than 7.6%. Error bars are one standard deviation.

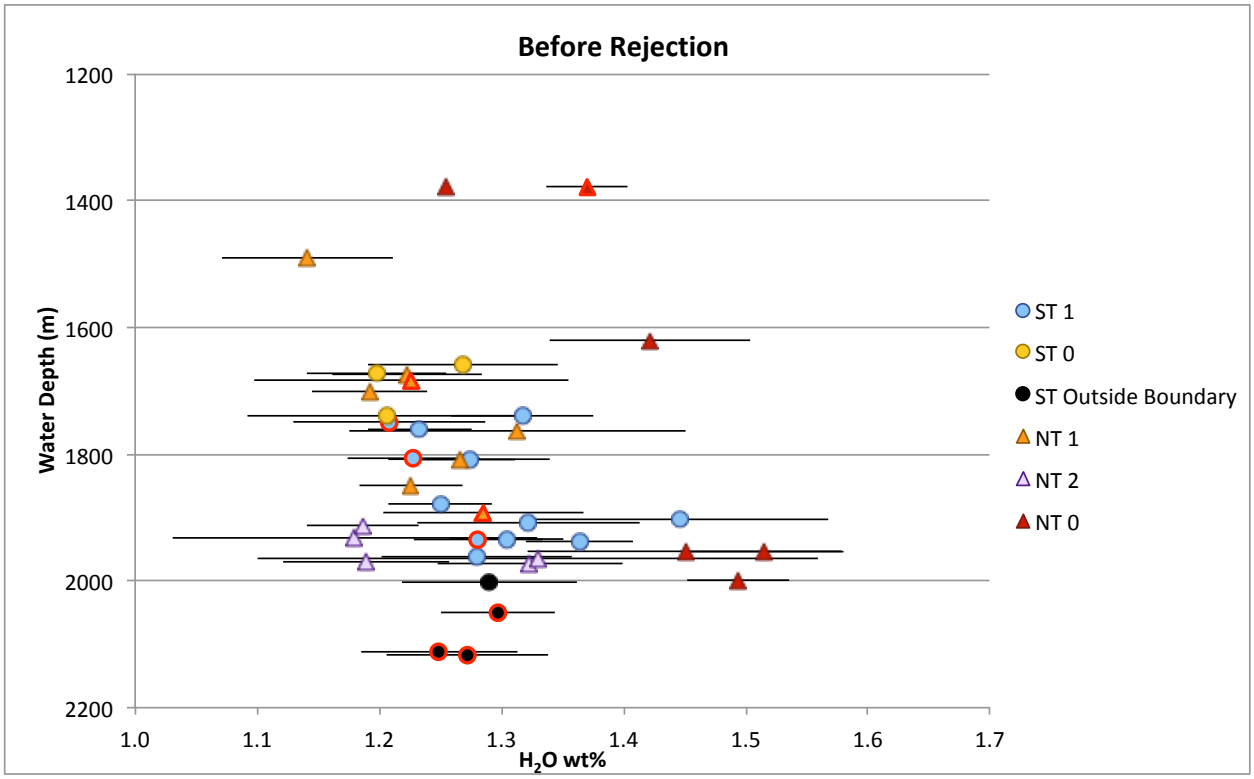

Figure 10.10a.

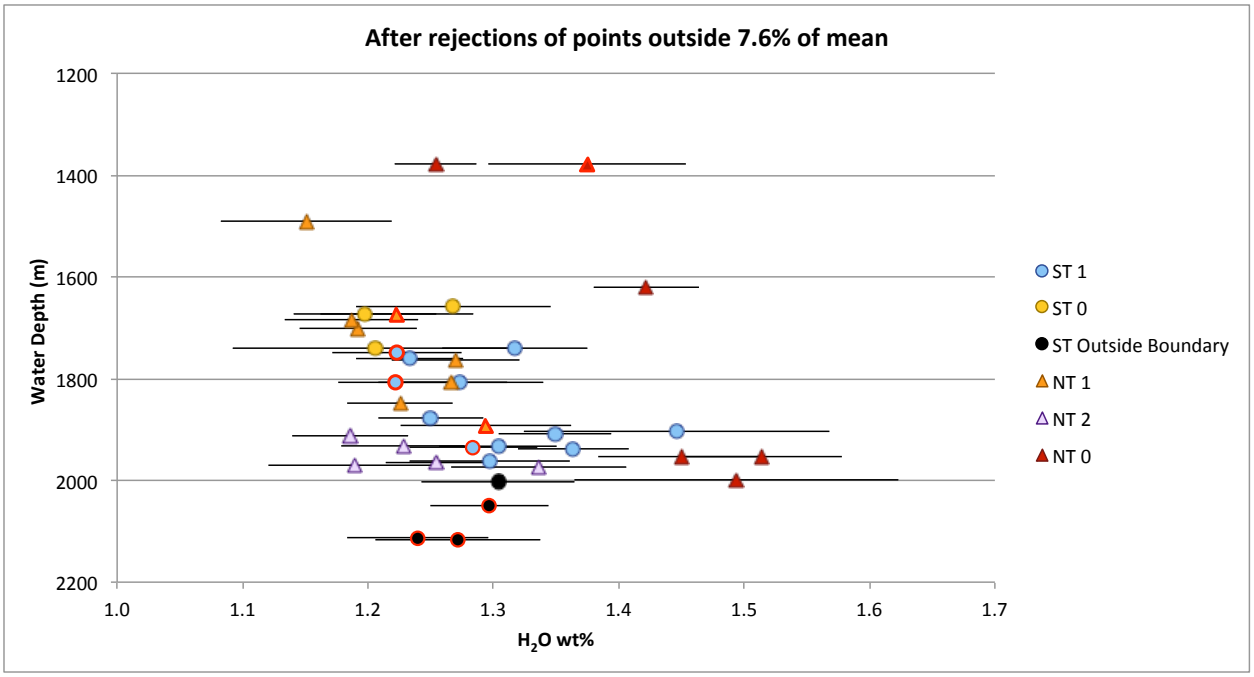

Figure 10.10b. wt.% H_2O vs. water depth. A has no rejection procedure applied, and B has points rejected for samples whose percent variation is greater than 7.6%. Error bars are one standard deviation. Samples that are either talus or sediment are highlighted with a bright red outline.

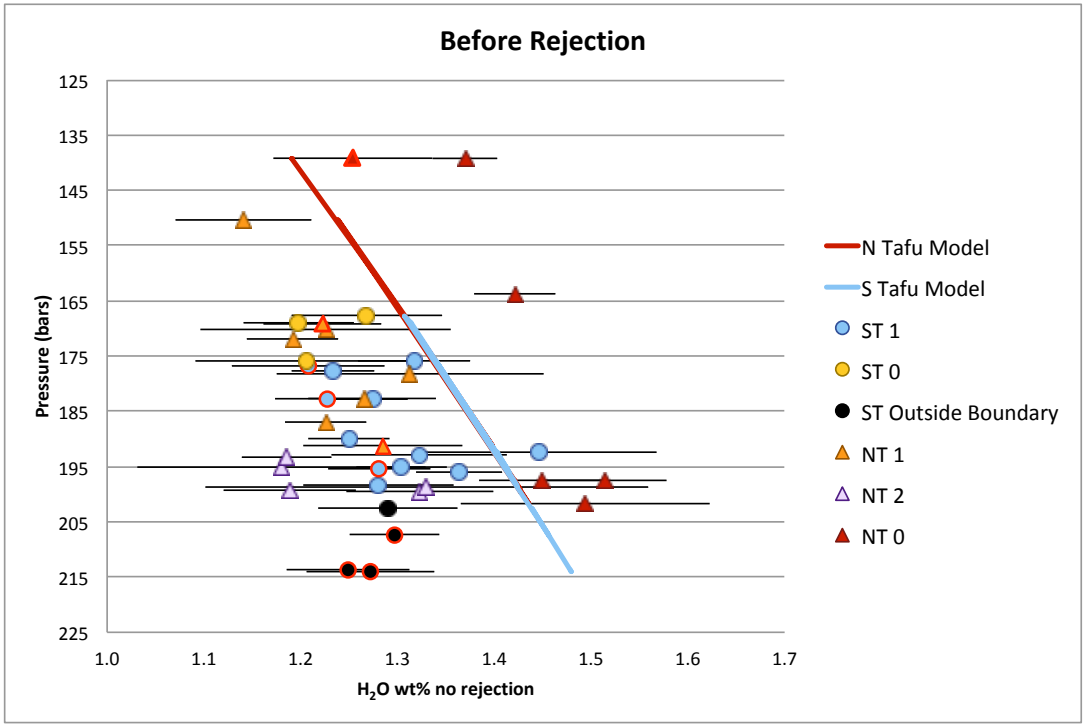

Figure 10.11a.

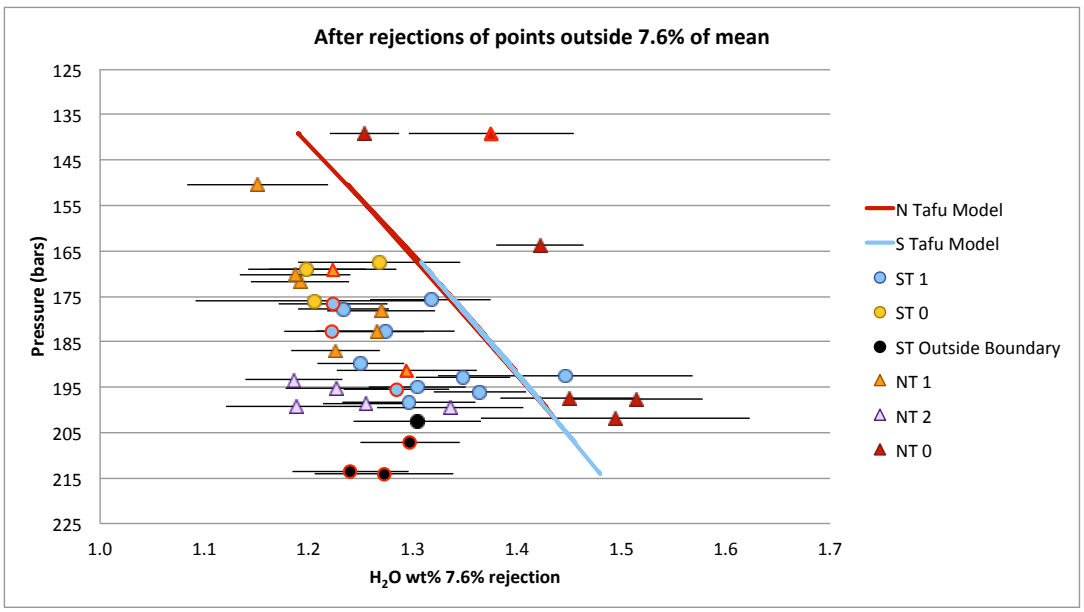

Figure 10.11a. Wt.% H_2O v. pressure in bars. A has no rejection procedure applied, and B has the >7.6% variation rejection procedure applied. Pressure in bars of location of collection of samples was taken from the CTD pressure sensor on the ROV SuBastian. Error bars indicate one standard deviation. Bright red outlines indicate a sample that is either sediment or talus, and therefore could have been erupted at a depth (and therefore pressure) different from the depth the sample was collected. Both North and South Tafu models are from VolatileCalc 2.0 (Newman and Lowenstern, 2002).

10.6 Appendix F: Additional MELTS Models

Many models were completed using MELTS, though only the models of best fit were shown in the main text. Additional MELTS models are shown here. Conditions used for each model are shown in Table 10.1.

Model Name	Parent Melt Composition	Oxygen Fugacity Buffer	Pressure (bars)	wt.% FeO*	wt.% Fe_2O_3*	wt.% SiO_2 *
A1	Parent Melt 1	QFM-1	500	-	-	-
A2	Parent Melt 1	QFM-2	500	-	-	-
A3	Parent Melt 1	QFM-3	500	-	-	-
A4	Parent Melt 1	Ni-NiO	500	-	-	-
B1	Parent Melt 1	QFM-1	400	-	-	-
B2	Parent Melt 1	QFM-2	400	-	-	-
B3	Parent Melt 1	QFM-3	400	-	-	-
B4	Parent Melt 1	Ni-NiO	400	-	-	-
C1	Parent Melt 1	QFM-1	500	-	-	-
C2	Parent Melt 1	QFM-2	500	-	-	-
C3	Parent Melt 1	QFM-3	500	-	-	-
C4	Parent Melt 1	Ni-NiO	500	-	-	-
D1	Parent Melt 2	QFM-3	500	-	-	-
D2	Parent Melt 3	QFM-3	400	-	-	-
E1	Parent Melt 1	QFM-3	400	8.00	-	-
E2	Parent Melt 1	QFM-3	400	-	1.30	-
E3	Parent Melt 1	QFM-3	400	8.00	-	48.50
E4	Parent Melt 1	QFM-3	400	8.00	-	50.00

Figure 10.1. Conditions used for each MELTS model. *indicates that a wt.% is only given here if it has been adjusted from the parent melt composition. Models with no entry in these columns have the same parent melt compositions as those listed in Table 9.1.

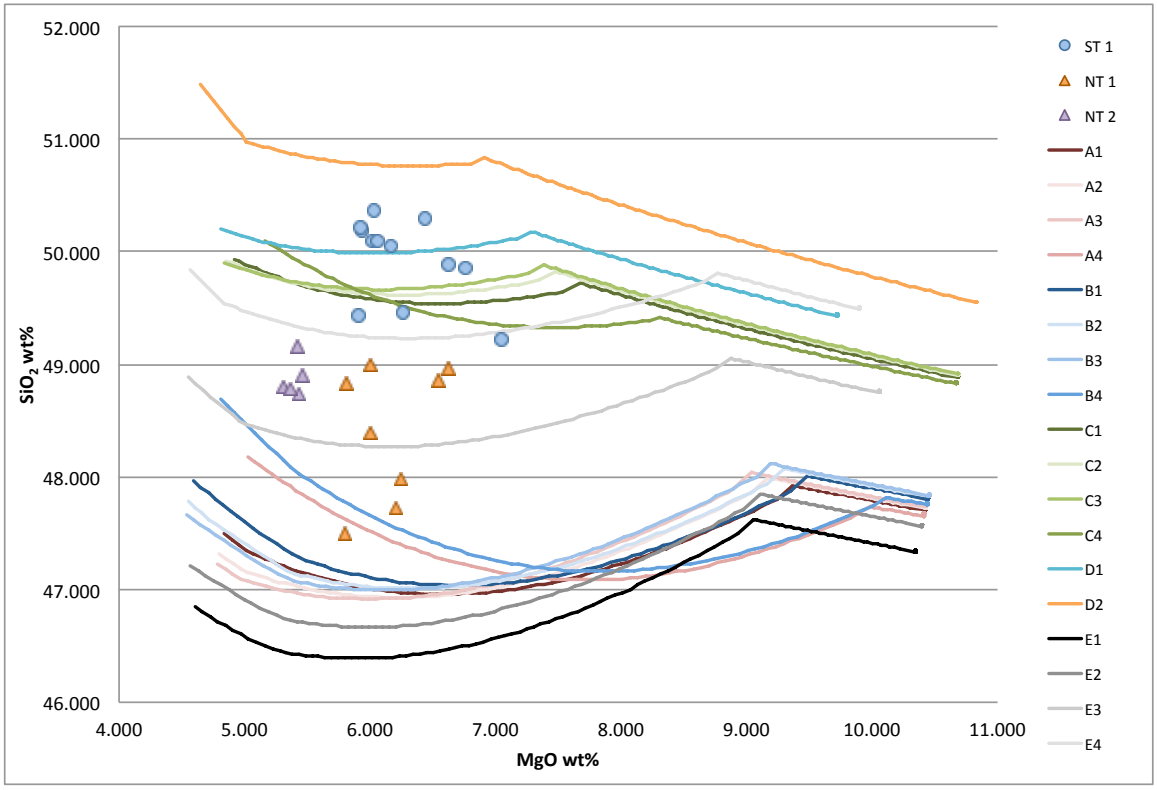

Figure 10.12a. wt.% MgO vs. wt.% SiO_2

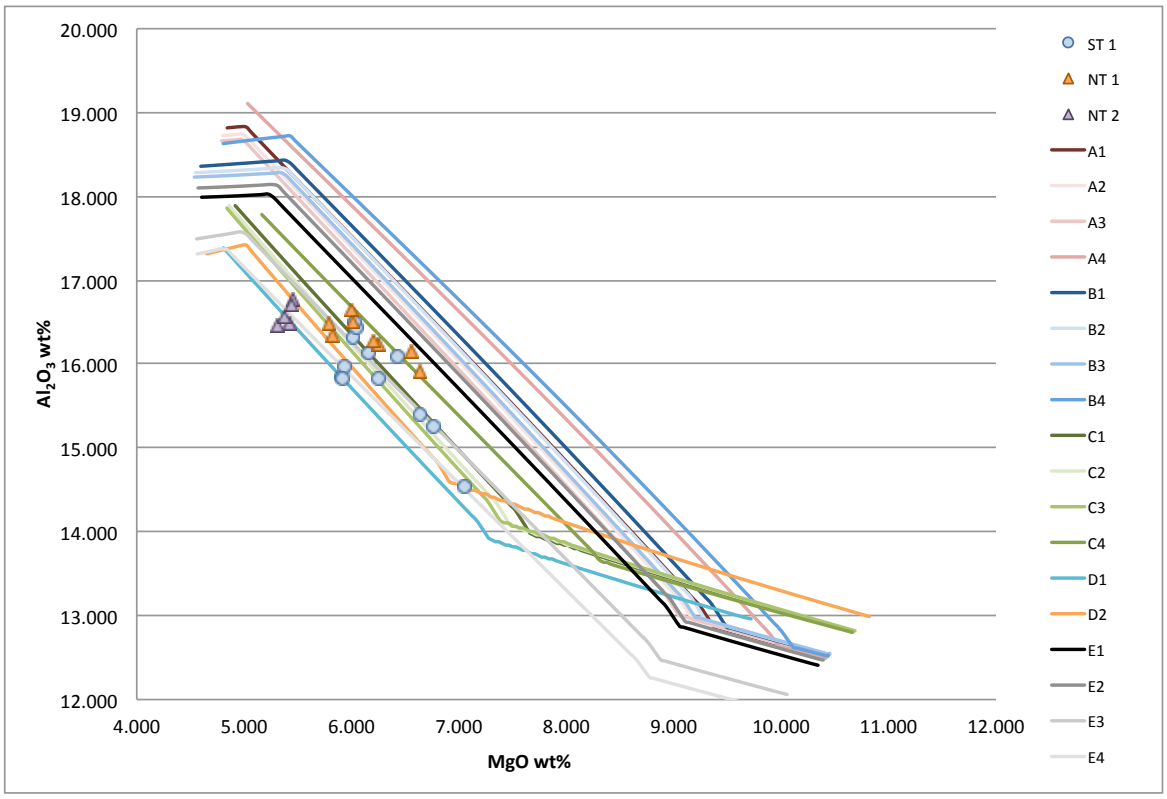

Figure 10.12b. wt.% MgO vs. wt.% Al_2O_3.

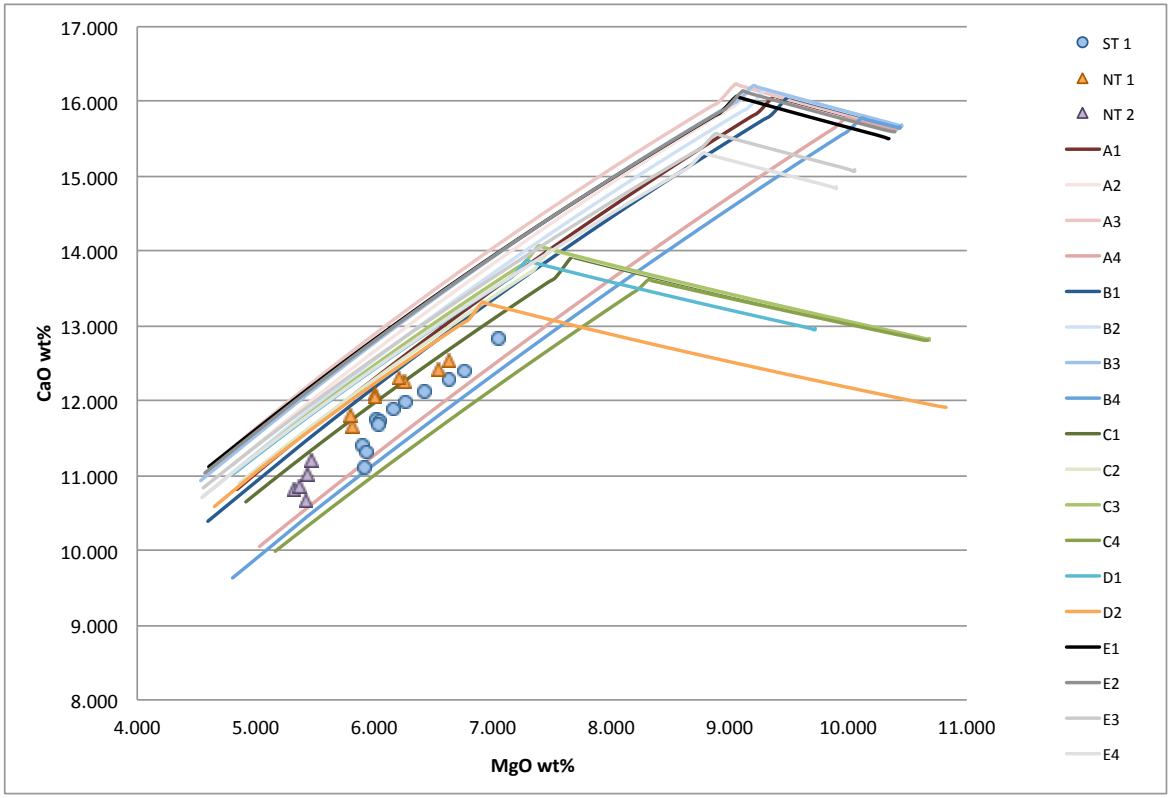

Figure 10.12c. wt.% MgO vs. wt.% CaO.

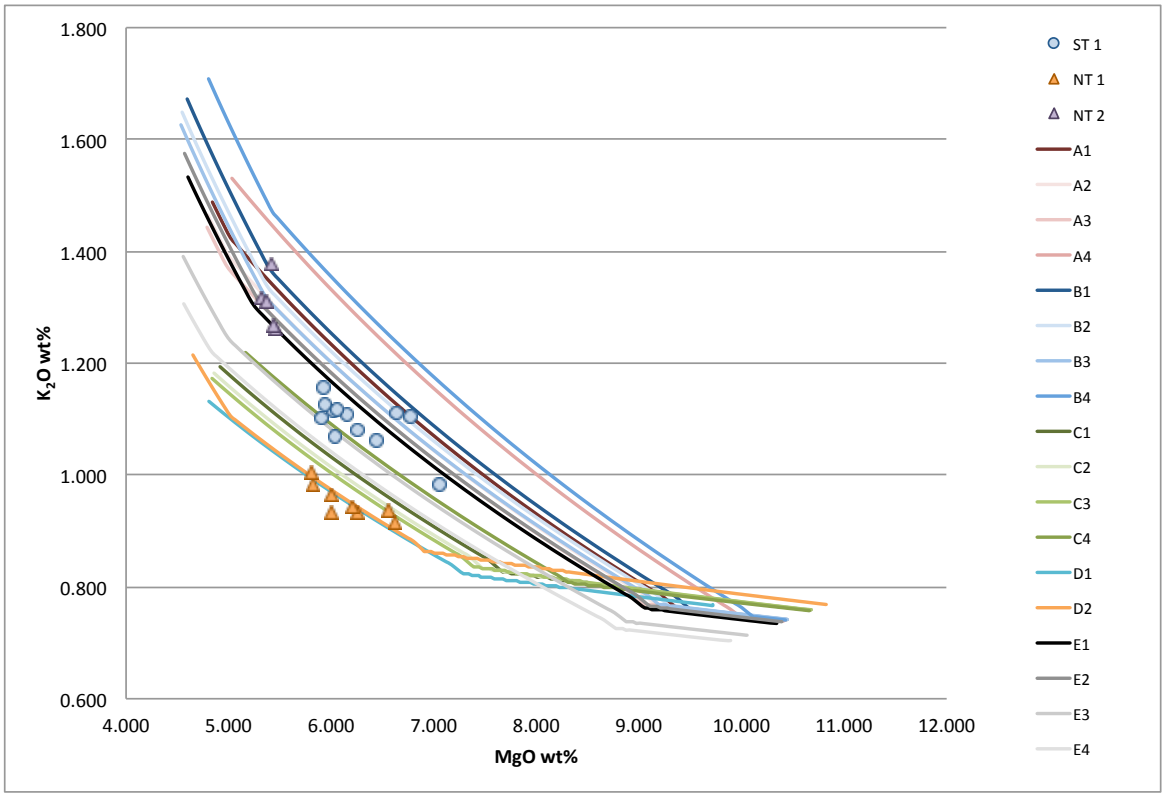

Figure 10.12d. wt.% MgO vs. wt.% K_2O.

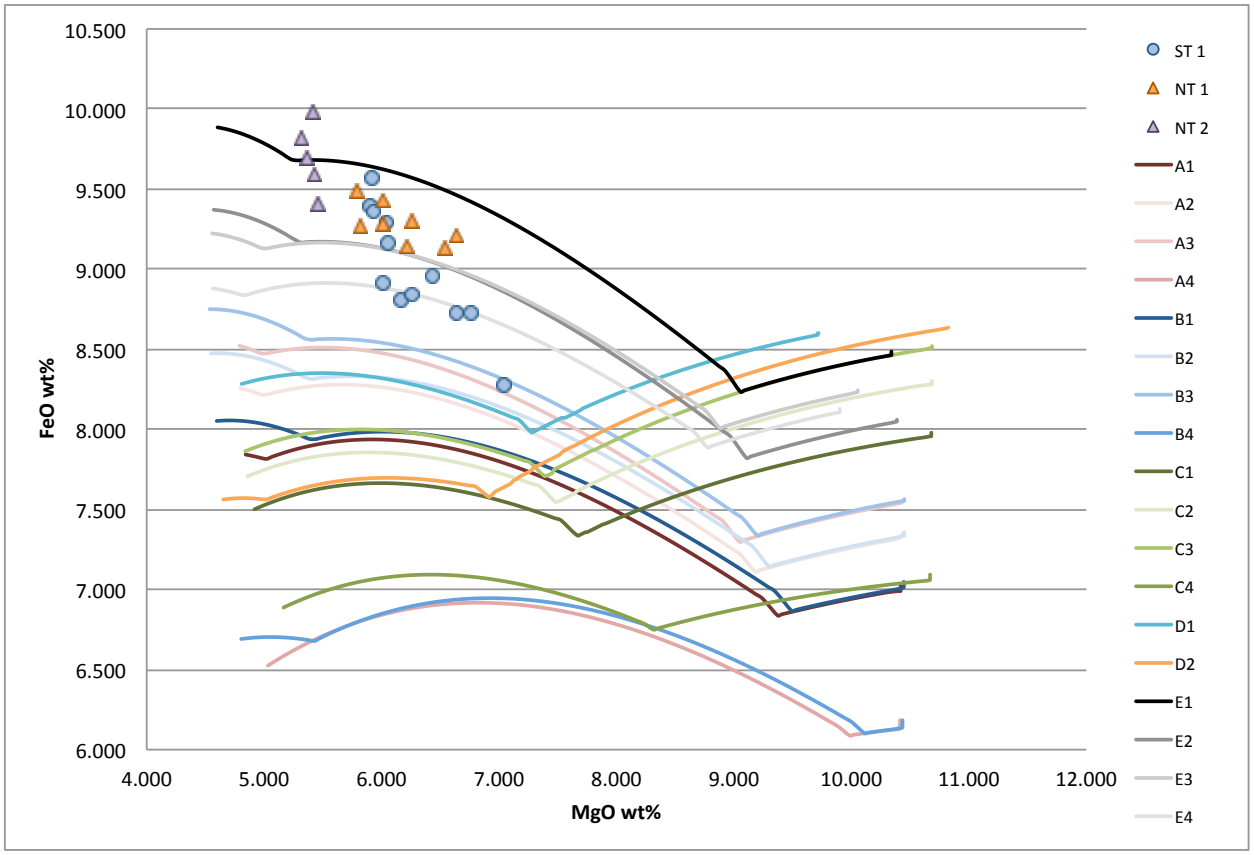

Figure 10.12e. wt.% MgO vs. wt.% FeO.

Figure 10.12. MELTS models shown by colored lines with eruptive groups ST 1, NT 1, and NT 2. Conditions used for each model are in Table 10.1.

11. References

Baker, Edward T., John E. Lupton, Joseph A. Resing, Tamara Baumberger, Marvin D. Lilley, Sharon L. Walker, and Ken H. Rubin. 2011. "Unique event plumes from a 2008 eruption on the Northeast Lau Spreading Center." *Geochemistry, Geophysics, Geosystems* 12 (9):n/a-n/a. doi: 10.1029/2011GC003725.

Baker, Et, Sl Walker, Gj Massoth, and Ja Resing. 2019. "The NE Lau Basin: Widespread and Abundant Hydrothermal Venting in the Back-Arc Region Behind a Superfast Subduction Zone." *Frontiers In Marine Science* 6. doi: 10.3389/fmars.2019.00382.

Ballard, R. D., R. T. Holcomb, and T. H. van Andel. 1979. "Galapagos Rift at 86/sup 0/W: 3. Sheet flows, collapse pits, and lava lakes of the rift valley." *J. Geophys. Res.; (United States)* 84 (B10). doi: 10.1029/JB084iB10p05407.

Bird, Peter. 2003. "An updated digital model of plate boundaries." *Geochemistry, Geophysics, Geosystems* 4 (3):n/a-n/a. doi: 10.1029/2001GC000252.

Bobbitt, Andra, Kenneth Rubin, David Butterfield, Kevin Roe, Tamara Baumberger, Camilla Wilkinson, Sharon Walker, Tim Shank, Walter Cho, Bill Chadwick, and Susan Merle. 2017. 2017 NE Lau Basin Cruise Report FK171110. Schmidt Ocean Institute.

Bonatti, Enrico, C. G. A. Harrison, and John A. Orcutt. 1988. "Eruption styles of basalt in oceanic spreading ridges and seamounts; effect of magma temperature and viscosity." *Journal of Geophysical Research* 93 (B4):2967-2980. doi: 10.1029/JB093iB04p02967.

Caulfield, John, Simon Turner, Richard Arculus, Chris Dale, Frances Jenner, Julian Pearce, Colin Macpherson, and Heather Handley. 2012. "Mantle flow, volatiles, slab-surface temperatures and melting dynamics in the north Tonga arc–Lau back-arc basin." *Journal of Geophysical Research: Solid Earth* 117 (B11):n/a-n/a. doi: 10.1029/2012JB009526.

Edward, T. Baker, W. Chadwick William, Jr., P. Cowen James, P. Dziak Robert, H. Rubin Kenneth, and J. Fornari Daniel. 2012. "Hydrothermal Discharge During Submarine Eruptions: The Importance of Detection, Response, and New Technology." *Oceanography (Washington, D.C.)* 25 (1):128-141. doi: 10.5670/oceanog.2012.11.

Embley, Robert, and Kenneth Rubin. 2018. "Extensive young silicic volcanism produces large deep submarine lava flows in the NE Lau Basin." *Bulletin of Volcanology* 80 (4):1-23. doi: 10.1007/s00445-018-1211-7.

Fox, Christopher G., Kim Marie Murphy, and Robert W. Embley. 1988. "Automated display and statistical analysis of interpreted deep-sea bottom photographs." *Marine Geology* 78 (3):199-216. doi: 10.1016/0025-3227(88)90109-0.

Ghiorso, Mark, and Guilherme Gualda. 2015. "An H 2 O–CO 2 mixed fluid saturation model compatible with rhyolite-MELTS." *Contributions to Mineralogy and Petrology* 169 (6):1-30. doi: 10.1007/s00410-015-1141-8.

Glancy, Sarah. 2011. Submarine Lava Morphology. In *GG 711*.

Gregg, Tracy K. P., and Jonathan H. Fink. 1995. "Quantification of submarine lava-flow morphology through analog experiments." *Geology (Boulder)* 23 (1):73-76. doi: 10.1130/0091-7613(1995)023<0073:QOSLFM>2.3.CO;2.

Gualda, Guilherme A. R., Mark S. Ghiorso, Robin V. Lemons, and Tamara L. Carley. 2012. "Rhyolite-MELTS: a Modified Calibration of MELTS Optimized for Silica-rich, Fluid-bearing Magmatic Systems." *Journal of Petrology* 53 (5):875-890. doi: 10.1093/petrology/egr080.

Hannington, Mark. 2016. "East Meets West: The Cutting Edge of the Pacific Plate." Schmidt Ocean Institute.

Hawkins, James W., Jr. 1995. *The geology of the Lau Basin*. Edited by Brian Taylor. New York, NY: Plenum Press.

National Museum of Natural History. 2019a. Smithsonian Microbeam Standards Datasheets. In *Basaltic Glass*.

National Museum of Natural History. 2019b. Smithsonian Microbeam Standards Datasheets. In *Basaltic Glass*.

Iacovino, Kayla. 2017. "Tools for Petrologists." WordPress.

Jarosewich, E., J. A. Nelen, and Julie A. Norberg. 1980. "Reference Samples for Electron Microprobe Analysis*." *Geostandards Newsletter* 4 (1):43-47. doi: 10.1111/j.1751-908X.1980.tb00273.x.

Kim, Jonguk, Seung-Kyu Son, Ju-Won Son, Kyeong-Hong Kim, Won Joon Shim, Chang Hwan Kim, and Kyeong-Yong Lee. 2009. "Venting sites along the Fonualei and Northeast Lau spreading centers and evidence of hydrothermal activity at an off-axis caldera in the northeastern Lau Basin." *Geochemical Journal* 43 (1):1-13. doi: 10.2343/geochemj.0.0164.

Le Losq, Charles, Daniel R. Neuville, Roberto Moretti, and Jacques Roux. 2012. "Determination of water content in silicate glasses using Raman spectrometry; implications for the study of explosive volcanism." *American Mineralogist* 97 (5-6):779-790. doi: 10.2138/am.2012.3831.

Le Maitre, R. W, A Streckeisen, B Zanettin, M. J Le Bas, B Bonin, and P Bateman. *Igneous Rocks: A Classification and Glossary of Terms: Recommendations of the International Union of Geological Sciences Subcommission on the Systematics of Igneous Rocks*, 2002.

Lupton, John, Ken H. Rubin, Richard Arculus, Marvin Lilley, David Butterfield, Joseph Resing, Edward Baker, and Robert Embley. 2015. "Helium isotope, C/3He, and Ba-Nb-Ti signatures in the northern Lau Basin: Distinguishing arc, back-arc, and hotspot affinities." *Geochemistry, Geophysics, Geosystems* 16 (4):1133-1155. doi: 10.1002/2014GC005625.

Luyendyk, Bruce P., and Ken C. MacDonald. 1985. "A geological transect across the crest of the East Pacific Rise at 21 degrees N latitude made from the deep submersible Alvin." *Marine Geophysical Researches* (4):467-488.

Merle, Susan, Robert Embley, John Lupton, Ed Baker, Joseph Resing, Marvin Lilley, and Sharon Walker. 2008. Northeast Lau Bain R/V *Thompson* Expedition TN227. Oregon State University NOAA Vents Program

Merle, Susan, Joseph Resing, Edward Baker, John Lupton, Cornel de Ronde, Richard Arculus, Sharon Walker, Nathan Buck, Eric Olsen, Pam Barrett, and Kenneth Rubin. 2010. 2010 NE Lau Basin R/V *Kilo Moana* Expedition KM1008.

Merle, Susan, Joseph Resing, Robert Embley, Bill Chadwick, Kenneth Rubin, Andra Bobbitt, Paula Keener, Peter Crowhurst, Simon Richards, Fabio Caratori Tontini, Tim Shank, Bradley M. Tebo, Richard E. Davis, Carolyn J. Sheehan, Kerry McPhail, Mark Zabriskie, Dave Butterfield, Eric Olson, John Lupton, Edward Baker, Sharon Walker, Nathan Buck, and Matt Fowler. 2012. Submarine Ring of Fire - 2012 (SRoF-12) Northeast Lau Basin. R/V *Roger Revelle* Expedition RR1211.: NOAA VENTS Program NOAA West Coast Charter Ship Fund Office of Ocean Exploration and Research GNS Science Nautilus Minerals Inc. .

Merle, Susan, Joseph Resing, Robert Embley, Akel Kevin-Stirling, Ken Rubin, Nicole Keller, Dave Clague, Dave Caress, Tim Shank, Liz Podowski, Julie Huber, Rick Davis, Anna Louise Reysenbach, James Cowen, Huei-Ting Lin, David Butterfield, Tamara Baumberger, Marvin Lilley, John Lupton, Leigh Evans, Sharon Walker, and Nathan Buck. 2009. Northeast Lau Basin Response Cruise (NELRC) R/V *Thomas G. Thompson* Expedition TN-234. National Science Foundation National Oceanographic and Atmospheric Administration

Merle, Susan, Kenneth Rubin, Ron Greene, and Sharon Walker. 2010. NE Lau Basin Rock Dredging Expedition. R/V *Kilo Moana* KM1024.: National Science Foundation National Oceanographic and Atmospheric Administration University of Hawai‘i.

Newman, Sally, and Jacob B. Lowenstern. 2002. "VolatileCalc: a silicate melt–H2O–CO2 solution model written in Visual Basic for excel." *Computers and Geosciences* 28 (5):597-604. doi: 10.1016/S0098-3004(01)00081-4.

Rubin, Kenneth H., S. Adam Soule, William W. Chadwick, Daniel J. Fornari, David A. Clague, Robert W. Embley, Edward T. Baker, Michael R. Perfit, David W. Caress, and Robert P. Dziak. 2012. "Volcanic Eruptions in the Deep Sea." *Oceanography* 25 (1):142-157. doi: 10.5670/oceanog.2012.12.

Shea, Thomas, Eric Hellebrand, Lucia Gurioli, and Hugh Tuffen. 2014. "Conduit- to Localized-scale Degassing during Plinian Eruptions: Insights from Major Element and Volatile (Cl and H 2 O) Analyses within Vesuvius ad 79 Pumice." *Journal of Petrology* 55 (2):315-344. doi: 10.1093/petrology/egt069.

Smith, Ian E. M., and Richard C. Price. 2006. "The Tonga–Kermadec arc and Havre–Lau back-arc system: Their role in the development of tectonic and magmatic models for the western Pacific." *Journal of Volcanology and Geothermal Research* 156 (3):315-331. doi: 10.1016/j.jvolgeores.2006.03.006.

Taylor, Brian, and Fernando Martinez. 2003. "Back-arc basin basalt systematics." *Earth and Planetary Science Letters* 210 (3-4):481-497. doi: 10.1016/S0012-821X(03)00167-5.

Van Keken, Peter E., Bradley R. Hacker, Ellen M. Syracuse, and Geoff A. Abers. 2011. "Subduction factory: 4. Depth-dependent flux of H 2 O from subducting slabs worldwide." *Journal of Geophysical Research: Solid Earth* 116 (B1):n/a-n/a. doi: 10.1029/2010JB007922.

Wiens, Douglas A., Katherine A. Kelley, and Terry Plank. 2006. "Mantle temperature variations beneath back-arc spreading centers inferred from seismology, petrology, and bathymetry." *Earth and Planetary Science Letters* 248 (1):30-42. doi: 10.1016/j.epsl.2006.04.011.

Zellmer, Ke, and B. Taylor. 2001. "A three-plate kinematic model for Lau Basin opening." *Geochemistry Geophysics Geosystems* 2.